

SLAC-R-628

UC-414

# BRANCHING FRACTION AND TIME-DEPENDENT CP ASYMMETRY IN NEUTRAL B DECAYS TO PSI AND A NEUTRAL PION<sup>1</sup>

Aron L. Soha

Stanford Linear Accelerator Center  
Stanford University  
Stanford, CA 94309

SLAC-Report-628

May 2003

Prepared for the Department of Energy  
under contract number DE-AC03-76SF00515

Printed in the United States of America. Available from the National Technical Information Service, U.S. Department of Commerce, 5285 Port Royal Road, Springfield, VA 22161.

---

<sup>1</sup>Ph.D. thesis, Stanford University, Stanford, CA 94309.

I certify that I have read this dissertation and that, in my opinion, it is fully adequate in scope and quality as a dissertation for the degree of Doctor of Philosophy.

---

Aaron Roodman  
(Principal Adviser)

I certify that I have read this dissertation and that, in my opinion, it is fully adequate in scope and quality as a dissertation for the degree of Doctor of Philosophy.

---

Patricia Burchat

I certify that I have read this dissertation and that, in my opinion, it is fully adequate in scope and quality as a dissertation for the degree of Doctor of Philosophy.

---

Michael Peskin

I certify that I have read this dissertation and that, in my opinion, it is fully adequate in scope and quality as a dissertation for the degree of Doctor of Philosophy.

---

Charles Prescott

Approved for the University Committee on Graduate Studies:

# Abstract

The invariance of physical laws under the combination of exchange of particles with antiparticles (charge conjugation,  $C$ ) and reversal of coordinates (parity,  $P$ ) is called  $CP$  symmetry. The violation of  $CP$  symmetry was first discovered in 1964 in the neutral kaon system, and is in general one of the great puzzles of particle physics. The recent observation of  $CP$  violation in the  $B$  meson system has been a simultaneous success for model predictions and experiment. The opportunity now exists to probe details of the underlying mechanisms.

This thesis presents measurements of the branching fraction and time-dependent  $CP$ -violating asymmetry in neutral  $B$  decays to  $J/\psi\pi^0$ . The decay amplitude for this channel features both tree and penguin diagram contributions, the interference of which can yield a result for the asymmetry differing from that found in the “golden mode”  $B^0 \rightarrow J/\psi K_S^0$ . Using the measured branching fraction and  $CP$  asymmetry, constraints are placed on the ratio of penguin to tree amplitudes in  $B^0 \rightarrow J/\psi\pi^0$ . In addition, the impact on the  $CP$  asymmetry measurement in  $B^0 \rightarrow J/\psi K_S^0$  is discussed.

The results are presented for  $e^+e^-$  annihilation data collected with the *BABAR* detector on the  $\Upsilon(4S)$  resonance at the PEP-II asymmetric-energy  $B$  Factory at SLAC. The measurement of the branching fraction, based on about 23 million  $B\bar{B}$  pairs collected between October 1999 and October 2000, yields  $\text{BF}(B^0 \rightarrow J/\psi\pi^0) = (2.0 \pm 0.6 \text{ (stat)} \pm 0.2 \text{ (syst)}) \times 10^{-5}$ . With about 88 million  $B\bar{B}$  pairs collected during the years 1999–2002, our results for the coefficients of the cosine and sine terms of the  $CP$  asymmetry are  $C_{J/\psi\pi^0} = 0.38 \pm 0.41 \text{ (stat)} \pm 0.09 \text{ (syst)}$  and  $S_{J/\psi\pi^0} = 0.05 \pm 0.49 \text{ (stat)} \pm 0.16 \text{ (syst)}$ .

# Acknowledgements

For providing me with the upbringing, opportunities, and support that motivated me and allowed me to pursue my interests, I thank my parents, Linda and Jim. I also thank my Sister, Jill, for joining my parents in setting the best of examples, and my Grandparents and Uncles for their love and wisdom.

I fully appreciate the efforts of all who have contributed to my education at Stanford and SLAC. I will forever be grateful to my principal adviser, Aaron Roodman, who generously shared his time, enthusiasm, and skills to work with and guide me, both as collaborator and mentor. I've recognized the value of our frequent discussions, and I am extremely proud to be his first student. I also thank Jonathan Dorfman, who helped attract me to Stanford. I extend my sincere appreciation to the members of my dissertation committee, Patricia Burchat, Michael Peskin, and Charles Prescott, who have helped me throughout my graduate career, with discussions, guidance, and classroom lectures. Thanks to Susan Holmes for chairing the committee. I thank Vera Lüth, for providing guidance and a valuable group environment. Thanks to Blair Ratcliff and Rafe Schindler for projects during my first year. Thanks to Art Snyder, Helen Quinn, Steve Wagner, and Mike Kelsey for discussions. I also thank David Coupal, Masahiro Morii, David Nelson, Karl Bouldin, and Jim McDonald, with whom I worked on hardware projects.

For playing roles in my earlier physics education, I am grateful to Richard Edelman, Arnold Engler, Thomas Ferguson, Stephen Garoff, Fred Gilman, Jim Russ, Reinhard Schumacher, Robert Schumacher, and the many others from whom I learned at Carnegie Mellon University.

During every stage of my life, I have had the fortune of wonderful friendships. I sincerely thank the following for what they have given and for what we have shared: Stuart and Danny Abrams, Berzas Bichnevicius, Patrick Cormier, Alex Werner, Keith Bacon, Mark Felton, Mark House, Jonathan Olsen, Ben Sullivan, Mike Quilty, Chris Adukaitis, Jay Blanco, Jim Buck, Elias Fallon, Brian Humensky, Aron Ralston, Ronak Singhal, Dave Barkin, Tim and Danielle Braje, Danielle Javier, George Marcus, Tarek Saab, Molly Uhl, and longtime friend and roommate Craig Johnson.

# Contents

<b>Abstract</b>	<b>iv</b>
<b>Acknowledgements</b>	<b>v</b>
<b>1 Introduction</b>	<b>1</b>
1.1 Historical Perspective . . . . .	1
1.2 Why $B^0 \rightarrow J/\psi \pi^0$ ? . . . . .	6
1.3 The <i>BABAR</i> Collaboration . . . . .	7
<b>2 Theory of Time-Dependent <math>B</math> Decays</b>	<b>9</b>
2.1 The Standard Model . . . . .	9
2.2 Discrete Transformations: $C$ , $P$ , and $T$ . . . . .	11
2.3 Neutral $B$ -Meson Flavor Oscillations . . . . .	14
2.4 Neutral $B$ -Meson $CP$ Asymmetry . . . . .	16
2.4.1 Three Types of $CP$ Violation . . . . .	16
2.4.2 The CKM Matrix and the Unitarity Triangle . . . . .	17
2.4.3 Tree and Penguin Amplitudes . . . . .	19
2.4.4 Observable Quantities . . . . .	22
<b>3 The <i>BABAR</i> Detector at PEP-II</b>	<b>25</b>
3.1 Overview of PEP-II . . . . .	25
3.2 The <i>BABAR</i> Detector . . . . .	30
3.2.1 Silicon Vertex Tracker . . . . .	34
3.2.2 Drift Chamber . . . . .	37

3.2.3	Particle Identification . . . . .	45
3.2.4	Electromagnetic Calorimeter . . . . .	48
3.2.5	Instrumented Flux Return . . . . .	53
<b>4</b>	<b>Branching Fraction of <math>B^0 \rightarrow J/\psi \pi^0</math> Decays</b>	<b>60</b>
4.1	Introduction . . . . .	60
4.2	Data Sample and <i>BABAR</i> Software Releases . . . . .	61
4.3	Candidate Pre-selection . . . . .	61
4.3.1	$B$ -Counting . . . . .	62
4.3.2	Lepton Pre-selection . . . . .	63
4.3.3	Photon Pre-selection . . . . .	64
4.4	Final Candidate Selection . . . . .	65
4.4.1	Final $J/\psi$ selection . . . . .	65
4.4.2	Final $\pi^0$ Selection . . . . .	67
4.4.3	Formation of $B$ Candidates . . . . .	67
4.5	Signal Region and Event Selection Variables . . . . .	68
4.5.1	$m_{ES}$ and $\Delta E$ . . . . .	68
4.5.2	Thrust Angle . . . . .	69
4.5.3	Lepton Helicity Angle . . . . .	69
4.5.4	Additional Angular Variables Studied . . . . .	72
4.6	Cut Optimization . . . . .	72
4.7	Background Studies . . . . .	75
4.7.1	Overall Background Strategy . . . . .	75
4.7.2	The $J/\psi_{\text{fake}}$ Sample . . . . .	76
4.7.3	Continuum $u\bar{u}/d\bar{d}/s\bar{s}$ and $c\bar{c}$ . . . . .	78
4.7.4	<i>Offpeak</i> Data . . . . .	79
4.7.5	Generic $B\bar{B}$ . . . . .	79
4.7.6	Inclusive $J/\psi$ . . . . .	82
4.7.7	$B^0 \rightarrow J/\psi K_S^0$ ( $K_S^0 \rightarrow \pi^0\pi^0$ ) Feed-Through . . . . .	82
4.8	Results from <i>Onpeak</i> Data . . . . .	85
4.8.1	Background Extracted from Data . . . . .	85

4.8.2	Cross-Check Using the $\Delta E$ Sidebands . . . . .	85
4.8.3	Event Counting Cross-Check . . . . .	89
4.8.4	Additional Background Study Using Loose Selection . . . . .	89
4.8.5	Systematic Uncertainties . . . . .	89
4.8.6	Efficiency Corrections . . . . .	94
4.8.7	Yield, Purity, and Branching Fraction . . . . .	95
4.8.8	Statistical Significance of the Result . . . . .	96
<b>5</b>	<b>Time-Dependent <math>CP</math> Asymmetry in <math>B^0 \rightarrow J/\psi \pi^0</math></b>	<b>98</b>
5.1	Introduction . . . . .	98
5.2	Data Samples and Software Releases . . . . .	99
5.2.1	Data Sample . . . . .	99
5.2.2	Data Reconstruction Software Releases . . . . .	100
5.2.3	Monte Carlo Simulation Reconstruction Software Releases . . . . .	100
5.2.4	Reduced collections . . . . .	100
5.2.5	Analysis Releases . . . . .	101
5.3	Candidate Selection . . . . .	102
5.4	Event Selection Variables . . . . .	103
5.4.1	$m_{ES}$ . . . . .	103
5.4.2	$\Delta E$ . . . . .	104
5.4.3	Fisher Discriminant . . . . .	104
5.4.4	Correlations Among Analysis Variables . . . . .	118
5.5	Sources of Background and Strategy . . . . .	119
5.5.1	$B^0 \rightarrow J/\psi K_S^0(\pi^0\pi^0)$ . . . . .	121
5.5.2	Inclusive $J/\psi$ . . . . .	122
5.5.3	$B\bar{B}$ Generic . . . . .	122
5.5.4	Continuum . . . . .	124
5.6	PDFs for Event Selection Variables . . . . .	125
5.6.1	A Few Words About the Likelihood Fitting Technique . . . . .	125
5.6.2	$m_{ES}$ . . . . .	126
5.6.3	$\Delta E$ . . . . .	128

5.6.4	Fisher Discriminant . . . . .	132
5.7	Likelihood Fits for Yields, as Consistency Check . . . . .	133
5.7.1	Implementation of Unbinned Maximum Likelihood Fits . . . . .	133
5.7.2	Yield Fits to Single Signal and Background Samples . . . . .	135
5.7.3	Yield Fits to Mixtures of Samples . . . . .	136
5.8	Vertexing and $\Delta t$ . . . . .	145
5.9	Flavor Tagging . . . . .	146
5.9.1	The Moriond Tagger . . . . .	146
5.9.2	Tagging Results for Signal and Background Samples . . . . .	147
5.9.3	Tagging Dependence Study of Event Selection Variables and $\Delta t$ . . . . .	147
5.10	Probability Density Functions for $\Delta t$ . . . . .	154
5.10.1	Signal $B^0 \rightarrow J/\psi \pi^0$ . . . . .	154
5.10.2	$B^0 \rightarrow J/\psi K_s^0(\pi^0\pi^0)$ Background . . . . .	155
5.10.3	Inclusive $J/\psi$ Background . . . . .	159
5.10.4	$B\bar{B}$ Generic Background . . . . .	161
5.10.5	Continuum Background . . . . .	161
5.11	$CP$ Asymmetry Likelihood Fits . . . . .	161
5.11.1	Fit Implementation . . . . .	161
5.11.2	Blinding Strategy . . . . .	165
5.11.3	Time-Dependent Fits to Mixtures of Samples . . . . .	165
5.11.4	Time-Dependent Fit to Full Dataset . . . . .	166
5.12	Systematic Studies . . . . .	172
5.12.1	Variation of PDF Parameters and Tagging Fractions . . . . .	172
5.12.2	Additional Systematics . . . . .	178
5.12.3	Systematics in Common with the “golden modes” . . . . .	179
5.12.4	Summary of Systematic Uncertainties . . . . .	179
5.13	Cross-checks . . . . .	180
5.13.1	Larger Variation of Parameters . . . . .	180
5.13.2	Validation of the Fisher on an Alternate Data Sample . . . . .	180
5.13.3	Monte Carlo Samples with Different Asymmetries . . . . .	180
5.13.4	Toy Monte Carlo Study . . . . .	182

5.13.5	<i>CP</i> Fit, Including the Fisher as a PDF . . . . .	182
5.13.6	<i>CP</i> Fit, Fixing the Signal $\Delta E$ Peak Position to the Monte Carlo Value . . . . .	184
5.13.7	<i>CP</i> Fit, Cutting on Both the Fisher and $\Delta E$ . . . . .	184
5.14	Summary of <i>CP</i> Asymmetry Results . . . . .	184
<b>6</b>	<b>Conclusions</b>	<b>190</b>
6.1	Branching Fraction Measurement . . . . .	190
6.2	Time-Dependent <i>CP</i> Asymmetry Measurement . . . . .	192
6.3	Final Thoughts . . . . .	200
<b>A</b>	<b>IFR Cable Mapping and Chamber Alignment</b>	<b>201</b>
A.1	IFR Signal Readout Cable Mapping . . . . .	201
A.2	IFR Chamber Alignment . . . . .	206
<b>B</b>	<b>Study of RPC Efficiency Loss</b>	<b>209</b>
B.1	Motivation . . . . .	209
B.2	Experimental Apparatus . . . . .	209
B.3	Findings . . . . .	212
	<b>Bibliography</b>	<b>221</b>

# List of Tables

2.1	Quarks and leptons of the Standard Model . . . . .	10
2.2	Gauge bosons of the Standard Model . . . . .	10
2.3	Field bilinear term properties under discrete transformations . . . . .	13
3.1	Design parameters and typical performance for PEP-II . . . . .	27
3.2	Specifications and voltage settings for drift chamber wires . . . . .	40
3.3	Properties of CsI(Tl), used in the calorimeter . . . . .	50
4.1	Electron selectors . . . . .	65
4.2	Muon selectors . . . . .	66
4.3	Summary of background contributions in branching fraction measurement . . . . .	84
4.4	Cross-check of backgrounds in $\Delta E$ sideband . . . . .	88
4.5	Candidate counting cross-check in $\Delta E$ - $m_{ES}$ plane . . . . .	90
4.6	Cross-check of backgrounds using loose selection . . . . .	91
4.7	Candidate counting cross-check using loose selection . . . . .	91
4.8	Systematic uncertainties for branching fraction analysis . . . . .	94
4.9	Efficiency corrections . . . . .	95
4.10	Results of the branching fraction measurement . . . . .	96
5.1	Monte Carlo simulation releases and run ranges . . . . .	101
5.2	Correlations among variables considered for Fisher . . . . .	111
5.3	Optimized coefficients for the final Fisher discriminant . . . . .	115
5.4	Correlations among event selection variables . . . . .	118

5.5	Signal and background samples . . . . .	121
5.6	<i>Offpeak</i> data samples used . . . . .	125
5.7	Results of yield fits to single samples . . . . .	142
5.8	Yield fit results for two mixtures of signal and background samples . . . . .	143
5.9	Tagging algorithm performance . . . . .	147
5.10	Tagging results for signal Monte Carlo sample . . . . .	148
5.11	Tagging results for background samples . . . . .	148
5.12	Tagging results for <i>onpeak</i> data sample . . . . .	148
5.13	Resolution and physics model parameters from $B_{\text{flav}}$ sample . . . . .	157
5.14	Tagging fractions for signal and background samples . . . . .	165
5.15	Efficiencies for tagging, cut on Fisher, and expectations for $81 \text{ fb}^{-1}$ . . . . .	166
5.16	Results of $CP$ likelihood fits to mixtures of samples . . . . .	167
5.17	Results of a $CP$ fit to <i>onpeak</i> data . . . . .	169
5.18	Systematics from variation of event selection PDF parameters . . . . .	174
5.19	Systematics from variation of the tagging fractions . . . . .	175
5.20	Systematics from variation of $\Delta t$ PDF parameters (part 1) . . . . .	176
5.21	Systematics from variation of $\Delta t$ PDF parameters (part 2) . . . . .	177
5.22	Summary of systematic uncertainties . . . . .	179
5.23	Results of $CP$ fits using alternate configurations . . . . .	185
A.1	Cabling errors in IFR . . . . .	206
B.1	Efficiency and current changes in RPC test stand . . . . .	218

# List of Figures

1.1	Tree and penguin Feynman diagrams for $B^0 \rightarrow J/\psi \pi^0$ . . . . .	6
2.1	Mixing followed by decay . . . . .	17
2.2	The unitarity triangle . . . . .	19
3.1	Aerial view of the SLAC site . . . . .	26
3.2	Drawing of the linac and PEP-II beam-lines . . . . .	28
3.3	Luminosity and currents of PEP-II on one day . . . . .	30
3.4	Integrated luminosity for October 1999 through June 2002 . . . . .	31
3.5	Side-view drawing of the <i>BABAR</i> detector . . . . .	32
3.6	End-view drawing of the <i>BABAR</i> detector . . . . .	33
3.7	Photograph of the Silicon Vertex Tracker (SVT) and support . . . . .	34
3.8	Diagram of the $xy$ cross-section of the SVT . . . . .	35
3.9	Diagram of the longitudinal cross-section of the SVT . . . . .	36
3.10	Photograph of the drift chamber (DCH) . . . . .	37
3.11	Diagram of the longitudinal cross-section of the DCH . . . . .	38
3.12	Diagram of DCH cell, wire, and layer geometry . . . . .	39
3.13	Hit resolution as a function of distance from wire in the DCH . . . . .	41
3.14	Plot of $dE/dx$ as a function of momentum in the DCH . . . . .	42
3.15	Track reconstruction efficiency for DCH . . . . .	43
3.16	Distribution of the error on $\Delta z$ . . . . .	44
3.17	Radiator and light propagation in the DIRC . . . . .	45
3.18	Cherenkov angle and photon arrival time resolutions in DIRC . . . . .	47
3.19	DIRC Cherenkov angle versus momentum for kaons and pions . . . . .	48

3.20	DIRC kaon efficiency, pion mis-identification, and separation . . . . .	49
3.21	Photograph of the barrel portion of the EMC . . . . .	49
3.22	Diagram of the longitudinal cross-section of the EMC . . . . .	50
3.23	Energy resolution, as a function of energy, for the EMC . . . . .	52
3.24	Angular resolution, as a function of energy, for the EMC . . . . .	52
3.25	Efficiency for electron selector, and pion mis-identification . . . . .	53
3.26	Schematic cross-section view of an RPC . . . . .	54
3.27	Diagram of the layout of the IFR barrel and endcaps . . . . .	55
3.28	Efficiency of muon selection as a function of time . . . . .	57
3.29	Efficiency for muon selector, and pion mis-identification . . . . .	58
3.30	Angular difference between neutral clusters and missing momentum . . . . .	58
4.1	Diagram of lepton pre-selection lists . . . . .	64
4.2	Plots of $\pi^0$ mass . . . . .	67
4.3	Signal $B^0 \rightarrow J/\psi \pi^0$ Monte Carlo, $\Delta E$ versus $m_{ES}$ . . . . .	70
4.4	Angular variable $ \cos \theta_T $ . . . . .	71
4.5	Angular variable $\cos \theta_\ell$ . . . . .	73
4.6	Combined angular cuts . . . . .	74
4.7	$J/\psi_{\text{fake}} u\bar{u}/d\bar{d}/s\bar{s}$ Monte Carlo sample . . . . .	77
4.8	$u\bar{u}/d\bar{d}/s\bar{s}$ Monte Carlo sample . . . . .	80
4.9	$c\bar{c}$ Monte Carlo sample . . . . .	80
4.10	<i>Offpeak</i> data sample . . . . .	81
4.11	Generic $B\bar{B}$ Monte Carlo sample . . . . .	81
4.12	Inclusive $J/\psi$ and $B^0 \rightarrow J/\psi K_s^0(\pi^0\pi^0)$ Monte Carlo Samples . . . . .	83
4.13	<i>Onpeak</i> Data . . . . .	86
4.14	Comparison of data and simulation in $\Delta E$ . . . . .	87
4.15	Schematic of $\Delta E$ - $m_{ES}$ regions for counting cross-check . . . . .	90
5.1	Event shape variables considered for inclusion in a Fisher . . . . .	108
5.2	The nine momentum flow cones . . . . .	109
5.3	Legendre polynomial momentum flow . . . . .	110
5.4	Output of Fisher based on nine cones . . . . .	113

5.5	Output of Fisher based on Legendre polynomials . . . . .	114
5.6	Variables chosen for final Fisher . . . . .	115
5.7	Output of final Fisher, for signal and background . . . . .	116
5.8	Overlap between output of Fisher, for signal and background . . . . .	117
5.9	Plots of $\Delta E$ versus $m_{ES}$ . . . . .	120
5.10	PDFs for $m_{ES}$ . . . . .	129
5.11	PDFs for $\Delta E$ . . . . .	131
5.12	PDFs for Fisher . . . . .	134
5.13	Yield fit to signal $B^0 \rightarrow J/\psi \pi^0$ Monte Carlo sample . . . . .	137
5.14	Yield fit to $B^0 \rightarrow J/\psi K_s^0(\pi^0\pi^0)$ Monte Carlo sample . . . . .	138
5.15	Yield fit to inclusive $J/\psi$ Monte Carlo sample . . . . .	139
5.16	Yield fit to $B\bar{B}$ generic Monte Carlo sample . . . . .	140
5.17	Yield fit to $J/\psi_{\text{fake}}$ <i>offpeak</i> data sample . . . . .	141
5.18	Yield fit results for a mixture of signal and background samples . . . . .	144
5.19	Plots of $m_{ES}$ , split by tagging category . . . . .	150
5.20	Plots of $\Delta E$ , split by tagging category . . . . .	151
5.21	Plots of the Fisher discriminant, split by tagging category . . . . .	152
5.22	Plots of $\Delta t$ , split by tagging category . . . . .	153
5.23	Signal $\Delta t$ PDF fit . . . . .	156
5.24	$B^0 \rightarrow J/\psi K_s^0(\pi^0\pi^0)$ $\Delta t$ PDF fit . . . . .	158
5.25	Inclusive $J/\psi$ $\Delta t$ PDF fit . . . . .	160
5.26	$B\bar{B}$ generic $\Delta t$ PDF fit . . . . .	162
5.27	Continuum $\Delta t$ PDF fit . . . . .	163
5.28	Results of a $CP$ fit to a mixture of samples . . . . .	168
5.29	Results of a $CP$ likelihood fit to <i>onpeak</i> data . . . . .	170
5.30	Yields and asymmetry as functions of $\Delta t$ . . . . .	171
5.31	Validation of Fisher output on alternate data sample . . . . .	181
5.32	Monte Carlo samples with different generated asymmetries . . . . .	181
5.33	Toy Monte Carlo study . . . . .	183
5.34	$CP$ fit, including the Fisher as a PDF . . . . .	186
5.35	$CP$ fit, fixing the signal $\Delta E$ peak position . . . . .	187

5.36	<i>CP</i> fit, cutting on both the Fisher and $\Delta E$ . . . . .	188
6.1	$r$ versus $\delta$ for ratio of world average branching fractions . . . . .	192
6.2	Summary of asymmetry results, including world average . . . . .	193
6.3	$r$ versus $\delta$ for world average asymmetry . . . . .	195
6.4	$r$ versus $\delta$ for asymmetry, extrapolated to $2ab^{-1}$ . . . . .	195
6.5	$r$ versus $\delta$ extrapolated to $2ab^{-1}$ , assuming no penguins . . . . .	196
6.6	$r$ versus $\delta$ for combined asymmetry and ratio of branching fractions results . . . . .	197
6.7	Constraints on $ S_{J/\psi K_S^0} - \sin 2\beta $ . . . . .	199
A.1	Schematic of IFR readout cabling error types . . . . .	202
A.2	Example hit residual in RPC showing cabling correction . . . . .	203
A.3	Schematic of swaps between even and odd strips . . . . .	204
A.4	Example distribution of number of strips hit . . . . .	205
A.5	Example of residuals before and after alignment . . . . .	207
A.6	Alignment constants for IFR barrel and forward endcap . . . . .	208
B.1	Photograph of the RPC test stand . . . . .	210
B.2	Schematic of the RPC test stand . . . . .	211
B.3	Temperature and current for RPC test stand . . . . .	214
B.4	Current versus temperature for RPC test stand . . . . .	215
B.5	Efficiencies for RPC test stand . . . . .	216
B.6	Plateau curves for RPC test stand . . . . .	217
B.7	Photograph of damaged RPC surface . . . . .	219

# Chapter 1

## Introduction

The purpose of this introduction is threefold. First, a brief historical account of the search for  $CP$  violation will be given to provide a context for the current measurements. The details of the formalism, including the basic definitions, will be presented in Chapter 2. Second, the introduction is intended to motivate the research that led to the reported results. The third objective of this chapter is to make it clear that this work has been performed in the framework of a large collaboration, and there is a distinction between the primary work of the author and that of many other members of the collaboration.

### 1.1 Historical Perspective

In 1964, two groups performing experiments at Brookhaven decided to search for the violation of  $CP$  symmetry in the kaon system. Both looked in their data for the decay  $K_L^0 \rightarrow \pi^+\pi^-$ , which would be forbidden if  $CP$  were a true symmetry of nature. A group from Princeton [1] used a two arm spectrometer to reconstruct charged tracks originating from  $K_L^0$  candidates. The invariant mass of the charged particle candidates was calculated, to be compared with the nominal  $K_L^0$  mass. They also computed the angle between the original beam direction and the vector sum of the charged particle candidates to distinguish between two-body decays, where this angle peaks at zero, and the three-body decays  $K_L^0 \rightarrow \pi^\pm\mu^\mp\nu_\mu$  and  $K_L^0 \rightarrow \pi^\pm e^\mp\nu_e$ , where the angle is

non-zero due to the undetected neutrino. The ability of the detector to reconstruct the two pion signal was calibrated by temporarily adding material to the beam area to regenerate  $K_S^0$  particles, some of which decayed via the  $CP$ -allowed  $K_S^0 \rightarrow \pi^+\pi^-$  channel. The result of this experiment, expressed as the ratio of  $K_L^0 \rightarrow \pi^+\pi^-$  decays to all  $K_L^0$  charged mode decays, was  $(2.0 \pm 0.4) \times 10^{-3}$ . Less than a month later, a group from Illinois [2] published similar results from another experiment. While designed to study the  $K_L^0 \rightarrow \pi^\pm\mu^\mp\nu_\mu$  and  $K_L^0 \rightarrow \pi^\pm e^\mp\nu_e$  decays, their experiment found an indication of a handful of  $K_L^0 \rightarrow \pi^+\pi^-$  decays.

The results of these two experiments had a tremendous impact in the particle physics community. At the time, there were no reasonable theoretical interpretations for the observed  $CP$  violation. However, almost immediately, phenomenological models were introduced, such as that of Wu and Yang [3], which set forth much of the framework and notation that were used throughout later kaon  $CP$  violation experiments. Another example is a paper by Wolfenstein [4] that suggested the idea of an additional interaction, the superweak interaction, which remained a possibility until being essentially excluded by more recent kaon experiments. One of the strongest models, by Kobayashi and Maskawa [5], discussed in Chapter 2, would not come until almost a decade later, and would rely on an amazing prediction, namely the existence of a third generation of quarks (at a time when only the up, down, and strange quarks were known). Others, such as Sakharov [6], used the existence of  $CP$  violation as an input to the tantalizing puzzle of the matter–antimatter asymmetry of the universe. Part of the excitement also stemmed from the fact that  $CP$  violation, taken in combination with  $CPT$  invariance (discussed in Section 2.2), implied a violation of time-reversal invariance.

In the 1970s, experiments [7] verified that  $CP$  violation in the kaon system is dominated by effects associated with the the mixing of  $K$  and  $\bar{K}$  mesons, or so-called indirect  $CP$  violation, described by the real part of the complex parameter  $\epsilon$ . This is in contrast to a direct  $CP$  violation in the decay amplitudes, described by the real part of the complex parameter  $\epsilon'$ . The parameters  $\epsilon$  and  $\epsilon'$  appear in the ratios of the

$CP$ -violating to  $CP$ -conserving kaon decay amplitudes:

$$\eta_{+-} \equiv \frac{A(K_L^0 \rightarrow \pi^+\pi^-)}{A(K_S^0 \rightarrow \pi^+\pi^-)} = \epsilon + \epsilon' , \quad \text{and} \quad \eta_{00} \equiv \frac{A(K_L^0 \rightarrow \pi^0\pi^0)}{A(K_S^0 \rightarrow \pi^0\pi^0)} = \epsilon - 2\epsilon' . \quad (1.1)$$

A useful experimental quantity is the double ratio

$$\frac{\Gamma(K_L^0 \rightarrow \pi^0\pi^0)/\Gamma(K_S^0 \rightarrow \pi^0\pi^0)}{\Gamma(K_L^0 \rightarrow \pi^+\pi^-)/\Gamma(K_S^0 \rightarrow \pi^+\pi^-)} \approx 1 - 6 \mathcal{R}e\left(\frac{\epsilon'}{\epsilon}\right) , \quad (1.2)$$

where a deviation of this ratio from unity, or equivalently a deviation of the value of  $\mathcal{R}e(\frac{\epsilon'}{\epsilon})$  from zero, represents direct  $CP$  violation. The first evidence for direct  $CP$  violation came in 1988 from the experiment NA31 at the European physics laboratory CERN, with a result of  $\mathcal{R}e(\frac{\epsilon'}{\epsilon}) = (3.3 \pm 1.1) \times 10^{-3}$  [8]. This experiment and the collaboration E731, at Fermilab in Illinois, both published new results in 1993. They obtained  $\mathcal{R}e(\frac{\epsilon'}{\epsilon}) = (23.0 \pm 6.5) \times 10^{-4}$  and  $\mathcal{R}e(\frac{\epsilon'}{\epsilon}) = (7.4 \pm 5.9) \times 10^{-4}$ , respectively [9]. The inconclusive nature of these results motivated another generation of each of these two experiments. After an initial round of publications on partial data sets, the result for data collected from 1997 to 1999 for the NA48 experiment at CERN is  $\mathcal{R}e(\frac{\epsilon'}{\epsilon}) = (15.3 \pm 2.6) \times 10^{-4}$  [10] and the result from the KTEV collaboration at Fermilab on data collected from 1996 to 1997 is  $\mathcal{R}e(\frac{\epsilon'}{\epsilon}) = (20.7 \pm 2.8) \times 10^{-4}$  [11]. So, both direct and indirect  $CP$  violation have been established in the weak interactions of the neutral kaons.

A long standing question was whether or not  $CP$  violation existed, and could be observed, in any other system. In 1975, early theoretical work was published on  $CP$  violation in particles containing the charm quark [12]. While no such effects were detected in charmed particles, one of the search techniques was applied to an early study in the  $B$  meson system by the CLEO collaboration at Cornell [13]. They looked for a charge asymmetry in same-sign dilepton events in  $B^0\bar{B}^0$  pairs produced at an  $e^+e^-$  collider. In other words, the number of events in which both neutral  $B$  mesons decayed into sets of particles that included a negative or positive lepton was labeled

as  $N(\ell^-\ell^-)$  or  $N(\ell^+\ell^+)$ , respectively, in order to construct the asymmetry

$$a_{\ell\ell} \equiv \frac{N(\ell^+\ell^+) - N(\ell^-\ell^-)}{N(\ell^+\ell^+) + N(\ell^-\ell^-)} \approx 4 \mathcal{R}e(\epsilon_{B^0}) . \quad (1.3)$$

The result,  $|\mathcal{R}e(\epsilon_{B_z})| < 0.045$  at 90% C.L., was compatible with a null result, but lacked the sensitivity to probe the full theoretical expectations. In the early 1980s, the predictions for  $CP$  violation in the  $B$  system were  $\mathcal{O}(10^{-3})$  or  $\mathcal{O}(10^{-4})$  for inclusive measurements and  $\mathcal{O}(10^{-1})$  or  $\mathcal{O}(10^{-2})$  for exclusive measurements [14]. The authors in Ref. [14] also introduced a strategy of studying decay modes in which  $B^0$  and  $\bar{B}^0$  mesons decay into the same final state, and they derived time-integrated versions of expressions for  $CP$ -asymmetry observables. A handful of collider experiments in the late 1990s used this formalism, but without the restriction of the time-integration, to search for  $CP$  violation in the decay  $B^0 \rightarrow J/\psi K_s^0$ . The asymmetry can be written as (the details will be given in Chapter 2)

$$a_{CP} \equiv \frac{N(\bar{B}^0 \rightarrow J/\psi K_s^0) - N(B^0 \rightarrow J/\psi K_s^0)}{N(\bar{B}^0 \rightarrow J/\psi K_s^0) + N(B^0 \rightarrow J/\psi K_s^0)} = \sin(\Delta m_d t) \sin 2\beta , \quad (1.4)$$

where  $N(B^0 \rightarrow J/\psi K_s^0)$  and  $N(\bar{B}^0 \rightarrow J/\psi K_s^0)$  represent the number of decays to the  $J/\psi K_s^0$  final state at proper time  $t$  from an initial  $B^0$  or  $\bar{B}^0$  state, respectively. The  $B^0$ - $\bar{B}^0$  oscillation frequency is  $\Delta m_d$ , and the reported quantity  $\sin 2\beta$  is related to elements of the Cabibbo-Kobayashi-Maskawa (CKM) quark-mixing matrix [5, 15] through the expression  $\beta \equiv \arg[-V_{cd}V_{cb}^*/V_{td}V_{tb}^*]$ . A non-zero value of  $\sin 2\beta$  implies  $CP$  violation and an example of a prediction based on the Standard Model, using other parameters as inputs, is  $\sin 2\beta = 0.75 \pm 0.09$  [16]. In 1998, a measurement from the OPAL collaboration using the electron-positron collider LEP at CERN yielded  $\sin 2\beta = 3.2_{-2.0}^{+1.8} (\text{stat}) \pm 0.5 (\text{syst})$ , and a measurement from the CDF collaboration using the  $p\bar{p}$  collider at Fermilab gave  $\sin 2\beta = 1.8 \pm 1.1 (\text{stat}) \pm 0.3 (\text{syst})$  [17]. Two years later, an update came from CDF, with a value of  $\sin 2\beta = 0.79 \pm 0.39 (\text{stat}) \pm 0.16 (\text{syst})$ , and a new measurement was made by the ALEPH collaboration, again at LEP, with  $\sin 2\beta = 0.84_{-1.04}^{+0.82} (\text{stat}) \pm 0.16 (\text{syst})$  [18]. These results were still all consistent with zero, but supported the possibility of a non-zero positive value.

Meanwhile, there existed a highly motivated parallel effort to develop an accelerator and detector combination optimized for studying  $CP$  violation in the  $B$  system. The primary detector requirements were excellent exclusive decay mode reconstruction, the ability to distinguish events as originating from either  $B^0$  or  $\bar{B}^0$  mesons, and the ability to measure the proper decay time difference between the decay of two  $B$  mesons. The most favorable accelerator configuration, that of an asymmetric-energy  $e^+e^-$  storage ring operating at the  $\Upsilon(4S)$  resonance, was first proposed by P. Oddone in 1987 [19]. This would take advantage of the process  $e^+e^- \rightarrow \Upsilon(4S) \rightarrow B\bar{B}$ , and using beams of two different energies would provide a boost to the center-of-mass frame with respect to the lab frame, allowing for a resolvable spatial, and therefore temporal, separation between the  $B$  decay vertices. The PEP-II project, consisting of a 9 GeV electron beam and a 3.1 GeV positron beam fed by the SLAC linac and guided through storage rings to a single interaction region, was approved in 1993. Because of the low branching fractions of many of the exclusive modes ( $\mathcal{O}(10^{-5})$ ), the luminosity of the collider would have to be in the unprecedented range of  $10^{33} \text{ cm}^{-2} \text{ s}^{-1}$  (contributing to the popular usage of the  $B$  Factory moniker). The proposed detector designs had asymmetric layouts to match the boost of the beams and relied on advances in tracking and particle identification to meet the above requirements. A version was put forth by the newly formed *BABAR* collaboration, with a Letter of Intent in 1994 [20] and then a Technical Design Report in 1995 [21]. The *BABAR* detector is described in some detail in Chapter 3. A similar accelerator structure, KEKB, and detector, Belle, were constructed in Japan.

In the Spring of 1999, roughly 35 years after the first observation of  $CP$  violation in the kaon system, the  $B$  Factories began taking data. Two years later, the data sets were large enough to yield an observation of  $CP$  violation in the  $B$  system. The result from *BABAR* was  $\sin 2\beta = 0.59 \pm 0.14$  (stat)  $\pm 0.05$  (syst) [22], and the result from Belle was  $\sin 2\beta = 0.99 \pm 0.14$  (stat)  $\pm 0.06$  (syst) [23]. Together, these two experiments have answered in the affirmative the question of whether or not  $CP$  violation exists in the interactions of an additional set of particles. They have since produced updated measurements of  $\sin 2\beta$ , the latest result from *BABAR* being  $\sin 2\beta = 0.741 \pm 0.067$  (stat)  $\pm 0.033$  (syst) [24], confirming the theoretical predictions

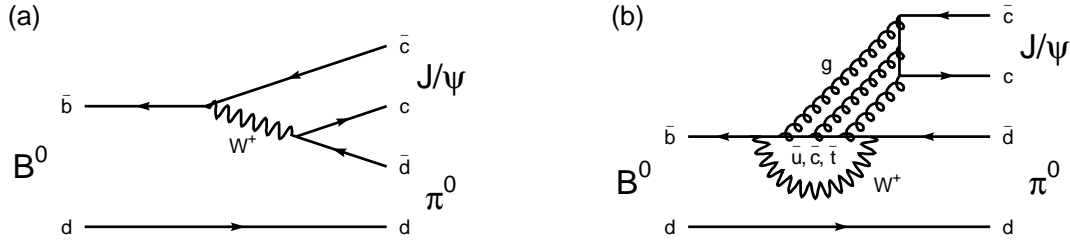


Figure 1.1: The (a) tree and (b) possible penguin Feynman diagrams contributing to the process  $B^0 \rightarrow J/\psi \pi^0$ . To obtain the equivalent diagrams for  $B^0 \rightarrow J/\psi K_S^0$ , the final state  $\bar{d}$  quark is replaced by an  $\bar{s}$  quark in each diagram, yielding  $K_S^0$  in place of  $\pi^0$ .

to an astounding precision. This is where the historical introduction to  $CP$  violation comes to a conclusion, but it is presumably just the beginning of the story.

## 1.2 Why $B^0 \rightarrow J/\psi \pi^0$ ?

The measurements from *BABAR*, discussed above, have been performed using the modes  $B^0 \rightarrow J/\psi K_S^0$ ,  $\psi(2S)K_S^0$ ,  $\chi_{c1}K_S^0$ ,  $\eta_c K_S^0$ ,  $J/\psi K_L^0$ , and  $J/\psi K^{*0}$  ( $K^{*0} \rightarrow K_S^0 \pi^0$ ), which have the advantage of a relatively straightforward link to the quantity  $\sin 2\beta$ , with minimal theoretical uncertainty. Efforts have now also turned toward a variety of other modes, including  $B^0 \rightarrow J/\psi \pi^0$ , with the goal of continuing to probe the parameters and mechanisms of  $CP$  non-conservation. We now address the question of why  $B^0 \rightarrow J/\psi \pi^0$  is of particular interest.

As alluded to in Section 1.1, the Standard Model of electroweak interactions describes  $CP$  violation in  $B$  meson decays by a complex phase in the three-generation Cabibbo-Kobayashi-Maskawa quark-mixing matrix. The  $\bar{b} \rightarrow c\bar{c}\bar{s}$  modes that decay through charmonium, such as  $B^0 \rightarrow J/\psi K_S^0$ , yield precise measurements of the quantity  $\sin 2\beta$ , as shown above. The decay  $B^0 \rightarrow J/\psi \pi^0$  is a Cabibbo-suppressed  $\bar{b} \rightarrow c\bar{c}\bar{d}$  decay, whose tree contribution (see Fig. 1.1a) has the same weak phase as the  $\bar{b} \rightarrow c\bar{c}\bar{s}$  modes. Penguin diagrams (Fig. 1.1b) and the suppressed tree diagram may enter at the same order, proportional to  $\sin^3 \theta_{12}$ , where  $\theta_{12}$  is the Cabibbo angle. A portion of the penguin amplitude has the same weak phase as the tree amplitude, while the

remainder of the penguin amplitude has a different weak phase, allowing for the possibility of a time-dependent  $CP$  asymmetry that differs from the one observed in  $\bar{b} \rightarrow c\bar{c}\bar{s}$  decays.

A deviation with respect to the result for the  $\bar{b} \rightarrow c\bar{c}\bar{s}$  modes may indicate penguin contributions not only in  $B^0 \rightarrow J/\psi\pi^0$ , but also in  $B^0 \rightarrow J/\psi K_S^0$ , at a reduced level governed by Cabibbo suppression. Investigating this issue may tell us whether or not we should expect such an effect to be detectable in  $B^0 \rightarrow J/\psi K_S^0$ . This could be of particular interest once the measurements of  $\sin 2\beta$  are sufficiently precise that other non-leading order effects, such as the higher order expansion in the CKM matrix elements, begin to contribute.

Chapter 2 elaborates upon these motivations, and explores the relationships between the mechanism of  $CP$  violation and the observable quantities. The first step in a complete analysis of  $B^0 \rightarrow J/\psi\pi^0$  decays is the measurement of the branching fraction, and this is described in Chapter 4. The full time-dependent  $CP$  asymmetry measurement is detailed in Chapter 5.

### 1.3 The *BABAR* Collaboration

The results reported in this text stem from research carried out within a large collaboration. In the Fall of 2002, the *BABAR* collaboration consisted of more than 550 physicists from 75 institutions in 9 countries: Canada, China, France, Germany, Italy, Norway, Russia, the United Kingdom, and the United States of America. There are also dozens of engineers, technicians, programmers, and administrators distributed among these sites who have contributed to the construction, maintenance, and operation of the detector and analysis software.

The effort in building and characterizing the *BABAR* detector, as described in Chapter 3, has been contributed by a large fraction of the members of the collaboration. Areas in which the author has made an individual contribution include specific tests and operational aspects of the drift chamber electronics system, calculations of crystal positions in the electromagnetic calorimeter, alignment and cable mapping in the muon tracking system, and a study of the efficiency loss in the resistive plate

chambers used in the muon system. Some of these projects are discussed in the relevant sections of Chapter 3, and in the Appendices.

The *BABAR* software, which now contains more than 2 million lines of code, is developed and shared by a large number of collaborators. The analysis reported here utilizes a great deal of this code, with functions as diverse as on-line event processing, candidate tracking, particle identification,  $B$ -flavor tagging, and vertex fitting. Additional unique software was developed for the analysis of  $B^0 \rightarrow J/\psi \pi^0$ .

Another aspect of working within a collaboration, and extending into the particle physics community as a whole, is the exchange of ideas and techniques. This applies here, where there are commonalities between  $B^0 \rightarrow J/\psi \pi^0$  and other modes. For example, methods of background suppression are shared when motivated by similar kinematics. Also, many of the general fitting techniques are used by other time-dependent  $CP$  analyses and some of the input parameters are extracted from the work of collaborators, so references are given where appropriate.

# Chapter 2

## Theory of Time-Dependent $B$ Decays

### 2.1 The Standard Model

The Standard Model of particle physics represents our current understanding of elementary particles and the forces that govern their interactions. Over the past decades, the precise determination of many parameters of the Standard Model has led to an increase in its predictive power. This is evident in the study of time-dependent  $B$  decays, and before seeking to verify, extend, or even contradict the theory, it is useful to review the most relevant aspects of the model.

The charges and masses of the fundamental fermions, the quarks and leptons, are shown in Table 2.1. The division into three generations is depicted by the horizontal lines and each particle in the table has a corresponding antiparticle (not shown). Information about the gauge bosons is given in Table 2.2. These particles mediate the strong, electromagnetic, and weak interactions, where the latter two of these forces have been unified into the electroweak interaction. Searches for other fundamental particles are underway. In particular, Higgs bosons may exist as massive scalar particles that spontaneously break the electroweak symmetry to that of the electromagnetic interaction. Furthermore, fermions and gauge bosons may acquire their masses through interactions with non-zero vacuum Higgs fields.

Table 2.1: Quarks and leptons of the Standard model. The charges are given in units of the proton charge and the masses are the evaluations of the 2002 Particle Data Group (PDG) [25], where the  $u$ ,  $d$ ,  $c$ ,  $s$ , and  $b$  quark masses are presented using the renormalization scheme called  $\overline{\text{MS}}$ . The electron and muon masses are rounded here, but are known to better than a part in 10 million.

Quarks			Leptons		
Symbol	Charge ( $e$ )	Mass ( $\text{MeV}/c^2$ )	Symbol	Charge ( $e$ )	Mass ( $\text{MeV}/c^2$ )
u	$\frac{2}{3}$	1.5–4.5	$e$	−1	0.51
d	$-\frac{1}{3}$	5.0–8.5	$\nu_e$	0	< 0.460 (68% CL)
c	$\frac{2}{3}$	$(1.0\text{--}1.4) \times 10^3$	$\mu$	−1	105.66
s	$-\frac{1}{3}$	80–155	$\nu_\mu$	0	< 0.19 (90% CL)
t	$\frac{2}{3}$	$(174.3 \pm 5.1) \times 10^3$	$\tau$	−1	$1776.99^{+0.29}_{-0.26}$
b	$-\frac{1}{3}$	$(4.0\text{--}4.5) \times 10^3$	$\nu_\tau$	0	< 18.2 (95% CL)

Table 2.2: Gauge bosons of the Standard Model. The charges are given in units of the proton charge and the masses are the evaluations of the 2002 PDG [25].

Gauge bosons			
Symbol	Charge ( $e$ )	Mass ( $\text{GeV}/c^2$ )	Mediated interaction
$\gamma$	0	0	electromagnetic
$W^\pm$	$\pm 1$	$80.423 \pm 0.039$	weak
$Z^0$	0	$91.1876 \pm 0.0021$	weak
gluon	0	0	strong

## 2.2 Discrete Transformations: $C$ , $P$ , and $T$

Invariances under discrete transformations give rise to multiplicative quantum numbers, which are associated with discrete symmetries and conservation laws. It is of equal interest when these symmetries are violated. In either case, it is useful to define the discrete operators and their effects on particles and fields.

The first of these transformations is that of charge conjugation, represented by the operator  $C$ . Charge conjugation reverses the sign of additive quantum numbers, thereby exchanging particles and antiparticles, while leaving spin and momentum unchanged. While it is a valid symmetry of the strong and electromagnetic interactions,  $C$  is not conserved in the weak interaction. Only particles with additive quantum numbers all equal to zero are eigenstates of  $C$ , with eigenvalues equal to  $\pm 1$ . The effect of charge conjugation on the Dirac fields  $\psi(x)$  and  $\bar{\psi}(x)$ , where  $\bar{\psi}(x) \equiv \psi^\dagger \gamma^0$ , is given by:<sup>1</sup>

$$C\psi(x)C = -i(\bar{\psi}\gamma^0\gamma^2)^T, \quad (2.1)$$

$$C\bar{\psi}(x)C = (-i\gamma^0\gamma^2\psi)^T, \quad (2.2)$$

where  $\gamma^0$  and  $\gamma^2$  are two of the Dirac matrices, written in a chiral basis as

$$\begin{aligned} \gamma^0 &= \begin{pmatrix} 0 & 0 & 1 & 0 \\ 0 & 0 & 0 & 1 \\ 1 & 0 & 0 & 0 \\ 0 & 1 & 0 & 0 \end{pmatrix}, & \gamma^1 &= \begin{pmatrix} 0 & 0 & 0 & 1 \\ 0 & 0 & 1 & 0 \\ 0 & 1 & 0 & 0 \\ 1 & 0 & 0 & 0 \end{pmatrix}, \\ \gamma^2 &= \begin{pmatrix} 0 & 0 & 0 & -i \\ 0 & 0 & i & 0 \\ 0 & -i & 0 & 0 \\ i & 0 & 0 & 0 \end{pmatrix}, & \gamma^3 &= \begin{pmatrix} 0 & 0 & 1 & 0 \\ 0 & 0 & 0 & -1 \\ 1 & 0 & 0 & 0 \\ 0 & -1 & 0 & 0 \end{pmatrix}. \end{aligned} \quad (2.3)$$

An example of the application of the conservation of the charge conjugation quantum number (also called the charge parity) to the decay  $B^0 \rightarrow J/\psi \pi^0$  is in the subsequent

---

<sup>1</sup>Full derivations of the results given in this section are elegantly presented in Ref. [26].

decay of the  $\pi^0$ . The  $\pi^0$  has a charge parity of  $+1$ , while a photon has a charge parity of  $-1$ . Thus, the decay  $\pi^0 \rightarrow \gamma\gamma$  is allowed, while the decay  $\pi^0 \rightarrow \gamma\gamma\gamma$  is forbidden and not observed.

The next discrete transformation to consider is the parity operator,  $P$ . Parity acts to reverse the sign of a momentum vector ( $\vec{p} \rightarrow -\vec{p}$ ) and spatial coordinates ( $\vec{x} \rightarrow -\vec{x}$ ), but leaves spin and angular momentum unchanged. Application of the parity transformation twice, returns a field to the original state, so  $P^2 = 1$ , and the eigenvalues are  $\pm 1$ . Like charge conjugation, parity has been found to be conserved in the strong and electromagnetic interactions. However, it is violated in the weak interaction, as proposed theoretically [27], and shown experimentally in beta decays [28]. Under parity, the Dirac fields transform in the following way:

$$P\psi(t, \vec{x})P = \gamma^0\psi(t, -\vec{x}) , \quad (2.4)$$

$$P\bar{\psi}(t, \vec{x})P = \bar{\psi}(t, -\vec{x})\gamma^0 . \quad (2.5)$$

The remaining individual discrete transformation presented here is time reversal,  $T$ . The time reversal operator flips the sign of the time coordinate ( $t \rightarrow -t$ ), but leaves the spatial coordinates unchanged. Therefore, the momentum and angular momentum also undergo sign reversal ( $\vec{p} \rightarrow -\vec{p}$  and  $\vec{J} \rightarrow -\vec{J}$ ). Unlike  $C$  and  $P$ , which are Hermitian ( $\mathcal{O} = \mathcal{O}^\dagger$ ) and unitary ( $\mathcal{O}^\dagger\mathcal{O} = \mathcal{O}\mathcal{O}^\dagger = 1$ ),  $T$  is Hermitian and antiunitary, so it does not have associated definite eigenvalues. The Dirac fields transform as follows under time reversal:

$$T\psi(t, \vec{x})T = \gamma^1\gamma^3\psi(-t, \vec{x}) , \quad (2.6)$$

$$T\bar{\psi}(t, \vec{x})T = \bar{\psi}(-t, \vec{x})[-\gamma^1\gamma^3] . \quad (2.7)$$

The combination of the three operations  $CPT$  is a strongly motivated symmetry of nature [29] that has thus far stood the test of experiment (see for example Ref. [30]). In simplified terms, it is thought to be impossible to construct a Lorentz-invariant Hermitian Hamiltonian that violates  $CPT$ . A consequence of invariance under  $CPT$  is that any process that violates  $CP$  symmetry implies a violation of  $T$  invariance. This

Table 2.3: The properties of Dirac field bilinear terms under  $C$ ,  $P$ ,  $T$ , and combined  $CP$  and  $CPT$  transformations. Here, the notation  $(-1)^\mu \equiv 1$  for  $\mu = 0$  and  $(-1)^\mu \equiv -1$  for  $\mu = 1, 2, 3$  is used.

	scaler $\bar{\psi}\psi$	pseudo-scaler $i\bar{\psi}\gamma^5\psi$	vector $\bar{\psi}\gamma^\mu\psi$	pseudo-vector $\bar{\psi}\gamma^\mu\gamma^5\psi$	tensor $\bar{\psi}\sigma^{\mu\nu}\psi$
$C$	+1	+1	-1	+1	-1
$P$	+1	-1	$(-1)^\mu$	$-(-1)^\mu$	$(-1)^\mu(-1)^\nu$
$T$	+1	-1	$(-1)^\mu$	$(-1)^\mu$	$-(-1)^\mu(-1)^\nu$
$CP$	+1	-1	$-(-1)^\mu$	$-(-1)^\mu$	$-(-1)^\mu(-1)^\nu$
$CPT$	+1	+1	-1	-1	+1

is relevant for the weak interaction, as the strong and electromagnetic interactions are each symmetric with respect to  $CP$  and hence time reversal.

Lagrangians of the Standard Model are Lorentz scalars, and are constructed from terms that are bilinear in the Dirac field. Therefore, it is important to examine the behavior of field bilinear terms under discrete transformations. Table 2.3 provides a summary for the individual transformations, as well as for the combinations  $CP$  and  $CPT$ , and requires the definitions of the pseudo-scalar and tensor quantities

$$\gamma^5 \equiv i\gamma^0\gamma^1\gamma^2\gamma^3, \quad (2.8)$$

$$\sigma^{\mu\nu} \equiv \frac{i}{2} [\gamma^\mu, \gamma^\nu] = \frac{i}{2} (\gamma^\mu\gamma^\nu - \gamma^\nu\gamma^\mu), \quad (2.9)$$

where the indices  $\mu$  and  $\nu$  may be any combination of 0, 1, 2, and 3.

The other fields used to construct the terms of a Lagrangian, as well as the derivative operator, also have definite behavior under the  $CP$  transformation. However, these terms have coefficients that represent coupling constants or masses and these coefficients may be complex numbers. Therefore, terms that are otherwise related by  $CP$  will have coefficients that are complex conjugates of each other, and may represent different rates for physical processes. This implies that  $CP$  is not necessarily a true symmetry of the Lagrangian. The exact location of any such complex phase in the Lagrangian is a matter of convention and it can be shifted around through redefining

the fields. If complex phases remain, after redefining fields in such a way as to remove as many complex phases as possible, they carry the same physical consequences regardless of location. Where these phases appear in the theory of  $B$ -meson decays, and how they give rise to  $CP$  asymmetry, will be discussed further in Section 2.4.

## 2.3 Neutral $B$ -Meson Flavor Oscillations

The neutral  $B$  meson system, like that of the  $K$  meson, is complicated by the fact that the states with definite quark content differ from those associated with an observable mass and lifetime. The flavor eigenstates are defined as  $B^0 = \bar{b}d$  and  $\bar{B}^0 = b\bar{d}$ .<sup>2</sup> The mass eigenstates, which are eigenstates of the Hamiltonian, are defined as

$$\begin{aligned} |B_L\rangle &= p|B^0\rangle + q|\bar{B}^0\rangle, \\ |B_H\rangle &= p|B^0\rangle - q|\bar{B}^0\rangle, \end{aligned} \quad (2.10)$$

where  $p$  and  $q$  are complex numbers that satisfy the normalization requirement  $|p|^2 + |q|^2 = 1$  and  $B_L$  ( $B_H$ ) is the lighter (heavier) mass eigenstate.

A linear combination of the flavor eigenstates, such as  $a|B^0\rangle + b|\bar{B}^0\rangle$ , mixes according to the time-dependent equation:

$$i\frac{d}{dt} \begin{pmatrix} a \\ b \end{pmatrix} = H \begin{pmatrix} a \\ b \end{pmatrix} = \left(M - \frac{i}{2}\Gamma\right) \begin{pmatrix} a \\ b \end{pmatrix}, \quad (2.11)$$

where  $H$  is the Hamiltonian and  $M$  and  $\Gamma$  are  $2 \times 2$  Hermitian matrices that quantify the mixing and decay portions of the time evolution. The discrete symmetry  $CPT$  (explained in Section 2.2) provides the constraints  $M_{11} = M_{22}$ ,  $M_{21} = M_{12}^*$ ,  $\Gamma_{11} = \Gamma_{22}$ , and  $\Gamma_{21} = \Gamma_{12}^*$ . With the definitions

$$\Delta m_d \equiv M_H - M_L, \quad \Delta\Gamma \equiv \Gamma_H - \Gamma_L, \quad (2.12)$$

---

<sup>2</sup>These particles are also sometimes written as  $B_d^0$  and  $\bar{B}_d^0$  to distinguish them from the  $B_s^0$  and  $\bar{B}_s^0$ , where the  $d$  quark is replaced by an  $s$  quark. The  $d$  subscript is omitted throughout this text.

diagonalizing the Hamiltonian of Equation 2.11 yields:

$$(\Delta m_d)^2 - \frac{1}{4}(\Delta\Gamma)^2 = 4(|M_{12}|^2 - \frac{1}{4}|\Gamma_{12}|^2), \quad (2.13)$$

$$\Delta m_d \Delta\Gamma = 4 \operatorname{Re}(M_{12}\Gamma_{12}^*), \quad (2.14)$$

$$\frac{q}{p} = -\frac{\Delta m_d - \frac{i}{2}\Delta\Gamma}{2(M_{12} - \frac{i}{2}\Gamma_{12})}. \quad (2.15)$$

Under the condition that  $\Delta\Gamma \ll \Delta m_d$ , these expressions can be simplified. To see that this is a reasonably safe assumption, note that decay modes common to  $B^0$  and  $\bar{B}^0$  enter with branching fractions less than or equal to  $10^{-3}$  and with  $CP$  eigenvalue signs and width difference signs that vary from mode to mode, thus keeping the total width difference much less than the average width,  $\Delta\Gamma \ll \Gamma_B$ , where  $\Gamma_B = \Gamma_{B^0} = \Gamma_{\bar{B}^0}$ . Also, the mass difference has been measured to be only slightly less than the average width,  $\Delta m_d/\Gamma_B = 0.755 \pm 0.015$  [25]. Thus  $\Delta\Gamma \ll \Delta m_d$ , and Equations 2.13–2.15 simplify to

$$\Delta m_d = 2|M_{12}|, \quad \Delta\Gamma = \frac{2 \operatorname{Re}(M_{12}\Gamma_{12}^*)}{|M_{12}|}, \quad \frac{q}{p} = -\frac{|M_{12}|}{M_{12}}. \quad (2.16)$$

The time evolutions of an initially pure  $B^0$  state,  $|B_{\text{phys}}^0\rangle$ , and an initially pure  $\bar{B}^0$  state,  $|\bar{B}_{\text{phys}}^0\rangle$ , are given by:

$$\begin{aligned} |B_{\text{phys}}^0(t)\rangle &= e^{-iMt} e^{-\Gamma t/2} \{ \cos(\Delta m_d t/2) |B^0\rangle + i \sin(\Delta m_d t/2) (q/p) |\bar{B}^0\rangle \}, \\ |\bar{B}_{\text{phys}}^0(t)\rangle &= e^{-iMt} e^{-\Gamma t/2} \{ i \sin(\Delta m_d t/2) (q/p) |B^0\rangle + \cos(\Delta m_d t/2) |\bar{B}^0\rangle \}, \end{aligned} \quad (2.17)$$

where  $M = \frac{1}{2}(M_H + M_L)$  and  $\Gamma = \frac{1}{2}(\Gamma_H + \Gamma_L)$ .

These flavor oscillations play a central role in the analysis of time-dependent physics in the  $B$  system. Furthermore, at the  $B$  Factories, the decay chain  $e^+e^- \rightarrow \Upsilon(4S) \rightarrow B^0\bar{B}^0$  produces  $B^0$  and  $\bar{B}^0$  mesons that are in an  $L = 1$  coherent state. Therefore, each of the two  $B$  mesons evolves in time according to Equation 2.17, with a fixed phase between the two, such that at the moment that one of the  $B$  mesons decays, one is a  $B^0$  and the other is a  $\bar{B}^0$ . The other  $B$  continues to evolve and may

decay as either a  $B^0$  or  $\bar{B}^0$ . The resulting theoretical implications and experimental strategies are discussed in the following sections.

## 2.4 Neutral $B$ -Meson $CP$ Asymmetry

Much of the formalism for  $CP$  violation in the decay  $B^0 \rightarrow J/\psi \pi^0$  is applicable to  $B$  physics in general. This section starts by describing the three categories of  $CP$  violation. It then takes a look at the CKM matrix and unitarity triangle, which contain Standard Model representations of  $CP$  violation. The final portions of this section turn more toward the  $B^0 \rightarrow J/\psi \pi^0$  decay mode, exploring the contributions of tree and penguin amplitudes, and casting  $CP$  violation into observable quantities of particular relevance to the measurements described in Chapter 5.

### 2.4.1 Three Types of $CP$ Violation

There are three broad categories for possible sources of  $CP$  asymmetries. (1)  $CP$  violation through mixing, also called indirect  $CP$  violation, occurs when the neutral mass eigenstates differ from the  $CP$  eigenstates. (2)  $CP$  violation through decay, also called direct  $CP$  violation, occurs when the amplitude of a decay and the amplitude of the  $CP$  conjugate of the decay have different magnitudes. This applies to both charged and neutral decays. (3)  $CP$  violation through interference of decays with and without mixing may occur when  $B^0$  and  $\bar{B}^0$  mesons decay to the same final state. As detailed below, this third process can coincide with contributions from the other two sources.

A special case, in which all three of the above sources may contribute, is shown in Figure 2.1. Here, a state originating as either pure  $B^0$  or pure  $\bar{B}^0$  evolves in time, and this mixing is followed by a decay to a final  $CP$  eigenstate  $f$ . The decay amplitudes of  $B^0$  and  $\bar{B}^0$  to the common final state  $f$  can be written as

$$\begin{aligned} A_f &= \langle f | H | B^0 \rangle , \\ \bar{A}_f &= \langle f | H | \bar{B}^0 \rangle . \end{aligned} \tag{2.18}$$

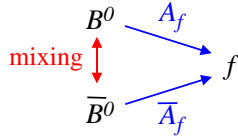


Figure 2.1: An initially pure  $B^0$  or pure  $\bar{B}^0$  state mixes and then decays to a final  $CP$  eigenstate  $f$  that is accessible from either neutral  $B$  meson. As explained in the text,  $CP$  violation can appear in the mixing, in the decay, or in the interference between the decays with and without mixing.

These amplitudes and the coefficients  $p$  and  $q$  of Equation 2.10 are combined into a quantity that is independent of the choice of phase convention:

$$\lambda \equiv \frac{q \bar{A}_f}{p A_f} . \quad (2.19)$$

The violation of  $CP$  invariance can then be expressed as  $\lambda \neq \pm 1$ . Going back to the three categories above,  $CP$  violation through mixing corresponds to the inequality  $|q/p| \neq 1$ ,  $CP$  violation through decay corresponds to  $|\bar{A}_f/A_f| \neq 1$ , and  $CP$  violation through interference of decays with and without mixing comes about cleanly (meaning without contributions from the other two sources) when  $|\lambda| = 1$  but  $\mathcal{I}m \lambda \neq 0$ .

### 2.4.2 The CKM Matrix and the Unitarity Triangle

As mentioned in Section 1.2,  $CP$  violation in the electroweak interaction of the Standard Model is represented by a complex phase in the CKM matrix [5, 15]. This  $3 \times 3$  unitary matrix transforms the mass eigenstates of the down, strange, and bottom quarks to the weak eigenstates, written here as  $d'$ ,  $s'$ , and  $b'$ :

$$\begin{pmatrix} d' \\ s' \\ b' \end{pmatrix} = \begin{pmatrix} V_{ud} & V_{us} & V_{ub} \\ V_{cd} & V_{cs} & V_{cb} \\ V_{td} & V_{ts} & V_{tb} \end{pmatrix} \begin{pmatrix} d \\ s \\ b \end{pmatrix} . \quad (2.20)$$

Different choices for the location of a complex phase within the CKM matrix give rise to different parameterizations. One standard choice uses rotation angles that have a

connection to the mixing between pairs of quark generations. This simplifies through an approximation that includes an expansion in powers of  $\lambda_{\text{CKM}} \equiv \sin \theta_{12} = 0.2229 \pm 0.0022$  [25], where  $\theta_{12}$  is the Cabibbo angle, and this  $\lambda_{\text{CKM}}$  is not to be confused with the  $\lambda$  introduced in Equation 2.19. This form of the CKM matrix, which is particularly useful in  $B$  physics, is referred to as the Wolfenstein parameterization [31]:

$$V = \begin{pmatrix} 1 - \lambda_{\text{CKM}}^2/2 & \lambda_{\text{CKM}} & A\lambda_{\text{CKM}}^3(\rho - i\eta) \\ -\lambda_{\text{CKM}} & 1 - \lambda_{\text{CKM}}^2/2 & A\lambda_{\text{CKM}}^2 \\ A\lambda_{\text{CKM}}^3(1 - \rho - i\eta) & -A\lambda_{\text{CKM}}^2 & 1 \end{pmatrix} + \mathcal{O}(\lambda_{\text{CKM}}^4), \quad (2.21)$$

The parameters  $A$ ,  $\rho$ , and  $\eta$  are real numbers and  $\eta$  represents the  $CP$ -violating phase. By definition, the unitarity of the CKM matrix gives

$$\begin{pmatrix} V_{ud}^* & V_{cd}^* & V_{td}^* \\ V_{us}^* & V_{cs}^* & V_{ts}^* \\ V_{ub}^* & V_{cb}^* & V_{tb}^* \end{pmatrix} \begin{pmatrix} V_{ud} & V_{us} & V_{ub} \\ V_{cd} & V_{cs} & V_{cb} \\ V_{td} & V_{ts} & V_{tb} \end{pmatrix} = \begin{pmatrix} 1 & 0 & 0 \\ 0 & 1 & 0 \\ 0 & 0 & 1 \end{pmatrix}. \quad (2.22)$$

One of the six orthogonality conditions contained in Equation 2.22 is

$$V_{ud}V_{ub}^* + V_{cd}V_{cb}^* + V_{td}V_{tb}^* = 0, \quad (2.23)$$

which is used to construct the *unitarity triangle* displayed in Figure 2.2a. The triangle lies in the complex plane, and can be rescaled, as shown in Figure 2.2b, so that the base has unit length and the apex is at  $(\bar{\rho}, \bar{\eta})$ , where  $\bar{\rho}$  and  $\bar{\eta}$  are related to the CKM matrix parameters  $\rho$  and  $\eta$  through the definitions

$$\bar{\rho} \equiv (1 - \lambda_{\text{CKM}}^2/2)\rho, \quad \bar{\eta} \equiv (1 - \lambda_{\text{CKM}}^2/2)\eta. \quad (2.24)$$

The angles  $\alpha$ ,  $\beta$ , and  $\gamma$  of Figure 2.2 are written in terms of elements of the CKM matrix:

$$\alpha \equiv \arg \left[ -\frac{V_{td}V_{tb}^*}{V_{ud}V_{ub}^*} \right], \quad \beta \equiv \arg \left[ -\frac{V_{cd}V_{cb}^*}{V_{td}V_{tb}^*} \right], \quad \gamma \equiv \arg \left[ -\frac{V_{ud}V_{ub}^*}{V_{cd}V_{cb}^*} \right]. \quad (2.25)$$

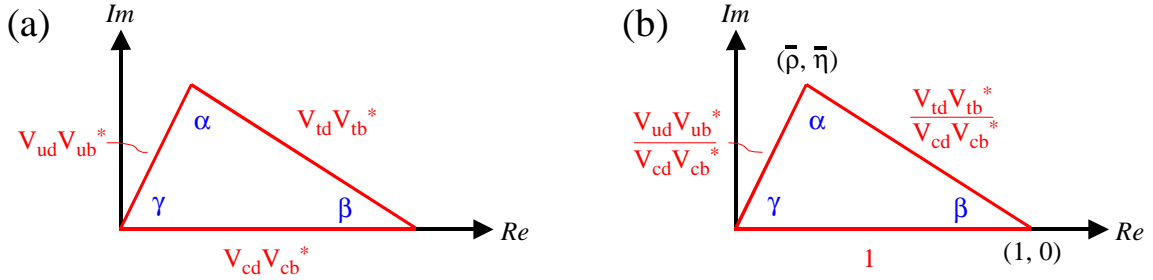


Figure 2.2: The unitarity triangle constructed in the complex plane. The triangles in (a) and (b) differ in scale and the apex position in (b) is given by the relations in Equation 2.24. Regardless of scale, a non-zero area corresponds to  $CP$  violation, which can be quantified by the angles  $\alpha$ ,  $\beta$ , and  $\gamma$ .

These angles can be directly related to measurable physical asymmetries and the connection between  $\beta$  and the time-dependent  $CP$  asymmetry in  $B^0 \rightarrow J/\psi \pi^0$  will be discussed in Section 2.4.4.

### 2.4.3 Tree and Penguin Amplitudes

In the decay  $B^0 \rightarrow J/\psi \pi^0$ , the tree (Figure 1.1a) and penguin (Figure 1.1b) diagrams may contribute at comparable levels. To see this, first the amplitude of the tree diagram is written by combining the CKM matrix elements given by the vertices:

$$A_{\text{tree}}^{J/\psi \pi^0} \sim V_{cb} V_{cd}^* = A \lambda_{\text{CKM}}^3. \quad (2.26)$$

Next, the same is done for the penguin diagram:

$$A_{\text{penguin}}^{J/\psi \pi^0} \sim V_{tb} V_{td}^* f(m_t) + V_{cb} V_{cd}^* f(m_c) + V_{ub} V_{ud}^* f(m_u), \quad (2.27)$$

where the functions  $f(m_q)$ , with  $q = u, c, t$ , depend upon the quark masses, and carry the associated uncertainties. To compare this with the tree amplitude, the

orthogonality relation in Equation 2.23 is used to rewrite Equation 2.27 as

$$\begin{aligned} A_{\text{penguin}}^{J/\psi \pi^0} &\sim V_{cb}V_{cd}^*[f(m_c) - f(m_t)] + V_{ub}V_{ud}^*[f(m_u) - f(m_t)] \\ &\sim \mathcal{O}(\lambda_{\text{CKM}}^3) + \mathcal{O}(\lambda_{\text{CKM}}^3) . \end{aligned} \quad (2.28)$$

Thus, the tree and both terms of the penguin amplitudes enter at  $\mathcal{O}(\lambda_{\text{CKM}}^3)$ . This is an important difference between  $B^0 \rightarrow J/\psi \pi^0$  and  $B^0 \rightarrow J/\psi K_S^0$  decays. The tree level process for  $B^0 \rightarrow J/\psi \pi^0$  contains the interaction  $W^+ \rightarrow \bar{c}d$  rather than  $W^+ \rightarrow \bar{c}s$ , which is found in  $B^0 \rightarrow J/\psi K_S^0$  decays. This Cabibbo suppression reduces the tree amplitude in  $B^0 \rightarrow J/\psi \pi^0$  with respect to that of  $B^0 \rightarrow J/\psi K_S^0$  by approximately [25]

$$\left| \frac{V_{cd}}{V_{cs}} \right| \approx 0.225 \pm 0.016 , \quad (2.29)$$

and rates enter as the square of the total amplitude. It has a similar impact on the first term of the penguin amplitude. Therefore, the second term of the penguin amplitude for  $B^0 \rightarrow J/\psi \pi^0$  is at a level that may interfere with the other contributions. As seen in the equations below, this is not the case for  $B^0 \rightarrow J/\psi K_S^0$ , where the second term of the penguin amplitude is reduced by two powers of  $\lambda_{\text{CKM}}$  compared to the others:

$$\begin{aligned} A_{\text{tree}}^{J/\psi K_S^0} &\sim V_{cb}V_{cs}^* \sim \mathcal{O}(\lambda_{\text{CKM}}^2) , \\ A_{\text{penguin}}^{J/\psi K_S^0} &\sim V_{cb}V_{cs}^*[f(m_c) - f(m_t)] + V_{ub}V_{us}^*[f(m_u) - f(m_t)] \\ &\sim \mathcal{O}(\lambda_{\text{CKM}}^2) + \mathcal{O}(\lambda_{\text{CKM}}^4) . \end{aligned} \quad (2.30)$$

The forms of Equations 2.26 and 2.28 also suggest (see, e.g., Ref. [32]) combining the part of the penguin amplitude that depends on  $V_{cb}V_{cd}^*$  with the tree amplitude (which also depends on  $V_{cb}V_{cd}^*$ ) when constructing a total amplitude. Therefore, in the following discussion, the subscript  $T$  refers to a portion of the total amplitude that contains both tree and penguin contributions proportional to  $V_{cb}V_{cd}^*$ , and the subscript  $P$  refers to a portion that is entirely due to the remaining penguin contribution.

To be general, we can write the amplitude for the decay of  $B^0$  and  $\bar{B}^0$  as

$$\begin{aligned} A &= A_T e^{+i\phi'_T} e^{i\delta_T} + A_P e^{+i\phi'_P} e^{i\delta_P} , \\ \bar{A} &= A_T e^{-i\phi'_T} e^{i\delta_T} + A_P e^{-i\phi'_P} e^{i\delta_P} , \end{aligned} \quad (2.31)$$

where  $\phi'_T$  and  $\phi'_P$  are convention-dependent weak phases, and  $\delta_T$  and  $\delta_P$  are convention-dependent strong phases. Because only the difference between the weak phases and the difference between the strong phases matter, we can rotate to the notation

$$\begin{aligned} \phi_T &= \phi'_T - \frac{\arg(q/p)}{2} , \\ \phi_P &= \phi'_P - \frac{\arg(q/p)}{2} , \\ \delta &= \delta_P - \delta_T , \end{aligned} \quad (2.32)$$

where  $p$  and  $q$  are from Equation 2.10. By inserting the amplitudes of Equation 2.31 into Equation 2.19, and using the substitutions of Equation 2.32, we arrive at

$$\lambda = \eta_f \frac{e^{-i\phi_T} + r e^{-i\phi_P} e^{i\delta}}{e^{i\phi_T} + r e^{i\phi_P} e^{i\delta}} , \quad (2.33)$$

where  $\eta_f = \pm 1$  is the  $CP$  eigenvalue and  $r \equiv A_P/A_T$ . We can also write the total amplitudes from  $B^0$  and  $\bar{B}^0$  to the  $J/\psi \pi^0$  final state as

$$\begin{aligned} A^{J/\psi \pi^0} &= V_{cb} V_{cd}^* (T + P_c - P_t) + V_{ub} V_{ud}^* (P_u - P_t) e^{i\delta} , \\ \bar{A}^{J/\psi \pi^0} &= V_{cb}^* V_{cd} (T + P_c - P_t) + V_{ub}^* V_{ud} (P_u - P_t) e^{i\delta} , \end{aligned} \quad (2.34)$$

where the shorthand  $T$ ,  $P_u$ ,  $P_c$ , and  $P_t$  has been introduced for the contributions from the tree and penguin diagrams. Inserting these expressions into Equation 2.19 yields

$$\lambda = \frac{e^{-i\beta} + r e^{-i(\pi-\gamma+\beta)} e^{i\delta}}{e^{i\beta} + r e^{i(\pi-\gamma+\beta)} e^{i\delta}} \quad \text{for } B^0 \rightarrow J/\psi \pi^0 . \quad (2.35)$$

The details of this calculation reveal that

$$r = \sqrt{\rho^2 + \eta^2} \frac{P_u - P_t}{T + P_c - P_t} . \quad (2.36)$$

Comparison of Equation 2.35 and Equation 2.33 gives  $\phi_T = \beta$  and  $\phi_P = \pi - \gamma + \beta$ , which are crucial in relating observable quantities to the angles of the unitarity triangle, as explained in the next section.

#### 2.4.4 Observable Quantities

The  $CP$  asymmetry, written in terms of the decay rates from initially pure  $B^0$  and  $\bar{B}^0$  states to a common final  $CP$  eigenstate, is

$$a_{CP} = \frac{\Gamma(B_{phys}^0(t) \rightarrow f) - \Gamma(\bar{B}_{phys}^0(t) \rightarrow f)}{\Gamma(B_{phys}^0(t) \rightarrow f) + \Gamma(\bar{B}_{phys}^0(t) \rightarrow f)} . \quad (2.37)$$

The strategy for relating this asymmetry to parameters of  $CP$  violation is guided by the fact that neutral  $B$  mesons produced at the  $\Upsilon(4S)$  resonance are in a coherent  $L = 1$  state. This means that when one of the two  $B$  mesons decays, the flavor of the other is determined at that instant, or at any other time using the time evolution (see Equation 2.17). Therefore, when one observes and reconstructs an exclusive final state such as  $J/\psi \pi^0$ , the other  $B$  in the event may be used to infer, or “tag”, the flavor of the  $B$  that decays into  $J/\psi \pi^0$ . The practical matter of how often this determination can be made, and the associated uncertainties, are presented in Chapter 5.

By manipulating expressions for decays into two states, at two different times, as done for example in Reference [33], the  $CP$  asymmetry can be rewritten in terms of the parameter  $\lambda$  introduced in Equation 2.19:

$$a_{CP} = \frac{2 \Im \lambda}{1 + |\lambda|^2} \sin(\Delta m_d \Delta t) - \frac{1 - |\lambda|^2}{1 + |\lambda|^2} \cos(\Delta m_d \Delta t) , \quad (2.38)$$

where  $\Delta t = t_{\text{rec}} - t_{\text{tag}}$  is the difference between the proper decay time of the reconstructed  $B$  meson ( $B_{\text{rec}}$ ) and the proper decay time of the tagging  $B$  meson ( $B_{\text{tag}}$ ), and  $\Delta m_d$  is the  $B^0$ - $\bar{B}^0$  oscillation frequency. Furthermore, the decay rate  $f_+(f_-)$ ,

when the tagging meson is a  $B^0(\bar{B}^0)$ , is given by

$$f_{\pm}(\Delta t) = \frac{e^{-|\Delta t|/\tau_{B^0}}}{4\tau_{B^0}} \left[ 1 \pm \frac{2\mathcal{I}m\lambda}{1+|\lambda|^2} \sin(\Delta m_d \Delta t) \mp \frac{1-|\lambda|^2}{1+|\lambda|^2} \cos(\Delta m_d \Delta t) \right], \quad (2.39)$$

where  $\tau_{B^0}$  is the  $B^0$  lifetime. The measurable coefficients of the time-dependent  $CP$  asymmetry are

$$S_f \equiv \frac{2\mathcal{I}m\lambda}{1+|\lambda|^2}, \quad C_f \equiv \frac{1-|\lambda|^2}{1+|\lambda|^2}, \quad (2.40)$$

where  $f$  is the final state. The determination of these quantities for the decay  $B^0 \rightarrow J/\psi \pi^0$  is the primary objective of this thesis. The relationship between these coefficients and the formulation of  $CP$  violation within the Standard Model, as expressed through the CKM matrix and the unitarity triangle (see Section 2.4.2), is particularly simple for  $B^0 \rightarrow J/\psi K_s^0$ , and is treated here first as an example.

As shown in Section 2.4.3, for  $B^0 \rightarrow J/\psi K_s^0$  the tree amplitude dominates, or  $A_P \ll A_T$ , and thus the ratio of the penguin to tree amplitudes can be taken as  $r = 0$ . Therefore, Equation 2.33 for  $\lambda$  simplifies:

$$\lambda = \eta_f \frac{e^{-i\phi_T}}{e^{i\phi_T}} = (-1)e^{-i2\phi_T} = -e^{-i2\beta} \quad \text{for } B^0 \rightarrow J/\psi K_s^0. \quad (2.41)$$

Here, the  $CP$  eigenvalue for  $B^0 \rightarrow J/\psi K_s^0$ , namely  $\eta_f = -1$ , has been used, as has the fact that the weak phase of the tree dominated portion of the amplitude is equal to one of the angles of the unitarity triangle,  $\phi_T = \beta$ . So, the asymmetry coefficients reduce to

$$\begin{aligned} S_{J/\psi K_s^0} &= \frac{2\sin 2\beta}{2} = \sin 2\beta && \text{for } B^0 \rightarrow J/\psi K_s^0, \\ C_{J/\psi K_s^0} &= 0 && \text{for } B^0 \rightarrow J/\psi K_s^0. \end{aligned} \quad (2.42)$$

These simple relations, with the associated asymmetry  $a_{CP} = \sin(\Delta m_d \Delta t) \sin 2\beta$ , and the relatively large branching fraction and reconstruction efficiency, have motivated the use of  $B^0 \rightarrow J/\psi K_s^0$  as the ‘‘golden mode’’ at the  $B$  Factories.

For  $B^0 \rightarrow J/\psi \pi^0$ , things are not as simple, but relations again exist between the

$CP$  asymmetry coefficients and the unitarity triangle. The form of  $\lambda$  is not simplified beyond how it appears in Equation 2.33, although again  $\phi_T = \beta$ . Another difference with respect to  $B^0 \rightarrow J/\psi K_S^0$  is the sign of the  $CP$  eigenvalue, which is  $\eta_f = +1$  for  $B^0 \rightarrow J/\psi \pi^0$ . The expressions for  $S_{J/\psi \pi^0}$  and  $C_{J/\psi \pi^0}$  remain rather general:

$$\begin{aligned} S_{J/\psi \pi^0} &= \frac{-\sin 2\beta - 2r \sin(\beta + \phi_P) \cos(\delta) - r^2 \sin 2\phi_P}{1 + r^2 + 2r \cos(\beta - \phi_P) \cos(\delta)}, \\ C_{J/\psi \pi^0} &= \frac{2r \sin(\beta - \phi_P) \sin(\delta)}{1 + r^2 + 2r \cos(\beta - \phi_P) \cos(\delta)}. \end{aligned} \quad (2.43)$$

To summarize the relations for  $S_{J/\psi \pi^0}$  and  $C_{J/\psi \pi^0}$ , we can also substitute in the expression  $\phi_P = \pi - \gamma + \beta$  that was determined at the end of Section 2.4.3:

$$\begin{aligned} S_{J/\psi \pi^0} &= \frac{-\sin 2\beta + 2r \sin(2\beta - \gamma) \cos(\delta) - r^2 \sin(2\beta - 2\gamma)}{1 + r^2 - 2r \cos(\gamma) \cos(\delta)}, \\ C_{J/\psi \pi^0} &= \frac{-2r \sin(\gamma) \sin(\delta)}{1 + r^2 - 2r \cos(\gamma) \cos(\delta)}, \end{aligned} \quad (2.44)$$

with

$$r = \sqrt{\rho^2 + \eta^2} \frac{P_u - P_t}{T + P_c - P_t}. \quad (2.45)$$

In the absence of penguin contributions, the coefficients given in Equation 2.44 for  $B^0 \rightarrow J/\psi \pi^0$  would reduce to  $S_{J/\psi \pi^0} = -\sin 2\beta$  and  $C_{J/\psi \pi^0} = 0$ . Therefore, deviations from these values may indicate a significant penguin amplitude. This, along with possible constraints on the ratio of penguin to tree amplitudes in both  $B^0 \rightarrow J/\psi \pi^0$  and  $B^0 \rightarrow J/\psi K_S^0$ , are discussed in the concluding chapter.

# Chapter 3

## The *BABAR* Detector at PEP-II

The *BABAR* detector and the PEP-II storage rings at SLAC have been optimized for the study of *CP* violation in *B* decays. This chapter presents some of the key features of these complex systems, first outlining the specifications and performance of the accelerator, and then focusing on the detector subsystems.

### 3.1 Overview of PEP-II

As mentioned in Section 1.1, there are substantial benefits to operating at the  $\Upsilon(4S)$  resonance and to producing *B* mesons that are boosted in the lab frame. The PEP-II storage rings, sitting at the end of the 3 km linear accelerator (linac) located at SLAC (Figure 3.1), were designed to meet these objectives [34].

Electrons and positrons are accelerated in alternate bunches within the linac. The former originate from an electron gun and the latter are produced by colliding some of the electrons with tungsten. The positrons are fed back into the linac out of phase with the electrons, thus allowing for the use of a single set of accelerator structures for the linear portion. The two particle types are extracted into separate damping rings, which reduce the transverse motion of the particles. They re-enter the linac, and at a point where they reach the appropriate energy they are extracted into bypass lines and redirected by dipoles at the beam switch yard into the PEP-II storage rings.

Within the PEP-II tunnel, the low energy ring (LER) contains a 3.1 GeV  $e^+$  beam



Figure 3.1: This aerial view of the Stanford Linear Accelerator Center shows the 3 km linac. The interaction region of the PEP-II beams, where *BABAR* is located, is housed in the building just to the left of center in the bottom of the photograph.

Table 3.1: Design goals and typical performance parameters for PEP-II. The quantities  $\sigma_x$ ,  $\sigma_y$ , and  $\sigma_z$  correspond to the horizontal, vertical, and longitudinal rms beam spot sizes, respectively.

Parameter	Design goal	Typical in first year	End of June 2002
Energy HER / LER (GeV)	9.0 / 3.1	9.0 / 3.1	9.0 / 3.1
Current HER / LER (A)	0.75 / 2.15	0.7 / 1.3	0.9 / 1.8
# of bunches	1658	553–829	800
Bunch spacing (ns)	4.2	6.3–10.5	8.4
$\sigma_x$ ( $\mu\text{m}$ )	110	120	150
$\sigma_y$ ( $\mu\text{m}$ )	3.3	5.6	6.4
$\sigma_z$ (mm)	9	9	13
Luminosity ( $10^{33} \text{ cm}^{-2} \text{ s}^{-1}$ )	3	2.5	4.5
Luminosity ( $\text{pb}^{-1}/\text{day}$ )	135	120	250

and the high energy ring (HER) contains a 9.0 GeV  $e^-$  beam, giving a center-of-mass energy of 10.58 GeV, which is equal to the  $\Upsilon(4S)$  rest mass. The beams are brought into collision at a single interaction region with zero crossing angle. The final steering is accomplished with tapered dipole permanent magnets, which are located  $\pm 21$  cm from the interaction point (IP), and a series of quadrupoles. The dipoles and the set of quadrupoles closest to the IP bend the incoming particles of one beam and the outgoing particles of the other. The quadrupoles farther from the IP are iron magnets and are positioned where the beams are sufficiently separated so that the magnets act on only one beam or the other. The beam-pipe surrounding the interaction region consists of two concentric cylinders of beryllium, with a 1.48 mm radial gap for a water cooling channel between the two layers. In addition, there is a  $4 \mu\text{m}$  layer of gold coating the inner surface of the inner beryllium cylinder to help block synchrotron radiation. The entire beam-line is summarized in Figure 3.2. The design goals and typical performance parameters for the PEP-II facility are shown in Table 3.1.

It takes about ten minutes to fill the storage rings from empty and the beams are typically held for just short of an hour before they need to be topped off with an additional injection from the linac, which takes about three minutes. A run is

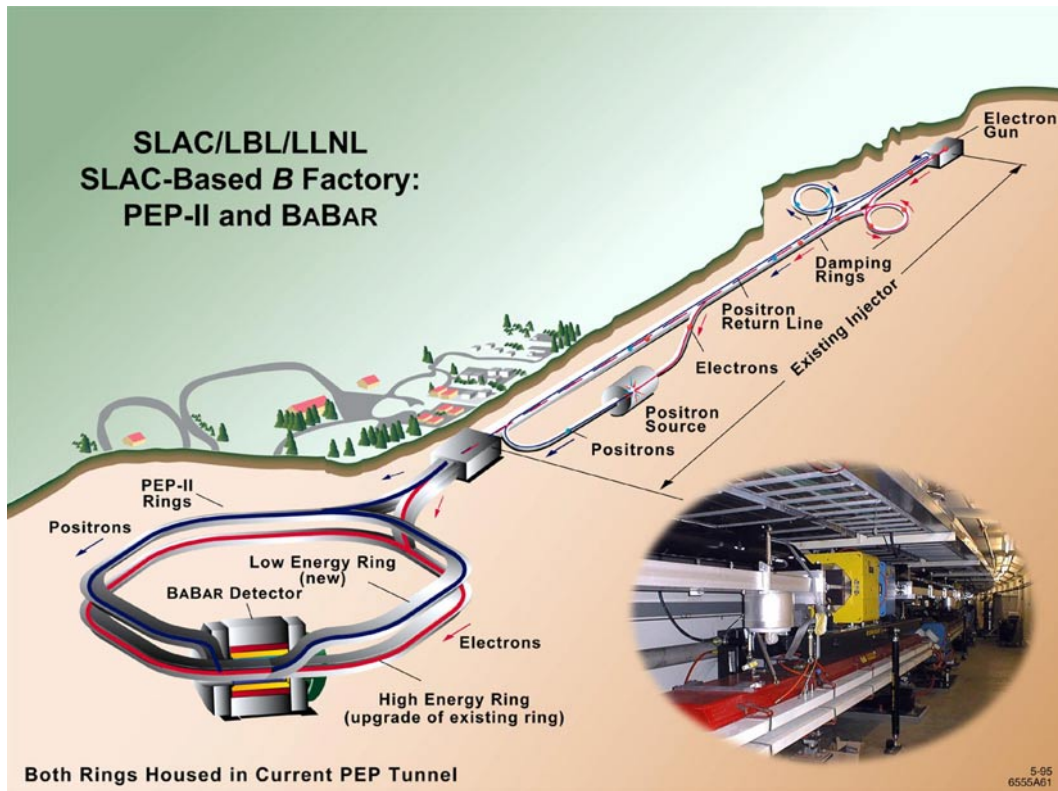


Figure 3.2: The  $e^-$  (red) and  $e^+$  (blue) beams, as described in the text, are depicted in the linac and PEP-II rings. The inset shows the HER situated above the LER in the PEP-II tunnel.

defined to be a period of about three hours or less when the conditions of the beam and detector are stable. During storage, energy loss due to synchrotron radiation is counteracted with acceleration at radio frequency cavity installations at sites along PEP-II.

About 90% of the data collected by *BABAR* are at the  $\Upsilon(4S)$  resonance, or *onpeak*, and the remaining are at 40 MeV below the resonance, or *offpeak*. The absolute beam energies are measured with a systematic uncertainty of 5–10 MeV and there is an uncertainty on the control of the beam energies of about 1 MeV. During *onpeak* running, it is important for the machine to operate as close to the  $\Upsilon(4S)$  resonance as possible, and the ultimate measure of the center-of-mass energy is calculated from the momentum of fully reconstructed  $B$  decays and the PDG value of the  $B$  mass. With  $1 \text{ fb}^{-1}$  of data, the center-of-mass energy can be determined to 1.1 MeV. In addition, the ratio of  $B\bar{B}$  events to lepton pair production serves as an on-line measurement that is sensitive to changes in the operating point.

The difference in beam energies provides a boost of approximately  $\beta\gamma = 0.56$  to the center-of-mass system with respect to the lab system. The direction of the boost,  $\vec{\beta}$ , is monitored from run to run using  $e^+e^- \rightarrow e^+e^-$  and  $e^+e^- \rightarrow \mu^+\mu^-$  events, with an associated uncertainty of about 1 mrad.

The position, size, and orientation of the beam spot are also measured using events with two tracks. The uncertainty on the average position in the transverse dimensions is on the order of a few  $\mu\text{m}$ , which is comparable to the beam size in the vertical direction, and roughly a factor of 40 smaller than the beam size in the horizontal direction. The uncertainty on the position in the longitudinal direction is about  $100 \mu\text{m}$ , to be compared with the 9–13 mm beam size. The beam position is stable from run to run, changing at a level comparable to the uncertainties on the position determination. The parameters representing the position, size, and orientation of the beam spot are stored in a database of accelerator and detector conditions, which is then used during analysis.

Real-time monitoring of the luminosity uses radiative Bhabha events, while an off-line measurement is made from  $e^+e^- \rightarrow e^+e^-$  and  $e^+e^- \rightarrow \mu^+\mu^-$  rates. The systematic uncertainty on the measurement is about 1.5% and is dominated by the

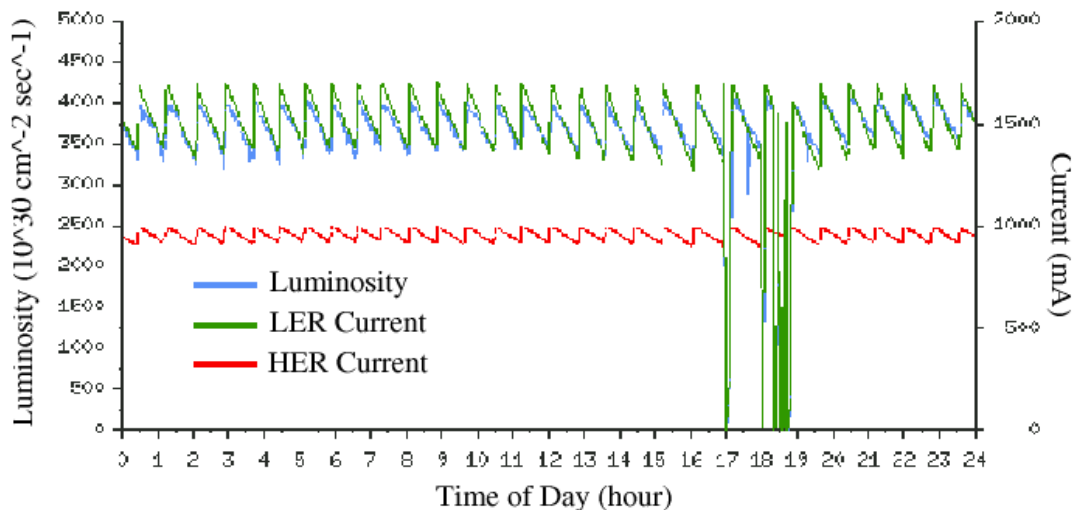


Figure 3.3: The luminosity (blue), LER current (green), and HER current (red) are shown for June 23, 2002. The topping off of the storage rings, which occurs approximately once every hour, is evident. This day was dedicated to physics data taking, rather than machine development.

Monte Carlo simulation and the understanding of the detector. An example of the luminosity performance, over the course of a day dedicated to data taking rather than machine development, is shown in Figure 3.3. The figure also includes the currents for the LER and HER. The integrated luminosity for the period beginning October 1999 and ending June 2002 is shown in Figure 3.4, including the total delivered and recorded luminosities, as well as the recorded *offpeak* luminosity. The details regarding the sizes of the data samples used in the  $B^0 \rightarrow J/\psi \pi^0$  branching fraction and  $CP$  asymmetry measurements are presented in Chapters 4 and 5.

## 3.2 The *BABAR* Detector

The *BABAR* detector has many features in common with other high energy physics detectors. It is composed of individual subsystems designed to contribute specific information utilized in reconstructing decay processes, and separating signal from background. It also includes unique features and technological advances required to

2002/07/08 17.14

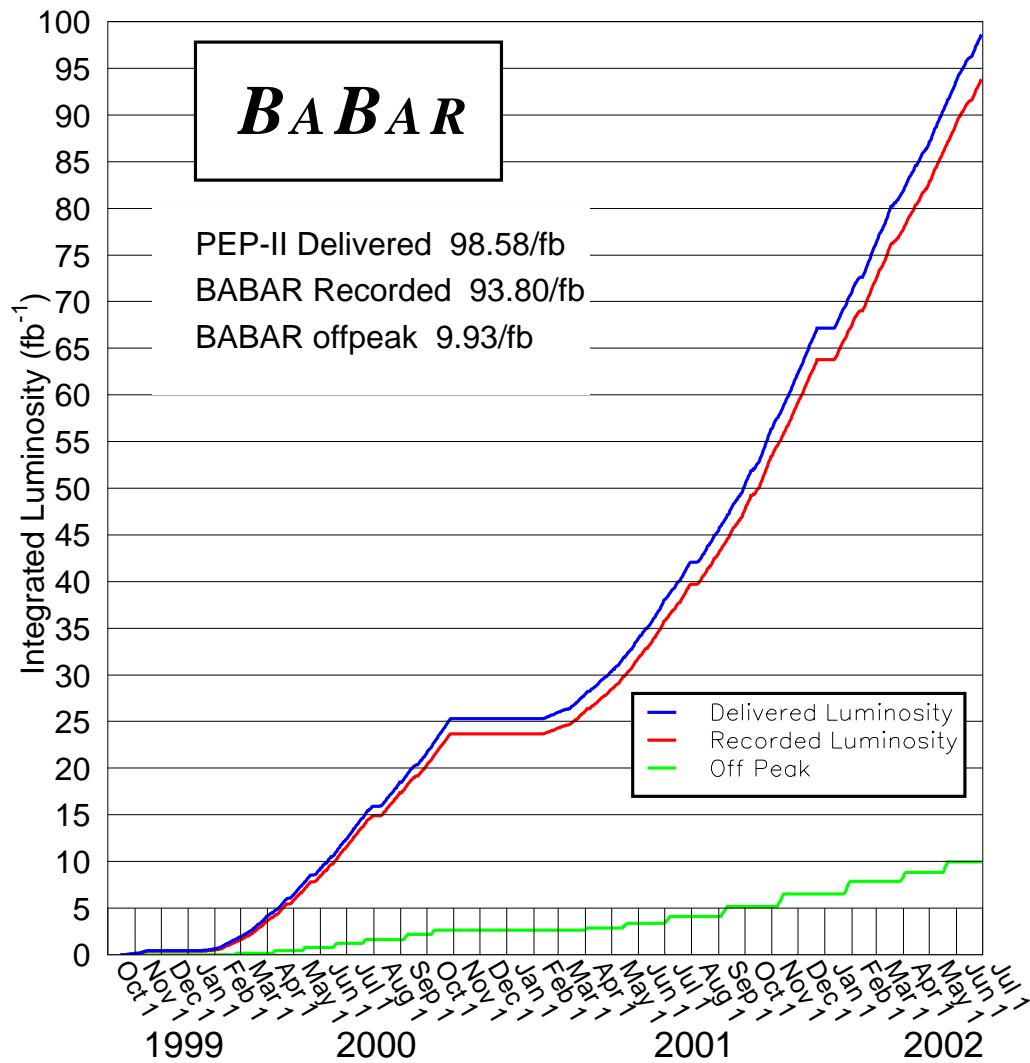


Figure 3.4: The PEP-II delivered (blue), *BABAR* recorded total (red), and *BABAR* recorded *offpeak* (green) luminosities are shown for October 1999 through June 2002. This represents a 95% data-taking efficiency.

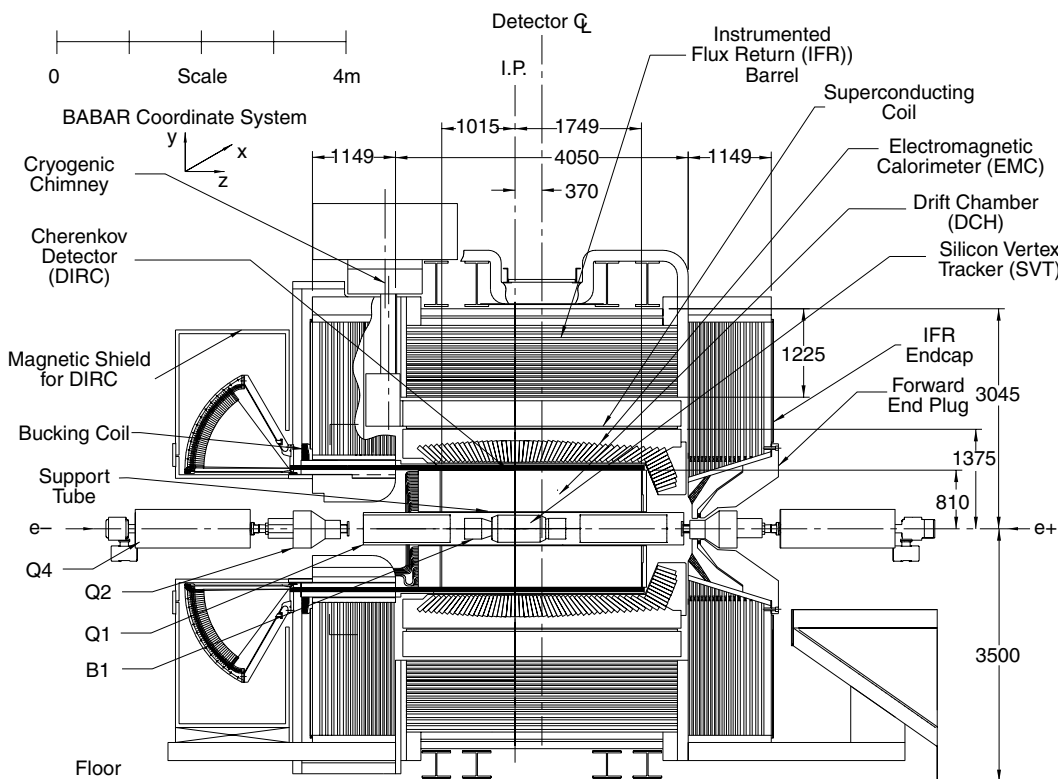


Figure 3.5: Side-view of the *BABAR* detector, with dimensions in millimeters. Figures in this section are courtesy of Ref. [35].

match the physics goals of the experiment. This section presents some of the key features of the subsystems of the *BABAR* detector. Most of the figures in this section, and the source material for many of the technical discussions, are courtesy of Ref. [35].

Side- and end-views of the *BABAR* detector are shown in Figures 3.5 and 3.6. The charged particle tracking is accomplished by combining information from a silicon vertex tracker (SVT) and a drift chamber (DCH). The SVT surrounds the beryllium section of the beam-pipe, and the DCH forms a cylinder around the SVT. Together, these detectors allow measurements of track momenta and trajectory in a 1.5-T magnetic field, as well as energy-loss measurements, which contribute to charged particle identification. Surrounding the DCH is a detector of internally reflected Cherenkov radiation (DIRC), which provides identification of charged hadrons. Surrounding this

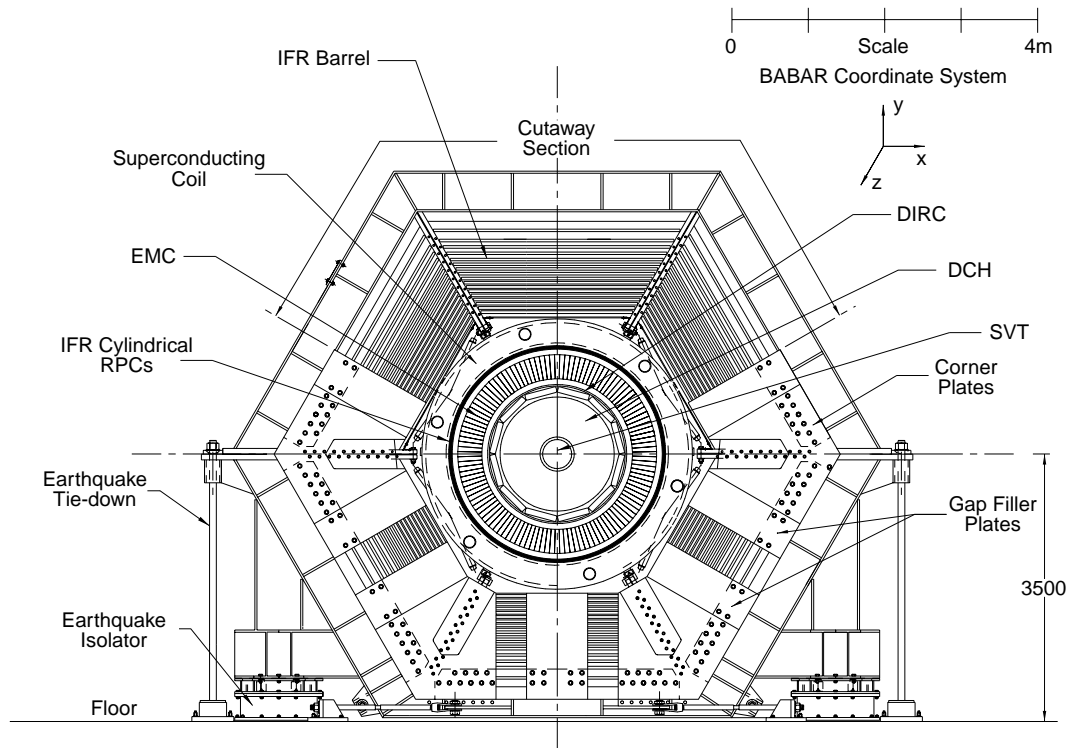


Figure 3.6: End-view of the *BABAR* detector, with dimensions in millimeters.

is an electromagnetic calorimeter (EMC), which detects photons and contributes to electron identification and the reconstruction of neutral hadrons. The EMC is surrounded by the superconducting coil, which creates the magnetic field for momentum and charge measurements. Outside of the coil, the flux return yoke is instrumented with resistive plate chambers interspersed with iron (IFR) for identification of muons and long-lived neutral hadrons.

### 3.2.1 Silicon Vertex Tracker

The silicon vertex tracker consists of five layers of double sided silicon strips. The silicon is held at a reverse bias, so that the material is depleted of mobile charge carriers and a voltage difference exists in the active region. The passage of a charged particle liberates charge carriers, which move under the influence of the potential and are picked up by electrodes.

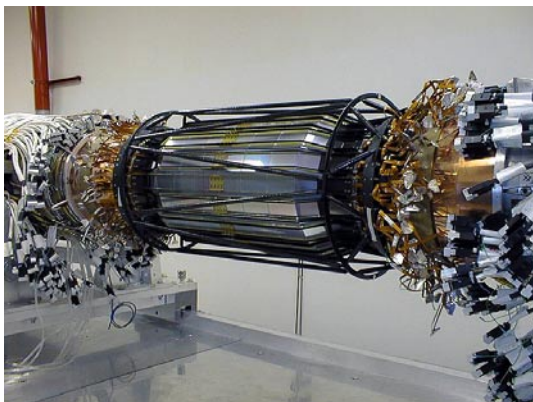


Figure 3.7: This photograph shows the SVT and the carbon-fiber support frame.

120 MeV/ $c$ , which is critical for the reconstruction of low momentum pions coming from  $D^*$  meson decays. Also, the SVT provides the best measurement of track angles, which are used in conjunction with the DIRC to resolve the Cherenkov angles, and therefore to perform particle identification.

The geometrical design of the SVT was driven by the desire to efficiently measure track trajectory parameters and momentum, along with the location of decay vertices near the interaction region. In particular, the study of time-dependent  $CP$  asymmetry calls for the ability to resolve the  $z$ -position of fully reconstructed  $B$ -decay vertices to better than  $80\ \mu\text{m}$ . The SVT also provides the tracking for particles with transverse momentum of less than

The complete SVT detector is pictured in Figure 3.7. The five concentric layers are each made up of staves, much like those of a wooden barrel. The inner three layers each have six of these staves, while the outer two layers have 16 and 18 staves, respectively. The arrangement can be seen in Figures 3.8 and 3.9, where the inner most layer is at a radius of 32 mm and the outer most layer is at a radius of 144 mm. The staves are mounted on forward and backward carbon-fiber support cones, with additional carbon-fiber bracing surrounding the SVT. The SVT, along with the beam-pipe and final focus magnets, is contained within a support tube that is anchored to PEP-II rather than *BABAR*. Therefore, monitoring of the beam spot location and alignment between the SVT and DCH are crucial.

One side of each double sided layer has strips running parallel to the beam axis, to measure  $\phi$ , while the opposite side of each layer has strips running in the orthogonal direction, to measure  $z$ . The strips have a readout pitch ranging from  $50\ \mu\text{m}$  to  $210\ \mu\text{m}$ , and make up a total of approximately 150,000 channels, covering a total area of about  $0.96\ \text{m}^2$ . The detector represents 4% of a radiation length and provides geometrical acceptance of 90% of the solid angle in the center-of-mass system.

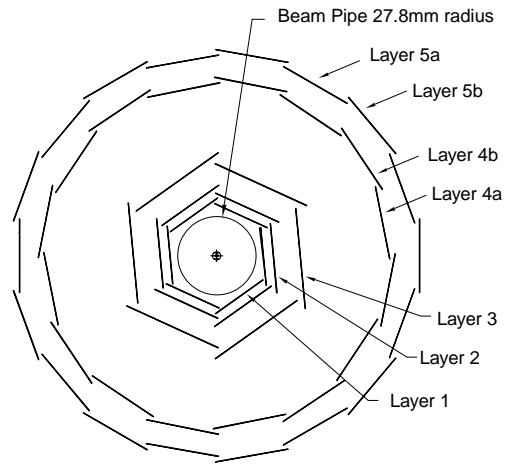


Figure 3.8: Schematic  $xy$ -view cross-section of the SVT.

The operating voltage of the silicon is about 10 V above depletion voltage, which is about 25–35 V. Initial leakage currents were around  $50\ \text{nA}/\text{cm}^2$ . The signals propagate from the silicon, through fanouts and front end electronics, and through conventional cables to outside the detector, where they are transferred to fiber optic transmission lines. The fanouts have low series resistance and inter-strip capacitance, and the combination of silicon and fanouts have input capacitances in the range 6.0–39.7 pF, and series resistances in the range 40–265  $\Omega$ , depending on the length of the strip. The SVT front end electronics include a custom integrated circuit called the ATOM (A

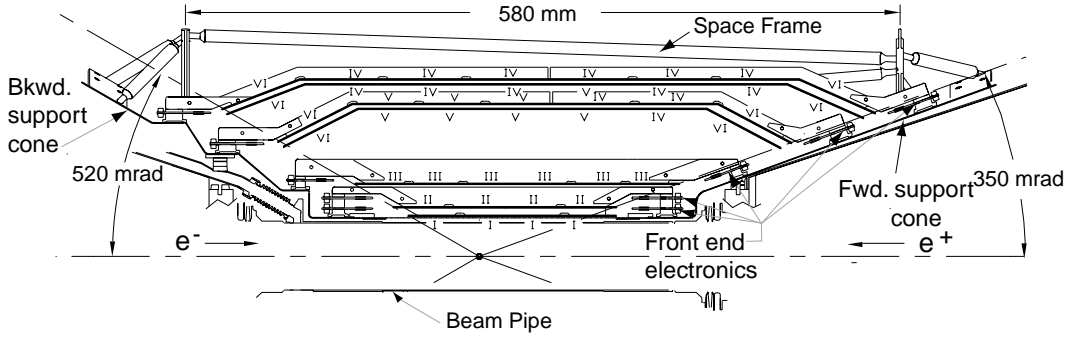


Figure 3.9: Schematic longitudinal cross-section of the SVT.

*Time-Over-Threshold Machine*). The ATOM contains a preamplifier, with a settable gain of 200 or 300 mV/fC, a signal shaper, and a threshold comparator, the output of which is sampled at 15 MHz and stored in a buffer. If there is a *level 1* trigger and accept, the event time, time-over-threshold and hit strip address are sent to the *BABAR* data acquisition system.

The average occupancy in the SVT, over the course of  $1 \mu\text{s}$ , is about 3% for layers one through three, and is less than 1% for layers four and five, with the greatest rates in the horizontal plane that includes the beams. The average efficiency over functional SVT modules is 97%. This is calculated from the ratio of the number of hits in a local region to the number of tracks crossing that region, and excludes nine out of 208 modules that are considered to be non-functional for a variety of reasons. Single dead channels are included in this calculation, but do not significantly impact the efficiency because usually more than one strip is hit.

The hit resolution of the SVT is calculated from the residuals between high momentum tracks and hits, subtracting off the uncertainty in the track trajectory. The hit resolution ranges from about  $15 \mu\text{m}$  to  $50 \mu\text{m}$  in  $z$ , and from about  $11 \mu\text{m}$  to  $35 \mu\text{m}$  in  $\phi$ , depending on the layer and track incident angle.

The time-over-threshold measurements mentioned above allow for the calculation of pulse heights, and therefore  $dE/dx$ . This is used in combination with  $dE/dx$

information from the drift chamber for particle identification purposes, as discussed in Section 3.2.2, but can also be used by itself. In particular, the resolution for the truncated mean  $dE/dx$  distribution for minimum ionizing particles is about 14% in the SVT. This enables a  $2\sigma$  separation of pions and kaons up to 500 MeV/ $c$ .

The next section, although primarily devoted to the drift chamber, includes some discussion of the tracking performance, which depends on both the SVT and the DCH.

### 3.2.2 Drift Chamber

When a charged particle passes through the *BABAR* drift chamber, it ionizes the gas along the particle trajectory, and the resulting ionization electrons drift under the influence of electric and magnetic fields to anode sense wires. Near the sense wires, the ionization electrons undergo an avalanche process. The generated positive ions drift under the influence of a  $1/r$  potential, and their image charge produces a signal, where the wire is treated as a voltage source.

The primary role of the DCH is to efficiently measure the momentum (magnitude and direction) of charged particles as they traverse the detector. Information is combined from the SVT and DCH to form helical fits to track trajectories, and tracks are extrapolated to the outer detectors. At low momenta, the  $dE/dx$  measurements from the DCH strongly contribute to particle identification, and outside of the angular acceptance of the dedicated particle identification device, the DCH is the only source of information for pion and kaon separation. Also, certain decays, such as  $K_s^0 \rightarrow \pi^+\pi^-$ , are primarily accessible via the DCH.



Figure 3.10: Photograph of the DCH. The 40 layers, grouped into 10 *superlayers*, are visible on the forward end of the chamber.

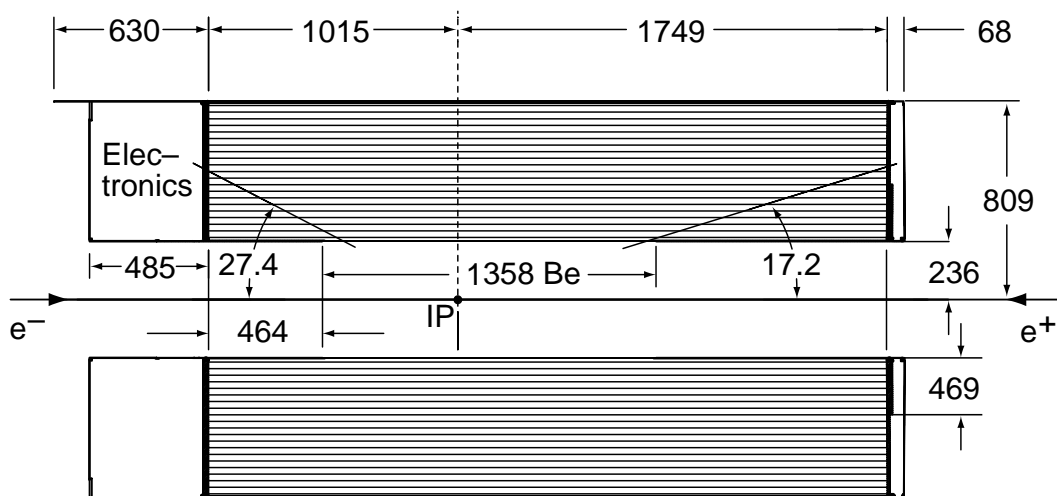


Figure 3.11: Schematic longitudinal cross-section of the DCH.

The DCH is pictured in Figure 3.10. The design of the chamber was dictated by the physics goals and associated performance requirements. It is a barrel with an inner radius of 23.6 cm, an outer radius of 80.9 cm, and a total length of 3.46 m. As shown in Figure 3.11, this includes space at the rear endplate of the chamber for mounting high voltage distribution and readout electronics, which is advantageous given the asymmetric particle production coming from the interaction point. The inner cylinder is constructed of beryllium in the central region, and aluminum closer to the endcaps. This was done to minimize the amount of material, and to provide good matching with tracks in the SVT, while still providing a portion of the necessary mechanical support to counter the tension of the chamber wires. The outer cylinder is a combination of aluminum and a carbon-fiber honeycomb, again to provide support with a small amount of material. In the radial direction, the inner and outer cylinders represent 0.28% and 0.6% of a radiation length, respectively. The gas, an 80:20 mixture of helium and isobutane, yields primary ions at the rate of 21.2/cm and gives a drift velocity of about  $22 \mu\text{m}/\text{ns}$ . The gas and the wires, taken in combination, represent just 0.2% of a radiation length.

The DCH contains 7104 sense wires centered in close-packed hexagonal cells, defined by field wires at the corners of the hexagons. These cells form 40 layers, which

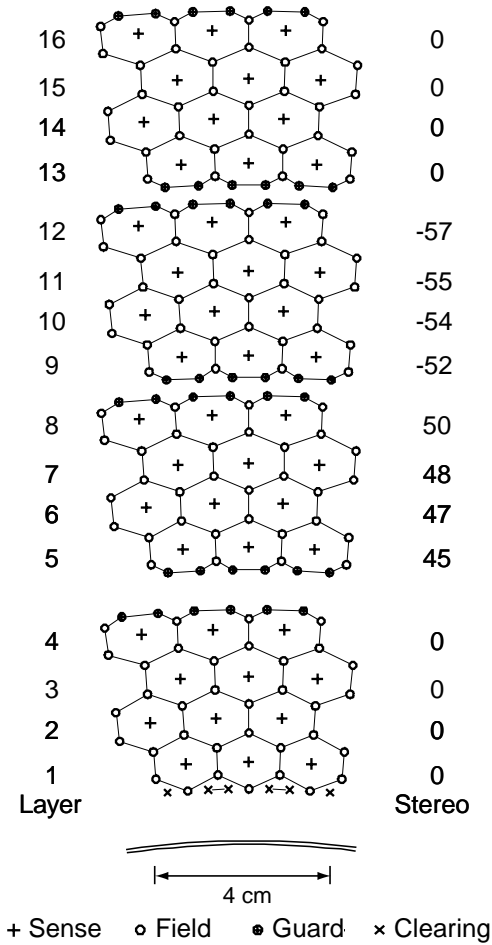


Figure 3.12: Arrangement of DCH cells into layers and superlayers for the first 4 of 10 superlayers. The left column gives the layer number, while the right column gives the stereo angle in mrad. The legend shows the different wire types, and a small section of the inner cylinder is shown at the bottom. The lines between wires are purely for illustration.

Table 3.2: Materials, specifications, and voltage settings for the four types of wires used in the DCH. The three voltage set points correspond to the time periods: (A) October, 1999 – July 10, 2000, (B) July 20, 2000 – October, 2000, and (C) 2001 onward.

Type	Material (gold plated)	Diameter ( $\mu\text{m}$ )	Tension (g)	Voltage set point (V)		
				A	B	C
Sense	Tungsten-Rhenium	20	30	1900	1960	1930
Field	Aluminum	120	155	0	0	0
Guard	Aluminum	80	74	329	340	334
Clearing	Aluminum	120	155	800	825	812

are grouped into 10 superlayers of 4 layers each. The layers of a given superlayer contain the same number of cells per layer. The superlayers cycle through a pattern of axial and stereo geometries: AUVAUVAUVA, where A is axial, and U and V are stereo of opposite signs. The inner and outer edges of each superlayer have additional guard wires that serve to keep the electric field uniform near the superlayer boundaries. There are also special field clearing wires inside of layer 1 and outside of layer 40 to collect charge produced at the chamber support cylinders. This pattern of wires is shown in Figure 3.12. The cell sizes vary from 17.0 mm to 20.0 mm, depending on the layer. The different wire material, specifications, and voltage settings are given in Table 3.2.

The wires are attached to the precision machined aluminum endplates using insulated feed-throughs, except for the field wires, which are grounded by way of copper feed-throughs. The endplates are deflected up to 2 mm by the 31,800 kN force of the wires. The wires are over-tensioned to account for this deflection, and to reduce the sagging due to gravity, which is limited to 200  $\mu\text{m}$  halfway along the chamber.

The readout electronics for the DCH are mounted in a compact way on the rear endplate. Signal wire readout and high voltage distribution service cards connect between the wire feed-throughs and front end assemblies (FEAs). The FEAs contain the amplification and digitization circuits. The amplifier provides a discriminator output and an analog pulse shape, and includes adjustable gain and threshold settings.

The digitizer is capable of 1 ns precision on the timing of the leading edge of the pulse, and uses a 6-bit 15 MHz FADC to construct a waveform of the total charge. These signals are stored in a  $12.9 \mu\text{s}$  buffer and, on the condition of a level 1 trigger accept, are serialized to data I/O modules and transferred to standard *BABAR* readout modules by fiber optic lines. The output of the digitizer also includes raw triggering information, in the form of a single bit for each wire with a signal. These bits are serialized, sent to trigger I/O modules, and transferred by fiber optics to track segment finding boards (located in the electronics building), which are part of the trigger system.

The signals from the DCH are immediately processed to extract the drift time and total charge. These are then used in the time to distance conversion and  $dE/dx$  measurement. The time to distance correspondence is identified using samples of  $e^+e^-$  and  $\mu^+\mu^-$  events by fitting the relationship between the estimated distance of closest approach (using other hits along the track) and the measured drift time. The position resolution, as a function of the distance from the wire, is shown in Figure 3.13. The worsening of the hit resolution near the wire is due to

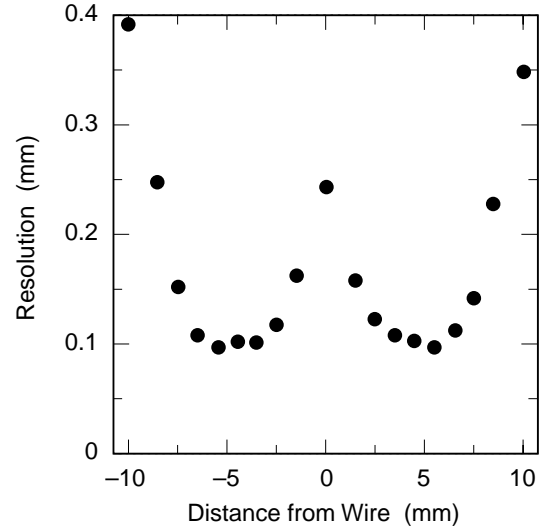


Figure 3.13: DCH hit position resolution, as a function of the distance from the sense wire.

a combination of a geometrical effect and the fact that the hit identification relies on the pulse leading edge. Specifically, because the primary ionization points are randomly distributed along the particle trajectory, there is a greater spread in the time of first signal detection for particles passing near the wire than there is for particles traveling further out in the cell. The best hit resolution is about  $100 \mu\text{m}$ .

The calculation of  $dE/dx$  for a given track is performed by assembling the individual charge measurements from the different cells along the track. A number

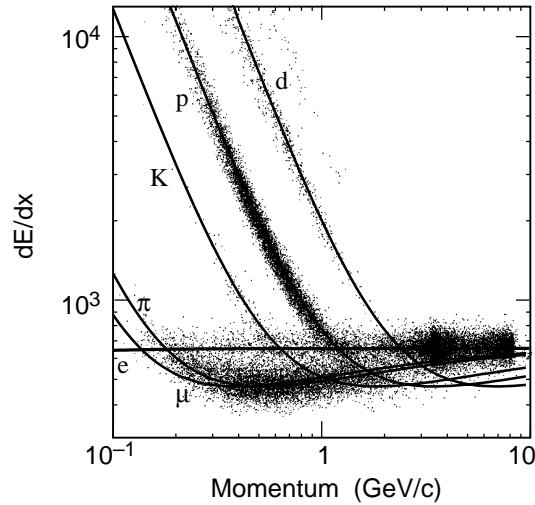


Figure 3.14: The energy loss,  $dE/dx$ , is shown as a function of momentum in the DCH. The curves are Bethe-Bloch functions for different particle types, as determined from control samples.

of corrections enter into this calculation, including those for gas pressure and temperature, variation in cell geometry, and track entrance angle. The resulting  $dE/dx$  distribution, as a function of momentum, is shown in Figure 3.14. The plot includes Bethe-Bloch curves for the loss of energy for different particle types, as determined using control samples. The  $dE/dx$  resolution is approximately 7.5%.

As mentioned previously, the overall charged particle tracking performance relies on both the SVT and the DCH. The reconstruction starts by using short track segments in the DCH to improve the estimate of the event start time. Track candidates are built by performing helical fits on elementary track possibilities provided by the software-based *level 3* trigger, and adding any other consistent hits from the DCH. Additional tracks are formed from patterns of hits that either traverse just part of the DCH or do not originate from the interaction point. Each of these tracks is refined using a Kalman filter that takes into account material and magnetic field distributions. Track segments in the SVT that are consistent with the tracks found in the DCH are added, and the Kalman filter process is repeated. Additional tracking algorithms assemble track candidates using the SVT hits alone.

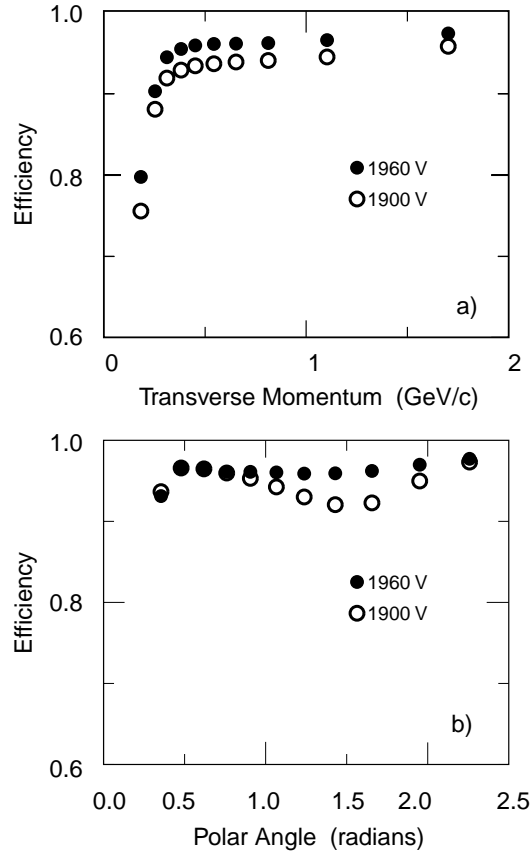


Figure 3.15: The DCH track reconstruction efficiency is shown, for operating points of 1960 V and 1900 V, as functions of (a) transverse momentum and (b) polar angle.

Efficiencies for track reconstruction in the DCH are shown in Figure 3.15, as functions of the transverse momentum and polar angle. The average efficiency above 200 MeV/ $c$  and polar angle greater than 500 mrad is  $98 \pm 1\%$  at 1960 V, and slightly lower for 1900 V. The SVT strongly contributes to the reconstruction of particles with low transverse momenta, such as pions originated from the decay chain  $B \rightarrow D^{*+}X$ ,  $D^{*+} \rightarrow D^0\pi^+$ . The SVT is efficient for these pions starting at momenta as low as 50 MeV/ $c$ .

Five parameters are used to represent each track:  $d_0$ ,  $z_0$ ,  $\phi_0$ ,  $\tan \lambda$ , and  $\omega$ . The parameters are defined at the point of closest approach, where  $d_0$  and  $z_0$  are the distances between this point and the origin in the  $x$ - $y$  plane and along the  $z$ -axis,

respectively. The parameter  $\phi_0$  is the azimuthal angle,  $\tan \lambda$  represent the dip angle with respect to the  $x$ - $y$  plane, and  $\omega$  is the curvature of the track. One way to study the resolution of these parameters is by using cosmic ray events, in which the top and bottom half of tracks that pass close to the interaction point can be reconstructed and fit separately. The width of the difference between the two sets of track parameters yields an estimate of the SVT and DCH resolution for these parameters for tracks with transverse momenta  $p_t > 3 \text{ GeV}/c$ . The values are  $\sigma_{d_0} = 23 \mu\text{m}$ ,  $\sigma_{z_0} = 29 \mu\text{m}$ ,  $\sigma_{\phi_0} = 0.43 \text{ mrad}$ , and  $\sigma_{\tan \lambda} = 0.53 \times 10^{-3}$ . Similar track parameter resolutions, in addition to the dependencies on  $p_t$ , are obtained from studying multi-hadron events by observing the difference between measured track parameters for single tracks and the vertex position of the remaining tracks in the event.

Another indicator for the performance of the tracking is the ability to measure the difference in position, along the  $z$ -axis, between the decay vertices of two neutral  $B$  mesons, where one is fully reconstructed into an exclusive final state and the other is inclusively reconstructed from the remaining tracks in the event. The estimated error on this measurement of  $\Delta z$  is shown in Figure 3.16. The rms width of about  $180 \mu\text{m}$  is dominated by the reconstruction of the inclusive vertex.

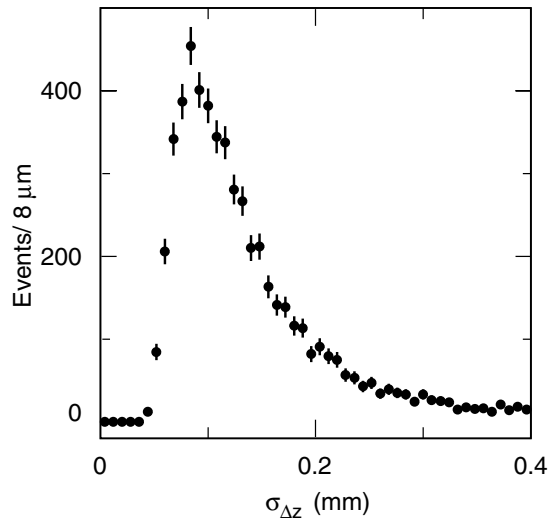


Figure 3.16: The error on the measurement of  $\Delta z$ , the position difference, along the  $z$ -axis, between the vertices of fully and inclusively reconstructed neutral  $B$  mesons.

Finally, the resolution on the measurement of  $p_t$ , as extracted from cosmic ray muons, is fit by a linear function, with  $p_t$  and  $\sigma_{p_t}$  in  $\text{GeV}/c$ :

$$\sigma_{p_t}/p_t = (0.13 \pm 0.01)\% p_t + (0.45 \pm 0.03)\% . \quad (3.1)$$

### 3.2.3 Particle Identification

One of the most novel aspects of *BABAR* is the Detector of Internally Reflected Cherenkov light, or DIRC. Within a given material, a particle traveling faster than the phase velocity of light in that media emits Cherenkov photons. This light is produced in a cone, and the cosine of the half-angle of this cone is inversely proportional to the velocity of the particle. Knowledge of this velocity, taken in combination with momentum measurements from other subsystems, allows for the formation of a particle mass hypothesis, which serves to identify the particle type.

The primary purpose of the DIRC is to distinguish between pions and kaons. For example, in neutral  $B$  decays to  $\pi^+\pi^-$  and  $K^+\pi^-$ , where the pions and kaons have momenta in the range 1.7–4.2 GeV/ $c$ , the DIRC is designed to provide  $4\sigma$  separation between the two particle species.

The most innovative aspect of the DIRC is that it uses fused silica as both the material in which Cherenkov radiation is produced and as a light guide to extract the photons for detection. This substantially reduces the volume of detector material required in the active area in comparison with more traditional ring imaging Cherenkov detectors. This provides cost savings in the form of a smaller calorimeter, and reduces the amount of material the particles encounter prior to the energy measurement. The final design takes up just 8 cm of radial space and represents 17% of a radiation length.

The fundamental detector units of the DIRC are fused silica bars, which are 17 mm high, 35 mm wide, and 4.9 m long (assembled from four pieces, glued end to

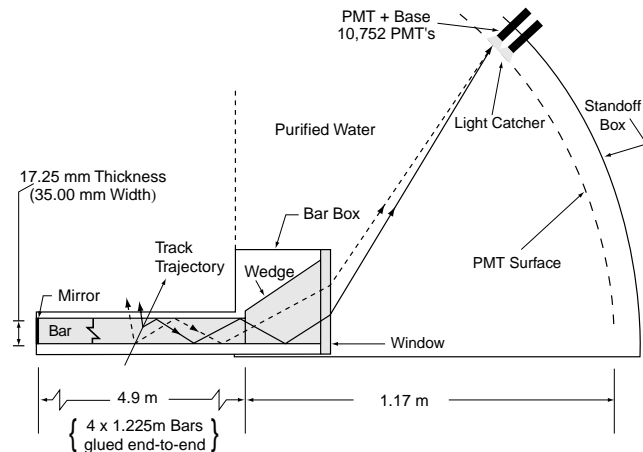


Figure 3.17: Schematic cross-sectional view of a fused silica bar, wedge, and window, along with the water-filled standoff box of the DIRC.

end to end).

end). These bars have a low chromatic dispersion, and are well polished to maximize the occurrence of total internal reflection. The bars are grouped, side by side, into collections of 12 bars each, and 12 of these collections form the sides of a 12-sided polygon, approximating a cylinder. At the backward end of these collections of bars, meaning in the direction of the lower energy beam, the bars are connected to fused silica wedges, which are in turn connected to fused silica windows. These windows provide an interface between the fused silica, which has an index of refraction of 1.473, and a 6,000 liter standoff box filled with purified water, which has an index of refraction of 1.346. This matching of the indices of refraction reduces reflections back into the bars. The water standoff box is instrumented with 10,752 photomultiplier tubes (PMTs). It is located at the backward end of the detector to make room for the endcap component of the calorimeter at the forward end. A cross-sectional view of these elements of the DIRC are shown schematically in Figure 3.17. Note that the forward end of the bars are covered with a mirror surface to reflect photons back toward the instrumented end. The detector has an 83% acceptance in the polar angle in the center-of-mass frame.

The number of photoelectrons detected for a particle entering a DIRC bar normal to the bar, and with  $\beta = 1$ , is approximately 28. This number increases by greater than a factor of two for particles traveling in the forward or backward direction. The efficiency for detection is dominated by the quantum efficiency of the PMTs. Another important factor is the coefficient of internal reflection within the fused silica bars, which is approximately 99.92%, which is significant because the number of reflections for photons produced from a normally incident  $\beta = 1$  particle can be about 365.

The PMTs are operated at about 1140 V. Their signals are amplified and shaped in customized integrated circuit boards mounted on the standoff box. A discriminator signal is also generated based on the peak time of the analog pulse. Digitization of the photon arrival time information is accomplished using integrated circuit TDC channels, which have a settable readout time window. A reasonable window for data collection is 600 ns, and further selection on the timing is useful for reducing the beam related background. The readout also buffers to match the 12  $\mu$ s allowed for the level 1 trigger decision.

The timing of the light propagation and electronics is calibrated both by using light pulses distributed to the standoff box by fiber optics and by using colliding beam data. The difference between expected and observed arrival times provides offsets. These calibrations, stable to 0.1 ns, are done once per day.

The extraction of the Cherenkov angle involves determining the vectors between PMTs with hits and the fused silica bar through which a track has passed. Identifying a candidate bar for a given track relies on information from the inner tracking detectors. The photon path is reconstructed back into the bar and the Cherenkov angle determined up to ambiguities due to symmetries of the bar and whether or not the photon reflected in the fused silica wedge. The timing information helps to reduce the number of ambiguities. Requirements on the timing also remove beam induced background PMT hits, and aid in the mapping between PMT hits and tracks in multi-track events.

Figure 3.18 shows the resolution in Cherenkov angle reconstruction and photon arrival time. The single photon Cherenkov angle ( $\theta_{C,\gamma}$ ) resolution is about  $\sigma_{C,\gamma} = 10$  mrad. The difference between measured and expected photon arrival time,  $\Delta t_\gamma$ , is calculated from the track time-of-flight, the photon propagation time, and the measured PMT time. The resolution on the time measurement is about 1.7 ns.

The resolution on the Cherenkov angle determination per track,  $\sigma_{C,\text{track}}$ , obeys the relation  $\sigma_{C,\text{track}} = \sigma_{C,\gamma} / \sqrt{N_{\text{pe}}}$ , where  $N_{\text{pe}}$  is the number of photoelectrons. The value of  $N_{\text{pe}}$  depends on the polar entrance angle of the track, and ranges between 20 and

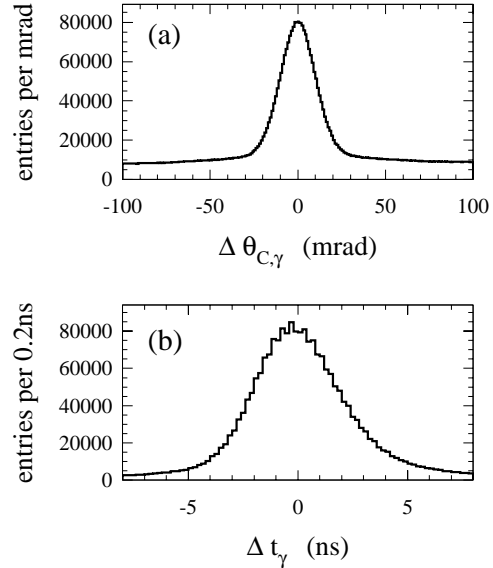


Figure 3.18: The differences between the measured and expected (a) single photon Cherenkov angle and (b) photon arrival time, shown for a sample of muons in  $e^+e^- \rightarrow \mu^+\mu^-$  events.

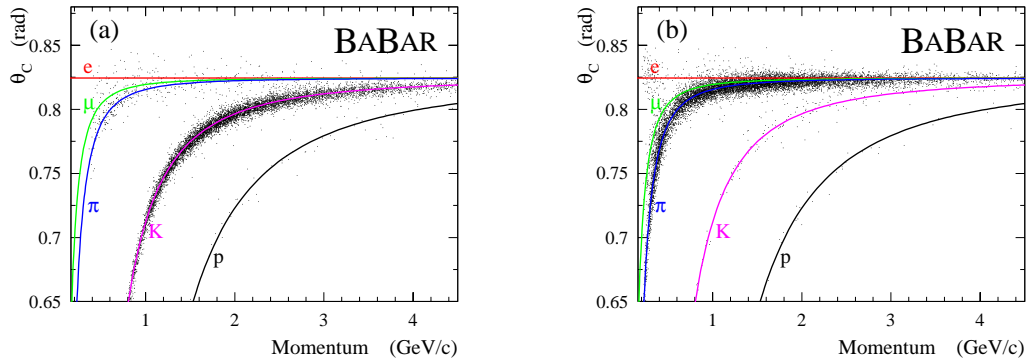


Figure 3.19: The DIRC Cherenkov angle as a function of momentum for (a) kaons and (b) pions from a control sample of  $D^{*-} \rightarrow D^0\pi^-$ ,  $D^0 \rightarrow K^-\pi^+$  decays. The superimposed lines represent different particle mass hypotheses.

65. This yields a track Cherenkov angle resolution of about 2.5 mrad.

The likelihoods for different mass hypothesis are calculated. If there are enough photons consistent with one of  $e$ ,  $\mu$ ,  $\pi$ ,  $K$ , or  $p$ , the corresponding value of  $\theta_C$  is made available. Because of restrictions on the photons used in the fit, the value of  $\theta_C$  is always within 40 mrad of the expected Cherenkov angle for one of the particle types. Figure 3.19 shows  $\theta_C$  versus momentum for kaons and pions from a control sample of  $D^{*-} \rightarrow D^0\pi^-$ ,  $D^0 \rightarrow K^-\pi^+$ , where the light mesons have been kinematically identified independent of DIRC information.

Using this same sample of  $D^{*-}$  decays, the efficiency for kaon identification, the mis-identification rate of kaons as pions, and the standard deviation separation of kaons and pions are shown as functions of momentum in Figure 3.20.

### 3.2.4 Electromagnetic Calorimeter

A photon or electron entering the EMC causes the development of an electromagnetic shower. A photon loses energy primarily through  $e^+e^-$  pair production, while an electron loses energy primarily through bremsstrahlung. These processes continue to produce more electrons and photons, thus perpetuating the shower, until the particle energies drop below critical thresholds where ionization and excitation begin to

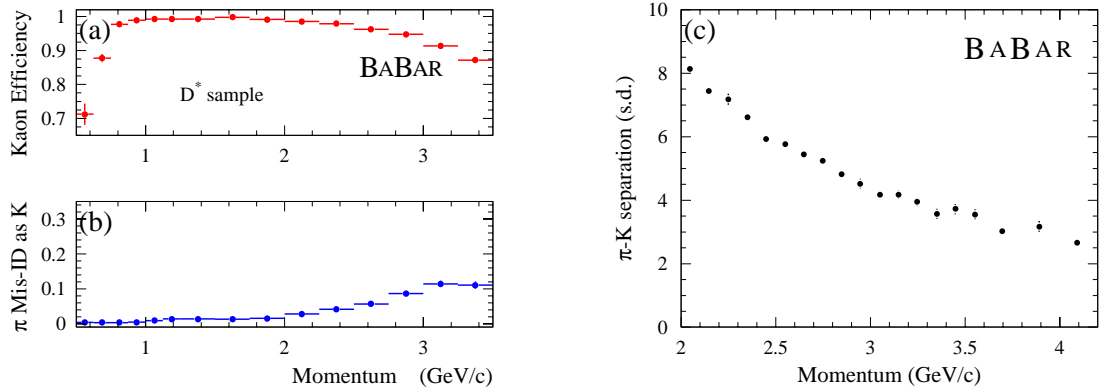


Figure 3.20: Plots of (a) kaon efficiency, (b) pion mis-identification as a kaon, and (c) separation between kaons and pions in terms of standard deviations, all as functions of momentum. These pions and kaons are kinematically identified in a sample of  $D^{*-} \rightarrow D^0\pi^-$ ,  $D^0 \rightarrow K^-\pi^+$  decays. In all three plots, the effects of combinatorial background have been taken into account.

dominate. Light from each shower is observed, yielding a measurement of the energy of the original particle.

For *BABAR*, the detection of photons is critical, for  $\pi^0$  and  $\eta$  reconstruction, as well as for studying radiative decays. Electron detection is important, for example, in  $J/\psi \rightarrow e^+e^-$  decays, semi-leptonic  $B$  decays, and in inferring the flavor of one of the  $B$  mesons in  $\Upsilon(4S) \rightarrow B^0\bar{B}^0$  decays by observing the charge of a high momentum electron. To meet these goals, the EMC needs to be efficient over the energy range 20 MeV to 9 GeV.

The EMC utilizes 6,580 thallium-doped cesium iodide (CsI(Tl)) crystals, arranged in a cylindrical barrel portion with 5,760 crystals (pictured in Figure 3.21) and an endcap with 820 crystals. The geometry of the detector is shown in Figure 3.22. Each crystal



Figure 3.21: Photograph of the barrel portion of the EMC.

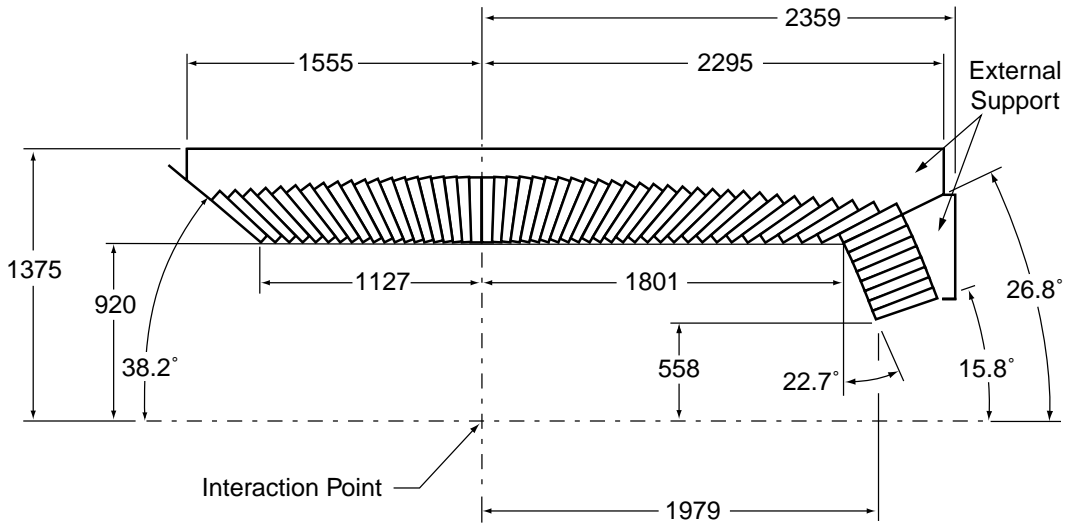


Figure 3.22: Schematic longitudinal cross-section of the EMC. Only the top half is shown. The dimensions are in millimeters.

has a trapezoidal cross-section, and is oriented such that the long axis of the crystal points at the beam interaction point. Each is wrapped with TYVEK, aluminum foil, and mylar, and is mounted in one of 300 carbon-fiber-epoxy composite modules. The modules are attached to a strong aluminum support structure. The detector has a solid-angle coverage of 90% in the center-of-mass frame.

The properties of CsI(Tl) are listed in Table 3.3. The values of the radiation length and Molière radius drive the choice of length and transverse dimensions of the crystals, respectively. The crystals range from 29.6 cm to 32.4 cm in length. The transverse dimensions vary for crystals at different  $z$  positions, but typical front-face dimensions are 4.7 cm  $\times$  4.7 cm and typical rear-face dimensions are 6.1 cm  $\times$

Table 3.3: Properties of CsI(Tl).

Parameter	Value
Radiation Length	1.85 cm
Molière Radius	3.8 cm
Density	4.53 g/cm <sup>3</sup>
Light Yield	50,000 $\gamma$ /MeV
Light Yield Temp. Coeff.	0.28%/°C
Peak Emission $\lambda_{\max}$	565 nm
Refractive Index ( $\lambda_{\max}$ )	1.80
Signal Decay Time	680 ns (64%) 3.34 $\mu$ s (36%)

6.0 cm. The high light yield and the value of the peak emission wavelength are compatible with the use of photodiodes, which instrument the rear end of each crystal.

There are two  $2\text{ cm} \times 1\text{ cm}$  photodiodes mounted on each crystal. They have a quantum efficiency of 85% for the emitted light, and dark currents of about 4 nA. Custom pre-amplifiers, which are mounted just beyond each photodiode, shape the signals and filter out high- and low-frequency noise. The signals are transmitted to mini-crates mounted on the end of the detector. Here they undergo further amplification, dependent upon four binned energy ranges, with the most amplification for the lowest energy range. The signals are digitized by 10-bit, 3.7 MHz ADCs, serialized, and sent by fiber optics to standard *BABAR* read out modules (ROMs). The ROMs execute pedestal and gain corrections, and provide information to the trigger system. In the event of a level 1 trigger accept, EMC signals within a  $2\ \mu\text{s}$  window are analyzed for the extraction of time and energy information. To keep data volume down, a threshold of 1 MeV is required, which means that on average 1,000 crystals are read out, where 150 might belong to a hadronic event, while about 100 are due to electronics noise, and the remainder originate from beam-induced backgrounds.

There are two primary components to calibrating the EMC. The first is to understand the correspondence between the readout signal and the actual energy deposited for each individual crystal. This is accomplished by using a 6.13 MeV radioactive photon source for low energies, and by analyzing  $e^+e^- \rightarrow e^+e^-$  events for higher energies between 3 GeV and 9 GeV. The second component of the calibration is to map from the amount of energy seen in a cluster of crystals to the energy of the original interacting photon or electron. This calibration corrects for energy leakage at the front and back of the crystals, or energy absorption in the material between or in front of the crystals. This correction, which is a function of the energy and polar angle, is derived from  $\pi^0$  decays for energies less than 800 MeV and from photon simulations for the remaining energies up to 9 GeV. Finally, the performance of the EMC is monitored by the daily use of a variable-intensity light-pulsar system.

The EMC reconstruction algorithm identifies clusters of crystals with either a single energy maximum or multiple local energy maxima. The latter case is referred to as a merged cluster, and represents the situation where two particles have entered

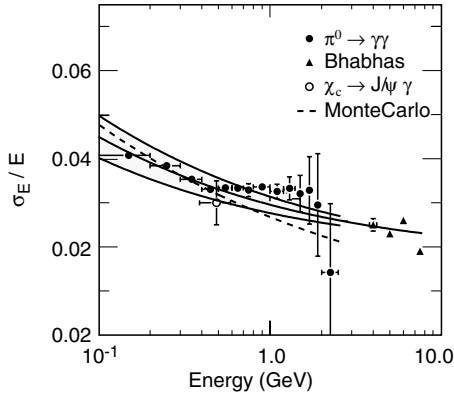


Figure 3.23: Energy resolution of the EMC, as a function of energy, for a variety of processes. The central solid line is a fit to the data, and the surrounding solid lines represent the rms error of the fit.

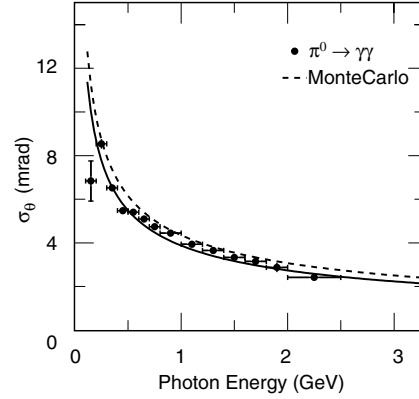


Figure 3.24: Angular resolution of the EMC, as a function of energy, derived from  $\pi^0 \rightarrow \gamma\gamma$  decays. The solid line is an empirical fit to the data.

the EMC with relatively little spacial separation. The candidate crystals of a cluster must pass certain energy and proximity requirements to be included. Each energy maximum is taken as resulting from a charged particle if it is consistent with an extrapolated track from the inner tracking detectors, otherwise it is assumed to have arisen from a neutral particle.

The energy resolution of the EMC is measured over a range of energies using a variety of decay processes. For example, photons are used from  $\pi^0 \rightarrow \gamma\gamma$  and  $\chi_{c1} \rightarrow J/\psi\gamma$  decays, and electrons are used from  $e^+e^- \rightarrow e^+e^-$  (Bhabha) events. Figure 3.23 shows the resolution over a range of energies. Fitting these data points yields the energy dependent resolution

$$\frac{\sigma_E}{E} = \frac{(2.32 \pm 0.30)\%}{\sqrt[4]{E(\text{GeV})}} \oplus (1.85 \pm 0.12)\% , \quad (3.2)$$

where the energy,  $E$ , and its rms error,  $\sigma_E$ , are in GeV. The first term of this empirical expression includes contributions from noise, either in the electronics or related to the beam-induced backgrounds, and a contribution from energy dependent leakage in the material around the crystals. The second term arises from absorption and leakage in

the material around the crystals, and from non-uniform light collection. The impact of photon statistics is negligible.

The angular resolution of the EMC is extracted using  $\pi^0 \rightarrow \gamma\gamma$  and  $\eta \rightarrow \gamma\gamma$  decays, in cases where the photons have similar energies. The energy dependent angular resolution is shown in Figure 3.24, and an empirical fit yields

$$\sigma_\theta = \sigma_\phi = \left( \frac{3.87 \pm 0.07}{\sqrt{E(\text{GeV})}} \pm 0.04 \right) \text{ mrad.} \quad (3.3)$$

The ability of the EMC to detect photons from  $\pi^0$  decays is critical for the analysis of  $B^0 \rightarrow J/\psi \pi^0$ . In addition, the EMC contributes to the identification of electrons through the use of lateral shower moments, and the cluster energy, which is used in the ratio of shower energy to track momentum,  $E/p$ . The EMC information is combined with  $dE/dx$  information from the tracking detectors and the Cherenkov angle from the DIRC, to give sets of electron identification criteria. The efficiency for a relatively restrictive, or tight, selection criteria is shown in Figure 3.25, as is the corresponding efficiency for mis-

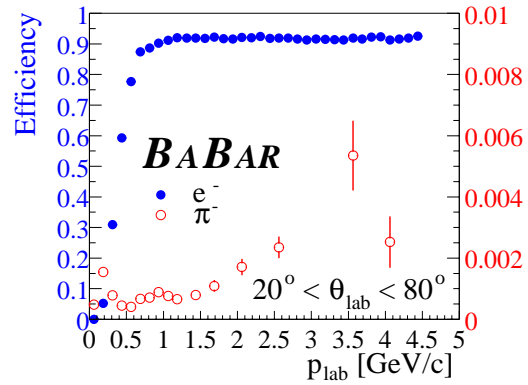


Figure 3.25: Efficiency as a function of momentum for electron identification (closed points, left scale) and pion mis-identification (open points, right scale), using a relatively tight selection criteria.

### 3.2.5 Instrumented Flux Return

The instrumented flux return (IFR) contains interspersed layers of steel and resistive plate chambers (RPCs). A charged particle passing through the active volume of an RPC ionizes the chamber gas, and the resulting streamer, in the presence of an electric field, is detected by orthogonal readout strips on the outer surfaces of the

detector planes.

The principal task of the IFR is to detect muons and neutral hadrons, specifically  $K_L^0$  mesons and neutrons. Muons are used, among other things, to reconstruct  $J/\psi \rightarrow \mu^+\mu^-$  and semi-leptonic  $B$  decays, as well as to infer the flavor of one of the  $B$  mesons in  $\Upsilon(4S) \rightarrow B^0\bar{B}^0$  decays by observing the charge of the primary muon, as with electrons. The detection of  $K_L^0$  mesons is important for the reconstruction of modes such as  $B^0 \rightarrow J/\psi K_L^0$ .

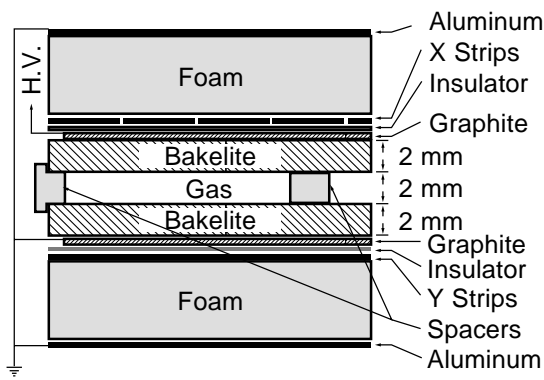


Figure 3.26: Schematic cross-section view of a portion of an RPC. The materials and the high voltage and grounding connection are indicated.

The inner surfaces of the bakelite are treated with a coating of linseed oil to provide a smooth surface, as compared to that of the bakelite, establishing a more uniform field. The graphite is covered with mylar sheets for electrical insulation, and aluminum strips for capacitive readout. The strips on opposite sides of the chambers are oriented in orthogonal directions, and are designated as  $x$ -strips and  $y$ -strips. Finally, this assembly is surrounded by foam and aluminum grounding planes to achieve the desired thickness and electrical properties.

The layout of the IFR, as shown in Figure 3.27, consists of a hexagonal barrel portion, and two endcaps. The RPCs are located in gaps between the steel of the flux return, where the steel plates vary from 2 cm thick for the inner layers to 10 cm

The materials and geometry of an RPC are shown in Figure 3.26. An RPC is a sandwich of two 2 mm thick bakelite planes, with a 2 mm gap between the bakelite sheets for a gas volume. The gap is held constant using polycarbonate spacers, located about every 10 cm. The outer surfaces of the bakelite are painted with thin layers of graphite. One graphite coating is connected to high voltage of nearly 8000 V and the other is connected to ground, thus providing the electric field within the RPC. The in-

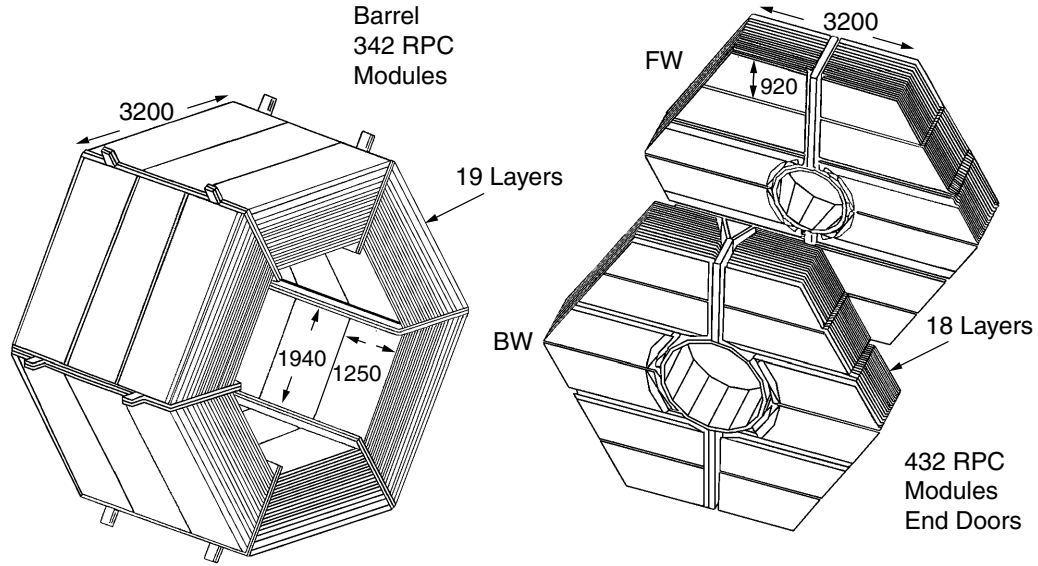


Figure 3.27: Diagram of the IFR barrel and the forward (FW) and backward (BW) endcaps. The individual modules are shown. Dimensions are in mm.

thick for the outer layers. The barrel has 19 layers, where each layer of each sextant is made up of three individual RPC modules. For these groups of three modules, the strips running parallel to the beams are connected from end to end to form single long strips that are the length of the barrel and measure hit positions in  $\phi$ . There are 96 such strips per layer per sextant. There are also 36 strips running perpendicular to the beams for each of these three modules. The endcaps each have 18 layers, and each is split into two doors, which can slide open to provide access to the ends of the detector. There are six modules in each layer of each of these doors. Strips running vertically measure the  $x$  coordinate and are connected across pairs of modules, while strips running horizontally measure the  $y$  coordinate. In between the EMC and the magnet coil, there are two additional layers of RPCs, but instead of a planar geometry, they form concentric cylinders. The strips of these RPCs are oriented to measure along  $z$ ,  $\phi$ , and two helical coordinates. All together, the chambers cover an area of about  $2,000 \text{ m}^2$ . There are about 21,900 channels in the barrel, 28,800 channels in the endcaps, and 2,048 channels in the cylinders. The strip widths range

from 1.60 cm to 3.85 cm.

The chambers operate in a limited streamer mode, using a gas mixture of approximately 56.7% Argon, 38.8% Freon 134a, and 4.5% isobutane. The flow is such that the gas in the chambers is exchanged about twice per day.

The signals are read out by 3,300 Front End Cards (FECs), each serving up to 16 strips. A given FEC reads out only even- or odd-numbered strips, so that an electronics failure does not necessarily cause the loss of a signal, given that a particle typically induces current in two or more strips in each coordinate of an efficient layer. The FECs shape and discriminate the signals, passing a bit-pattern of the hits and a logical OR to buffering and TDC boards, respectively, located in crates near the detector. These crates also contain calibration boards, which can send pulses to the FECs, and controller boards, which coordinate the activities of the other boards and pass the data to standard *BABAR* read out modules in the event of a level 1 trigger accept. Occupancy is low, with about 100–150 hit strips per event.

The efficiency of each RPC is measured using muons from colliding beam data and cosmic rays, and is stored for use during event reconstruction. The efficiency is calculated by grouping hit strips into clusters, built up either using position information of hits within a region of the IFR alone or by adding RPC hits consistent with extrapolated tracks from the DCH. A hit counts toward the efficiency of a chamber if it is within 10 cm of a straight line fit to the clusters in either coordinate.

Immediately after installation of the RPCs, 75% of the operational chambers had an efficiency greater than 90%. However, during the first Summer of operation a problem surfaced, ultimately impacting the performance of the muon system. The experimental hall, which is not temperature regulated, reached temperatures above 31 °C. Many of the FECs are mounted within the steel structure of the flux return and the low voltage circuits of those within the barrel were producing 3.3 kW, thus boosting the temperature in the steel to over 37 °C. Along with elevated dark currents, which increase with temperature, more than half of the chambers showed signs of efficiency loss. Water cooling loops were installed on exposed surfaces of the steel, and this brought the temperature under control, to between 20 °C and 24 °C. However,

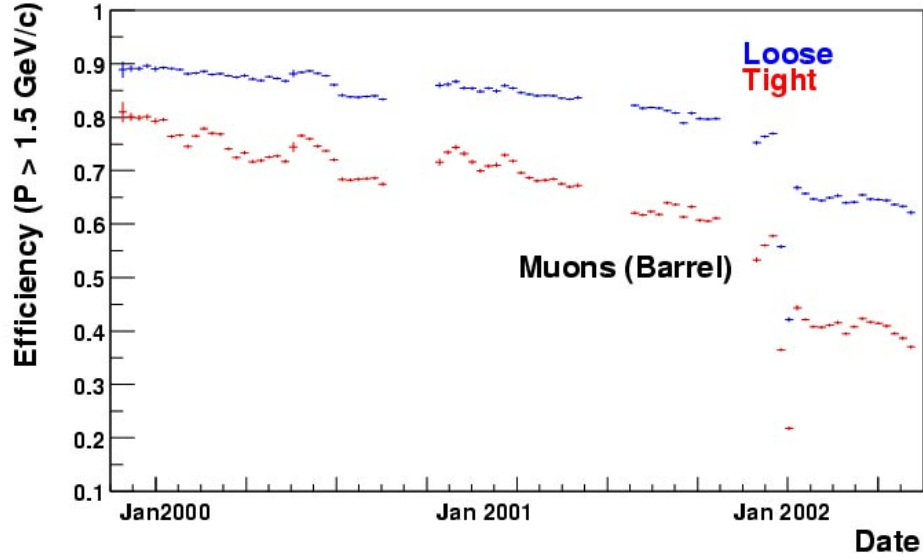


Figure 3.28: The efficiency for relatively loose (top, blue) and relatively tight (bottom, red) muon selection criteria, as functions of time, for muons detected using the IFR barrel. The initial bump in the middle of the year 2000 was due to a gas gain study. The gaps near the beginning of 2001 and 2002 were planned down times, while the gap in the middle of 2001 represents a software bug in reconstruction that has since been repaired and the data recovered. The drop in the final months corresponds to a large number (15%) of electronics modules disabled by backgrounds from a mistimed beam abort kicker. The electronics have been repaired to a level of about 5% dead, as compared to an initial status of about 2% dead. The underlying slope shows the decline in efficiency attributed to the overheating of the RPCs.

while the efficiencies of some of the chambers stabilized, others continued to deteriorate. The problem was reproduced using a temperature regulated test stand of RPCs. The work, as described in Appendix B, found that linseed oil, when heated and under the influence of the electric field, may migrate within the chamber. Any buildup of linseed oil, near spacers, or even bridging the the gap between the two bakelite planes, can disrupt the electrical properties of the chamber and cause a degradation in efficiency.

Figure 3.28 shows the efficiency for two different muon selection schemes as a function of time. A number of features in this plots are described in the caption. The

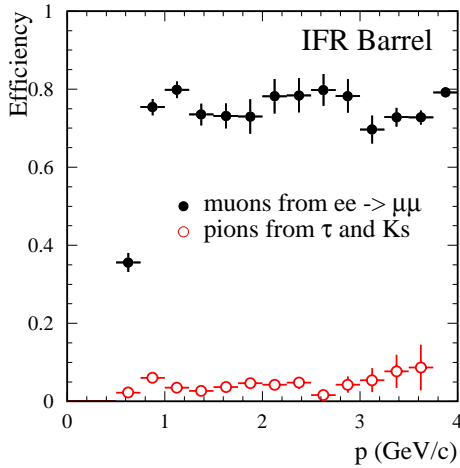


Figure 3.29: Efficiency as a function of momentum for muon identification (closed points) and pion misidentification (open points), using a relatively tight selection criteria.

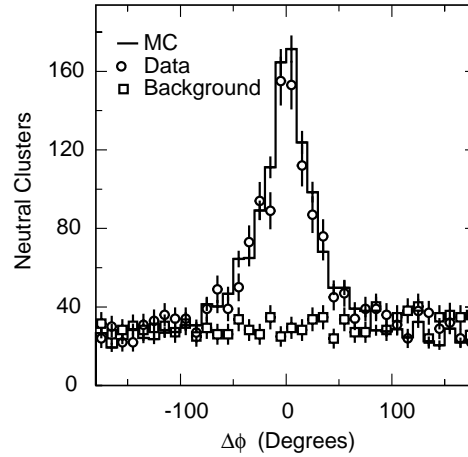


Figure 3.30: The angular difference between the direction of neutral clusters and the direction of missing momentum in events that contain a reconstructed  $J/\psi$ . The Monte Carlo simulation (MC) is normalized to the equivalent luminosity of the data.

underlying slope represents the loss in efficiency due to the overheating of the chambers. The muon efficiency and the efficiency for mis-identifying a muon as a pion, as functions of momentum, are shown in Figure 3.29 for a relatively tight selection criteria for a period during the first year of running. The muon selection requirements for the reconstruction of  $J/\psi \rightarrow \mu^+ \mu^-$  in  $B^0 \rightarrow J/\psi \pi^0$  decays are detailed in Section 5.3, where the impact of the RPC efficiency loss on this particular decay mode is also discussed.

The identification of  $K_L^0$  mesons and other neutral hadrons in the IFR proceeds by selecting any cluster that does not match a charged track in the inner detectors. Composite clusters are formed if there are multiple nearby clusters in the IFR that are unassociated with charged tracks. This information is combined with neutral shower information in the EMC. The direction of the neutral candidate is determined using the event vertex and the centroid of the cluster. Early in the running,  $K_L^0$  efficiency was in the range of 20% to 40% for momenta of 1 GeV/c to 4 GeV/c. The ability to detect neutral hadrons, here assumed to be the long-lived  $K_L^0$  mesons, is

demonstrated in Figure 3.30, which shows the angular difference between the direction of the reconstructed neutral cluster and the direction of the missing momentum in events that include a reconstructed  $J/\psi$ .

# Chapter 4

## Branching Fraction of $B^0 \rightarrow J/\psi \pi^0$ Decays

### 4.1 Introduction

This chapter describes a measurement of the branching fraction of the exclusive decay  $B^0 \rightarrow J/\psi \pi^0$ . This decay is expected to have a branching fraction on the order of  $10^{-5}$ . A prediction can be made under the assumption of no penguin diagram contributions using the expression  $\mathcal{B}(B^0 \rightarrow J/\psi \pi^0)_{\text{expected}} = \lambda_{\text{CKM}}^2 \mathcal{B}(B^0 \rightarrow J/\psi K^0)$ , and the measured world average  $\mathcal{B}(B^0 \rightarrow J/\psi K^0) = (8.7 \pm 0.5) \times 10^{-4}$  and  $\lambda_{\text{CKM}} = 0.2229 \pm 0.0022$  [25]. This yields  $\mathcal{B}(B^0 \rightarrow J/\psi \pi^0)_{\text{expected}} = (4.3 \pm 0.3) \times 10^{-5}$ , excluding the effects of penguin contributions.

Prior to the measurement reported in this chapter, there were only limits placed on the branching fraction:  $\mathcal{B}(B^0 \rightarrow J/\psi \pi^0) < 5.8 \times 10^{-5}$  at 90% confidence level from the CLEO experiment [36] and  $\mathcal{B}(B^0 \rightarrow J/\psi \pi^0) < 3.2 \times 10^{-4}$  at 90% confidence level from the L3 experiment at LEP [37]. Using data recorded in years 1999-2000 by *BABAR*, we have measured  $\mathcal{B}(B^0 \rightarrow J/\psi \pi^0) = (2.0 \pm 0.6 \text{ (stat)} \pm 0.2 \text{ (syst)}) \times 10^{-5}$  [38]. Conclusions based on this result, and comparisons with expectations, are given in Chapter 6.

The following sections give details about the data sample, particle candidate selection, and analysis variables used to distinguish between signal and background. In the

middle of this chapter, there are discussions about the estimation and measurement of the background sources, as well as descriptions of cross-checks. Finally, the results of the branching fraction measurement and the associated systematic uncertainties are reported.

## 4.2 Data Sample and *BABAR* Software Releases

This measurement utilizes  $20.7 \text{ fb}^{-1}$  of *onpeak* data collected in 1999 and 2000. This corresponds to  $(22.74 \pm 0.36) \times 10^6 B\bar{B}$  pairs. An additional  $2.6 \text{ fb}^{-1}$  of *offpeak* data, collected at roughly 40 MeV below the  $\Upsilon(4S)$  peak, are used in background studies. The data are reconstructed with *BABAR* software releases 8.6.x or newer and runs are selected using a *BABAR*-specific script called `skimData`, filtering for only those runs that surpass a set of quality assurance guidelines.

All Monte Carlo simulation used has been generated as part of the *BABAR* simulation production 3 (SP3) cycle, which is based on the Geant3 [39] simulation tools. Monte Carlo simulated events are processed using release 8.8.0  $\alpha$ , (where  $\alpha = c, g, h, \text{ or } i$ ). These events use background conditions that correspond to each month of running.

## 4.3 Candidate Pre-selection

The analysis is performed event-by-event, not on every event recorded by the *BABAR* detector, but rather on those that have been identified as having characteristics that suggest they are worth examining for the presence of the decay  $B^0 \rightarrow J/\psi \pi^0$ . Since the analysis reconstructs  $B^0 \rightarrow J/\psi \pi^0$  using the secondary decays  $J/\psi \rightarrow e^+e^-$  and  $J/\psi \rightarrow \mu^+\mu^-$ , the search for  $B^0 \rightarrow J/\psi \pi^0$  signal events is performed on a group of events that are likely to contain  $J/\psi \rightarrow \ell^+\ell^-$  decays. This is a useful group of events for a variety of other analyses as well. Rounding out the list of secondary decays is  $\pi^0 \rightarrow \gamma\gamma$ , therefore the analysis requires the presence photon candidates, in addition to lepton candidates for the secondary decays mentioned above. These fundamental candidates must appear in combinations that indicate the presence of suitable  $J/\psi$

and  $\pi^0$  candidates. Ultimately, these are combined to form a  $B$  meson candidate. This section, and Section 4.4, describe the selection procedures. The *BABAR*-specific terms, appearing in a different type style below, are included for readers familiar with *BABAR* software to such a level, but they are not critical for understanding the candidate selection process.

A portion of the particle selection takes place in the skimming that is done after initial event reconstruction. The  $J/\psi \rightarrow \ell^+ \ell^-$  stream, the definition of which is discussed in Section 4.3.2, is one of the many so-called streams of events that this procedure produces. Here, the files for data and Monte Carlo have been skimmed with compatible software releases. For special studies, or background decays of the type  $B \rightarrow J/\psi X$  and the signal mode, a more general Monte Carlo stream is used. In these cases, with the exception of the special studies, filtering is applied on a *TAG* bit that is set in the same way as the  $J/\psi \rightarrow \ell^+ \ell^-$  stream (explained further in Section 4.3.2).

### 4.3.1 *B*-Counting

Some of the event selection requirements are in common with those used to identify and count the number of produced  $B$  mesons. The quantities indicated below are calculated during reconstruction, and the results of the corresponding cuts are stored collectively in *TAG* bits. These *TAG* bits are filtered upon during the  $B^0 \rightarrow J/\psi \pi^0$  analysis chain. The quantities and cuts, chosen to identify multi-hadron events, are

- Number of `GoodTracksLoose` in fiducial region  $\geq 3$
- $R_2$  (using charged & neutral objects in fiducial region)  $< 0.5$
- $E_{total}$  in fiducial region  $> 4.5$  GeV

The fiducial region cuts for these objects are the following:

charged:  $0.41 < \theta < 2.54$  rad

neutrals:  $0.41 < \theta < 2.409$  rad

- $xy$  distance of closest approach (*doca*) to primary vertex  $< 0.5$  cm

- $z$  point of closest approach (poca) to primary vertex  $< 6$  cm

The `GoodTracksLoose` list of reconstructed objects contains all of the charged tracks in each event that meet the following criteria:

Transverse momentum,  $p_t \geq 0.1$  GeV/ $c$

Momentum,  $p \leq 10.0$  GeV/ $c$

Number of DCH hits  $\geq 12$

Track fit  $\chi^2$  probability  $\geq 0$

$xy$  poca  $< 1.5$  cm

$-10$  cm  $< z$  poca  $< 10$  cm

The quantity  $R_2$  is the ratio of the second-order to zeroth-order Fox-Wolfram moments [40].

### 4.3.2 Lepton Pre-selection

Figure 4.1 shows the way in which lepton candidates are combined to form a list of loose  $J/\psi$  candidates. In the *BABAR* analysis software framework, the list is called `JPsiLooseChm` and results from a number of so-called sequences in `CompJPsiSequence` of the `CompositionSequences` package. The pre-selection is accomplished by either using the  $J/\psi \rightarrow \ell^+ \ell^-$  stream, which requires the *TAG* bits that correspond to the `JPsiLooseEE` and `JPsiLooseMuMu` lists indicated in the diagram, or by using the `Jpsitoll` *TAG* bit, which is set in the same manner.

For  $J/\psi \rightarrow e^+ e^-$ , all charged tracks are assigned the electron mass and a list of photons (`GoodPhotonLoose`) is then used to perform Bremsstrahlung recovery to compensate for radiated photons. One of the two oppositely charged electron candidates must satisfy either a *loose* electron selection criteria or the so-called *noCal* selector if it does not have an associated EMC cluster (see Section 4.4.1 for definitions of these selectors). The combined mass must be between  $2.3$  GeV/ $c^2$  and  $3.5$  GeV/ $c^2$ , in which case the two candidates are kinematically vertexed. If the vertexer does not converge, a  $J/\psi$  candidate is still formed, just as the four-vector addition of the two electron candidates. A further cut is made on the  $J/\psi$  mass, requiring that it be between  $2.5$  GeV/ $c^2$  and  $3.5$  GeV/ $c^2$ .

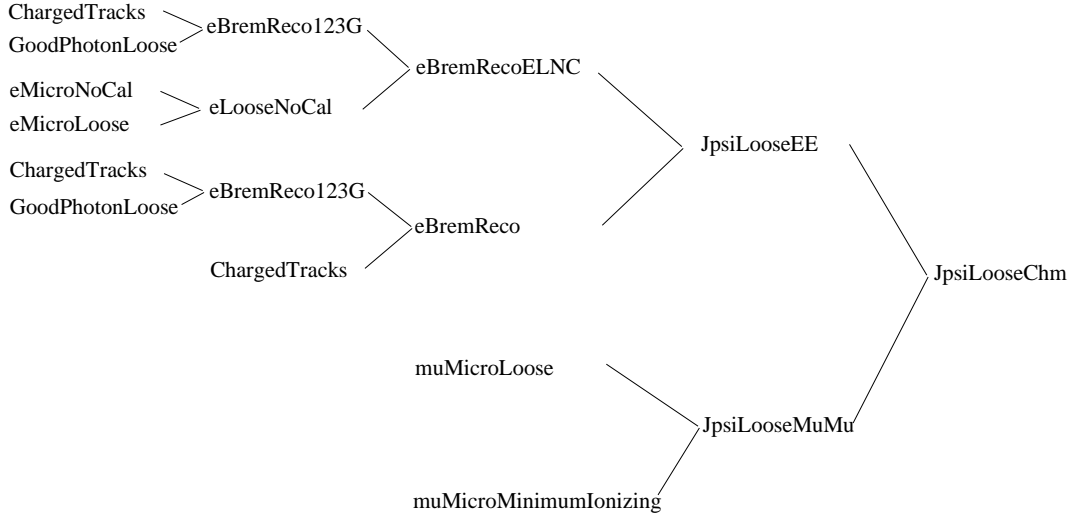


Figure 4.1: The various lists involved in the formation of the  $J/\psi$  candidates. The pre-selection is based upon the existence of the *TAG* bits corresponding to the `JPsiLooseEE` and `JPsiLooseMuMu` lists.

For  $J/\psi \rightarrow \mu^+ \mu^-$ , all tracks are given the muon mass, with one passing a *loose* muon selector and one passing the *minimum ionizing* selector (these selectors are defined in Section 4.4.1). Two oppositely charged candidates are combined and vertexed in the same manner as for the electron case, with the exception that the initial mass window is from  $2.5 \text{ GeV}/c^2$  to  $3.5 \text{ GeV}/c^2$  and the final mass window for this pre-selection is from  $2.8 \text{ GeV}/c^2$  to  $3.3 \text{ GeV}/c^2$ .

### 4.3.3 Photon Pre-selection

The starting point for the photon list used in this measurement is called the `CalorNeutral` list. It consists of single bumps in the EMC that are not matched with any tracks. If they have a minimum raw energy of 30 MeV and a maximum lateral moment (LAT) [41] of 0.8, they are included in the `GoodPhotonLoose` list for later use. The quantity LAT helps to distinguish between electromagnetic and hadronic showers. The former have a distribution of LAT that is peaked around 0.25, while the latter have a broader distribution.

Table 4.1: The criteria for the electron selectors used in the reconstruction of the  $J/\psi \rightarrow e^+e^-$  channel. The quantities used are the ratio of shower energy to track momentum ( $\frac{E}{p}$ ), the number of crystals in the associated calorimeter cluster ( $n_{\text{xtal}}$ ), the energy loss measured in the tracking detectors ( $\frac{dE}{dx}$ ), and the lateral moment (LAT). The *noCal* selector serves the case when there is no calorimeter information available and uses only information from the drift chamber. The fraction of electrons in a sample of inclusive  $J/\psi$  events that pass each selector is shown, as is the fraction of pions with momentum greater than 1.0 GeV/ $c$  that pass each selector.

	<i>tight</i>	<i>loose</i>	<i>noCal</i>
$\frac{dE}{dx}$ (measured-expected)	$-3$ to $+7\sigma_{\text{meas}}$	$-3$ to $+7\sigma_{\text{meas}}$	$-2$ to $+4\sigma_{\text{meas}}$
$\frac{E}{p}$	0.75 to 1.3	0.65 to 5.0	–
$n_{\text{xtal}}$	$> 3$	$> 3$	–
LAT	0.0 to 0.6	–	–
Efficiency (%)	95.4	97.2	94.9
$\pi$ mis-identification (%)	1.2	4.8	21.6

## 4.4 Final Candidate Selection

### 4.4.1 Final $J/\psi$ selection

The final selection of  $J/\psi$  candidates places additional restrictions upon the objects in the `JPsiLooseChm` list described above in Section 4.3.2.

- For  $J/\psi \rightarrow e^+e^-$ , the combined  $J/\psi$  candidate mass must be between 2.95 GeV/ $c^2$  and 3.14 GeV/ $c^2$ . One daughter must satisfy the *tight* electron selector and the other must satisfy the *loose* or *noCal* selector. The definitions of these selectors are shown in Table 4.1.
- For  $J/\psi \rightarrow \mu^+\mu^-$  the combined  $J/\psi$  candidate mass must be between 3.06 GeV/ $c^2$  and 3.14 GeV/ $c^2$ . One daughter must satisfy the *veryTight* muon selector and the other must satisfy the *loose* muon selector. The definitions of these selectors are shown in Table 4.2.

Table 4.2: The criteria for the muon selectors used in the reconstruction of the  $J/\psi \rightarrow \mu^+ \mu^-$  channel. The following quantities are used: the cluster energy in the EMC ( $E_{EMC}$ ) for tracks within the fiducial region of the EMC; the number of IFR layers with hits ( $N_{layers}$ ); the number of nuclear interaction lengths traversed ( $N_\lambda$ ); the difference between  $N_\lambda$  and the expected number of nuclear interaction lengths for a muon of the measured momentum ( $|N_\lambda - N_{\lambda Expected}|$ ); the average number of hits per IFR layer ( $\langle N_{hit} \rangle$ ), the RMS of the distribution of the number of hits in each layer ( $RMS_{hit}$ ); the fraction of layers between the innermost and outermost hit layers that also have hits ( $f_{hit}$ ), for tracks that traverse at least a portion of the IFR forward endcap; the  $\chi^2$  of a polynomial fit to the clusters of hits in RPC layers along a candidate track ( $\chi_{IFR}^2$ ); the  $\chi^2$  of a match between these clusters and an extrapolation of the track from the inner detectors ( $\chi_{match}^2$ ). The fraction of muons in a sample of inclusive  $J/\psi$  events that pass each selector is shown, as is the fraction of pions with momentum greater than 1.0 GeV/c that pass each selector.

	<i>veryTight</i>	<i>tight</i>	<i>loose</i>	<i>veryLoose</i>	<i>min. ionizing</i>
$E_{EMC}$ (GeV)	0.05 to 0.4	0.05 to 0.4	< 0.5	< 0.5	< 0.5
$N_{layers}$	> 1	> 1	> 1	> 1	—
$N_\lambda$	> 2.2	> 2.2	> 2.0	> 2.0	—
$ N_\lambda - N_{\lambda Expected} $	< 0.8	< 1.0	< 2.0	< 2.5	—
$\langle N_{hit} \rangle$	< 8	< 8	< 10	< 10	—
$RMS_{hit}$	< 4	< 4	< 6	< 6	—
$f_{hit}$	> 0.34	> 0.3	> 0.2	> 0.1	—
$\chi_{IFR}^2$	< $3 \times N_{layers}$	< $3 \times N_{layers}$	< $4 \times N_{layers}$	—	—
$\chi_{match}^2$	< $5 \times N_{layers}$	< $5 \times N_{layers}$	< $7 \times N_{layers}$	—	—
Efficiency (%)	67.0	70.3	86.2	92.2	99.6
$\pi$ mis-identification (%)	2.1	2.4	7.0	14.5	57.9

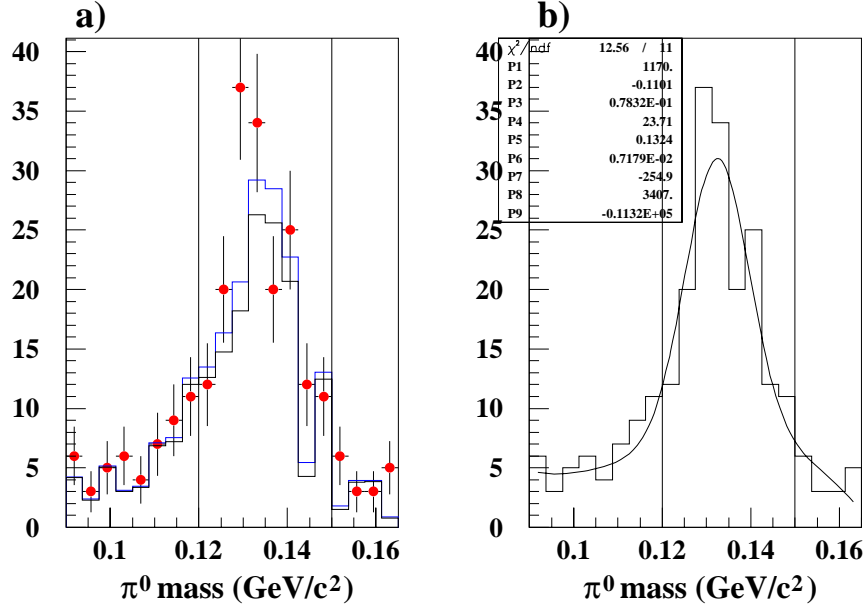


Figure 4.2: (a) The  $\pi^0$  mass, where the red points are *onpeak* data, the blue histogram is the scaled sum of signal and background Monte Carlo samples, and the black histogram is the scaled sum of just background Monte Carlo samples. (b) The  $\pi^0$  mass in *onpeak* data is fit with a double Gaussian and a second order polynomial. The resolution is roughly 7 MeV/ $c^2$ .

#### 4.4.2 Final $\pi^0$ Selection

The `Pi0ToGG_VeryLoose` selector of `CompPi0Sequence` makes combinations of two members of the `GoodPhotonLoose` list and requires the mass of the resulting  $\pi^0$  candidate to be within a large window. The final selection further restricts the mass to be in the range from 0.120 GeV/ $c^2$  to 0.150 GeV/ $c^2$ . This represents a  $3\sigma$  cut, as can be seen in Figure 4.2.

#### 4.4.3 Formation of $B$ Candidates

Once the  $J/\psi$  and  $\pi^0$  candidates are identified, they are boosted to the  $e^+e^-$  center-of-mass (CM) frame. The mass of each is constrained to the PDG [42] value and a

kinematically constrained fit is performed to form a  $B$  meson candidate. If the vertex fit does not converge, simple four-momentum addition is used.

## 4.5 Signal Region and Event Selection Variables

### 4.5.1 $m_{\text{ES}}$ and $\Delta E$

The values of the energy and momentum resulting from the fit are used in a calculation of the two kinematic variables  $m_{\text{ES}}$  and  $\Delta E$ . The variable  $m_{\text{ES}}$ , or beam-energy-substituted mass, is defined as

$$m_{\text{ES}} = \sqrt{(E_{\text{beam}}^*)^2 - (p_B^*)^2} , \quad (4.1)$$

where  $E_{\text{beam}}^*$  and  $p_B^*$  are the beam energy and  $B$ -candidate momentum in the  $e^+e^-$  CM frame. In this mass variable, the beam energy is used in place of the  $B$ -candidate energy because  $E_{\text{beam}}^*$  has the smaller measurement uncertainty of the two options. Note that  $E_{\text{beam}}^* = \sqrt{s}/2$ , where  $\sqrt{s}$  is the total CM energy. The  $\Delta E$  variable is defined as

$$\Delta E = E_B^* - E_{\text{beam}}^* , \quad (4.2)$$

where  $E_B^*$  is the  $B$ -candidate energy in the  $e^+e^-$  CM frame, calculated from  $E_B^* = E_{J/\psi}^* + E_{\pi^0}^*$ . Plots of these variables, over the ranges  $-0.4 < \Delta E < 0.4$  GeV and  $5.2 < m_{\text{ES}} < 5.2$  GeV/ $c^2$ , are shown for a sample of signal  $B^0 \rightarrow J/\psi \pi^0$  Monte Carlo events in Figure 4.3. A signal box is defined that is  $3\sigma$  in each variable:

$$\begin{aligned} -0.112 < \Delta E < 0.112 \text{ GeV} \\ 5.270 < m_{\text{ES}} < 5.288 \text{ GeV}/c^2 . \end{aligned} \quad (4.3)$$

The raw efficiency for events to be in this signal box is  $(30.1 \pm 0.3)\%$ .

During the initial development of the analysis, a  $5\sigma$  box in  $\Delta E$  and  $m_{\text{ES}}$ , surrounding the signal box, was kept hidden from view when looking at *onpeak* data, so as not to bias the choice of cuts. For the rare case (a few %) when there are multiple

$B^0 \rightarrow J/\psi \pi^0$  candidates within one event, only the candidate with the smallest  $|\Delta E|$  is kept.

### 4.5.2 Thrust Angle

The first of two angular variables used to suppress background from  $e^+e^- \rightarrow q\bar{q}$  ( $q = u, d, s, c$ ) continuum events is  $|\cos \theta_T|$ . The quantity  $\theta_T$  is defined as the angle between the thrust axis of the  $B$  and the thrust axis of the rest of the event. A thrust axis points along  $\hat{a}$  when the following is maximized:

$$\left| \frac{\sum_i (\vec{p}_i^* \cdot \hat{a})}{\sum_i (\vec{p}_i^* \cdot \vec{p}_i^*)} \right|, \quad (4.4)$$

where  $p_i^*$  are the CM momentum vectors of the  $i$  candidates being considered. The thrust of the  $B$  candidate is calculated using the  $J/\psi$  candidate and the  $\pi^0$  candidate. The thrust of the rest of the event is obtained using all remaining charged tracks in the fiducial region and all remaining neutral objects in the fiducial region that surpass a 30 MeV threshold. As can be seen in Figure 4.4, the signal events are uniformly distributed in  $|\cos \theta_T|$ , while the continuum background events are strongly peaked at 1. This peaking behavior results from the jet-like nature of the continuum events. The candidates which fake the signal particles lie within these forward and backward cones, as do most of the rest of the particles. Therefore, the angle between the signal candidate thrust axis and the thrust axis of the rest of the event is strongly peaked toward 0 and 180 degrees. A cut is placed on the absolute value of the cosine of the thrust angle:

$$|\cos \theta_T| < 0.95. \quad (4.5)$$

### 4.5.3 Lepton Helicity Angle

The second angular variable used to separate signal and continuum background is  $\cos \theta_\ell$ . The lepton helicity angle,  $\theta_\ell$ , is the angle between the negative lepton direction in the  $J/\psi$  rest frame and the  $B$  direction in the  $J/\psi$  rest frame. The  $B$  is a

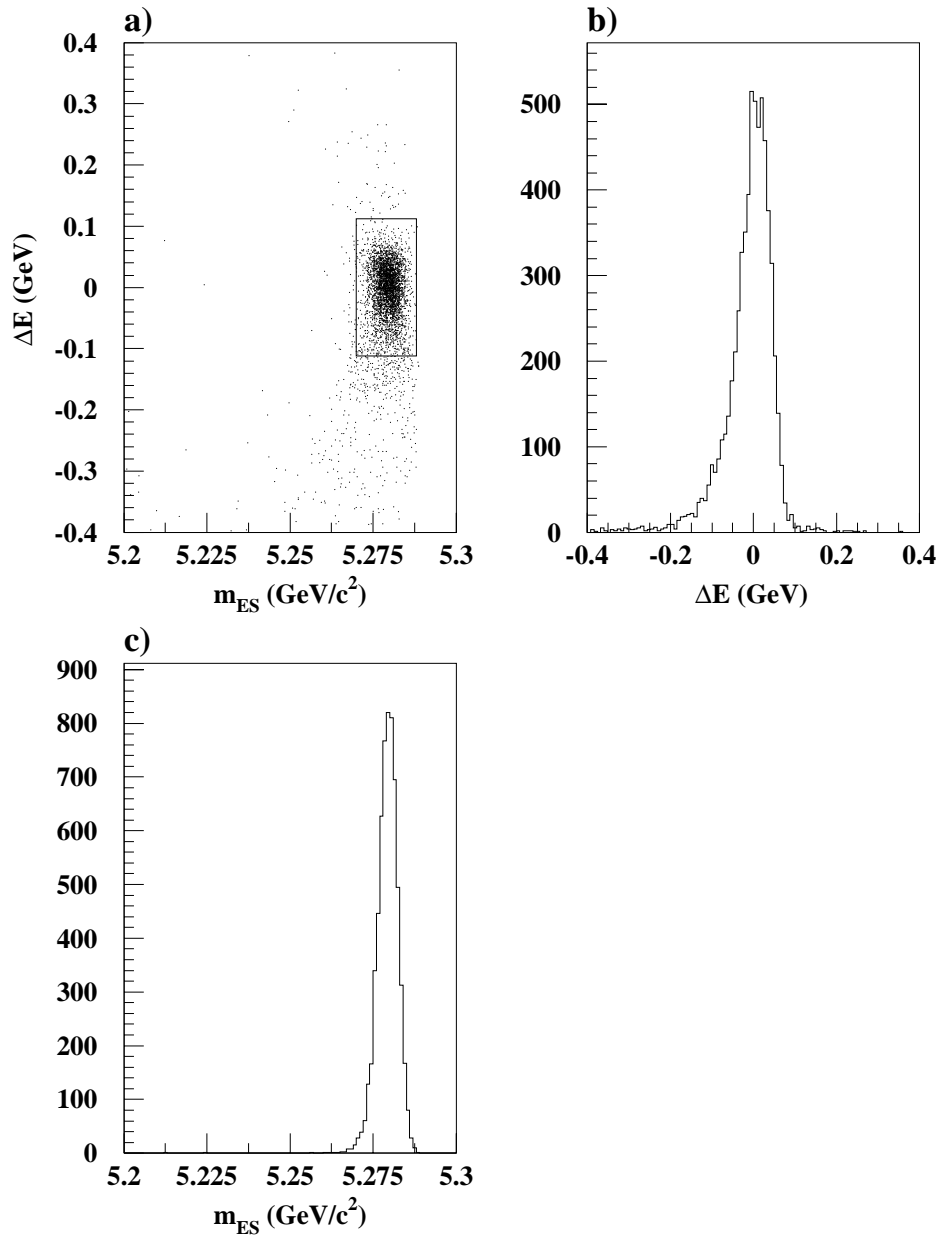


Figure 4.3: Signal  $B^0 \rightarrow J/\psi \pi^0$  Monte Carlo (20,000 events) plots of (a)  $\Delta E$  versus  $m_{ES}$ , (b)  $\Delta E$  projection of  $m_{ES}$  signal band ( $5.270 < m_{ES} < 5.288$  GeV/c<sup>2</sup>), and (c)  $m_{ES}$  projection of  $\Delta E$  signal band ( $-0.112 < \Delta E < 0.112$  GeV).

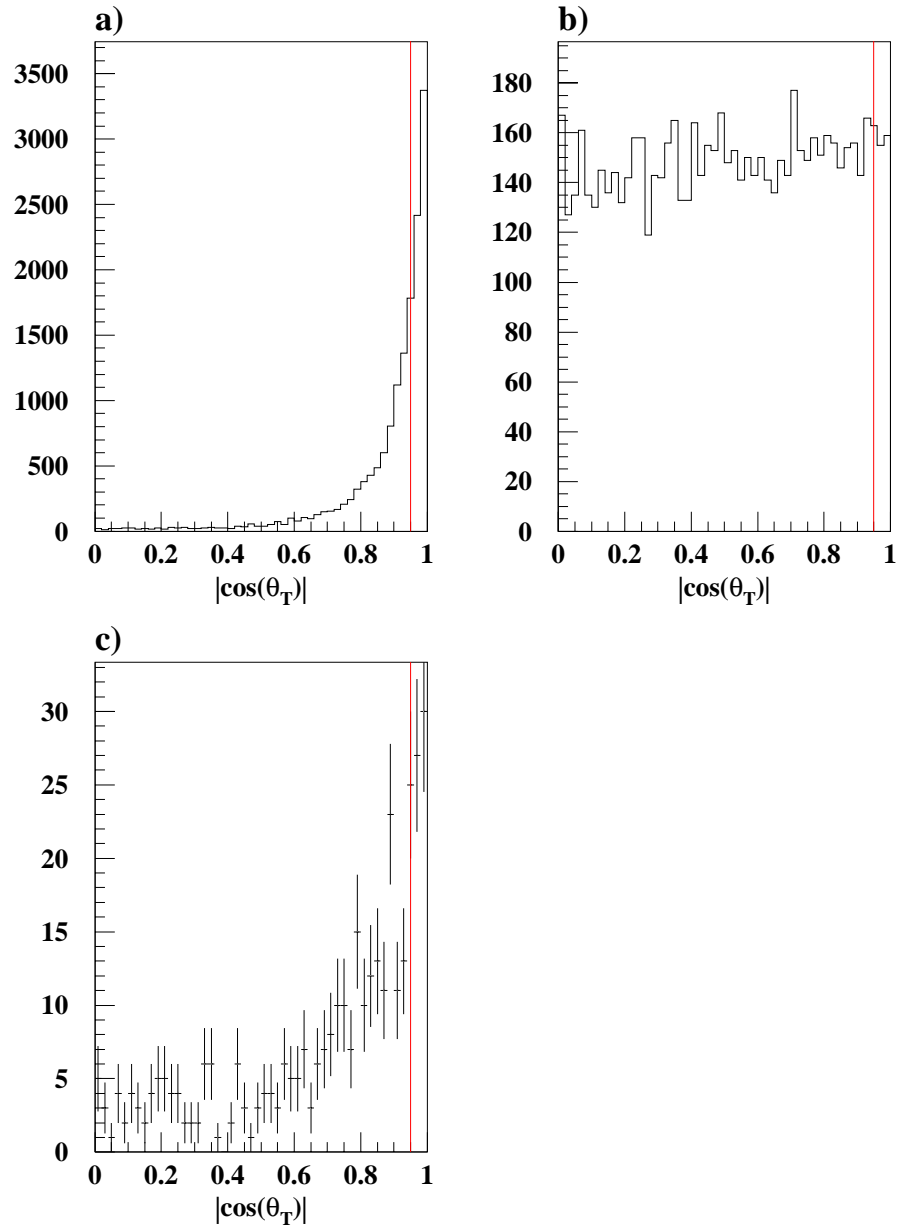


Figure 4.4: Plots of  $|\cos \theta_T|$  in (a) continuum background Monte Carlo events, with loosened cuts, (b) signal mode Monte Carlo events, and (c) *onpeak* data.

pseudoscalar, and its two decay products, the  $J/\psi$  and the  $\pi^0$ , must have equal helicities. The  $\pi^0$  is also a pseudoscalar, so the  $J/\psi$  must have a helicity of 0. The leptons that emerge from the  $J/\psi \rightarrow \ell^+ \ell^-$  decay have opposite spins and momenta, and the angular distribution is  $\sin^2 \theta_\ell$  for signal events. On the other hand, the continuum background events, which fall more along the beam directions, have a distribution of the lepton helicity angle that peaks toward  $\cos \theta_\ell = \pm 1$ . This behavior can be seen in Figure 4.5.

A small correlation has been observed between the thrust angle and the lepton helicity angle. This can be seen in a two-dimensional plot of the two angular variables. Figure 4.6 shows a collection of events in the corners for a sample of continuum background Monte Carlo with a loosened set of cuts. This is compared to the expected distribution for signal events, as observed in the signal Monte Carlo sample. The thrust angle cut is still applied as seen along the right side of the plot, but an additional cut is made across the corners:

$$|\cos \theta_T| + |\cos \theta_\ell| < 1.8 . \quad (4.6)$$

#### 4.5.4 Additional Angular Variables Studied

A handful of additional angles were studied, including the  $B$  direction, the  $J/\psi$  direction, the  $\pi^0$  direction, and the angle between the two photons resulting from the  $\pi^0$  decay. None of these were found to provide significant improvements to the background suppression.

## 4.6 Cut Optimization

Cut optimization is performed by varying the choice of particle identification and angular cuts. For each set of particle selection requirements and angular cuts, the signal ( $S$ ) and background ( $B$ ) levels, as determined from running on Monte Carlo samples, are used to calculate the ratio  $S/\sqrt{S+B}$ . The types of events that contribute to the background, and the evaluation of  $B$ , are discussed in Section 4.7. The set of cuts

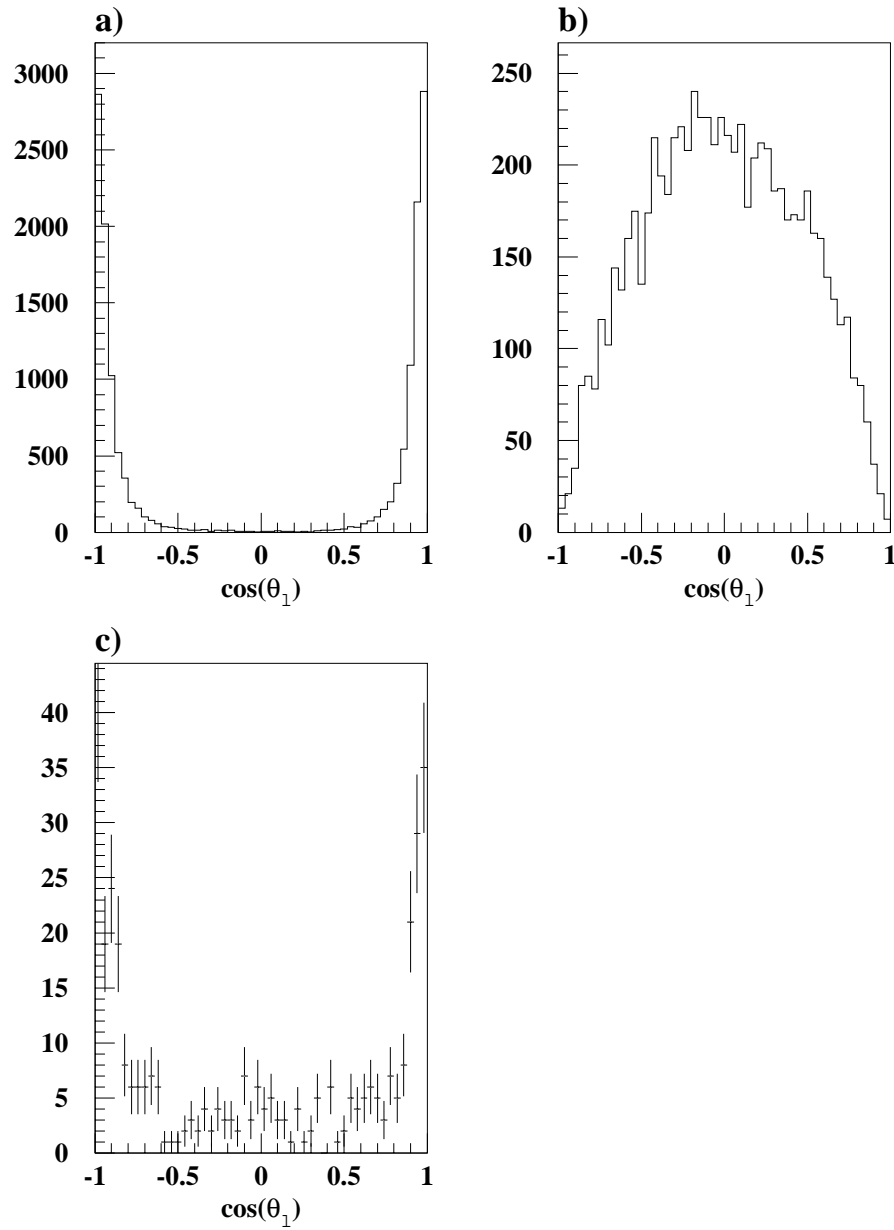


Figure 4.5: The cosine of the lepton helicity angle is shown for (a) continuum background Monte Carlo events, with loosened cuts, (b) signal mode Monte Carlo events, and (c) *onpeak* data.

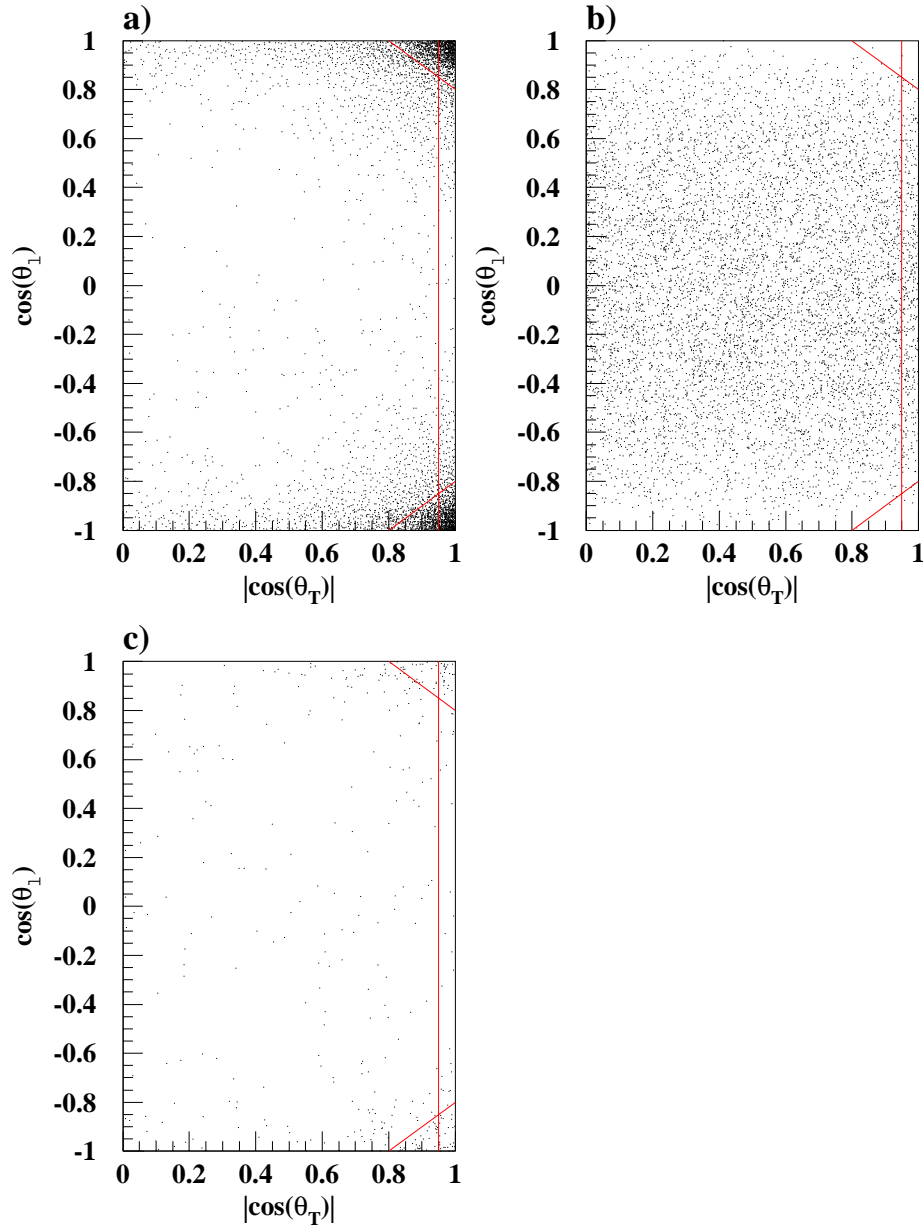


Figure 4.6: Plots of  $\cos\theta_\ell$  versus  $|\cos\theta_T|$ . The correlation can be seen for (a) continuum background events (with loosened cuts), while (b) signal Monte Carlo events are distributed as  $\sin^2\theta_\ell$  in  $\cos\theta_\ell$  and evenly in  $|\cos\theta_T|$ . The distribution is also shown for (c) the *onpeak* data.

that maximizes this ratio is selected. While for some variations the ratio changes by less than its uncertainty, this procedure gives a sensible set of cuts.

## 4.7 Background Studies

### 4.7.1 Overall Background Strategy

The backgrounds affecting the branching fraction analysis of  $B^0 \rightarrow J/\psi \pi^0$  decays can be split into two primary categories:  $e^+e^- \rightarrow q\bar{q}$  ( $q = u, d, s, c$ ) continuum events and feed-through from events that contain a  $J/\psi$  from  $B$  decays ( $B \rightarrow J/\psi X$ ). There are additional minor contributions from random combinations in  $B\bar{B}$  decays ( $B\bar{B}$  generic).

The backgrounds to  $B^0 \rightarrow J/\psi \pi^0$  decays have distributions in  $m_{\text{ES}}$  that can be associated with the different background types and are predictable. Therefore, the  $m_{\text{ES}}$  distributions in a region encompassing the signal box are used to extract the background contributions within the signal box. For the largest contribution, the continuum background, this takes advantage of the fact that the  $m_{\text{ES}}$  distribution follows a phase-space threshold function, first used by the Argus experiment [43] and often called the Argus function:

$$\text{Argus}(m_{\text{ES}}) = \begin{cases} N m_{\text{ES}} \sqrt{\left(1 - \frac{m_{\text{ES}}^2}{E_{\text{beam}}^2}\right)} e^{\xi\left(1 - \frac{m_{\text{ES}}^2}{E_{\text{beam}}^2}\right)} & \text{if } m_{\text{ES}} < E_{\text{beam}} \\ 0 & \text{otherwise.} \end{cases} \quad (4.7)$$

It contains a normalization,  $N$ , a fixed kinematic cut-off at  $E_{\text{beam}} = 5.289$  GeV, and an empirically determined exponential component, with a parameter  $\xi$ .

As is preferable, data is used wherever possible for evaluating the size of the background contributions for the final result. Ultimately, the amount of continuum background is extracted using the *onpeak* data. However, with a limited number of events passing the final selections, some information is extracted using Monte Carlo samples. A detailed study is performed using continuum and  $B\bar{B}$  generic Monte Carlo samples, as well as *offpeak* data. A number of comparisons between these samples are

made as cross-checks. Section 4.7.2 describes the development and use of a special high statistics Monte Carlo sample to aid in the background studies. This sample, among other things, allows for proper scaling and fitting of limited continuum Monte Carlo.

The background from  $B \rightarrow J/\psi X$  feed-through consists of cases where different charmonium modes are falsely reconstructed as  $B^0 \rightarrow J/\psi \pi^0$ . The contribution from this source is estimated from Monte Carlo samples and confidence is gained by comparing the data and Monte Carlo in the  $\Delta E$  sideband. The details of the fitting strategy for  $B \rightarrow J/\psi X$  feed-through are given in Sections 4.7.6 and 4.7.7.

### 4.7.2 The $J/\psi_{\text{fake}}$ Sample

As an aid to characterizing the background, it is useful to develop a high statistics sample ( $J/\psi_{\text{fake}}$ ) of events that resembles the continuum background. In the continuum background events, two candidates that are mistakenly identified as leptons are combined to form an incorrect  $J/\psi$  candidate. To model this case, and create the  $J/\psi_{\text{fake}}$  sample, the  $J/\psi$  candidate is reconstructed from two tracks that are not consistent with a lepton hypothesis. In other words, the particle identification requirements on the two tracks have been reversed to form what amounts to a *not-a-lepton* selector. In this study, the `jpsitoll TAG` bit is not used, as it includes particle identification requirements. The  $J/\psi \rightarrow \ell^+ \ell^-$  stream is also avoided for the same reason. This special selection is run on Monte Carlo simulated continuum events, which are generated and examined independently for the cases when the produced quark pair is  $u\bar{u}$ ,  $d\bar{d}$ , or  $s\bar{s}$  (referred to as  $u\bar{u}/d\bar{d}/s\bar{s}$ ), or when the quark pair is  $c\bar{c}$ . The  $\Delta E$  versus  $m_{\text{ES}}$  distribution for the  $J/\psi_{\text{fake}} u\bar{u}/d\bar{d}/s\bar{s}$  Monte Carlo sample, is shown in Figure 4.7, as are the projections in  $m_{\text{ES}}$  and  $\Delta E$ . The  $m_{\text{ES}}$  distribution is fit with the Argus function in equation 4.7. The exponential factor resulting from this fit can then be fixed when fitting the Argus shape to continuum Monte Carlo, generic  $B\bar{B}$  Monte Carlo, and *offpeak* data events, but in samples with the standard particle identification. This allows for successful modeling with the Argus function, even when very few events are available.

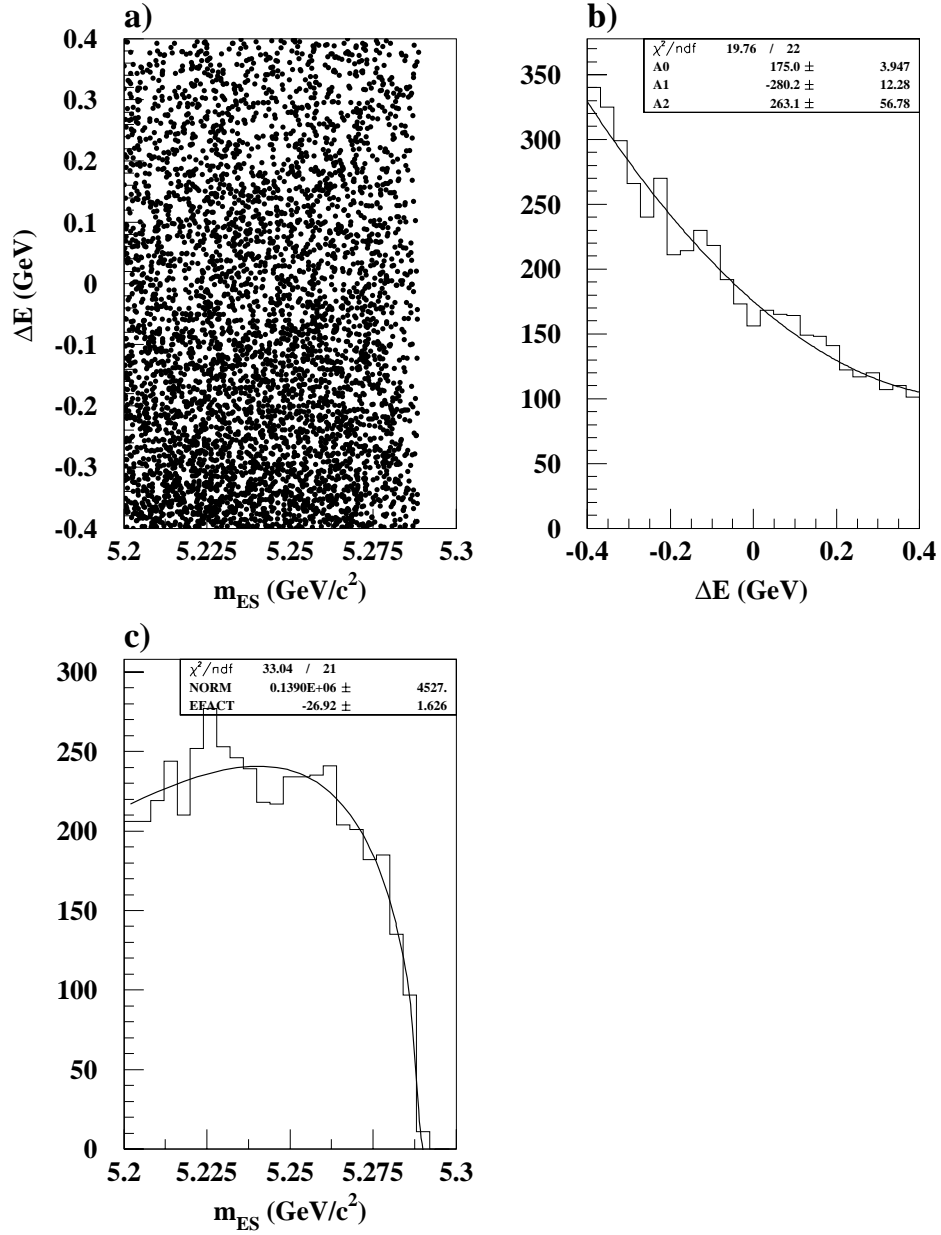


Figure 4.7: Distributions for the  $J/\psi_{\text{fake}} u\bar{u}/d\bar{d}/s\bar{s}$  Monte Carlo sample, showing (a)  $\Delta E$  versus  $m_{ES}$ , (b) the  $\Delta E$  projection for the entire  $m_{ES}$  range, with a polynomial fit, and (c) the  $m_{ES}$  projection for the entire  $\Delta E$  range, with an Argus function fit.

Another useful feature of this  $J/\psi_{\text{fake}}$  sample is that the distribution in  $\Delta E$  gives information about how to scale from the entire  $\Delta E$  window,  $-0.4$  GeV to  $0.4$  GeV, to the  $\Delta E$  signal region,  $-0.112$  GeV to  $0.112$  GeV. Figure 4.7(b) shows a polynomial fit to the  $\Delta E$  projection. A scaling factor  $R$  is found by integrating the function over the two ranges mentioned above:

$$R = \frac{\int_{-0.112}^{0.112} A_0 + A_1x + A_2x^2 dx}{\int_{-0.4}^{0.4} A_0 + A_1x + A_2x^2 dx}, \quad (4.8)$$

where  $A_0$ ,  $A_1$ , and  $A_2$  are the values from the fit. The resulting scale factor,  $R = 0.261$ , is applied to the continuum Monte Carlo, generic  $B\bar{B}$  Monte Carlo, and *offpeak* data samples, which are discussed in more detail below. This procedure allows for the use of the larger  $\Delta E - m_{\text{ES}}$  region in the background studies, while avoiding the naive assumption of a flat distribution in  $\Delta E$ . The scale factor is determined in this way, as opposed to using the *onpeak* data, because the *onpeak* data contains a mixture of backgrounds from continuum and  $B \rightarrow J/\psi X$  sources.

### 4.7.3 Continuum $u\bar{u}/d\bar{d}/s\bar{s}$ and $c\bar{c}$

Figure 4.8 shows the  $\Delta E$  versus  $m_{\text{ES}}$  distribution resulting from running over 18.2 million  $u\bar{u}/d\bar{d}/s\bar{s}$  Monte Carlo events, using the nominal lepton particle identification. This corresponds to  $8.7 \text{ fb}^{-1}$  and needs to be scaled up by 2.38 to be equivalent to the  $20.7 \text{ fb}^{-1}$  of *onpeak* data. To calculate the number of events of this type that contribute to the signal region, an Argus fit is made to the  $m_{\text{ES}}$  projection of the entire  $\Delta E - m_{\text{ES}}$  window, fixing the exponential factor in the fit to the value determined from the  $J/\psi_{\text{fake}}$  study,  $\xi = -26.9$ . The Argus function is integrated across the  $m_{\text{ES}}$  signal range of  $5.270 \text{ GeV}/c^2$  to  $5.288 \text{ GeV}/c^2$ . This result is then multiplied by  $R$  to scale to the  $\Delta E$  signal region and multiplied by 2.38 to scale to the size of the full data sample. The error on the number of events is calculated from the fractional error on the normalization parameter of the Argus fit.

Monte Carlo  $c\bar{c}$  events are used in a similar manner. The sample consists of 10.2 million events, which corresponds to  $7.9 \text{ fb}^{-1}$ . A factor of 2.63 is required to scale

to  $20.7 \text{ fb}^{-1}$  of data. Figure 4.9 shows the distributions and Argus fit for this sample. The results for the number of  $u\bar{u}/d\bar{d}/s\bar{s}$  and  $c\bar{c}$  Monte Carlo events contributing to the signal region can be found together on the first line of Table 4.3, which summarizes the quantity of background from each source.

#### 4.7.4 *Offpeak Data*

The  $2.6 \text{ fb}^{-1}$  of *offpeak* data collected in run1 are used to validate our understanding of the continuum Monte Carlo simulation. The analysis is done in much the same way, but for the purpose of calculating  $m_{\text{ES}}$  and  $\Delta E$ , the beam energy is fixed to  $\sqrt{s} \approx 10.58 \text{ GeV}$ , a value typical of *onpeak* running. This compensates for the 40 MeV shift in center of mass energy and the  $m_{\text{ES}}$  distribution can be fit with the Argus function in the same way as for the continuum Monte Carlo samples, with the same end-point. The plots are shown in Figure 4.10. The background level is again determined by integrating under the Argus function in the  $m_{\text{ES}}$  signal range and scaling by the ratio  $R$  found in Section 4.7.2, and multiplying by a factor to scale to the full data sample. The results are shown on line two of Table 4.3 and they agree, within error, with the continuum Monte Carlo simulation.

#### 4.7.5 *Generic $B\bar{B}$*

To measure the contribution from generic  $B\bar{B}$  decays, we use a generic  $B\bar{B}$  Monte Carlo sample, treated in much the same way as the  $u\bar{u}/d\bar{d}/s\bar{s}$  and  $c\bar{c}$  Monte Carlo discussed above. However, when running over these events, any event of the type  $B \rightarrow J/\psi X$  is removed from further analysis to avoid double counting, since we have Monte Carlo to study that background source separately. The generic  $B\bar{B}$  sample consists of 3.6 million  $B^0\bar{B}^0$  events and 4.3 million  $B^+B^-$  events, for a total of 7.9 million. Therefore, a factor of 2.88 is used to scale the number of events found in the signal region of an Argus fit to the  $m_{\text{ES}}$  distribution of this sample up to the level of the *onpeak* data sample. The distribution of  $\Delta E$  versus  $m_{\text{ES}}$  and the projection in  $m_{\text{ES}}$  are shown in Figure 4.11, and the contribution from this source is listed in Table 4.3.

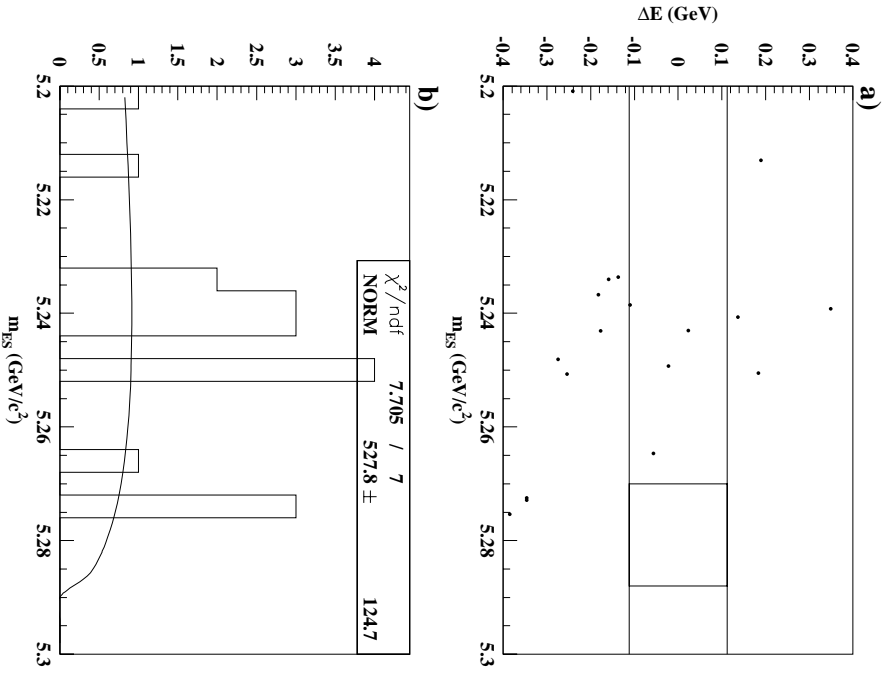


Figure 4.8: Plots of (a)  $\Delta E$  versus  $m_{ES}$  and (b) the Argus fit to the  $m_{ES}$  projection in the  $\Delta E$  signal band, for the  $u\bar{u}/d\bar{d}/s\bar{s}$  Monte Carlo sample, using the nominal  $J/\psi$  selection.

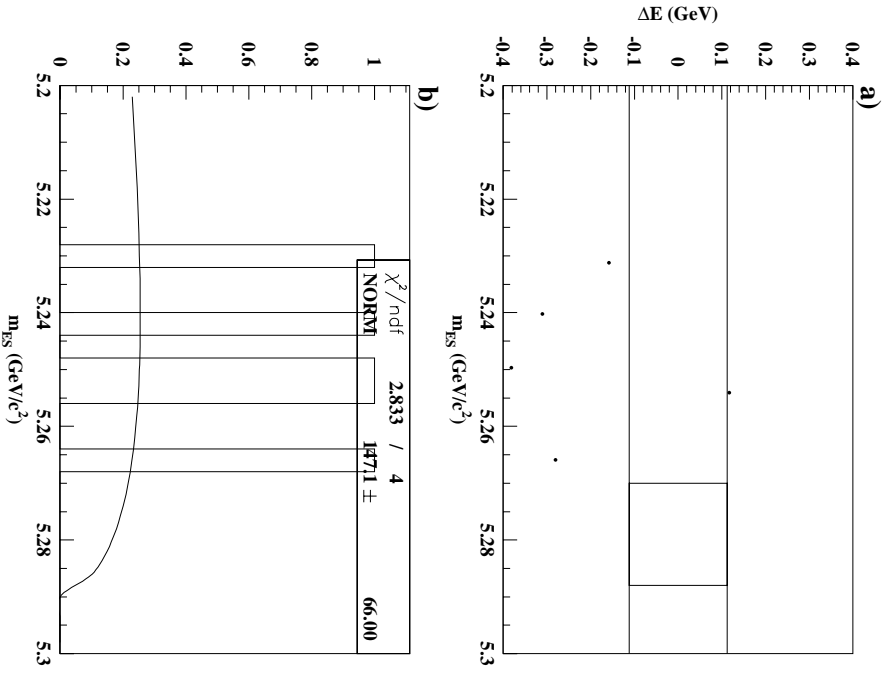


Figure 4.9: Plots of (a)  $\Delta E$  versus  $m_{ES}$  and (b) the Argus fit to the  $m_{ES}$  projection in the  $\Delta E$  signal band, for the  $c\bar{c}$  Monte Carlo sample, using the nominal  $J/\psi$  selection.

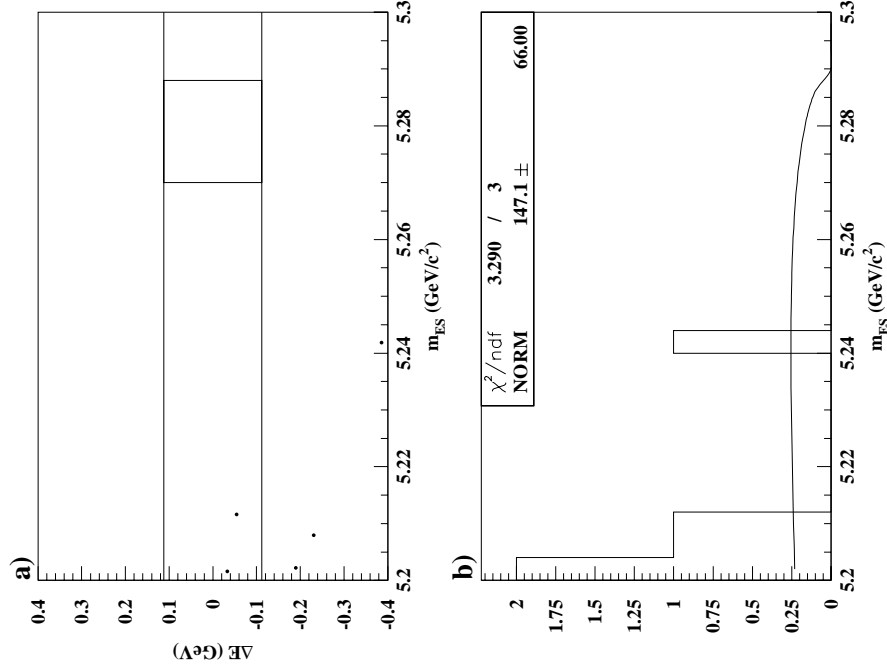


Figure 4.10: Plots of (a)  $\Delta E$  versus  $m_{ES}$  and (b) the Argus fit to the  $m_{ES}$  projection in the  $\Delta E$  signal band, for the *Offpeak* data sample, using the nominal  $J/\psi$  selection.

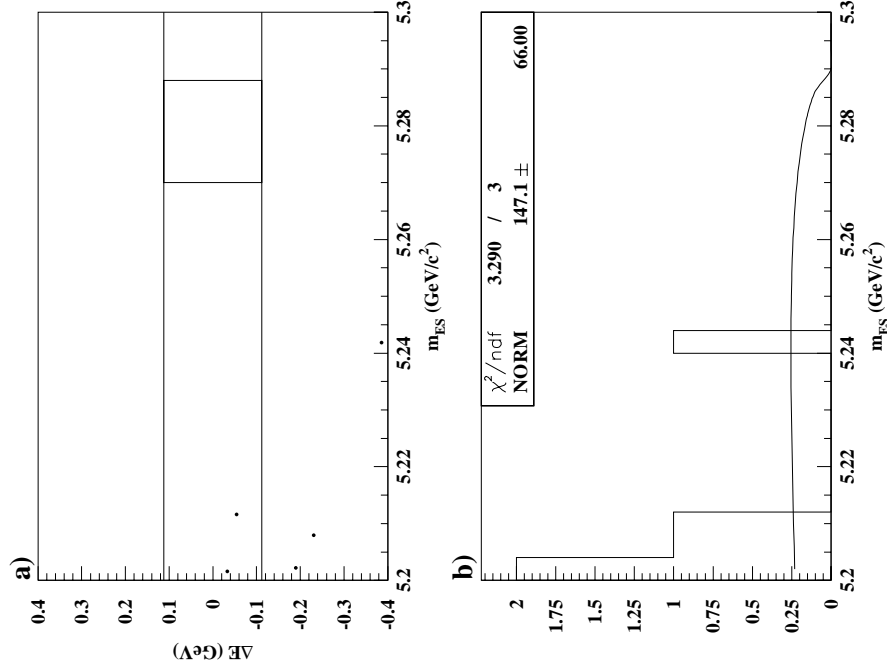


Figure 4.11: Plots of (a)  $\Delta E$  versus  $m_{ES}$  and (b) the Argus fit to the  $m_{ES}$  projection in the  $\Delta E$  signal band, for the generic  $B\bar{B}$  Monte Carlo sample, using the nominal  $J/\psi$  selection.

### 4.7.6 Inclusive $J/\psi$

A Monte Carlo sample of inclusive  $J/\psi$  decays is used to measure a portion of the contributions from  $B \rightarrow J/\psi X$  feed-through. When running on this sample, any event that contains the decay  $B^0 \rightarrow J/\psi \pi^0$  or the decay  $B^0 \rightarrow J/\psi K_s^0$  with  $K_s^0 \rightarrow \pi^0 \pi^0$ , is excluded from analysis. The former is the signal mode and of course should not be counted as background and the latter mode is found to dominate the  $B \rightarrow J/\psi X$  background and is investigated separately (Section 4.7.7). The inclusive  $J/\psi$  sample used here is generated with a cut on  $p^* > 1.3 \text{ GeV}$  to provide a greater number of events in the kinematic range of the charmonium modes. This adds a factor of approximately 2.5 to the number of events passing the selection, as compared to an inclusive  $J/\psi$  Monte Carlo sample without the  $p^*$  cut. Taking into account the branching fraction of  $B$  mesons to inclusive  $J/\psi$  and the branching fractions of  $J/\psi \rightarrow e^+e^-$  and  $J/\psi \rightarrow \mu^+\mu^-$ , along with the number of  $B\bar{B}$  pairs in data and the size of the inclusive  $J/\psi$  sample used (291,000 events), a factor is calculated which scales from this sample to the full data sample. This factor comes out to  $0.084 \pm 0.005$ . To allow for the possibility of both peaking and phase-space components, the full  $m_{\text{ES}}$  distribution in the restricted  $\Delta E$  signal region from  $-0.112 \text{ GeV}$  to  $0.112 \text{ GeV}$  is fit with the combination of an Argus function plus a Gaussian. The Gaussian component is found to be negligible. The  $\Delta E$  versus  $m_{\text{ES}}$  plot and the Argus fit to the  $m_{\text{ES}}$  distribution are shown in Figure 4.12. The background contribution is found by integrating the Argus fit across the  $m_{\text{ES}}$  signal range of  $5.270 \text{ GeV}/c^2$  to  $5.288 \text{ GeV}/c^2$ , and scaling up by the factor to adjust to the size of the full data set. The result and the uncertainty are listed as a subcategory of  $N_{J/\psi \text{ ArgMC}}$  in Table 4.3.

### 4.7.7 $B^0 \rightarrow J/\psi K_s^0$ ( $K_s^0 \rightarrow \pi^0 \pi^0$ ) Feed-Through

The dominant  $B \rightarrow J/\psi X$  background comes from  $B^0 \rightarrow J/\psi K_s^0$  where the  $K_s^0$  decays to  $\pi^0 \pi^0$ . The direction and momentum of either of the  $\pi^0$  mesons can be such that when vertexed with the  $J/\psi$  during analysis, an incorrect  $B$  candidate is formed that has a  $\Delta E$ - $m_{\text{ES}}$  combination that falls into the signal box as defined in equation 4.3. Most events of this sort fall into a triangular region of the  $\Delta E$ - $m_{\text{ES}}$

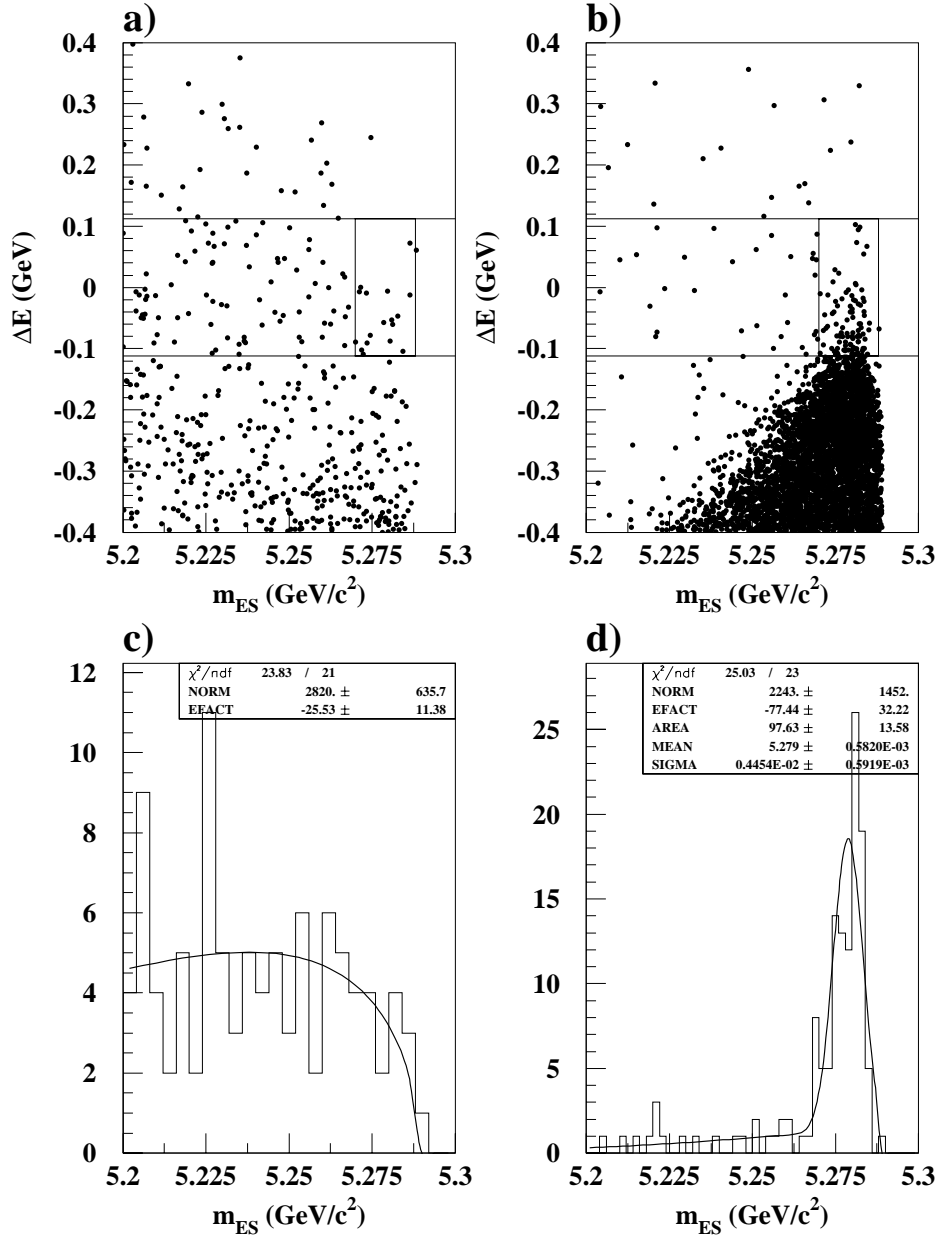


Figure 4.12: Plots of (a)  $\Delta E$  versus  $m_{ES}$  and (c) the Argus fit to the  $m_{ES}$  projection in the  $\Delta E$  signal band for the inclusive  $J/\psi$  Monte Carlo sample. Plots of (b)  $\Delta E$  versus  $m_{ES}$  and (d) the Argus plus Gaussian fit to the  $m_{ES}$  projection in the  $\Delta E$  signal band for the  $B^0 \rightarrow J/\psi K_S^0(\pi^0\pi^0)$  Monte Carlo sample.

Table 4.3: Summary of background contributions within the signal region. The first two lines show agreement between the Monte Carlo simulation (MC) and the *offpeak* data for cross-checking the contribution from continuum events. The last two lines show agreement between the summation of Monte Carlo simulated combinatorial background sources (fit using Argus functions) and the Argus fit to the *onpeak* data. The components that enter into the branching fraction calculation are the Argus fit to *onpeak* data and the Gaussian fit to the  $B^0 \rightarrow J/\psi K_s^0(\pi^0\pi^0)$  Monte Carlo sample.

Background source	Fit function	In signal box
Continuum:	Argus	
Continuum MC ( $N_{\text{cont MC}}$ )		$2.1 \pm 0.6$
<i>Offpeak</i> Data		$3.6 \pm 1.1$
Generic $B\bar{B}$ MC ( $N_{B\bar{B} \text{MC}}$ )	Argus	$0.6 \pm 0.2$
$B \rightarrow J/\psi X$ MC:		
$N_{J/\psi \text{ Arg MC}}$	Argus	$1.01 \pm 0.24$
from $B^0 \rightarrow J/\psi K_s^0(\pi^0\pi^0)$		$0.05 \pm 0.03$
from inclusive $J/\psi$		$0.96 \pm 0.24$
$N_{J/\psi \text{ Gaus MC}}$	Gaussian	$0.68 \pm 0.08$
from $B^0 \rightarrow J/\psi K_s^0(\pi^0\pi^0)$		$0.68 \pm 0.08$
<i>Onpeak</i> data	Argus	$4.7 \pm 0.9$
Predicted value:		
$N_{\text{cont MC}} + N_{B\bar{B} \text{MC}} + N_{J/\psi \text{ Arg MC}}$	Argus	$3.7 \pm 0.6$

plane, below the signal box, as shown in Figure 4.12(b). Also shown is the combined Argus plus Gaussian fit, where the fit is just made to the restricted  $\Delta E$  signal region from  $-0.112$  GeV to  $0.112$  GeV. Two quantities are extracted from this fit. The first is found by integrating the Argus portion of the fit across the  $m_{\text{ES}}$  signal range of  $5.270$  GeV/ $c^2$  to  $5.288$  GeV/ $c^2$ . The second is calculated by subtracting the results of the Argus portion from the integral of the combined Argus plus Gaussian fit in the  $m_{\text{ES}}$  signal range. These two numbers and their uncertainties are scaled by a factor to adjust up to the full *onpeak* data set, as done for the inclusive  $J/\psi$  sample, but now also using the branching fractions for  $B^0 \rightarrow J/\psi K_s^0$  and  $K_s^0 \rightarrow \pi^0\pi^0$ . For 52,000 Monte Carlo events, the scale factor is  $0.007 \pm 0.001$ . The results are listed as subcategories of  $N_{J/\psi \text{ Arg MC}}$  and  $N_{J/\psi \text{ Gaus MC}}$  in Table 4.3.

## 4.8 Results from *Onpeak* Data

The plots of  $\Delta E$  versus  $m_{ES}$ , and the projection of  $m_{ES}$  for the  $\Delta E$  signal region are shown in Figure 4.13 for the  $20.7 \text{ fb}^{-1}$  of run1 *onpeak* data. The combined Argus plus Gaussian fit to the  $m_{ES}$  distribution is performed using the fixed exponential factor,  $\xi = -26.9$ , from the Argus fit to the *fake*  $J/\psi_{\text{fake}}$  sample. With the statistics used in this measurement, this is required for a successful fit.

Figure 4.14 shows the level of agreement between the data and Monte Carlo simulation for the  $\Delta E$  projection.

### 4.8.1 Background Extracted from Data

The Argus function obtained from the fit to the *onpeak* data is integrated across the  $m_{ES}$  signal region and the result,  $4.7 \pm 0.9$  events, is included in Table 4.3. This value is compared with the sum of the background estimates from the continuum ( $u\bar{u}/d\bar{d}/s\bar{s}$  and  $c\bar{c}$ ), generic  $B\bar{B}$ , and the  $B \rightarrow J/\psi X$  (Argus portion) Monte Carlo samples, which total to  $3.7 \pm 0.6$  events in the signal box. The agreement is good, with a difference of just under one sigma.

### 4.8.2 Cross-Check Using the $\Delta E$ Sidebands

The background fitting procedures described in Sections 4.7.3–4.7.7 are repeated for the  $\Delta E$  sideband regions, which are defined as

$$\begin{aligned}
 \text{upper sideband :} & & 0.112 < \Delta E < 0.4 \text{ GeV} & & (4.9) \\
 & & 5.2 < m_{ES} < 5.3 \text{ GeV}/c^2, & & \\
 \text{lower sideband :} & & -0.4 < \Delta E < -0.112 \text{ GeV} & & \\
 & & 5.2 < m_{ES} < 5.3 \text{ GeV}/c^2. & &
 \end{aligned}$$

As before, the  $u\bar{u}/d\bar{d}/s\bar{s}$ ,  $c\bar{c}$ , and generic  $B\bar{B}$  Monte Carlo samples, as well as the *offpeak* data, are fit with the Argus function in the entire  $\Delta E$ – $m_{ES}$  window, and the functions are integrated across the  $m_{ES}$  signal range of  $5.270 \text{ GeV}/c^2$  to  $5.288 \text{ GeV}/c^2$ .

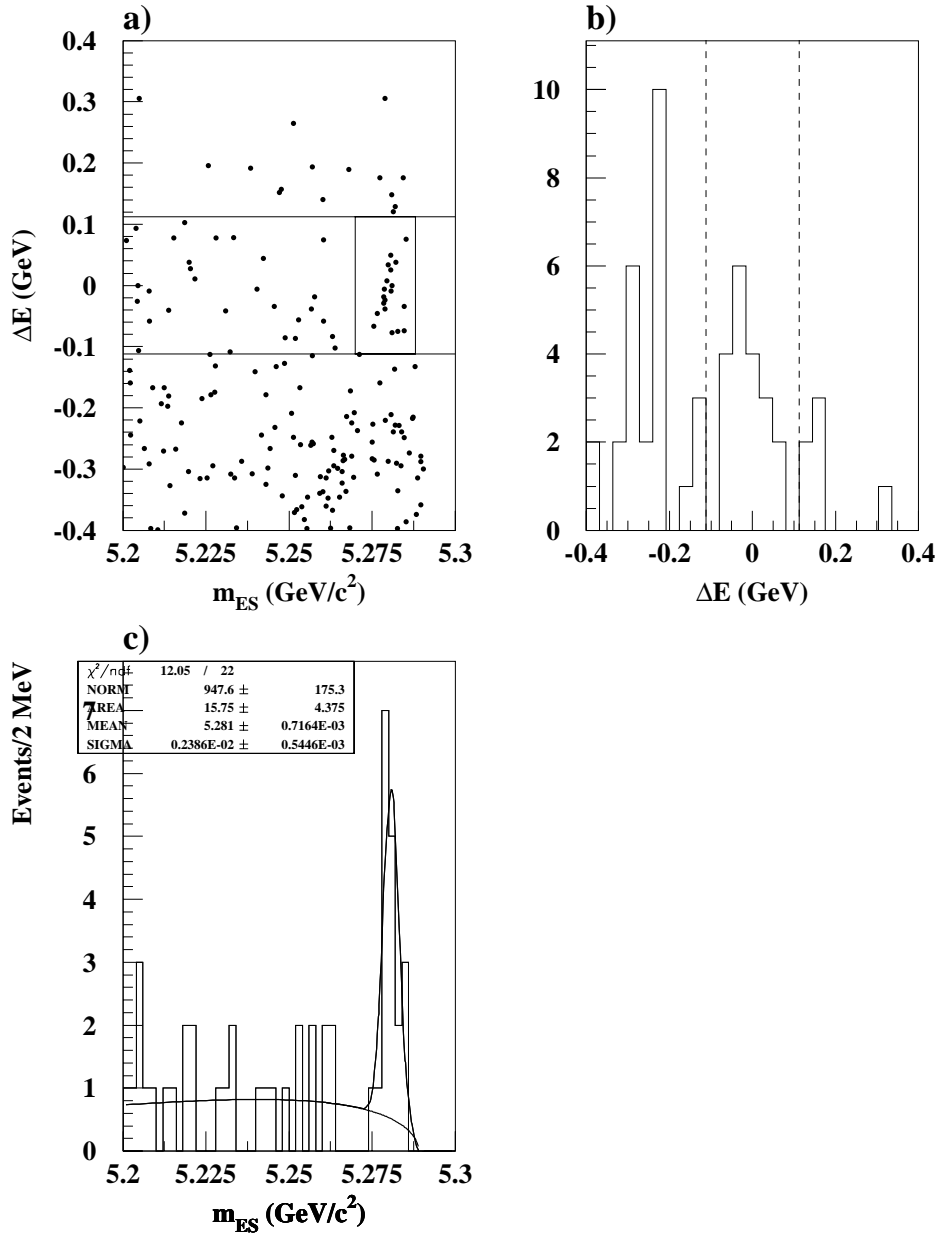


Figure 4.13: Plots for  $20.7 \text{ fb}^{-1}$  of *onpeak* data showing (a)  $\Delta E$  versus  $m_{ES}$ , (b) the  $\Delta E$  projection in the  $m_{ES}$  signal band, and (c) the  $m_{ES}$  projection in the  $\Delta E$  signal band, fit with an Argus plus a Gaussian.

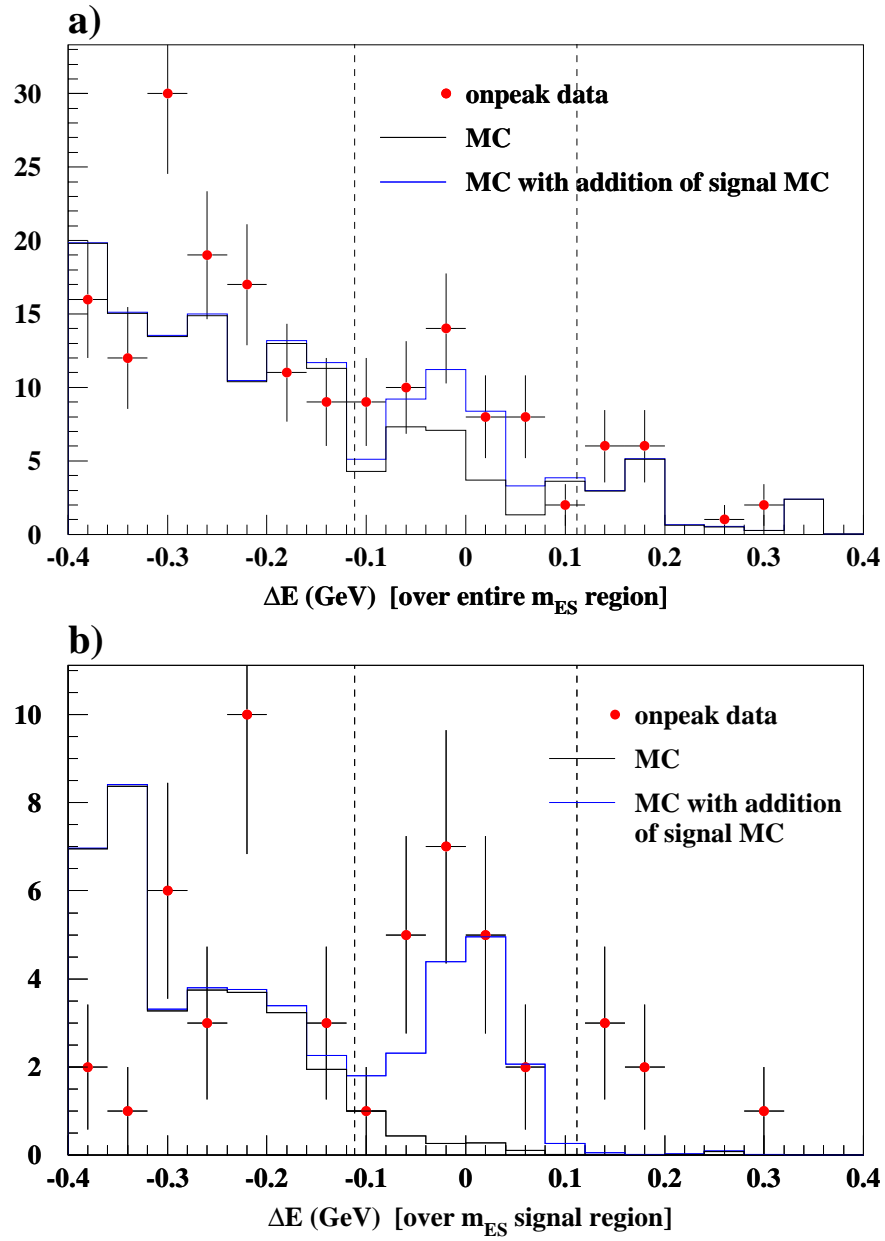


Figure 4.14: The  $\Delta E$  distributions are shown for (a) the entire  $m_{ES}$  region and (b) the  $m_{ES}$  signal region, for *onpeak* data (red points), a sum of Monte Carlo samples without the signal Monte Carlo (black histograms), and the sum of Monte Carlo including the signal (blue histograms).

Table 4.4: Summary of background contributions within the  $\Delta E$  sidebands. The first two lines show agreement between the continuum Monte Carlo simulation and the *offpeak* data. The last four lines show agreement between the summation of the Monte Carlo Argus components and the Argus component of the data, and between the summation of the Monte Carlo Gaussian components and the Gaussian component of the data, all within the  $\Delta E$  sidebands.

Background source	Fit function	In sidebands
Continuum:	Argus	
Continuum MC ( $N_{\text{cont MC}}$ )		$6.1 \pm 1.8$
<i>Offpeak</i> Data		$10.3 \pm 3.0$
Generic $B\bar{B}$ MC ( $N_{B\bar{B}MC}$ )	Argus	$1.6 \pm 0.7$
$B \rightarrow J/\psi X$ MC:		
$N_{J/\psi \text{ Arg MC}}$	Argus	$4.86 \pm 1.63$
from $B^0 \rightarrow J/\psi K_s^0(\pi^0\pi^0)$		$2.31 \pm 0.14$
from inclusive $J/\psi$		$2.55 \pm 1.62$
$N_{J/\psi \text{ Gaus MC}}$	Gaussian	$19.67 \pm 2.17$
from $B^0 \rightarrow J/\psi K_s^0(\pi^0\pi^0)$		$15.24 \pm 0.35$
from inclusive $J/\psi$		$4.43 \pm 2.14$
Signal mode MC $N_{\text{signal}}$	Gaussian	$0.9 \pm 0.1$
<i>Onpeak</i> data	Argus	$12.8 \pm 1.9$
	Gaussian	$25.2 \pm 6.1$
Predicted value:		
$N_{\text{cont MC}} + N_{B\bar{B}MC} + N_{J/\psi \text{ Arg MC}}$	Argus	$12.5 \pm 2.2$
$N_{J/\psi \text{ Gaus MC}} + N_{\text{signal}}$	Gaussian	$20.5 \pm 2.2$

For this cross-check, the results are then scaled to the upper and lower sidebands using  $1-R$ , where  $R$  is defined in equation 4.8. The contributions from  $B^0 \rightarrow J/\psi K_s^0(\pi^0\pi^0)$ , and from other inclusive  $J/\psi$  decays, are found as before, but the fits are performed to the sum of the upper and lower  $\Delta E$  sidebands. Again, the yield from each sample is scaled to match the full run1 *onpeak* data sample. The *onpeak* data is also fit in the sidebands with the combination of an Argus function and a Gaussian function, and all of the results, including a comparison of the data and the sum of various Monte Carlo samples (separately for the Argus and Gaussian components), can be seen in Table 4.4.

### 4.8.3 Event Counting Cross-Check

The  $\Delta E$ - $m_{ES}$  plane is divided into regions as shown in Figure 4.15, and the number of candidates in each region, scaled to the size of the *onpeak* data sample, is counted for each sample of Monte Carlo and data. The results appear in Table 4.5.

### 4.8.4 Additional Background Study Using Loose Selection

To improve the understanding of the degree to which the Monte Carlo simulation resembles the data, the number of candidates is increased by removing the angular cuts and loosening the particle identification selection. In this study, for  $J/\psi \rightarrow e^+e^-$ , one electron must satisfy the *loose* selector and the other must satisfy the *loose* or *noCal* selectors (this is instead of one *tight* and one *loose* or *noCal*). For  $J/\psi \rightarrow \mu^+\mu^-$ , one muon must pass a *tight* selector and the other must pass a *veryLoose* selector (this is instead of one *veryTight* and one *loose*). The requirements of each of these selectors are detailed in tables 4.1 and 4.2. The results of the background analysis are summarized in Table 4.6. The difference between the continuum Monte Carlo and the *offpeak* data is  $1.4\sigma$  and the difference between the sum of the Monte Carlo samples and the *onpeak* data is  $0.8\sigma$ . The increase in the statistics, with respect to the normal analysis, can be seen by comparing these results to those found in Table 4.3.

In addition, the cross-check of counting candidates in various regions of the  $\Delta E$ - $m_{ES}$  plane is repeated. Again the plane is subdivided as in Figure 4.15. The results are shown in Table 4.7.

### 4.8.5 Systematic Uncertainties

The systematic uncertainties are obtained from a variety of sources. Some are taken from external studies, some are derived from imposing smearing or shifting on variables in the analysis, and some are determined by a variation of the selection cuts. The source of each systematic uncertainty is described here and Table 4.8 provides a summary.

**Product Branching Fractions** This systematic arises from the uncertainties in the

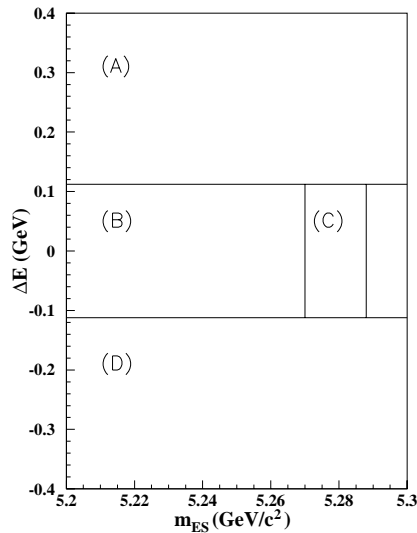


Figure 4.15: As a cross-check, the  $\Delta E$ – $m_{ES}$  plane is divided into the regions shown for counting the number of candidates in each sample.

Table 4.5: The numbers of candidates in four different regions are shown for each sample. The factor by which each sample is scaled, to be equivalent in size to the *onpeak* data, is shown in the last column. Some of the numbers are scaled up from very few events, so the associated Poisson errors are large.

Sample	(A)	(B)	(C)	(D)	Scaling
Continuum:					
$u\bar{u}/d\bar{d}/s\bar{s}$ MC	9.5	9.5	0.0	23.8	2.38
$c\bar{c}$ MC	2.6	0.0	0.0	10.5	2.63
<i>Offpeak</i> Data	47.6	7.9	0.0	39.6	7.93
Generic $B\bar{B}$ MC	0.0	5.8	0.0	8.6	2.88
$B \rightarrow J/\psi X$ MC:					
from $B^0 \rightarrow J/\psi K_s^0(\pi^0\pi^0)$	0.1	0.2	0.7	29.5	0.0072
from inclusive $J/\psi$	2.4	6.8	1.0	25.8	0.0840
Signal MC	0.2	0.1	13.5	1.1	0.0024
Sum of MC	14.8	22.4	15.2	99.3	-
<i>Onpeak</i> Data	15	29	19	117	1

Table 4.6: Summary of background contributions within the signal region after removing the angular variable requirements and using relaxed particle identification criteria.

Background source	Fit function	In signal box
Continuum:	Argus	
Continuum MC ( $N_{\text{cont MC}}$ )		$8.5 \pm 2.3$
<i>Offpeak</i> Data		$12.7 \pm 2.0$
Generic $B\bar{B}$ MC ( $N_{B\bar{B} \text{MC}}$ )	Argus	$1.1 \pm 0.4$
$B \rightarrow J/\psi X$ MC:		
$N_{J/\psi \text{ Arg MC}}$ from $B^0 \rightarrow J/\psi K_s^0(\pi^0\pi^0)$	Argus	$1.35 \pm 0.28$
from inclusive $J/\psi$		$0.04 \pm 0.03$
$N_{J/\psi \text{ Gaus MC}}$ from $B^0 \rightarrow J/\psi K_s^0(\pi^0\pi^0)$	Gaussian	$1.31 \pm 0.28$
		$0.78 \pm 0.08$
<i>Onpeak</i> data	Argus	$12.3 \pm 1.4$
Predicted value:		
$N_{\text{cont MC}} + N_{B\bar{B} \text{MC}} + N_{J/\psi \text{ Arg MC}}$	Argus	$10.9 \pm 1.0$

Table 4.7: The numbers of candidates in four different regions are shown for each sample, after removing the angular variable requirements and using relaxed particle identification criteria. The factor by which each sample is scaled, to be equivalent in size to the *onpeak* data, is shown in the last column.

Sample	(A)	(B)	(C)	(D)	Scaling
Continuum:					
$u\bar{u}/d\bar{d}/s\bar{s}$ MC	35.7	38.1	2.4	90.5	2.38
$c\bar{c}$ MC	13.2	7.9	5.3	29.0	2.63
<i>Offpeak</i> Data	79.3	55.5	7.9	198.1	7.93
Generic $B\bar{B}$ MC	0.0	5.8	0.0	23.0	2.88
$B \rightarrow J/\psi X$ MC:					
from $B^0 \rightarrow J/\psi K_s^0(\pi^0\pi^0)$	0.1	0.2	0.8	32.7	0.0072
from inclusive $J/\psi$	2.9	7.5	1.6	30.2	0.0840
Signal MC	0.2	0.1	14.9	1.2	0.0024
Sum of MC	52.1	59.6	25.0	206.6	-
<i>Onpeak</i> Data	45	72	23	235	1

product branching fractions as obtained from the 2000 PDG [42]. The branching fractions are:  $\mathcal{B}(J/\psi \rightarrow e^+e^-) = (5.93 \pm 0.10)\%$ ,  $\mathcal{B}(J/\psi \rightarrow \mu^+\mu^-) = (5.88 \pm 0.10)\%$ , and a negligible contribution from  $\mathcal{B}(\pi^0 \rightarrow \gamma\gamma) = (99.798 \pm 0.032)\%$ . Thus, the systematic error is 1.7%.

**Particle Identification (PID)** A detailed study provides the systematic uncertainties for a variety of PID selectors, as obtained from analyzing  $B \rightarrow J/\psi X$  events. Both the electron and muon selector combinations yield an uncertainty of about 2.0%, and an additional 0.5% is added to allow for the fact that the  $B^0 \rightarrow J/\psi \pi^0$  measurement is performed without fiducial cuts on the daughters of the  $J/\psi$ . This choice of 0.5% is based on a study of the effect of the fiducial cuts in the case of the relatively high statistics  $B^+ \rightarrow J/\psi K^+$  sample. The total systematic attributed to this source is therefore 2.5%.

**Track Momentum** To obtain this systematic uncertainty, the analysis is repeated with the distribution of the momentum of the charged tracks smeared by 1.15%. The branching fraction is recalculated and the fractional deviation from the nominal branching fraction, 0.4%, is taken as the systematic.

**Tracking Efficiency** This systematic is taken from the work of the tracking group, which finds that 1.2% per track (`GoodTracksLoose`) is a conservative result which takes into account a number of cross-checks. This gives a 2.4% systematic for this analysis.

**Neutrals Efficiency** For  $\pi^0$  mesons that do not have a momentum far exceeding 3 GeV/c, the neutrals group has suggested a systematic error of 1.25% per photon. In the  $B^0 \rightarrow J/\psi \pi^0$  mode, the  $\pi^0$  mesons are restricted, through a combination of kinematics and the detector acceptance, to lie within the momentum range 1.2 GeV/c to 3.1 GeV/c in the lab frame. Therefore, the systematic can be taken as 2.5%.

**Background Parameterization** To determine the systematic due to the choice of the background parameterization, the exponential factor that is used to fit the continuum and generic  $B\bar{B}$  Monte Carlo samples, as well as the *onpeak* and

*offpeak* data, is varied by  $\pm 1\sigma$ . The analysis is repeated in each case and the average fractional deviation of the resulting branching fraction from the nominal one is taken as the systematic. This yields a 1.7% systematic uncertainty.

**Monte Carlo Statistics** Using the efficiency calculated for the signal Monte Carlo sample, and the associated binomial error, the systematic is 1.1%.

**B-Counting** The systematic uncertainty associated with the event selection requirements that identify hadronic  $B$  events (Section 4.3.1) is 1.6%.

**Cut Variations** For each cut specific to this analysis, the possible systematic is studied by varying the cut up and down (by  $\pm 1\sigma$  where possible), and taking the average fractional deviation of the recalculated branching fraction from the nominal one. The error on the systematic uncertainty is calculated, taking into account the events moving in and out of the signal region, both in signal and in background. Here, the cut variables are listed, along with the variations and the resulting average fractional change in the branching fraction:

Variable	Variation	Systematic
$J/\psi$ mass	$\pm 11 \text{ MeV}/c^2$	$(3.9 \pm 7.5)\%$
$\pi^0$ mass	$\pm 4 \text{ MeV}/c^2$	$(7.7 \pm 6.6)\%$
$ \cos(\theta_T)  < 0.95$	$\pm 0.05$	$(5.9 \pm 8.1)\%$
$ \cos(\theta_T)  +  \cos(\theta_\ell)  < 1.8$	$\pm 0.1$	$(1.0 \pm 5.3)\%$

As an additional study, the cut variation on the  $\pi^0$  mass was repeated using  $\pm 5 \text{ MeV}/c^2$ ,  $\pm 6 \text{ MeV}/c^2$ , and  $\pm 7 \text{ MeV}/c^2$ , yielding average fractional changes in the branching fraction of  $(12.1 \pm 7.3)\%$ ,  $(12.8 \pm 10.7)\%$ , and  $(19.6 \pm 11.7)\%$  respectively, suggesting a non-pathological scaling with cut size. A conservative systematic of 10.0% is selected for this source because the error on the uncertainty is less than the uncertainty itself. The other cut variations are not included in the final total systematic, as the errors on these uncertainties are larger than the uncertainties themselves, indicating a statistical effect. The  $\Delta E$  cut is also varied by  $\pm 1\sigma$ , and the result of  $(17 \pm 26)\%$  shows that it is also

Table 4.8: The systematic uncertainties from various sources are listed and the total is given as the sum in quadrature.

Source	Systematic uncertainty (%)
Product Branching Fractions	1.7
Particle Identification	2.5
Track Momentum	0.4
Tracking Efficiency	2.4
Neutrals Efficiency	2.5
Background Parameterization	1.7
Monte Carlo Statistics	1.1
$B$ -Counting	1.6
$\pi^0$ mass cut	10.0
Total:	11.3

a case in which the systematic error would be artificially high due to the low statistics.

#### 4.8.6 Efficiency Corrections

There are several corrections made to the raw efficiency obtained from the signal Monte Carlo sample. Random removal of a fraction of particle candidates is activated for both muons and electrons, using lookup tables of efficiencies that are binned in momentum and theta. While these tables were created from clean leptonic control samples, the identification of particle candidates in data occurs in a hadronic environment, so an additional particle identification correction is applied. A correction is also applied by introducing a random removal of 2.5% of the photon candidates, and a smearing of 1.5% to the energy of those that remain. Charged track energies are also smeared by 1.15%, for an additional correction. Finally, there is a correction factor for the tracking efficiency. These corrections are listed in Table 4.9.

Table 4.9: The series of successive corrections applied to the efficiency obtained from the signal Monte Carlo simulation. The second column shows the progression of corrections to the raw Monte Carlo simulation and the third column shows the impact of each correction.

Efficiency correction	Absolute efficiency (%)	Relative efficiency (%)
Raw Monte Carlo	30.1	-
Particle ID Killing	29.3	97.4
Particle ID Correction	28.4	97.0
Photon Killing	26.6	93.4
Track Smearing	26.4	99.6
Tracking Efficiency	25.8	97.6

#### 4.8.7 Yield, Purity, and Branching Fraction

The yield is calculated from the number of candidates ( $N_{\text{cand}}$ ) counted in the signal box defined in equation 4.3, the Argus fit to *onpeak* data ( $N_{\text{data Argus}}$ ), and the Gaussian portion of the background estimate from the  $B^0 \rightarrow J/\psi K_S^0(\pi^0\pi^0)$  Monte Carlo sample ( $N_{J/\psi \text{Gaus MC}}$ ):

$$\text{yield} = N_{\text{cand}} - N_{\text{data Argus}} - N_{J/\psi \text{Gaus MC}} , \quad (4.10)$$

$$\sigma_{\text{yield}} = \sqrt{N_{\text{cand}} + \sigma_{N_{\text{data Argus}}}^2 + \sigma_{N_{J/\psi \text{Gaus MC}}}^2} . \quad (4.11)$$

The purity is defined as  $S/(S+B)$ . The quantity  $S$ , which is the same as the yield, can be formulated as  $N_{\text{cand}} - B$ , where  $B$  is  $N_{\text{data Argus}} + N_{J/\psi \text{Gaus MC}}$ , and the quantity  $S+B$  is just  $N_{\text{cand}}$  from above. So, the purity can be written as

$$\text{purity} = \frac{S}{S+B} = \frac{N_{\text{cand}} - B}{N_{\text{cand}}} = 1 - \frac{B}{N_{\text{cand}}} , \quad (4.12)$$

$$\sigma_{\text{purity}} = \frac{B}{N_{\text{cand}}} \sqrt{\left(\frac{\sigma_B}{B}\right)^2 + \left(\frac{\sigma_{N_{\text{cand}}}}{N_{\text{cand}}}\right)^2} . \quad (4.13)$$

Table 4.10: Results obtained by running over  $20.7 \text{ fb}^{-1}$  of *onpeak* data. The values are from Table 4.9 and equations 4.10–4.15. The result for the branching fraction includes the statistical error (equation 4.15) and the systematic error (Table 4.8).

Efficiency	$(25.8 \pm 0.3)\%$
Yield	$13.6 \pm 4.4$
Purity	$(72 \pm 8)\%$
$\mathcal{B}(B^0 \rightarrow J/\psi \pi^0)$	$(2.0 \pm 0.6 \pm 0.2) \times 10^{-5}$

The branching fraction and associated statistical uncertainty are calculated as follows:

$$\mathcal{B}(B^0 \rightarrow J/\psi \pi^0) = \frac{\text{yield}}{(\#B\bar{B})(\text{eff})(\mathcal{B}(J/\psi \rightarrow e^+e^-, \mu^+\mu^-))(\mathcal{B}(\pi^0 \rightarrow \gamma\gamma))}, \quad (4.14)$$

$$\sigma_{\mathcal{B}} = \frac{\sigma_{\text{yield}}}{(\#B\bar{B})(\text{eff})(\mathcal{B}(J/\psi \rightarrow e^+e^-, \mu^+\mu^-))(\mathcal{B}(\pi^0 \rightarrow \gamma\gamma))}. \quad (4.15)$$

The results of this section are summarized in Table 4.10. The branching fraction, with statistical and systematic errors, is  $\mathcal{B}(B^0 \rightarrow J/\psi \pi^0) = (2.0 \pm 0.6 \text{ (stat)} \pm 0.2 \text{ (syst)}) \times 10^{-5}$ . The significance of the final result is discussed in the next section, and conclusions are drawn in Chapter 6.

#### 4.8.8 Statistical Significance of the Result

The significance of the branching fraction result is evaluated by determining the probability of the expected background level fluctuating up to at least the number of candidates observed in the signal region. This is done by running a simulation that generates a random number, uses a Poisson distribution to calculate the probability of this number fluctuating up to the number of candidates observed, and then weights this probability by the position of the random number in a Gaussian centered at the value of the expected background level, where this Gaussian has a width equal to the error on the expected background.

The expected background is  $5.41 \pm 0.87$  events, with  $4.73 \pm 0.87$  events coming from

the Argus fit to *onpeak* data and  $0.68 \pm 0.08$  events coming from the feed-through of  $B^0 \rightarrow J/\psi K_S^0(\pi^0\pi^0)$  events. There are 19 candidates observed in the signal region, and the probability of this being a fluctuation is 0.0022%, which represents a significance of  $4.3\sigma$ .

# Chapter 5

## Time-Dependent $CP$ Asymmetry in $B^0 \rightarrow J/\psi \pi^0$

### 5.1 Introduction

This chapter describes in detail a time-dependent  $CP$  asymmetry measurement using  $B^0 \rightarrow J/\psi \pi^0$  decays. There were no prior measurements of the  $CP$  asymmetry in this mode. Using approximately 88 million  $B\bar{B}$  pairs, our results for the coefficients of the cosine and sine terms of the  $CP$  asymmetry are  $C_{J/\psi \pi^0} = 0.38 \pm 0.41$  (stat)  $\pm 0.09$  (syst) and  $S_{J/\psi \pi^0} = 0.05 \pm 0.49$  (stat)  $\pm 0.16$  (syst). These results were first presented at the 31<sup>st</sup> International Conference on High Energy Physics in 2002 [44], and then submitted for publication in Physical Review Letters in 2003 [45].

As with the branching fraction measurement, this analysis is carried out by sequentially running over events of interest. Candidate  $B^0 \rightarrow J/\psi \pi^0$  decays are identified, first by identifying candidates for the decay products of  $J/\psi$  and  $\pi^0$  mesons, and then by finding combinations of candidate  $J/\psi$  and  $\pi^0$  mesons that suggest they come directly from a  $B$  meson. Kinematic quantities, determined for each event, and their carefully studied distributions over many events, are used to distinguish between signal and background. Combined with this is an essential understanding of the decay time behavior of the signal and background events, allowing us to learn about the  $CP$  behavior of  $B^0 \rightarrow J/\psi \pi^0$  decays.

This chapter begins with a description of the data sample, followed by a presentation of a number of technical details. In particular, there are brief descriptions of the software releases that are used and the logistics of obtaining reduced collections of events. This is followed by issues of physical significance, including the candidate and event selections, which have a great deal in common with those of the branching fraction measurement. There is an introduction to the sources of backgrounds that explains which processes partially mimic the  $B^0 \rightarrow J/\psi \pi^0$  signal and indicates which samples of Monte Carlo simulation and data are used to model these backgrounds. There is also documentation on fitting methods employed and the probability density functions (PDFs) used to model each of the event selection variables and decay-time distributions. These PDFs are used in a series of likelihood fits, both for an initial set of yields as a cross-check and for the final time-dependent  $CP$  asymmetry measurement. Included toward the end of this chapter are discussions of additional cross-checks and the systematic uncertainty studies. The comparison of the results to those from the Belle collaboration, and discussion about the implications for learning about penguin diagram contributions, is left for the concluding chapter.

## 5.2 Data Samples and Software Releases

In describing the software releases and data reduction, this section utilizes some *BABAR*-specific terminology. This is included for completeness, and to provide documentation for those most familiar with the *BABAR* framework, but is not critical for understanding this measurement. The same is true for some *BABAR*-specific terminology in Section 5.3, describing the candidate selection.

### 5.2.1 Data Sample

The *BABAR* data sample used in this measurement is called the “Summer 2002” sample, or alternatively the “run1 + run2” sample. It includes data collected between the startup in 1999 and a Summer shutdown in 2002, and is therefore a superset of the run1 sample introduced in Section 4.2. It contains  $81.1 \text{ fb}^{-1}$  of integrated *onpeak*

luminosity. It also includes  $9.6 \text{ fb}^{-1}$  of *offpeak* data, of which  $5 \text{ fb}^{-1}$  are used in this analysis. The total number of  $B\bar{B}$  pairs in the *onpeak* data sample is  $(88.0 \pm 1.0) \times 10^6$ .

### 5.2.2 Data Reconstruction Software Releases

All of the data presented here have been reconstructed using the 10-series releases of the *BABAR* software. Specifically, the data from 1999, 2000, 2002, and a portion of 2001 have been reconstructed using releases 10.2.3b, 10.2.3c, 10.2.3e, 10.2.3f, 10.2.3g, and 10.2.3h. The remainder of the data from 2001 (about  $18.5 \text{ fb}^{-1}$ ) have been reconstructed using releases 10.0.2b, 10.0.3a, 10.0.3b, and 10.1.0a.

### 5.2.3 Monte Carlo Simulation Reconstruction Software Releases

All of the Monte Carlo simulation used in this measurement is generated using Geant4 [46] as part of the *BABAR* simulation production cycle 4 (SP4) and is reconstructed in the 10-series releases. Each Monte Carlo sample consists of events reconstructed using background conditions information from each month of running. Table 5.1 shows the releases used and run range for each year. The releases 10.3.1 and 10.3.1a include a bug fix that allows for proper simulation of  $K_s^0 \rightarrow \pi^0 \pi^0$  decays, and so samples of  $B^0 \rightarrow J/\psi K_s^0(\pi^0 \pi^0)$ , inclusive  $J/\psi$ , and signal  $B^0 \rightarrow J/\psi \pi^0$  Monte Carlo events used in this analysis were required to come from these release. The other Monte Carlo samples described in this chapter were reconstructed with an additional module (named `VubRemoveMCOorphans`) included to correct for the flawed simulation in the effected run ranges.

### 5.2.4 Reduced collections

Where possible, the general strategy is to acquire a reduced set of events, thereby allowing an increase in speed and efficiency for the later portions of the analysis. The procedure involves running two different *BABAR* software release applications. The first of these executables (`CharmFilterApp`) reads the events from the database

Table 5.1: Monte Carlo simulation software releases and run range by year.

Year	Release	Run range
2000	10.2.2a	600000 – 759999
	10.3.1(a)	1200000 – 1349999
2001	10.3.0d,e	770000 – 1009999
	10.3.1(a)	1370000 – 1609999
2002	10.3.1(a)	1010000 – 1199999

(stored in an object oriented format called *Objectivity*), applies loose selection criteria, and then writes the reduced set of events back out in *Objectivity* format. The second executable (*CharmApp*) runs over the reduced collections to make the final particle identification and candidate selection, and writes kinematic, event classification, and book-keeping information to ntuples and ASCII files.

Additional complexity arises due to the distribution of *Objectivity* data among so-called “slave federations”. For example, in running over *onpeak* and *offpeak* data, the procedure is to write the reduced collections back to the slave federations where the original data resides. In the case of the *onpeak* data, the production for charmonium modes is run centrally and an additional step has been devised to add pointer collections so that the distribution of the reduced collections among the slave federations is transparent. For the *offpeak* data the solution is to run the executable that reads back the reduced set of events successively over each relevant slave federation. The Monte Carlo samples used in this analysis are also distributed among various slave federations and, for technical reasons, it has been most efficient to run the second of the analysis executables directly over these events.

### 5.2.5 Analysis Releases

The executable used to write the reduced collections is based on *BABAR* software release 10.4.0-physics-1a, with a number of additional updated packages. The executable used to read the events back out and perform the final event selection is based

on release 10.4.4-physics-1, also with a number of updated packages.<sup>1</sup>

### 5.3 Candidate Selection

The candidate selection is almost identical to that presented in sections 4.3 and 4.4 for the branching fraction measurement, so this section focuses on the minor differences. The portion of the selection that is tied in with the counting of  $B$  mesons is identical (Section 4.3.1).

The lepton pre-selection differs only slightly, and the final lepton and  $J/\psi$  candidate selection is the same (Section 4.4.1), so the overall difference is only procedural. The way in which lepton candidates are combined to form a list of loose  $J/\psi$  candidates is still well represented by Figure 4.1, with two minor modifications: the list called `muMicroLoose` is substituted by `MuMicroVeryLoose` and the list called `muMicroMinimumIonizing` is substituted by `ChargedTracks`. The outcome of these changes is that for the  $J/\psi \rightarrow \mu^+ \mu^-$  mode, the initial  $J/\psi$  candidates are formed by one muon candidate that passes the *veryLoose* muon selector (as defined in Table 4.2) and one muon candidate that is simply a charged track. Also, the intermediate mass window for both the  $J/\psi \rightarrow e^+ e^-$  and  $J/\psi \rightarrow \mu^+ \mu^-$  channels is  $2.3 \text{ GeV}/c^2$  to  $3.5 \text{ GeV}/c^2$ . However, the final  $J/\psi$  candidates are exactly as described in Section 4.4.1.

Here, it is worth commenting on the impact of the declining RPC efficiency mentioned in Section 3.2.5 on the reconstruction of  $J/\psi \rightarrow \mu^+ \mu^-$  over the course of the collection of the data used in the  $CP$  asymmetry measurement. For the  $B^0 \rightarrow J/\psi \pi^0$  mode, the impact is softened by the fact that there are so many RPC layers in the IFR, and by the fact that one of the two muon candidates is allowed to pass a *loose* selection. For data collected near the beginning of run1, the ratio of  $B^0 \rightarrow J/\psi \pi^0$  candidate events attributed to the  $J/\psi \rightarrow e^+ e^-$  and  $J/\psi \rightarrow \mu^+ \mu^-$  channels is approximately 1 : 1, while for data collected near the end of the Summer 2002 data sample the ratio is approximately 3 : 2.

---

<sup>1</sup>Lists of the version numbers of software packages can be found in the internal document for this measurement: *BABAR* Analysis Document #425.

The photon pre-selection is identical to that of the branching fraction measurement (described in Section 4.3.3). The final  $\pi^0$  selection differs slightly, in that it is the `Pi0ToGG_LooseMass` selector of `CompPi0Sequence` that makes combinations of two members of the `GoodPhotonLoose` list. This selector requires the mass of the resulting  $\pi^0$  candidate to be in the range from 0.100 GeV to 0.160 GeV. In calculating the mass, it takes the primary vertex (or the beam spot if the primary vertex is not available) to be the origin of the photons. It then constrains the  $\pi^0$  mass to the nominal PDG value.

The formation of the  $B$  meson candidate is the same as described in Section 4.4.3.

## 5.4 Event Selection Variables

After the final  $B$  candidate is formed, the event selection variables are calculated. Cuts are applied to these variables before information about the events is written to ntuples and ASCII files. These variables are also used in a maximum likelihood yield fit as a consistency check, and ultimately two of the following variables are used directly in the  $CP$  asymmetry fit. The definitions of the selection variables and the values of the cuts are given in the following sections.

### 5.4.1 $m_{\text{ES}}$

One of the event selection variables is  $m_{\text{ES}}$ , already defined in equation 4.1, and repeated here for reference:

$$m_{\text{ES}} = \sqrt{(E_{\text{beam}}^*)^2 - (p_B^*)^2} , \quad (5.1)$$

where  $E_{\text{beam}}^*$  and  $p_B^*$  are the beam energy and  $B$ -candidate momentum in the  $e^+e^-$  CM frame. Events are required to have  $m_{\text{ES}}$  between  $5.2 \text{ GeV}/c^2$  and  $5.3 \text{ GeV}/c^2$  for further consideration.

### 5.4.2 $\Delta E$

The variable  $\Delta E$ , as defined in equation 4.2 is also used. It repeated here for reference:

$$\Delta E = E_B^* - E_{beam}^* , \quad (5.2)$$

where  $E_B^*$  is the  $B$ -candidate energy in the  $e^+e^-$  CM frame. There is a requirement that events have  $\Delta E$  between  $-0.4$  GeV and  $0.4$  GeV.

### 5.4.3 Fisher Discriminant

Event shape variables contain valuable information for discriminating between signal and continuum background. Due to its ability to cope with correlations among input variables, a Fisher discriminant [47] is a powerful tool for combining the event shape information into a single variable. The Fisher is a linear combination of the input variables, where the coefficients multiplying each variable are optimized on the two samples for which the separation is desired.

This section includes a method for determining the coefficients of a Fisher. It then details the variables considered for inclusion in the Fisher used in this measurement, with a comparison of some of the possibilities. Finally, it shows the chosen variables and the resulting Fisher discriminant.

#### Method for Determining the Fisher Coefficients

Let  $\alpha$  and  $\beta$  be indices that represent the  $n$  different input variables. The first step is to get the average value of each variable  $v$  and the average value of the product of each pair of variables over the samples, both for signal and background (S and B):

$$\begin{aligned} \langle v_\alpha \rangle^{S,B} &= \sum_{i=1}^N \frac{v_{\alpha_i}^{S,B}}{N_{S,B}} , \\ \langle v_\alpha v_\beta \rangle^{S,B} &= \sum_{i=1}^N \frac{v_{\alpha_i}^{S,B} v_{\beta_i}^{S,B}}{N_{S,B}} , \end{aligned} \quad (5.3)$$

where  $N_{S,B}$  is the number of events in the signal or background sample. Now define the coefficients:

$$\begin{aligned} a_\alpha &= \frac{2}{\langle v_\alpha \rangle^S - \langle v_\alpha \rangle^B} , \\ b_\alpha &= -\frac{\langle v_\alpha \rangle^S + \langle v_\alpha \rangle^B}{\langle v_\alpha \rangle^S - \langle v_\alpha \rangle^B} . \end{aligned} \quad (5.4)$$

Use the results of equations 5.3 and 5.4 to calculate the matrix elements:

$$V_{\alpha\beta} = \langle u_\alpha u_\beta \rangle^S + \langle u_\alpha u_\beta \rangle^B , \quad (5.5)$$

where

$$\langle u_\alpha u_\beta \rangle^{S,B} = a_\alpha a_\beta \langle v_\alpha v_\beta \rangle^{S,B} + a_\alpha \langle v_\alpha \rangle^{S,B} b_\beta + a_\beta \langle v_\beta \rangle^{S,B} b_\alpha + b_\alpha b_\beta .$$

This matrix is inverted to find  $V_{\alpha\beta}^{\text{inv}}$ , and this is used to calculate the coefficients  $c_\alpha$ :

$$c_\alpha = \frac{\sum_{\beta=1}^n V_{\alpha\beta}^{\text{inv}}}{\sum_{\alpha=1}^n \sum_{\beta=1}^n V_{\alpha\beta}^{\text{inv}}} . \quad (5.6)$$

The three coefficients  $a_\alpha$ ,  $b_\alpha$ , and,  $c_\alpha$  are thus optimized to separate the signal and background, and the final value for the Fisher discriminant,  $\mathcal{F}_i$ , for a particular event  $i$  is

$$\mathcal{F}_i = \sum_{\alpha=1}^n c_\alpha (a_\alpha v_{\alpha_i} + b_\alpha) . \quad (5.7)$$

### Variables Considered for Use in a Fisher

This section defines and discusses a number of variables that are considered for use in a Fisher discriminant. The main issues include the separation power provided by each variable and the degree to which it is correlated with the other variables. The former is studied by comparing the distributions in signal and background samples and by observing the impact of the variable on a computed Fisher. The latter is studied by calculating a table of correlation coefficients and has bearing on whether

it is preferable to include the variable in the Fisher (the case for correlated variables) or directly in the likelihood fit (the case for uncorrelated variables). Table 5.2 shows the correlation coefficients for all of the variables considered for use in a Fisher, both among themselves, and with  $m_{ES}$  and  $\Delta E$ .

**R2** The ratio of the second-order to zeroth-order Fox-Wolfram moments [40], R2, is calculated using charged tracks (`ChargedTracksAcc` list) and neutral candidates (`GoodNeutralLooseAcc` list), which pass a set of fiducial requirements, but excludes those that are used to reconstruct the signal candidate. The separation between Monte Carlo samples of signal and background can be seen in Figure 5.1. This variable was selected for inclusion in the Fisher.

**$|\cos \theta_T|$**  This variable is defined, and its distributions for signal and continuum background are explained, in Section 4.5.2. The distributions can also be seen in Figure 5.1. The  $|\cos \theta_T|$  was selected for inclusion in the Fisher.

**$|\cos \theta_\ell|$**  The cosine of the lepton helicity angle is defined, and its distributions for signal and continuum background are explained, in Section 4.5.3. The distributions can also be seen in Figure 5.1. This variable provides excellent separation and is included in the Fisher.

**$\cos(J/\psi \text{ Direction})$**  The  $J/\psi$  direction is defined as the angle between the  $J/\psi$  momentum vector in the  $B$  rest frame and the  $B$  momentum vector in the  $\Upsilon(4S)$  rest frame. It can be seen in Figure 5.1 that this variable provides little discrimination between signal and continuum background. It was tested in a Fisher, in various combinations with other input variables, and found to contain no additional significant separation, and has been omitted.

**$\cos(B \text{ Direction})$**  The  $B$  direction is defined as the angle between the  $B$  momentum vector in the  $\Upsilon(4S)$  frame and the  $\Upsilon(4S)$  momentum vector in the lab frame. The plot in Figure 5.1 shows the  $\sin^2 \theta$  distribution for signal and a relatively flat distribution for the continuum background, however this variable provides no significant

additional separation when used in combination with other variables in a Fisher, and is therefore omitted.

**Nine Momentum Flow Cones** This variable is a measure of the momentum flow of the event, divided into nine cones around the thrust axis of the signal candidates. This method uses the magnitude of the momentum of each track (`ChargedTracksAcc`) and neutral object (`GoodNeutralLooseAcc`), excluding any candidates that belong to the reconstructed signal candidate. These momenta are divided into nine cones with opening angles from 0 to  $\pi/2$ , where any momentum vector greater than  $\pi/2$  from the signal thrust axis is folded into the set of nine cones by the transformation  $\pi - \theta$ . The plots of the momentum flow cones are shown for signal and continuum background in Figure 5.2.

**Legendre Polynomial Momentum Flow** Another way to parameterize the momentum flow is to multiply the magnitude of the momenta by Legendre polynomials. The procedure is similar to the 9 cone case: the magnitude of the CM momentum,  $|\mathbf{p}_i^*|$ , for each track (`ChargedTracksAcc`) and neutral (`GoodNeutralLooseAcc`), again excluding the candidates that belong to the reconstructed signal, is multiplied by the Legendre polynomial, where  $\theta_i$  is the angle between  $\mathbf{p}_i^*$  and the thrust axis of the signal candidates. Polynomials thus have the form:

$$\begin{aligned}
 L0 &= \sum_i |\mathbf{p}_i^*| , \\
 L1 &= \sum_i |\mathbf{p}_i^*| \cos \theta_i , \\
 L2 &= \sum_i |\mathbf{p}_i^*| \frac{3 \cos^2 \theta_i - 1}{2} , \\
 L3 &= \sum_i |\mathbf{p}_i^*| \frac{5 \cos^3 \theta_i - 3 \cos \theta_i}{2} .
 \end{aligned} \tag{5.8}$$

The plots for these four Legendre polynomials are shown for signal and continuum background in Figure 5.3. The next section gives a more detailed comparison of the two momentum flow techniques, with the goal of picking between the two.

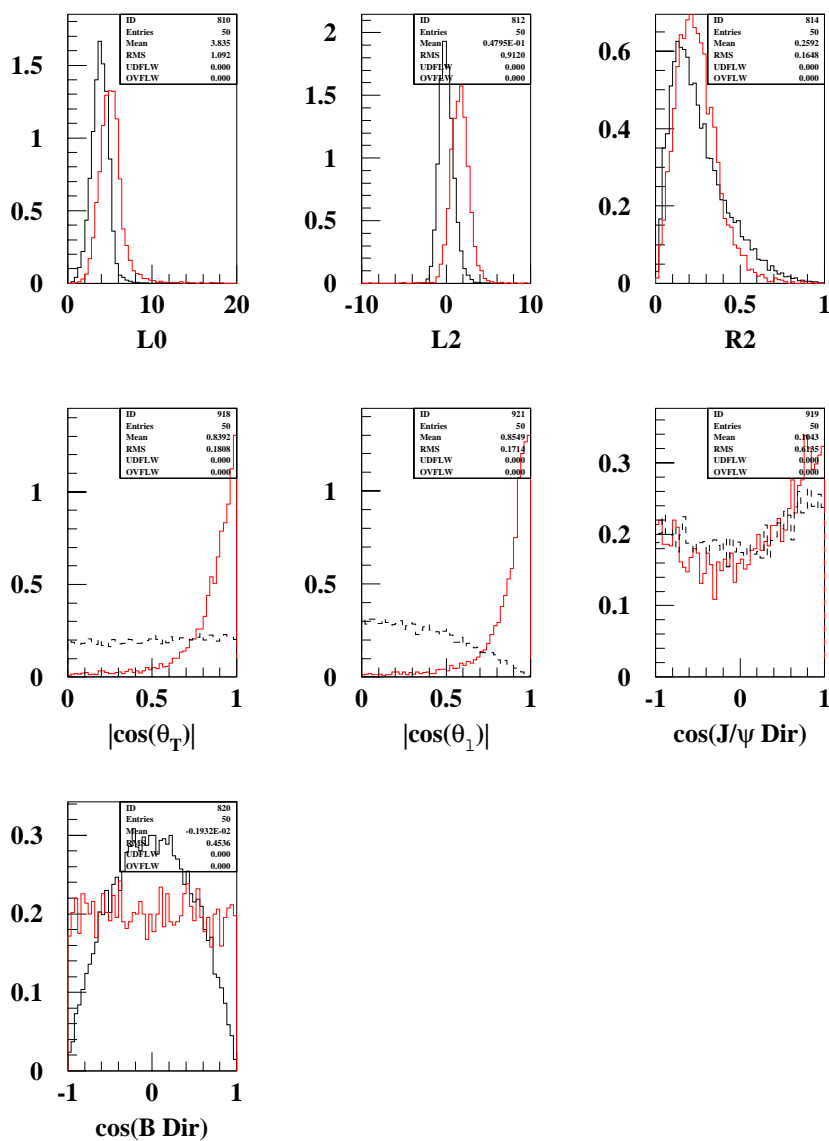


Figure 5.1: Event shape variables considered for inclusion in a Fisher discriminant. In each plot, the black histogram shows the distribution for roughly 11,300 signal Monte Carlo events and the red histogram shows the distributions for roughly 4,300 events of *offpeak* data that have been selected to model the continuum background. The histograms are normalized to equal areas.

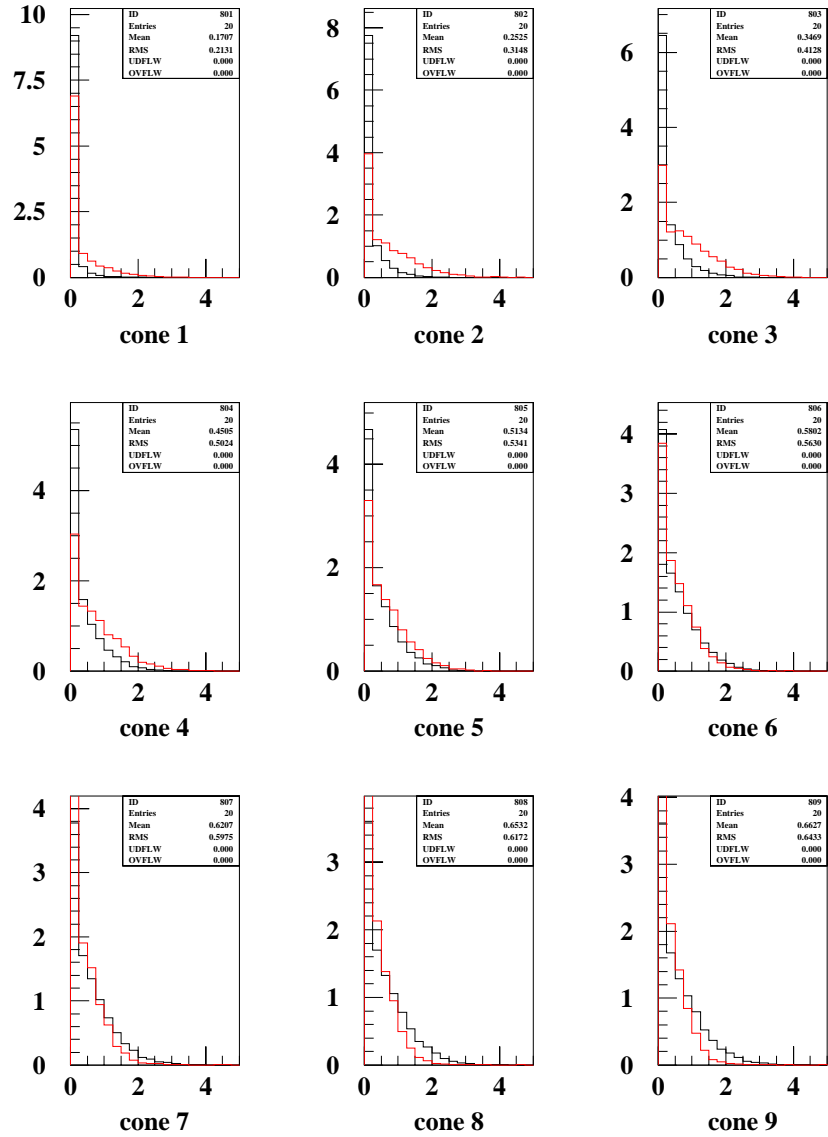


Figure 5.2: The nine momentum flow cones are shown for about 11,300 signal Monte Carlo events (black histograms) and about 4,300 events of *offpeak* data (red histograms) with a selection that models the continuum background. The histograms are normalized to equal areas.

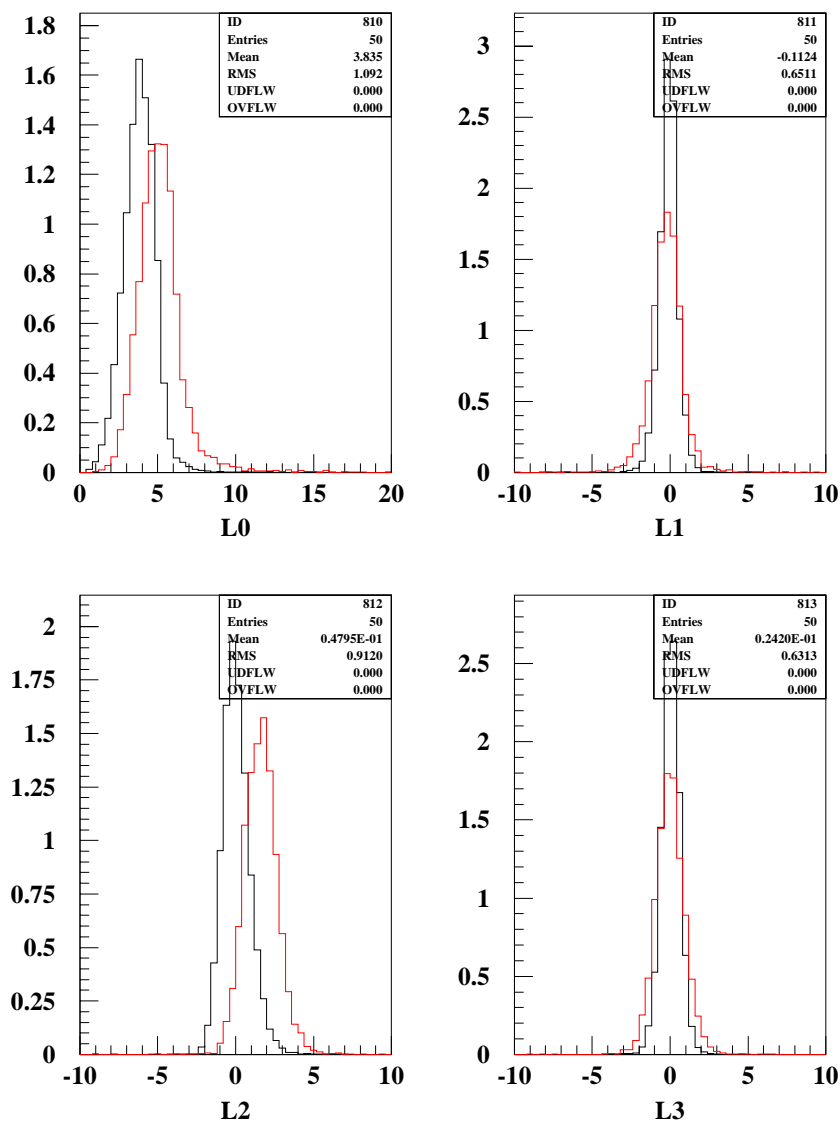


Figure 5.3: The first four moments of the Legendre polynomial composition of the momentum flow are shown for roughly 11,300 signal Monte Carlo events (black histograms) and for roughly 4,300 events of *offpeak* data (red histograms) with a selection that models the continuum background. The histograms are normalized to equal areas.

Table 5.2: Correlations among the variables considered for use in a Fisher. Those event shape variables that are correlated ( $\gtrsim 15\%$ ) with one another are not suited for direct use in likelihood fits. The variables  $m_{\text{ES}}$  and  $\Delta E$  are just given for reference, since they are not considered for the Fisher.

$B^0 \rightarrow J/\psi \pi^0$	$R2$	$ \cos \theta_T $	$ \cos \theta_L $	$\cos(J/\psi \text{ Dir})$	$\cos(B \text{ Dir})$	$L0$	Cone 0
$m_{\text{ES}}$	$-0.0111 \pm 0.0093$	$-0.0007 \pm 0.0093$	$-0.0025 \pm 0.0093$	$-0.1358 \pm 0.0091$	$0.0194 \pm 0.0093$	$-0.0133 \pm 0.0093$	$-0.0162 \pm 0.0093$
$\Delta E$	$0.0165 \pm 0.0093$	$0.0040 \pm 0.0093$	$0.0062 \pm 0.0093$	$-0.2305 \pm 0.0088$	$0.0362 \pm 0.0092$	$-0.0152 \pm 0.0093$	$0.0122 \pm 0.0093$
$R2$	$1.0000 \pm 0.0000$	$-0.0177 \pm 0.0093$	$-0.0158 \pm 0.0093$	$-0.0154 \pm 0.0093$	$-0.0135 \pm 0.0093$	$-0.0653 \pm 0.0092$	$-0.0103 \pm 0.0093$
$ \cos \theta_T $	$-0.0177 \pm 0.0093$	$1.0000 \pm 0.0000$	$-0.0009 \pm 0.0093$	$-0.0020 \pm 0.0093$	$-0.0050 \pm 0.0093$	$0.0290 \pm 0.0092$	$0.2311 \pm 0.0088$
$ \cos \theta_L $	$-0.0158 \pm 0.0093$	$-0.0009 \pm 0.0093$	$1.0000 \pm 0.0000$	$-0.0115 \pm 0.0093$	$0.0110 \pm 0.0093$	$0.0122 \pm 0.0093$	$0.0093 \pm 0.0093$
$\cos(J/\psi \text{ Dir})$	$-0.0154 \pm 0.0093$	$-0.0020 \pm 0.0093$	$-0.0115 \pm 0.0093$	$1.0000 \pm 0.0000$	$-0.0002 \pm 0.0093$	$0.0128 \pm 0.0093$	$-0.0193 \pm 0.0093$
$\cos(B \text{ Dir})$	$-0.0135 \pm 0.0093$	$-0.0050 \pm 0.0093$	$0.0110 \pm 0.0093$	$-0.0002 \pm 0.0093$	$1.0000 \pm 0.0000$	$0.0139 \pm 0.0093$	$-0.0082 \pm 0.0093$
$L0$	$-0.0653 \pm 0.0092$	$0.0290 \pm 0.0092$	$0.0122 \pm 0.0093$	$0.0128 \pm 0.0093$	$0.0139 \pm 0.0093$	$1.0000 \pm 0.0000$	$0.1306 \pm 0.0091$
Cone 0	$-0.0103 \pm 0.0093$	$0.2311 \pm 0.0088$	$0.0093 \pm 0.0093$	$-0.0193 \pm 0.0093$	$-0.0082 \pm 0.0093$	$0.1306 \pm 0.0000$	$1.0000 \pm 0.0000$
$B^0 \rightarrow J/\psi K_S^0(\pi^0 \pi^0)$							
$m_{\text{ES}}$	$-0.0013 \pm 0.0119$	$-0.0007 \pm 0.0119$	$-0.0196 \pm 0.0118$	$-0.4721 \pm 0.0092$	$0.0012 \pm 0.0119$	$-0.0213 \pm 0.0118$	$-0.0044 \pm 0.0119$
$\Delta E$	$0.0460 \pm 0.0118$	$-0.0020 \pm 0.0119$	$-0.0093 \pm 0.0119$	$-0.3845 \pm 0.0101$	$0.0034 \pm 0.0119$	$-0.0602 \pm 0.0118$	$-0.0063 \pm 0.0119$
$R2$	$1.0000 \pm 0.0000$	$-0.0312 \pm 0.0118$	$-0.0174 \pm 0.0118$	$-0.0215 \pm 0.0118$	$-0.0156 \pm 0.0118$	$-0.0178 \pm 0.0118$	$-0.0253 \pm 0.0118$
$ \cos \theta_T $	$-0.0312 \pm 0.0118$	$1.0000 \pm 0.0000$	$0.0239 \pm 0.0118$	$-0.0069 \pm 0.0119$	$0.0111 \pm 0.0119$	$0.0110 \pm 0.0119$	$0.2394 \pm 0.0112$
$ \cos \theta_L $	$-0.0174 \pm 0.0118$	$0.0239 \pm 0.0118$	$1.0000 \pm 0.0000$	$0.0165 \pm 0.0118$	$-0.0061 \pm 0.0119$	$0.0056 \pm 0.0119$	$0.0035 \pm 0.0119$
$\cos(J/\psi \text{ Dir})$	$-0.0215 \pm 0.0118$	$-0.0069 \pm 0.0119$	$0.0165 \pm 0.0118$	$1.0000 \pm 0.0000$	$-0.0153 \pm 0.0118$	$0.0274 \pm 0.0118$	$0.0074 \pm 0.0119$
$\cos(B \text{ Dir})$	$-0.0156 \pm 0.0118$	$0.0111 \pm 0.0119$	$-0.0061 \pm 0.0119$	$-0.0153 \pm 0.0118$	$1.0000 \pm 0.0000$	$0.0138 \pm 0.0118$	$0.0117 \pm 0.0119$
$L0$	$-0.0178 \pm 0.0118$	$0.0110 \pm 0.0119$	$0.0056 \pm 0.0119$	$0.0274 \pm 0.0118$	$0.0138 \pm 0.0118$	$1.0000 \pm 0.0000$	$0.1172 \pm 0.0117$
Cone 0	$-0.0253 \pm 0.0118$	$0.2394 \pm 0.0112$	$0.0035 \pm 0.0119$	$0.0074 \pm 0.0119$	$0.0117 \pm 0.0119$	$0.1172 \pm 0.0117$	$1.0000 \pm 0.0000$
Inclusive $J/\psi$							
$m_{\text{ES}}$	$0.0021 \pm 0.0310$	$-0.1355 \pm 0.0304$	$-0.0748 \pm 0.0308$	$0.2008 \pm 0.0298$	$0.0567 \pm 0.0309$	$-0.0766 \pm 0.0308$	$-0.0227 \pm 0.0310$
$\Delta E$	$0.1498 \pm 0.0303$	$0.1074 \pm 0.0307$	$0.0360 \pm 0.0310$	$-0.4622 \pm 0.0244$	$-0.0480 \pm 0.0309$	$-0.0184 \pm 0.0310$	$-0.0342 \pm 0.0310$
$R2$	$1.0000 \pm 0.0000$	$0.0762 \pm 0.0308$	$-0.0570 \pm 0.0309$	$-0.0845 \pm 0.0308$	$0.0277 \pm 0.0310$	$-0.0081 \pm 0.0310$	$-0.0529 \pm 0.0309$
$ \cos \theta_T $	$0.0762 \pm 0.0308$	$1.0000 \pm 0.0000$	$0.3101 \pm 0.0280$	$-0.0910 \pm 0.0308$	$0.0196 \pm 0.0310$	$0.0765 \pm 0.0308$	$0.2008 \pm 0.0298$
$ \cos \theta_L $	$-0.0570 \pm 0.0309$	$0.3101 \pm 0.0280$	$1.0000 \pm 0.0000$	$-0.0405 \pm 0.0310$	$-0.0091 \pm 0.0310$	$0.0397 \pm 0.0310$	$0.0694 \pm 0.0309$
$\cos(J/\psi \text{ Dir})$	$-0.0845 \pm 0.0308$	$-0.0910 \pm 0.0308$	$-0.0405 \pm 0.0310$	$1.0000 \pm 0.0000$	$0.0235 \pm 0.0310$	$-0.0153 \pm 0.0310$	$0.0115 \pm 0.0310$
$\cos(B \text{ Dir})$	$0.0277 \pm 0.0310$	$0.0196 \pm 0.0310$	$-0.0091 \pm 0.0310$	$0.0235 \pm 0.0310$	$1.0000 \pm 0.0000$	$0.0276 \pm 0.0310$	$0.0220 \pm 0.0310$
$L0$	$-0.0081 \pm 0.0310$	$0.0765 \pm 0.0308$	$0.0397 \pm 0.0310$	$-0.0153 \pm 0.0310$	$0.0276 \pm 0.0310$	$1.0000 \pm 0.0000$	$0.0912 \pm 0.0308$
Cone 0	$-0.0529 \pm 0.0309$	$0.2008 \pm 0.0298$	$0.0694 \pm 0.0309$	$0.0115 \pm 0.0310$	$0.0220 \pm 0.0310$	$0.0912 \pm 0.0308$	$1.0000 \pm 0.0000$
$BB$ generic							
$m_{\text{ES}}$	$0.0408 \pm 0.0320$	$-0.0162 \pm 0.0321$	$0.0824 \pm 0.0319$	$-0.1071 \pm 0.0317$	$-0.0213 \pm 0.0321$	$0.0154 \pm 0.0321$	$-0.0756 \pm 0.0319$
$\Delta E$	$0.0725 \pm 0.0319$	$-0.0868 \pm 0.0318$	$0.0177 \pm 0.0321$	$-0.1733 \pm 0.0311$	$-0.0426 \pm 0.0320$	$-0.0974 \pm 0.0318$	$-0.0323 \pm 0.0321$
$R2$	$1.0000 \pm 0.0000$	$-0.0204 \pm 0.0321$	$-0.0446 \pm 0.0320$	$-0.0107 \pm 0.0321$	$0.0376 \pm 0.0320$	$-0.1382 \pm 0.0315$	$-0.0107 \pm 0.0321$
$ \cos \theta_T $	$-0.0204 \pm 0.0321$	$1.0000 \pm 0.0000$	$-0.0481 \pm 0.0320$	$0.0259 \pm 0.0321$	$0.0078 \pm 0.0321$	$0.1728 \pm 0.0311$	$0.1984 \pm 0.0308$
$ \cos \theta_L $	$-0.0446 \pm 0.0320$	$-0.0481 \pm 0.0320$	$1.0000 \pm 0.0000$	$-0.4800 \pm 0.0247$	$-0.0089 \pm 0.0321$	$0.1343 \pm 0.0315$	$0.0381 \pm 0.0320$
$\cos(J/\psi \text{ Dir})$	$-0.0107 \pm 0.0321$	$0.0259 \pm 0.0321$	$-0.4800 \pm 0.0247$	$1.0000 \pm 0.0000$	$0.0132 \pm 0.0321$	$-0.0221 \pm 0.0321$	$0.0474 \pm 0.0320$
$\cos(B \text{ Dir})$	$0.0376 \pm 0.0320$	$0.0078 \pm 0.0321$	$-0.0089 \pm 0.0321$	$0.0132 \pm 0.0321$	$1.0000 \pm 0.0000$	$0.0896 \pm 0.0318$	$-0.0346 \pm 0.0321$
$L0$	$-0.1382 \pm 0.0315$	$0.1728 \pm 0.0311$	$0.1343 \pm 0.0315$	$-0.0221 \pm 0.0321$	$0.0896 \pm 0.0318$	$1.0000 \pm 0.0000$	$0.1561 \pm 0.0313$
Cone 0	$-0.0107 \pm 0.0321$	$0.1984 \pm 0.0308$	$0.0381 \pm 0.0320$	$0.0474 \pm 0.0320$	$-0.0346 \pm 0.0321$	$0.1561 \pm 0.0313$	$1.0000 \pm 0.0000$
Continuum							
$m_{\text{ES}}$	$-0.0137 \pm 0.0142$	$-0.0016 \pm 0.0142$	$0.0037 \pm 0.0142$	$-0.0224 \pm 0.0142$	$0.0005 \pm 0.0142$	$-0.0124 \pm 0.0142$	$-0.0039 \pm 0.0142$
$\Delta E$	$-0.0524 \pm 0.0142$	$-0.0754 \pm 0.0141$	$0.0125 \pm 0.0142$	$0.0407 \pm 0.0142$	$-0.0062 \pm 0.0142$	$-0.1045 \pm 0.0140$	$-0.0544 \pm 0.0142$
$R2$	$1.0000 \pm 0.0000$	$0.1545 \pm 0.0139$	$-0.2501 \pm 0.0133$	$0.0178 \pm 0.0142$	$-0.0048 \pm 0.0142$	$0.1896 \pm 0.0137$	$0.0954 \pm 0.0141$
$ \cos \theta_T $	$-0.1545 \pm 0.0139$	$1.0000 \pm 0.0000$	$0.0800 \pm 0.0141$	$0.0187 \pm 0.0142$	$0.0611 \pm 0.0141$	$0.1131 \pm 0.0140$	$0.2107 \pm 0.0136$
$ \cos \theta_L $	$-0.2501 \pm 0.0133$	$-0.0800 \pm 0.0141$	$1.0000 \pm 0.0000$	$0.0465 \pm 0.0142$	$-0.0089 \pm 0.0142$	$0.0487 \pm 0.0142$	$-0.0083 \pm 0.0142$
$\cos(J/\psi \text{ Dir})$	$0.0178 \pm 0.0142$	$0.0187 \pm 0.0142$	$0.0465 \pm 0.0142$	$1.0000 \pm 0.0000$	$0.0482 \pm 0.0142$	$0.0284 \pm 0.0142$	$-0.0133 \pm 0.0142$
$\cos(B \text{ Dir})$	$-0.0048 \pm 0.0142$	$-0.0089 \pm 0.0142$	$-0.0089 \pm 0.0142$	$0.0482 \pm 0.0142$	$1.0000 \pm 0.0000$	$0.0036 \pm 0.0142$	$-0.0386 \pm 0.0142$
$L0$	$-0.1896 \pm 0.0137$	$0.1131 \pm 0.0140$	$0.0487 \pm 0.0142$	$0.0284 \pm 0.0142$	$0.0036 \pm 0.0142$	$1.0000 \pm 0.0000$	$0.2386 \pm 0.0134$
Cone 0	$0.0954 \pm 0.0141$	$0.2107 \pm 0.0136$	$-0.0083 \pm 0.0142$	$-0.0133 \pm 0.0142$	$0.0198 \pm 0.0142$	$0.2386 \pm 0.0134$	$1.0000 \pm 0.0000$

### Comparison of Energy Cones and Legendre Polynomials

The nine energy cone and Legendre polynomial techniques are quite similar in implementation and informational content. One advantage of the Legendre method is simply that it uses fewer variables, however since there is a good deal more experience with the cones formulation (e.g. CLEO analyses and earlier *BABAR* analyses), it is worth making a comparison of the performance of a Fisher constructed from each.

For this test, one Fisher ( $\mathcal{F}_{\text{Cones}}$ ) is constructed using the nine cones,  $R2$ , and  $|\cos \theta_T|$ . A second Fisher ( $\mathcal{F}_{\text{Lgndr}}$ ) is constructed using four Legendre polynomials,  $R2$ , and  $|\cos \theta_T|$ . The optimization procedure is performed separately for the two Fishers and the final output for signal and background is shown in Figure 5.4 for  $\mathcal{F}_{\text{Cones}}$  and Figure 5.5 for  $\mathcal{F}_{\text{Lgndr}}$ . Each output Fisher shape is fit with a triple Gaussian and an overlap function is calculated:

$$\mathcal{O} \equiv \frac{1}{N_{bins}} \sum_{i=1}^{N_{bins}} \frac{2S_i B_i}{S_i^2 + B_i^2}, \quad (5.9)$$

where  $S_i$  and  $B_i$  are the values of the fit functions at each bin for signal and background respectively. This expression is smaller for better separation of signal and background, and in this case  $\mathcal{O}(\mathcal{F}_{\text{Cones}}) = 0.29$ , while  $\mathcal{O}(\mathcal{F}_{\text{Lgndr}}) = 0.19$ . The Legendre parameterization is thus chosen for use in the final Fisher discriminant because of the separation performance, as well as the simplicity of having fewer variables. Furthermore, it has been found that this separation is almost entirely provided by the two variables  $L0$  and  $L2$ , which are both included in the final Fisher discriminant.

### Final Fisher

The final variables used for the construction of a Fisher are  $L0$ ,  $L2$ ,  $R2$ ,  $|\cos \theta_T|$ , and  $|\cos \theta_\ell|$ . The distributions for these variables are shown for signal and continuum background in Figure 5.6. The values of the optimized coefficients, as defined in equation 5.7, are given in Table 5.3. The Fisher outputs are shown, with triple Gaussian fits, in Figure 5.7, and the overlap of the two distributions is shown in Figure 5.8.

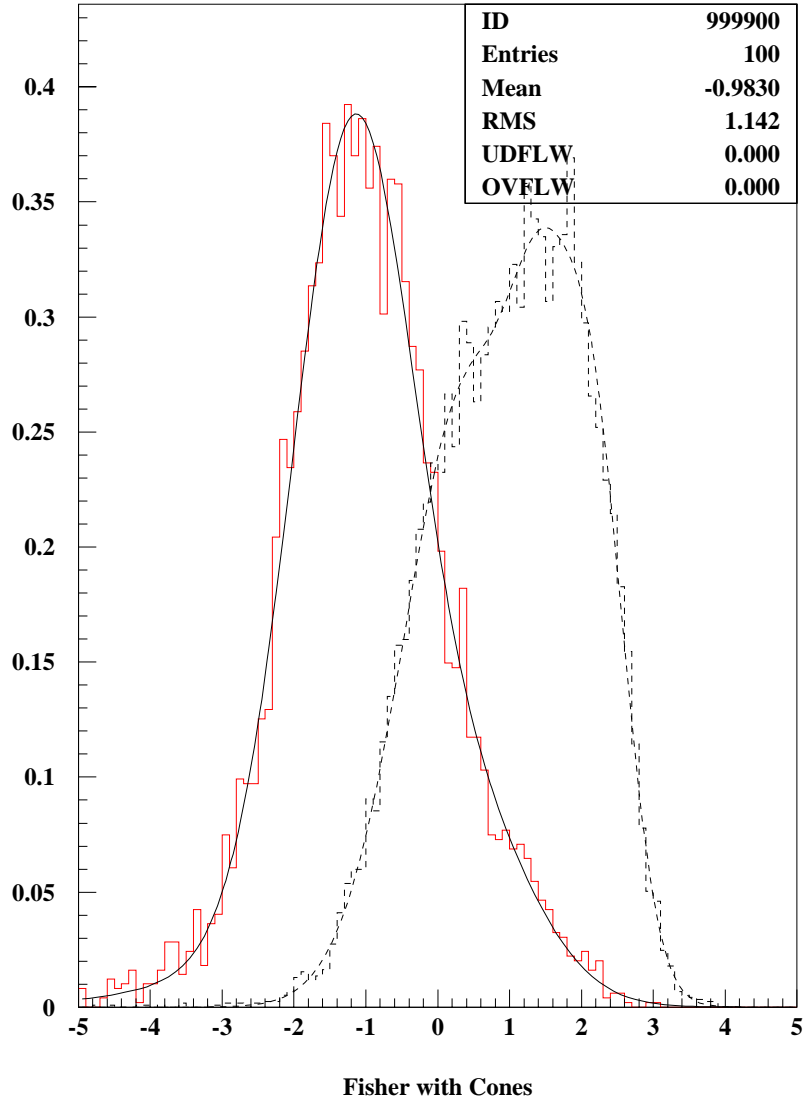


Figure 5.4: The Fisher  $\mathcal{F}_{\text{Cones}}$ , which includes the nine momentum flow cones, R2, and  $|\cos\theta_T|$ , is shown for signal Monte Carlo events (black histogram with dashed triple Gaussian fit) and *offpeak* data to model continuum backgrounds (red histogram with a solid triple Gaussian fit). The  $\chi^2/\text{dof}$  for the signal fit is 68.7/67 and is 90.0/68 for the background. The overlap between the two fits is 0.29, calculated using equation 5.9.

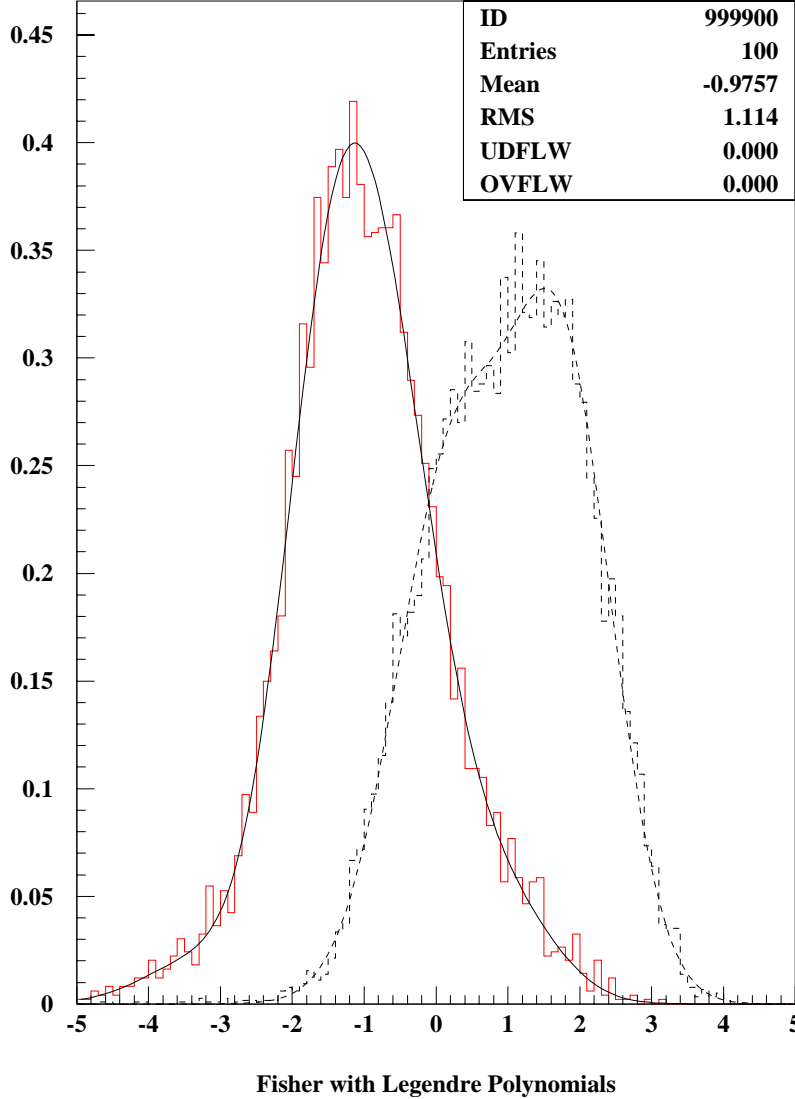


Figure 5.5: The Fisher  $\mathcal{F}_{\text{Lgndr}}$ , which includes the four Legendre polynomial momentum flow variables,  $R_2$ , and  $|\cos \theta_T|$ , is shown for signal Monte Carlo events (black histogram with dashed triple Gaussian fit) and *offpeak* data to model continuum backgrounds (red histogram with a solid triple Gaussian fit). The  $\chi^2/\text{dof}$  for the signal fit is 93.3/70 and is 113.4/71 for the background. The overlap between the two fits is 0.19, calculated using equation 5.9.

Table 5.3: Optimized coefficients for the final Fisher discriminant.

Input variable	$a$	$b$	$c$
$L0$	-1.5315	6.87566	0.0619607
$L2$	-1.27825	1.0601	0.233296
$R2$	146.884	-37.1505	0.00174747
$ \cos \theta_T $	-6.18844	4.19439	0.0649449
$ \cos \theta_\ell $	-4.1447	2.54398	0.638051

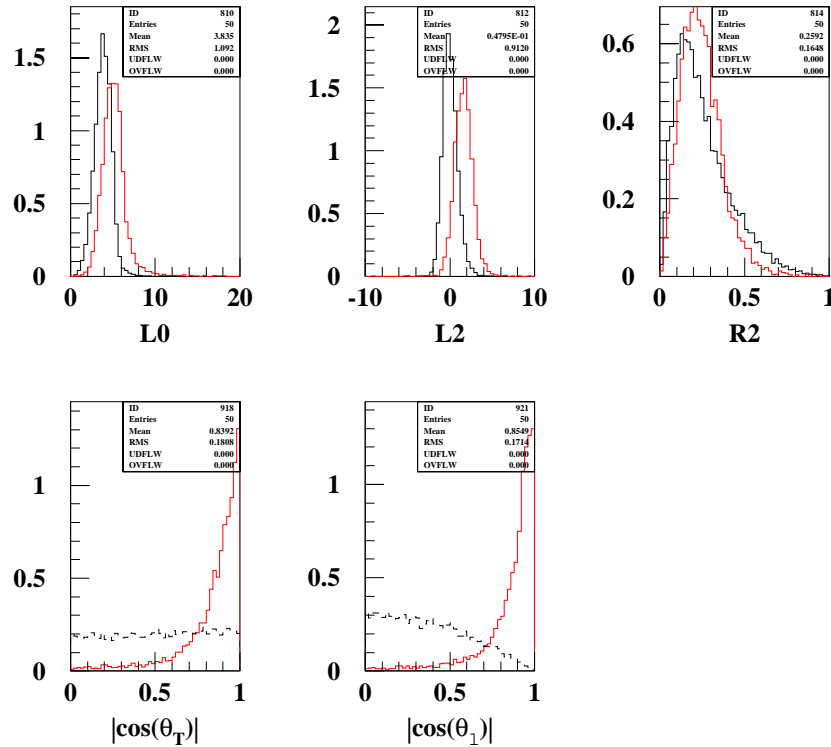


Figure 5.6: These are the event shape variables chosen for the final Fisher. The black histograms are for around 11,300 signal Monte Carlo events and the red histograms are for around 4,300 events of *offpeak* data that have been selected to model the continuum background. The histograms are normalized to equal areas.

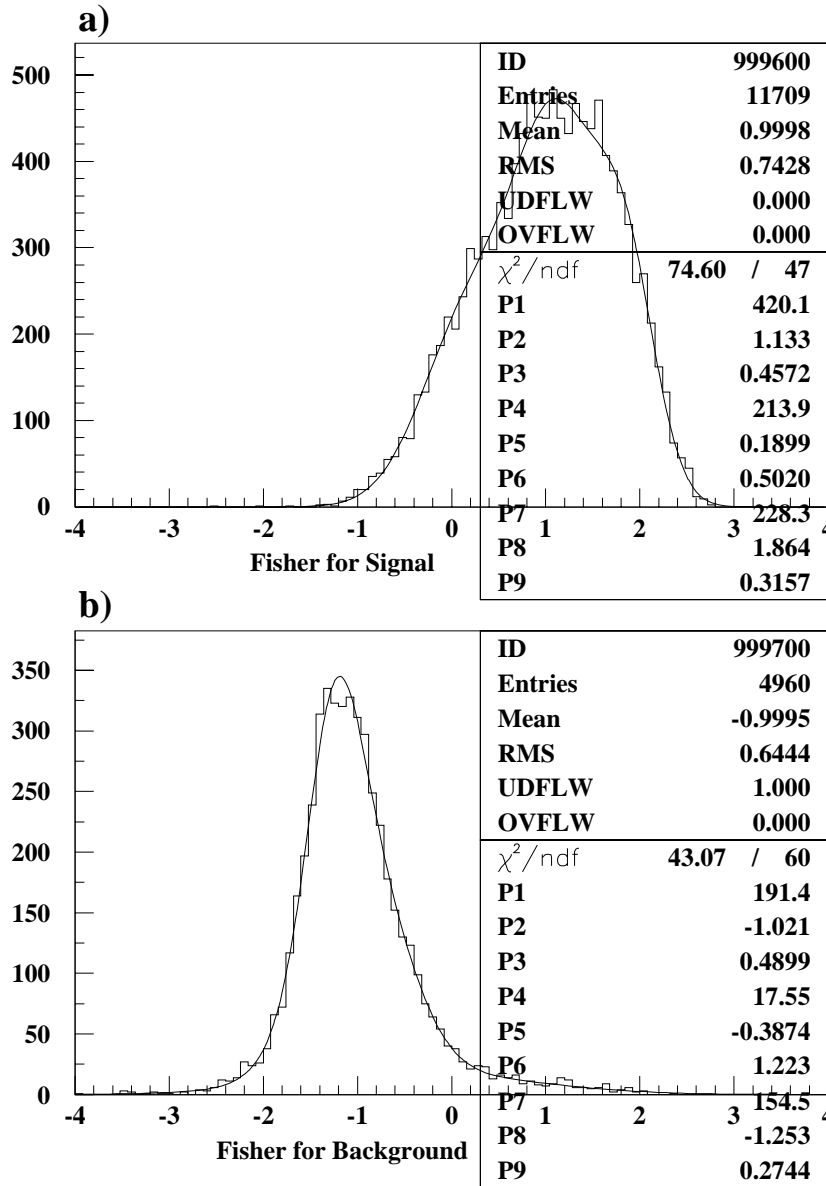


Figure 5.7: The output of the final Fisher discriminant, which includes  $L0$ ,  $L2$ ,  $R2$ ,  $|\cos \theta_T|$ , and  $|\cos \theta_\ell|$ , is shown for (a) signal Monte Carlo events, with a triple Gaussian fit, and for (b) *offpeak* data to model continuum backgrounds, with a triple Gaussian fit. The fit parameters are shown are superimposed.

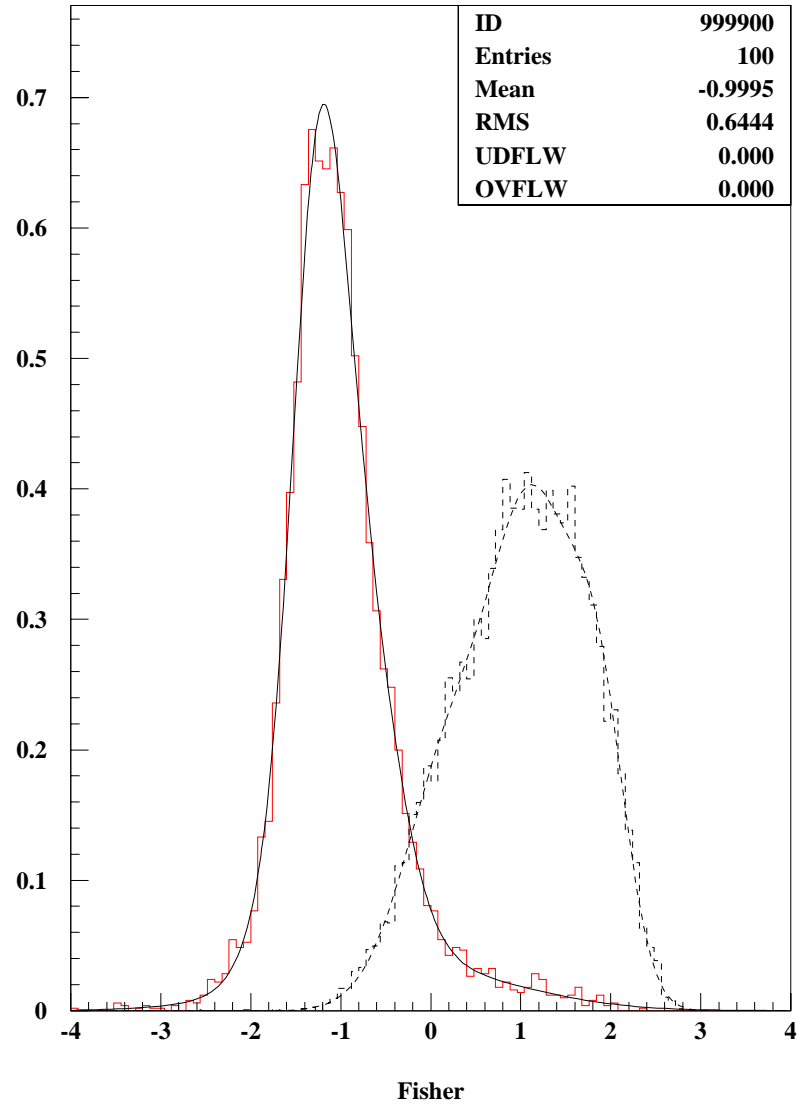


Figure 5.8: The Fisher output for signal and continuum background for the final choice of input variables (as in Figure 5.7) is shown on a single plot to visualize the overlap, which is calculated to be 0.16 from equation 5.9. The histograms are normalized to equal areas.

Table 5.4: Correlations among the event selection variables, for signal and for each background sample.

Variable	$m_{\text{ES}}$	$\Delta E$	Fisher $\mathcal{F}$
$B^0 \rightarrow J/\psi \pi^0$			
$m_{\text{ES}}$	$1.0000 \pm 0.0000$	$0.1990 \pm 0.0089$	$0.0072 \pm 0.0093$
$\Delta E$	–	$1.0000 \pm 0.0000$	$-0.0035 \pm 0.0093$
Fisher $\mathcal{F}$	–	–	$1.0000 \pm 0.0000$
$B^0 \rightarrow J/\psi K_s^0(\pi^0 \pi^0)$			
$m_{\text{ES}}$	$1.0000 \pm 0.0000$	$0.2160 \pm 0.0113$	$0.0243 \pm 0.0118$
$\Delta E$	–	$1.0000 \pm 0.0000$	$0.0148 \pm 0.0118$
Fisher $\mathcal{F}$	–	–	$1.0000 \pm 0.0000$
Inclusive $J/\psi$			
$m_{\text{ES}}$	$1.0000 \pm 0.0000$	$-0.2242 \pm 0.0294$	$0.1112 \pm 0.0306$
$\Delta E$	–	$1.0000 \pm 0.0000$	$-0.0622 \pm 0.0309$
Fisher $\mathcal{F}$	–	–	$1.0000 \pm 0.0000$
$B\bar{B}$ generic			
$m_{\text{ES}}$	$1.0000 \pm 0.0000$	$-0.1065 \pm 0.0317$	$-0.0630 \pm 0.0320$
$\Delta E$	–	$1.0000 \pm 0.0000$	$0.0425 \pm 0.0320$
Fisher $\mathcal{F}$	–	–	$1.0000 \pm 0.0000$
Continuum			
$m_{\text{ES}}$	$1.0000 \pm 0.0000$	$-0.0043 \pm 0.0142$	$0.0018 \pm 0.0142$
$\Delta E$	–	$1.0000 \pm 0.0000$	$0.0821 \pm 0.0141$
Fisher $\mathcal{F}$	–	–	$1.0000 \pm 0.0000$

#### 5.4.4 Correlations Among Analysis Variables

The complete set of event selection variables consists of  $m_{\text{ES}}$ ,  $\Delta E$ , and a Fisher discriminant,  $\mathcal{F}$ . It is necessary to understand the correlations between these variables, for the signal and each background, prior to determining the PDFs to use in a likelihood fit. For example, if there is a significant correlation between two of the analysis variables, a two-dimensional PDF may be used. The definition of the likelihood fit and PDFs will be given later in this chapter, as will be more details of the different background sources. The correlations, for each sample type are shown in Table 5.4.

The correlations are under 10% except for three cases that deserve special attention: correlations between  $\Delta E$  and  $m_{\text{ES}}$  for signal  $B^0 \rightarrow J/\psi \pi^0$ , and for the backgrounds from  $B^0 \rightarrow J/\psi K_s^0(\pi^0\pi^0)$  and inclusive  $J/\psi$ . The plots of  $\Delta E$  versus  $m_{\text{ES}}$  for each sample are shown in Figure 5.9. The correlation is particularly apparent for the  $B^0 \rightarrow J/\psi K_s^0(\pi^0\pi^0)$  sample, where the events populate a triangle below the signal region. A hint of such a triangular region can also be seen in the inclusive  $J/\psi$  sample. This is enough to warrant the use of two-dimensional PDFs for these two background sources.

The signal Monte Carlo sample is further studied by splitting the  $\Delta E$  distribution into a signal region of approximately  $3\sigma$  of a Gaussian fit (signal region =  $-0.112 < \Delta E < 0.112$  GeV) and sideband regions ( $|\Delta E| > 0.112$  GeV). The correlation coefficient is determined independently for each of these regions:

$$\begin{aligned} \rho &= -0.4012 \pm 0.0763 \text{ for the upper } \Delta E \text{ sideband,} \\ \rho &= -0.0834 \pm 0.0096 \text{ for the } \Delta E \text{ signal region,} \\ \rho &= 0.3860 \pm 0.0303 \text{ for the lower } \Delta E \text{ sideband.} \end{aligned}$$

Therefore the bulk of the correlation for the signal occurs in the tail, which contains approximately 8% of the events. There is a proportionally large fraction of events in the sideband region that fail to have a successful association with the Monte Carlo truth (200 out of 910 events in this region, as compared to 470 out of the roughly 11,300 events in the entire  $\Delta E$  versus  $m_{\text{ES}}$  plane). These events are also peaked toward zero in the energy ratio of the lower energy photon candidate to the higher energy photon candidate. We prefer to model the signal with one-dimensional PDFs, and we attribute a systematic uncertainty to this by substituting a two-dimensional PDF (Section 5.12.2).

## 5.5 Sources of Background and Strategy

As implied by the discussions in this chapter thus far, the categorization of the backgrounds is similar to that of the branching fraction measurement (Section 4.7). Again, we split the backgrounds into four mutually exclusive categories, two of which have

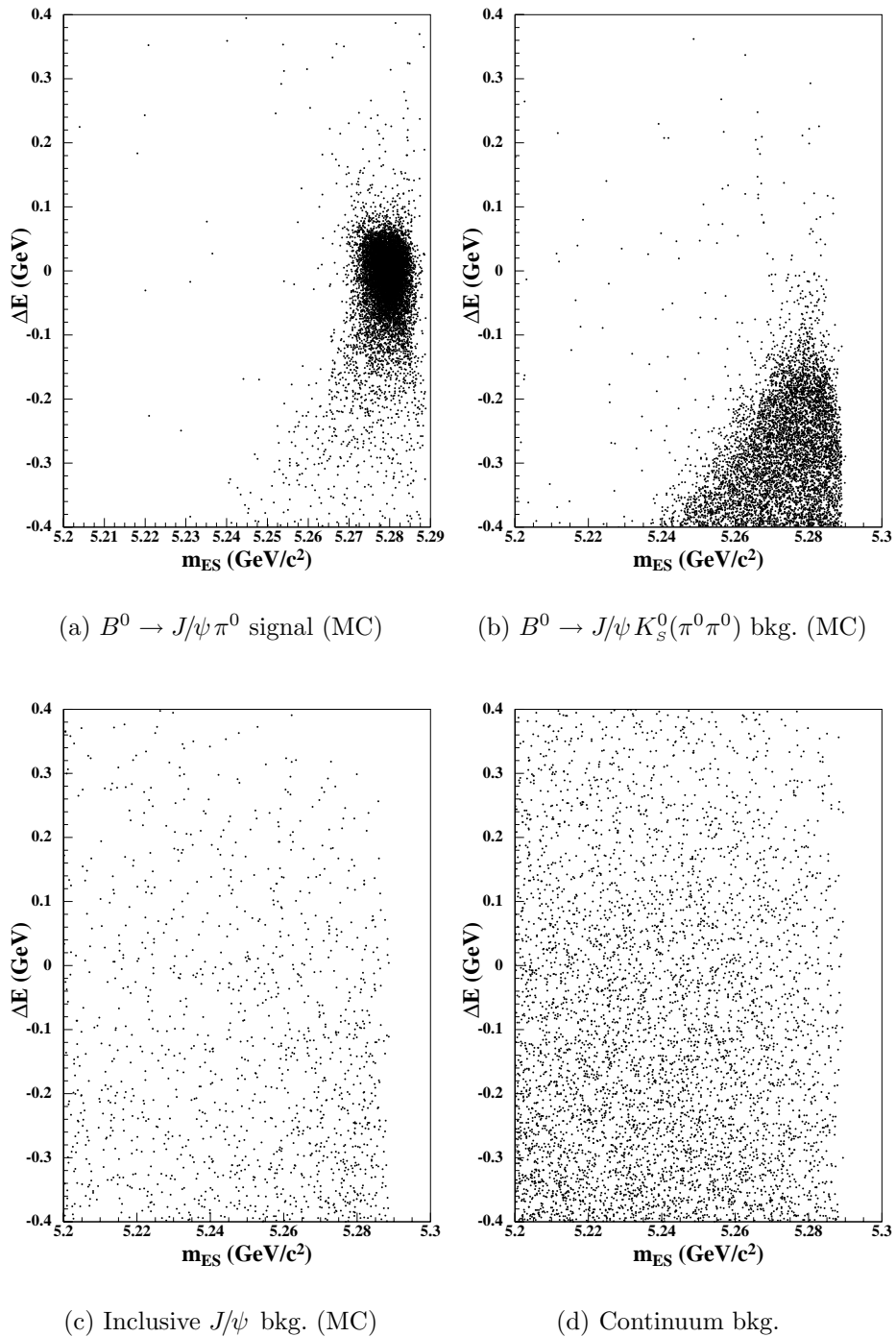


Figure 5.9: Plots of  $\Delta E$  versus  $m_{ES}$ , shown for signal Monte Carlo events and three of the background samples.

Table 5.5: Sizes and raw yields for signal and background samples.

Type	Source	Sample size	Yield (events)	Efficiency (%)
$B^0 \rightarrow J/\psi \pi^0$	SP4 MC	30000 events	11209	37.4
$B^0 \rightarrow J/\psi K_s^0(\pi^0\pi^0)$	SP4 MC	52000 events	6769	13.0
Inclusive $J/\psi$	SP4 MC	494000 events	1018	2.1
$B\bar{B}$ generic	Filtered SP4 MC	equiv. to $1.47 \times 10^9$ events	911	$6.2 \times 10^{-5}$
Continuum	<i>Offpeak</i> Data	$5.06 \text{ fb}^{-1}$	4290	–

a  $J/\psi$  from  $B$  decays ( $B \rightarrow J/\psi X$ ). This section discusses each in more detail, first dealing with the two that include a real  $J/\psi$  particle, and then dealing with the two where a  $J/\psi$  candidate is reconstructed purely through the combinatorics of lepton candidates (which are either true leptons or pairs where one are both candidates are mis-identified as leptons). In each case, the Monte Carlo truth information is used to determine the event topology.

### 5.5.1 $B^0 \rightarrow J/\psi K_s^0(\pi^0\pi^0)$

One of the  $B \rightarrow J/\psi X$  decays that requires special attention is  $B^0 \rightarrow J/\psi K_s^0$ , where the  $K_s^0$  decays into two  $\pi^0\pi^0$ . In this case, nearly all of the reconstructed  $J/\psi$  candidates are truly  $J/\psi$  particles. The  $\pi^0$  that is taken as the candidate in  $B^0 \rightarrow J/\psi \pi^0$  reconstruction is a true  $\pi^0$  (meaning that the candidate correctly represents a detected  $\pi^0$  meson) a bit more than 90% of the time. The remaining 10% are made up of true photons, but in incorrect combinations. So, this mode is a background when one of the  $\pi^0$  mesons from the  $K_s^0$  decay is taken in combination with the true  $J/\psi$  to give an incorrect signal  $B^0$  candidate, or when the photons from the  $\pi^0$  decays are reconstructed in an incorrect pairing, and combined with the  $J/\psi$ . The characteristic distributions of the event selection variables for this background are shown in detail in Section 5.6.2. This source is studied using 52,000 events of SP4 Monte Carlo simulation, giving 6,769 candidates passing the event selection, as described in Section 5.4. The raw event yield and efficiencies are summarized in Table 5.5.

### 5.5.2 Inclusive $J/\psi$

The more general class of decays that contain a real  $J/\psi$  particle also contributes as a background. This includes both prompt  $B \rightarrow J/\psi X$  and cascade style decays through other charmonium states. Again, “inclusive  $J/\psi$ ” refers to this source (or the Monte Carlo sample used to model it) but will implicitly exclude the specific  $B^0 \rightarrow J/\psi K_s^0(\pi^0\pi^0)$  mode discussed above. The studies of the inclusive  $J/\psi$  background are performed using 494,000 events of SP4 Monte Carlo simulation with a cut on  $p^* > 1.3 \text{ GeV}/c$ , giving a total of 1,018 final candidates to study. Events in this Monte Carlo sample are skipped if the truth information shows it to be a  $B^0 \rightarrow J/\psi K_s^0(\pi^0\pi^0)$  or  $B^0 \rightarrow J/\psi \pi^0$  decay. The reconstruction releases used for these simulated events include a bug-fix for the duplicate photons that come from the incorrect implementation of  $K_s^0 \rightarrow \pi^0\pi^0$  and  $\bar{A} \rightarrow \bar{n}\pi^0$  decays in earlier SP4.

As will be seen in Section 5.10.3, knowing whether or not the  $J/\psi$  candidate is truly a  $J/\psi$  meson impacts the way we model the time decay distribution for this background. It is also useful to examine the true origins of the candidates that are combined to form the  $\pi^0$  candidate in this background contribution, to learn why it mimicks the signal. The Monte Carlo truth information for inclusive  $J/\psi$  events is used for both of these, and is as follows:

- Approximately 100% of the candidate  $J/\psi$ 's are true  $J/\psi$ 's.
- 38% of the candidate  $\pi^0$ 's are *fake*  $\pi^0$ 's. The breakdown of the fake  $\pi^0$ 's (as percentage of total  $\pi^0$ 's) is

17% have both legs = true  $\gamma$ 's,

9% have one leg = true  $\gamma$ , other leg = true  $K_L^0, \pi^\pm, e^\pm, n, K^\pm$ ,

8% have one leg = true  $\gamma$ , other leg has no MC match,

3% have both legs = true  $K_L^0, \pi^\pm, e^\pm, n, K^\pm$ .

### 5.5.3 $B\bar{B}$ Generic

Another background contribution comes from generic decays of charged or neutral  $B$  mesons. Excluded from this definition are those decays already considered above.

Initial studies of this background source were done using 23 million pairs of  $B^0\bar{B}^0$  and 21 million pairs of  $B^+B^-$  generated in SP4, yielding 51 candidates after the selection that is explained in Section 5.4. The event topology is as follows:

- 96% of the candidate  $J/\psi$ 's are fake. The breakdown of the fake  $J/\psi$ 's (as percentage of total  $J/\psi$ 's) is

57% both legs = true leptons,

31% one leg = true lepton, other leg = true  $\pi^\pm, K^\pm$ ,

8% both legs = true  $\pi^\pm, K^\pm$ .

- 70% have  $J/\psi$  legs from different  $B$ 's.
- 30% have  $J/\psi$  legs from the same  $B$ .
- 84% of the candidate  $\pi^0$ 's are true  $\pi^0$ 's.

Due to the relatively low statistics of the available  $B\bar{B}$  generic Monte Carlo samples, we have generated more events, using a generator level filter to only fully simulate events that contain specified true particles and pass loose restrictions on the kinematics. The particle type requirements are that the  $\pi^0$  must be a true  $\pi^0$ , there must not be a true  $J/\psi$  in the event, and the  $J/\psi$  candidate must be made up of two true leptons ( $e^+e^-$  or  $\mu^+\mu^-$ ). The specific kinematic requirements are

- The combination of true  $e^+$  and true  $e^-$  must have:

$$2.85 < m_{e^+e^-} < 3.2 \text{ GeV}/c^2 \quad ,$$

$$1.3 < p_{e^+e^-}^* < 10.0 \text{ GeV}/c \quad .$$

- The combination of true  $\mu^+$  and true  $\mu^-$  must have:

$$3.0 < m_{\mu^+\mu^-} < 3.2 \text{ GeV}/c^2 \quad ,$$

$$1.3 < p_{\mu^+\mu^-}^* < 10.0 \text{ GeV}/c \quad .$$

- The combination of the lepton pair with a true  $\pi^0$  must have:

$$5.15 \text{ GeV}/c^2 < m_{ES} \quad ,$$

$$-0.5 < \Delta E < 0.5 \text{ GeV} \quad .$$

The filter accepts only about 1 in every 19,400 generated trials. The accumulated sample that passes the filter contains 7,600 events from  $B^+B^-$  and 6,581 events from  $B^0\bar{B}^0$ . After the event selection is applied (Section 5.4), the sample available for fitting contains 911 events.

### 5.5.4 Continuum

The other combinatoric background is due to  $u$ ,  $d$ ,  $s$ , and  $c$  quark production following the  $e^+e^-$  annihilation. Using the sidebands of *onpeak* data to determine the level and distributions of this background is not feasible since large portions of the event selection variable space are occupied by the other sources of background as well. To avoid relying exclusively on Monte Carlo simulation, and to obtain a larger sample on which to base the probability density functions, a selection is used in which the particle identification on the legs of the  $J/\psi$  candidate decay is reversed (similar to that of Section 4.7.2). The requirement is thus that the  $J/\psi$  candidate is reconstructed from two candidates that are not leptons (i.e.  $J/\psi \rightarrow \text{not-lepton not-lepton}$ ). It is verified in SP3 Monte Carlo simulation that this is a valid selection procedure, for when applying the standard selection to a sample of 20.1 million  $u\bar{u}/d\bar{d}/s\bar{s}$  and 12.5 million  $c\bar{c}$  simulated events, about 85% of the  $J/\psi$  candidates have both legs associated with true particles other than leptons. The remainder have one leg that is something other than a lepton and one leg that is truly a lepton. Another key aspect of this procedure is that the selection is run over *offpeak* data due to the fact that running over *onpeak* data would be contaminated by  $B$  decays where, as has been explained above, the rate of combinations of true and fake  $J/\psi$  legs is different. The sample ( $J/\psi_{\text{fake}}$ ) for modeling the continuum background is obtained by running over  $5.06 \text{ fb}^{-1}$  of *offpeak* data, with all of the standard cuts applied, except that the particle identification requirements for the  $J/\psi$  legs are reversed. Table 5.6 shows the distribution and size of the *offpeak* data samples selected for this purpose. The number of events passing the full selection is 4,290 (see Table 5.5).

Table 5.6: *Offpeak* data samples used to model the continuum background. The file format convention contains information about the year, block, set, release, and Objectivity slave federation.

Filename	Luminosity ( $\text{pb}^{-1}$ )
good_2000-b1-s0-r10B-off_phys14	141.324
good_2000-b1-s2-r10B-off_phys14	278.395
good_2000-b1-s2-r10B-off_phys15	174.212
good_2000-b1-s2-r10B-off_phys19	45.923
good_2000-b1-s2-r10B-off_phys6	459.281
good_2000-b1-s2-r10B-off_phys9	110.742
good_2000-b2-s0-r10B-off_phys9	399.010
good_2000-b2-s2-r10B-off_phys14	456.256
good_2000-b2-s2-r10B-off_phys13	452.875
good_2000-b2-s2-r10B-off_phys6	87.832
Total used for 2000	2606.850
good_2001-b1-s2-r10A-off_phys1	172.285
good_2001-b1-s2-r10A-off_phys2	1139.574
good_2001-b1-s2-r10A-off_phys5	99.420
good_2001-b1-s3-r10A-off_phys5	1039.861
Total used for 2001	2451.140

## 5.6 PDFs for Event Selection Variables

### 5.6.1 A Few Words About the Likelihood Fitting Technique

The likelihood fitting strategy for event yields (as a consistency check) will be discussed in Section 5.7.1 and the time-dependent  $CP$  asymmetry likelihood fit will be detailed in Section 5.11.1. However, at this point it is desirable to motivate the use of the probability density functions.

In contrast to  $\chi^2$ -minimization fitting, unbinned maximum likelihood fitting can function well with unbinned, multi-dimensional, sparse data. The basic structure of the likelihood,  $\mathcal{L}$ , is

$$\mathcal{L}(a_1, a_2, \dots) = \prod_{i=1}^N \mathcal{P}(x_i; a_1, a_2, \dots), \quad (5.10)$$

where  $N$  is the total number of input events,  $\mathcal{P}$  is a probability density function,  $x_i$  are independent observables, such as  $m_{\text{ES}}$  and  $\Delta E$ , and  $a_1, a_2, \dots$  are PDF

parameters. The function  $\mathcal{P}$  may itself be a product of several PDFs, where each is a normalized fitting function for each independent observable. The likelihood may also have contributions from signal and background. The fit is performed by maximizing  $\ln \mathcal{L} = \sum_{i=1}^N \ln \mathcal{P}$ .

The following describes the event selection variable PDFs for the signal and the background sources. The PDFs themselves are determined using maximum likelihood fits.

### 5.6.2 $m_{\text{ES}}$

#### Signal $B^0 \rightarrow J/\psi \pi^0$

The  $m_{\text{ES}}$  distribution for the signal is modeled by the sum of a “running” Gaussian and an Argus function. The running Gaussian is defined as

$$G_{\text{run}}(m_{\text{ES}}) = C_1 e^{-\frac{(m_{\text{ES}}-m)^2}{2\sigma_{\text{run}}^2}}, \quad (5.11)$$

$$\sigma_{\text{run}} = \begin{cases} \sigma + r(m - m_{\text{ES}}) & \text{if } m_{\text{ES}} < m \\ \sigma & \text{otherwise} \end{cases},$$

where  $m$  and  $\sigma$  are the standard Gaussian mean and width, and  $r$  is a scale factor. The running Gaussian has a sigma which varies with the distance from the mean and nicely models the  $m_{\text{ES}}$  line shape. The Argus function was defined in equation 4.7, and is repeated here:

$$\text{Argus}(m_{\text{ES}}) = \begin{cases} C_2 m_{\text{ES}} \sqrt{1 - \frac{m_{\text{ES}}^2}{E_{\text{beam}}^2}} e^{\xi(1 - \frac{m_{\text{ES}}^2}{E_{\text{beam}}^2})} & \text{if } m_{\text{ES}} < E_{\text{beam}} \\ 0 & \text{otherwise} \end{cases}. \quad (5.12)$$

The one remaining parameter to fit is the relative fraction of the running Gaussian component. The resulting fit to signal Monte Carlo simulation and the values of the parameters can be seen in Figure 5.10(a). For reference, the correspondence between the parameter symbols in the above equations and the names of the floating

parameters, as used in fitting for the PDF, are shown in the caption.

### **$B^0 \rightarrow J/\psi K_s^0(\pi^0\pi^0)$ Background**

Because of the correlation between  $m_{\text{ES}}$  and  $\Delta E$  for the  $B^0 \rightarrow J/\psi K_s^0(\pi^0\pi^0)$  background, a two-dimensional PDF is employed. The procedure is to construct a two-dimensional histogram of the two variables from the Monte Carlo sample and then use third order interpolation to fill in the values of the PDF between histogram bins. By allowing for variable binning in each dimension of the original histogram, it is possible to construct a PDF that is smoothly varying and matches the seed Monte Carlo distribution.

The projections of the two-dimensional PDF and the  $B^0 \rightarrow J/\psi K_s^0(\pi^0\pi^0)$  Monte Carlo sample, onto the  $m_{\text{ES}}$  axis, are shown in Figure 5.10(b).

### **Inclusive $J/\psi$ Background**

The same procedure, as just described, is used to determine the two-dimensional  $\Delta E$  versus  $m_{\text{ES}}$  PDF for the inclusive  $J/\psi$  background. Once again, the two-dimensional histogram is constructed with variable binning, this time from the inclusive  $J/\psi$  Monte Carlo sample, and interpolation is used to form the PDF. The shape of the projection of this non-parametric PDF onto the  $\Delta E$  axis, along with the distribution of the Monte Carlo sample, is shown in Figure 5.10(c).

### **$B\bar{B}$ Generic Background**

The  $m_{\text{ES}}$  line shape for the  $B\bar{B}$  generic background is modeled by the Argus function, as given in equation 5.12. The kinematic cut-off is fixed at  $E_{\text{beam}} = 5.289$  GeV, and the exponential factor,  $\xi$ , is left floating in a fit to the  $B\bar{B}$  generic Monte Carlo sample that was obtained through the use of the generator-level filter. The distribution of these events and the resulting PDF are shown in Figure 5.10(d).

### Continuum Background

The PDF for the  $m_{\text{ES}}$  distribution of the continuum background is well modeled by the Argus function, which has the form given in equation 5.12. As before, the kinematic cut-off is fixed at  $E_{\text{beam}} = 5.289 \text{ GeV}$ . The overall normalization is unimportant here, so the only parameter that is extracted from this fit is the exponential factor,  $\xi$ . The fit to the  $J/\psi_{\text{fake}}$  sample (*offpeak* data), is shown in Figure 5.10(e).

### 5.6.3 $\Delta E$

#### Signal $B^0 \rightarrow J/\psi \pi^0$

The  $\Delta E$  distribution in signal is modeled by the sum of a so-called crystal ball function [48] (equation 5.13) and a second order polynomial, P2 (equation 5.14):

$$\text{CB}(\Delta E) = C_3 \begin{cases} e^{-\frac{(\Delta E - m)^2}{2\sigma^2}} & \text{if } \Delta E > m - \alpha\sigma \\ \frac{(\frac{n}{\alpha})^n e^{-\frac{\alpha^2}{2}}}{(\frac{m - \Delta E}{\sigma} + \frac{n}{\alpha} - \alpha)^n} & \text{if } \Delta E \leq m - \alpha\sigma \end{cases}, \quad (5.13)$$

$$\text{P2}(\Delta E) = C_4 (1 + A_1 \Delta E + A_2 (\Delta E)^2). \quad (5.14)$$

The parameter  $\alpha$  determines the cross-over point from a Gaussian behavior to a power-law, and is expressed in units of the peak width  $\sigma$ . A positive value for  $\alpha$  means that the tail is below the mean, and values in the range of 0.6 – 1.1 are typical for describing  $\Delta E$  distributions. The parameter  $n$  is a real number that enters into the power-law portion of the function.

The parameters of these functions, plus the relative fraction that is fit by the crystal ball function, are determined by performing an unbinned likelihood fit to the signal Monte Carlo sample. The resulting PDF is shown in Figure 5.11(a).

#### $B^0 \rightarrow J/\psi K_s^0(\pi^0\pi^0)$ Background

The procedure for acquiring the two-dimensional PDF for  $\Delta E$  versus  $m_{\text{ES}}$  of the  $B^0 \rightarrow J/\psi K_s^0(\pi^0\pi^0)$  background is described above in Section 5.6.2. The variable

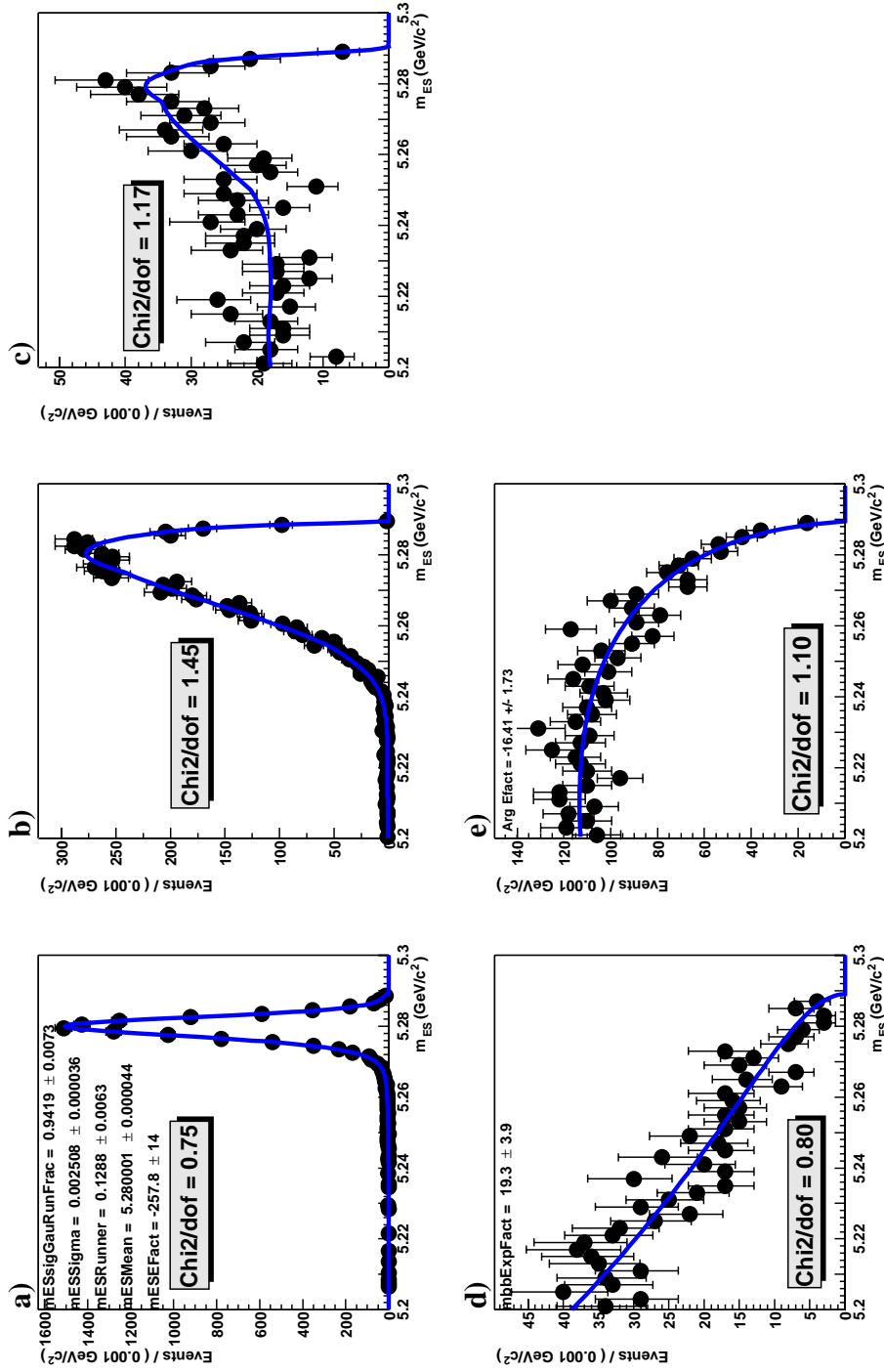


Figure 5.10: PDFs (shown as curves) for  $m_{ES}$  on top of the distributions from which they are determined (points). Where applicable, the plots also contain the values of the parameters for the PDFs. (a) Signal  $B^0 \rightarrow J/\psi \pi^0$  (parameters from equations 5.11 and 5.12 are  $\sigma_{\text{run}} = mESSigma$ ,  $m = mESMean$ ,  $r = mESRunner$ , and  $\xi = mESFact$ . The fraction of running Gaussian component is  $mESsigGauRunFrac$ ). (b)  $B^0 \rightarrow J/\psi K_s^0(\pi^0 \pi^0)$  background. (c) Inclusive  $J/\psi$  background. (d)  $B\bar{B}$  generic background. (e) Continuum background. Each PDF is described in detail in the text of Section 5.6.2.

binning of the  $\Delta E$  dimension of the original two-dimensional histogram of the Monte Carlo sample is different than that for  $m_{ES}$ , so as to allow for a smooth PDF once the interpolation is performed. This means that the PDF does not simply get pulled to the value at the center of each bin, but at the same time is able to follow the shape of the distribution in the more rapidly varying regions.

The  $\Delta E$  projections, of the PDF and the Monte Carlo sample, are shown in Figure 5.11(b).

### **Inclusive $J/\psi$ Background**

The PDF for the  $\Delta E$  and  $m_{ES}$  distributions of the inclusive background is described in Section 5.6.2. The projection of this two-dimensional PDF in the  $\Delta E$  variable is shown in Figure 5.11(c).

### **$B\bar{B}$ Generic Background**

A P2 function, with the parameterization given in equation 5.14, is used as the PDF for modeling the  $\Delta E$  distribution of the  $B\bar{B}$  generic background. The fit is made to the Monte Carlo sample obtained using the generator-level filter, and the results are shown in Figure 5.11(d). The parameter values displayed on the plot have a straight forward correspondence to the ones in equation 5.14.

### **Continuum Background**

The PDF used to model the  $\Delta E$  distribution of the continuum background is a P2 of the form given in equation 5.14. The two parameters are determined from a fit to the reversed lepton particle identification *offpeak* data sample,  $J/\psi_{\text{fake}}$ , and the resulting PDF is shown in Figure 5.11(e).

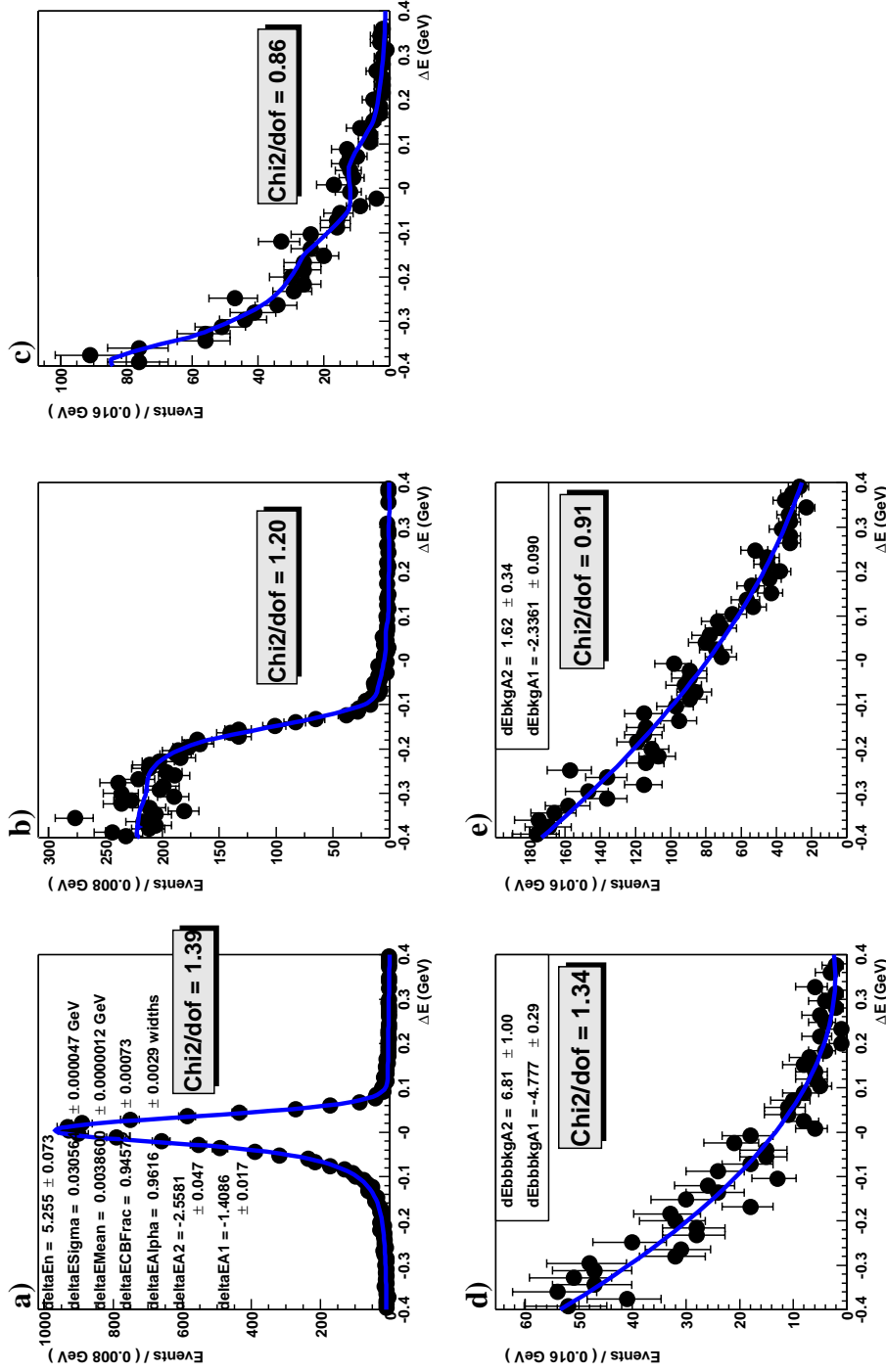


Figure 5.11: PDFs (shown as curves) for  $\Delta E$  on top of the distributions from which they are determined (points). Where applicable, the plots also contain the values of the parameters for the PDFs. (a) Signal  $B^0 \rightarrow J/\psi \pi^0$  (parameters from equations 5.13 and 5.14 are  $\sigma = \text{deltaE} \Sigma$ ,  $m = \text{deltaE} \text{Mean}$ ,  $\alpha = \text{deltaE} \text{Alpha}$ ,  $n = \text{deltaE} \text{En}$ ,  $A1 = \text{deltaEA}1$ , and  $A2 = \text{deltaEA}2$ ). The fraction of crystal ball component is  $\text{deltaECBFrac}$ . (b)  $B^0 \rightarrow J/\psi K_S^0(\pi^0 \pi^0)$  background. (c) Inclusive  $J/\psi$  background. (d)  $B\bar{B}$  generic background. (e)  $B\bar{B}$  generic background. Each PDF is described in detail in the text of Section 5.6.3.

### 5.6.4 Fisher Discriminant

#### Signal $B^0 \rightarrow J/\psi \pi^0$

The distribution of the Fisher variable for signal is modeled by a PDF that is the sum of three standard Gaussians. While some *BABAR* analyses utilize a Fisher that can be modeled by a single Gaussian, that is not the case here, as the input to the Fisher includes additional thrust and helicity information.

The PDF that results from fitting to the signal Monte Carlo sample, and the associated parameter values for the three Gaussians (with expected naming conventions), are shown in Figure 5.12(a). The two additional parameters shown on the plot are the relative fractions for the first and second Gaussians.

#### $B^0 \rightarrow J/\psi K_s^0(\pi^0\pi^0)$ Background

The Fisher output for this background is also modeled by the sum of three Gaussians. The fit is performed on the  $B^0 \rightarrow J/\psi K_s^0(\pi^0\pi^0)$  Monte Carlo sample and, as may be expected, the resulting parameters are all within error of those for the  $B^0 \rightarrow J/\psi \pi^0$  signal.

The results of the fit are shown in Figure 5.12(b), where again the parameter values are superimposed on the plot, and the parameter naming convention is similar to that of the signal.

#### Inclusive $J/\psi$ Background

The best function that is found to describe the Fisher output for the inclusive  $J/\psi$  background is the sum of two Gaussians. Because the distributions of the  $|\cos \theta_T|$  and  $|\cos \theta_\ell|$  variables, both inputs to the Fisher, differ for inclusive  $J/\psi$  as compared with  $B^0 \rightarrow J/\psi \pi^0$  and  $B^0 \rightarrow J/\psi K_s^0(\pi^0\pi^0)$  it is not surprising that the Fisher takes a slightly different functional form.

The PDF, as obtained from an unbinned likelihood fit to the Monte Carlo sample, is displayed in Figure 5.12(c), along with the parameter names and values.

### $B\bar{B}$ Generic Background

The PDF for the Fisher discriminant in the case of the  $B\bar{B}$  background is also constructed as the sum of two Gaussians. The parameters are obtained by fitting to the filtered  $B\bar{B}$  generic Monte Carlo sample and the results are included in Figure 5.12(d).

### Continuum Background

The PDF for the continuum background is the sum of three Gaussians. About 60% of the distribution is in a core Gaussian centered near  $-1.1$ , and the rest of the distribution is in asymmetric low side and high side tails (roughly 15% and 25% respectively).

The resulting PDF, as obtained by fitting the special  $J/\psi_{\text{fake}}$  data sample, is shown in Figure 5.12(e), along with the parameter names and values.

## 5.7 Likelihood Fits for Yields (Consistency Check)

### 5.7.1 Implementation of Unbinned Maximum Likelihood Fits

A fit for the signal and background yields, in Monte Carlo samples and data, is performed as a step along the way to the  $CP$  asymmetry fit. The following outlines the formulation of the fit, which is implemented using a C++ package called `Roofit`. The quantity that is maximized is the logarithm of the extended likelihood:

$$\mathcal{L} = \frac{e^{-\sum_{j=1}^5 n_j}}{N!} \prod_{i=1}^N \sum_{j=1}^5 n_j \mathcal{P}_j, \quad (5.15)$$

where  $n_j$  is the number of events for each of the five hypotheses (one signal and four background) and  $N$  is the total number of input events.  $\mathcal{P}_j$  is the total probability for observing that event  $i$  matches one of the five hypotheses  $j$ . These PDFs are assembled from those defined in Section 5.6 by taking the product of the one- or two-dimensional PDFs for the contributing discriminating variables for each source type.

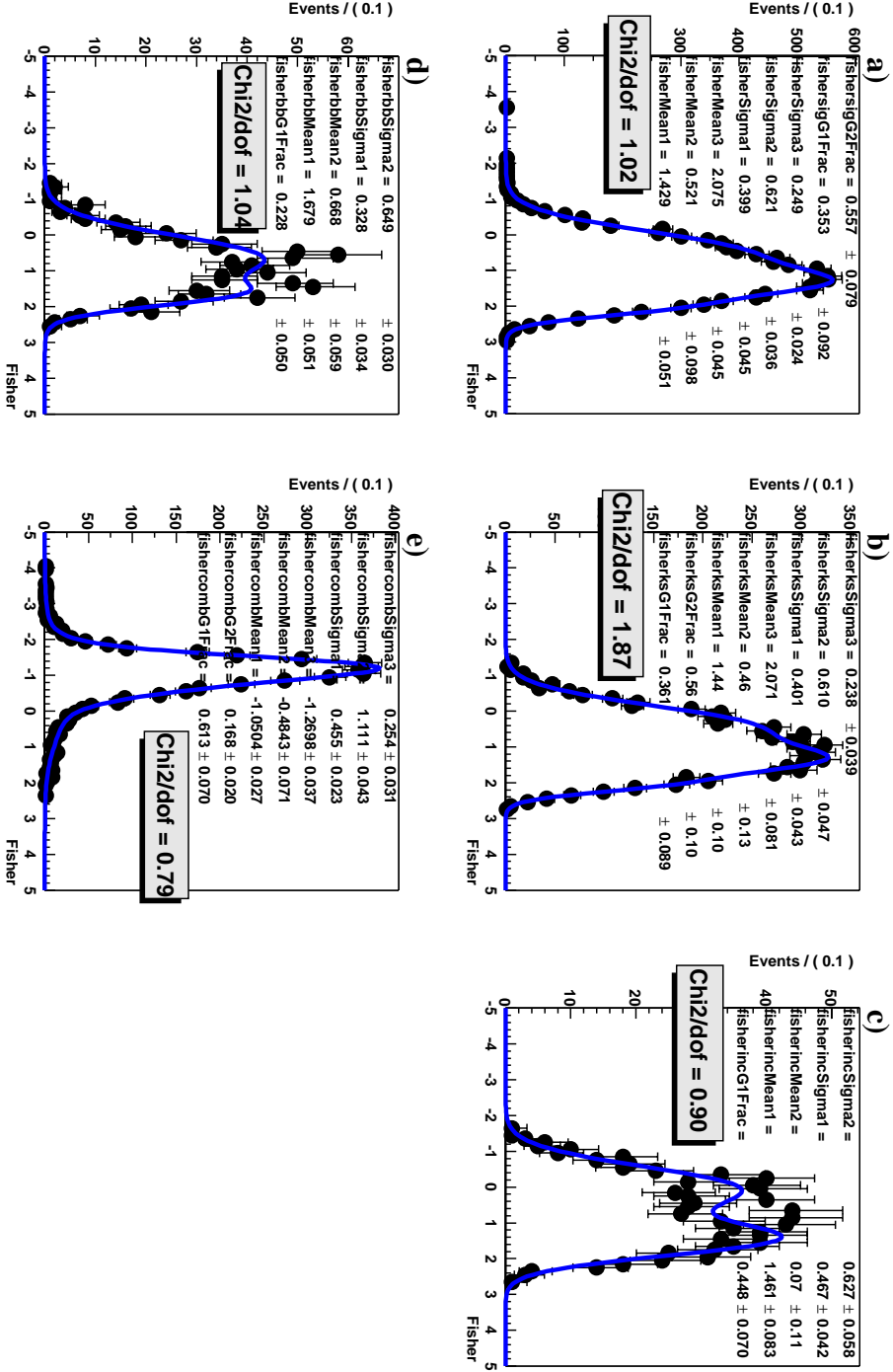


Figure 5.12: PDFs (shown as curves) for the Fisher on top of the distributions from which they are determined (points). The plots also contain the values of the parameters for the PDFs, as determined from unbinned likelihood fits. (a) Signal  $B^0 \rightarrow J/\psi\pi^0$ . (b)  $B^0 \rightarrow J/\psi K_S^0 (\pi^0\pi^0)$  background. (c) Inclusive  $J/\psi$  background. (d)  $B\bar{B}$  generic background. (e) Continuum background. Each PDF is described in detail in the text of Section 5.6.4.

To make the procedure completely explicit, the number of events that get assigned to each sample type are

$$\begin{aligned}
 n_{\text{Sig}} &= \text{number of signal } B^0 \rightarrow J/\psi \pi^0 \text{ events} \\
 n_{\text{Ks}} &= \text{number of } B^0 \rightarrow J/\psi K_s^0 (\pi^0 \pi^0) \text{ background events} \\
 n_{\text{Inc}} &= \text{number of Inclusive } J/\psi \text{ background events} \\
 n_{\text{BB}} &= \text{number of } B\bar{B} \text{ generic background events} \\
 n_{\text{Cont}} &= \text{number of continuum background events}
 \end{aligned}$$

and so the extended likelihood can be written as:

$$\begin{aligned}
 \mathcal{L} = \frac{e^{-\sum_{j=1}^5 n_j}}{N!} \prod_{i=1}^N \{ &n_{\text{Sig}} (\mathcal{P}_{\text{Sig}} m_{\text{ES}} \mathcal{P}_{\text{Sig}} \Delta E \mathcal{P}_{\text{Sig}} \text{Fisher}) \\
 &+ n_{\text{Ks}} (\mathcal{P}_{\text{Ks}} m_{\text{ES}-\Delta E} \mathcal{P}_{\text{Ks}} \text{Fisher}) \\
 &+ n_{\text{Inc}} (\mathcal{P}_{\text{Inc}} m_{\text{ES}-\Delta E} \mathcal{P}_{\text{Inc}} \text{Fisher}) \\
 &+ n_{\text{BB}} (\mathcal{P}_{\text{BB}} m_{\text{ES}} \mathcal{P}_{\text{BB}} \Delta E \mathcal{P}_{\text{BB}} \text{Fisher}) \\
 &+ n_{\text{Cont}} (\mathcal{P}_{\text{Cont}} m_{\text{ES}} \mathcal{P}_{\text{Cont}} \Delta E \mathcal{P}_{\text{Cont}} \text{Fisher}) \} . \quad (5.16)
 \end{aligned}$$

### 5.7.2 Yield Fits to Single Signal and Background Samples

As a means of checking both the fitting code and the quality of the PDFs, the yield fit is run independently on each of the five sample types. The fit is made to all of the available events for the particular sample, and the results are summarized in Table 5.7. The projections of the fit results in  $m_{\text{ES}}$ ,  $\Delta E$ , and the Fisher can be seen in figures 5.13–5.17. The dashed curves represent the contributions allocated to each source type (the color code is the same for each plot, and is given in the captions), while the solid blue curves represent the total fits and are to be compared with the black points, which are the input distributions. In several cases, the dashed curve corresponding to the sample type being fit almost entirely tracks the solid blue curve, making the blue curve look dashed rather than solid. Note that the samples being fit are the same ones used to determine the PDF parameters. The matches between the

contributions from the samples being fit and the black points show that the PDFs defined in Section 5.6 correctly describe the event selection variables within these samples. It also reveals that the fitting code is functioning as expected.

### 5.7.3 Yield Fits to Mixtures of Samples

For this study, samples are constructed that contain the estimated number of signal and background events equivalent to  $71 \text{ fb}^{-1}$  of data. For signal  $B^0 \rightarrow J/\psi \pi^0$ ,  $B^0 \rightarrow J/\psi K_s^0(\pi^0 \pi^0)$  background, and inclusive  $J/\psi$  background these estimates are obtained by running over Monte Carlo events and multiplying the efficiency for candidates that pass the final selection by the relevant branching fractions for the sample and the number of  $B\bar{B}$  pairs in  $71 \text{ fb}^{-1}$  of data. The procedure differs slightly for the estimate of the  $B\bar{B}$  generic and continuum backgrounds. These estimated numbers of events are calculated by running over SP4  $B\bar{B}$  generic, and SP3  $u\bar{u}/d\bar{d}/s\bar{s}$  and  $c\bar{c}$  Monte Carlo events, dividing  $71 \text{ fb}^{-1}$  by the luminosity of each Monte Carlo sample, and multiplying that quotient by the number of candidates that pass the final selection. The third column of Table 5.8 lists these estimates.

Mixtures are created by taking groups of events from each of the complete samples. Here, once again, the  $J/\psi_{\text{fake}}$  *offpeak* data sample is used to model the continuum background, and the generator-level filtered  $B\bar{B}$  generic Monte Carlo sample is also used. The extended maximum likelihood fit for the yields (defined in Section 5.7.1) is applied, and the results are shown in Table 5.8 and Figure 5.18. From the fact that the individual contributions of signal and backgrounds match well with the predictions, and the fact that the total fit results agree well with the black points for each of the projections, we can conclude that the PDFs are sufficiently diverse to distinguish among the different sub-samples. This also serves as another check that the fitting code is working properly.

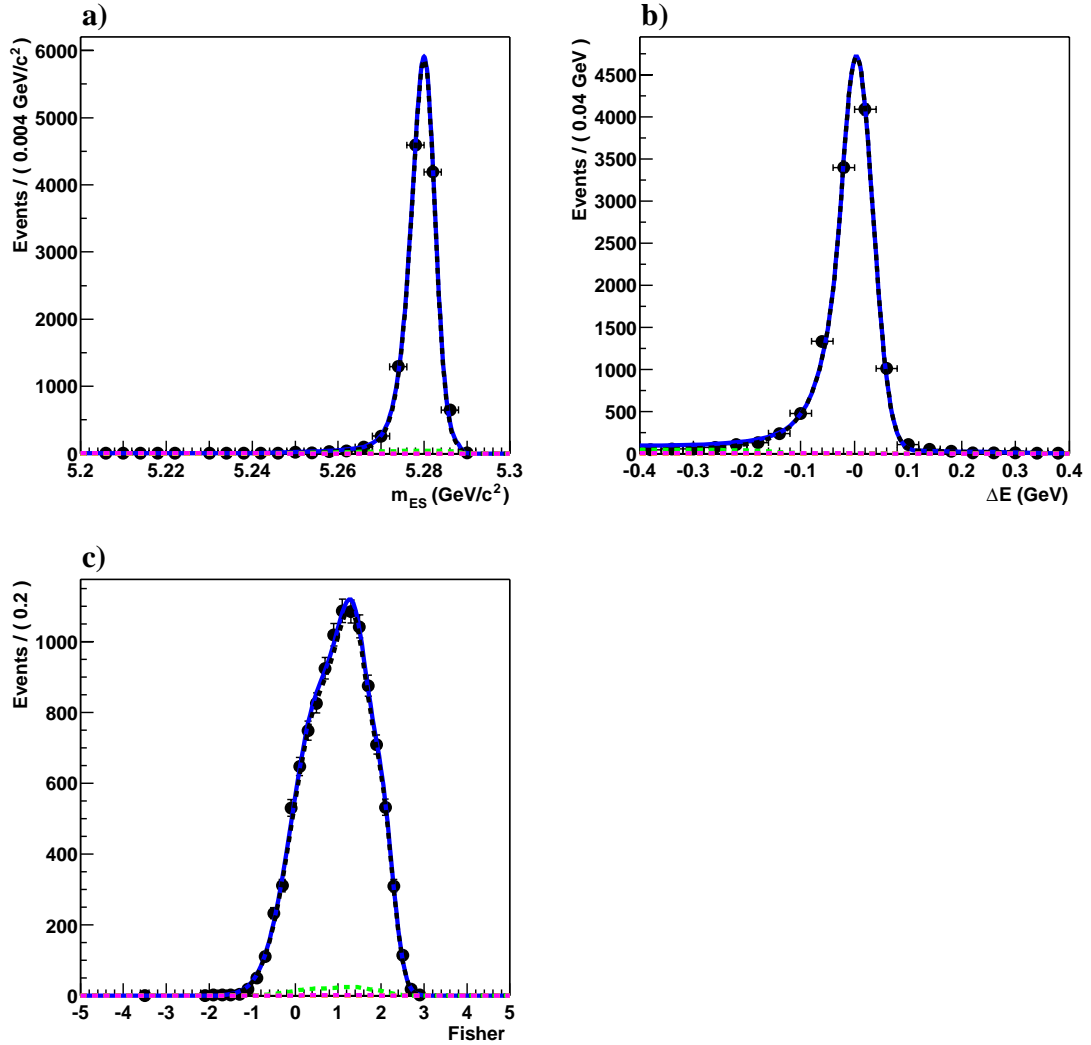


Figure 5.13: Projections in (a)  $m_{ES}$ , (b)  $\Delta E$ , and (c) the Fisher for the results of a yield fit to the entire signal  $B^0 \rightarrow J/\psi \pi^0$  Monte Carlo sample. Black dashed: signal  $B^0 \rightarrow J/\psi \pi^0$ . Green dashed:  $B^0 \rightarrow J/\psi K_S^0(\pi^0 \pi^0)$  background. Yellow dashed: inclusive  $J/\psi$  background. Magenta dashed:  $B\bar{B}$  generic background. Red dashed: continuum background. Blue solid: total. Note that the black and blue curves are nearly on top of each other. The expectations and results are given in Table 5.7.

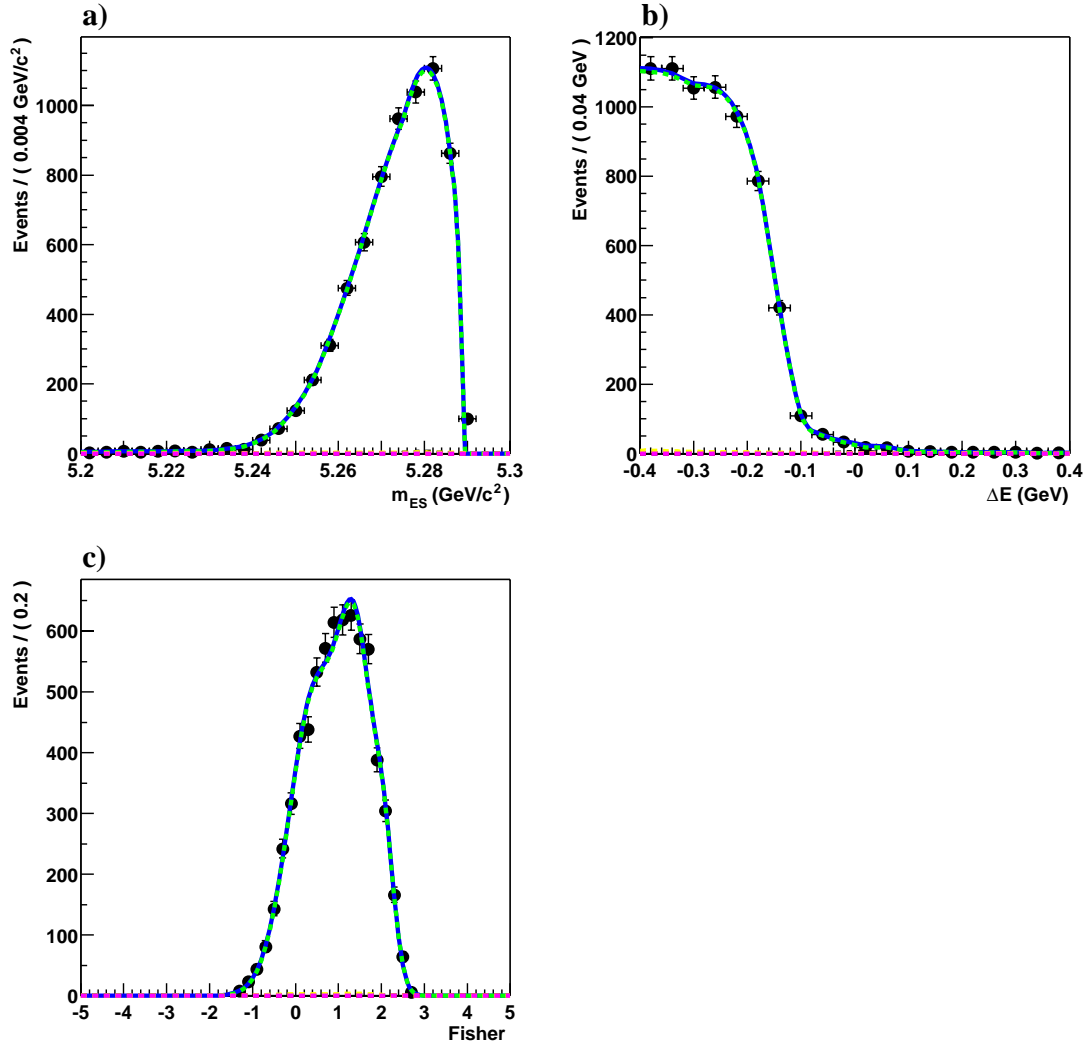


Figure 5.14: Projections in (a)  $m_{ES}$ , (b)  $\Delta E$ , and (c) the Fisher for the results of a yield fit to the entire  $B^0 \rightarrow J/\psi K_s^0(\pi^0\pi^0)$  background Monte Carlo sample. Black dashed: signal  $B^0 \rightarrow J/\psi \pi^0$ . Green dashed:  $B^0 \rightarrow J/\psi K_s^0(\pi^0\pi^0)$  background. Yellow dashed: inclusive  $J/\psi$  background. Magenta dashed:  $B\bar{B}$  generic background. Red dashed: continuum background. Blue solid: total. The green and blue curves nearly coincide. The expectations and results are given in Table 5.7.

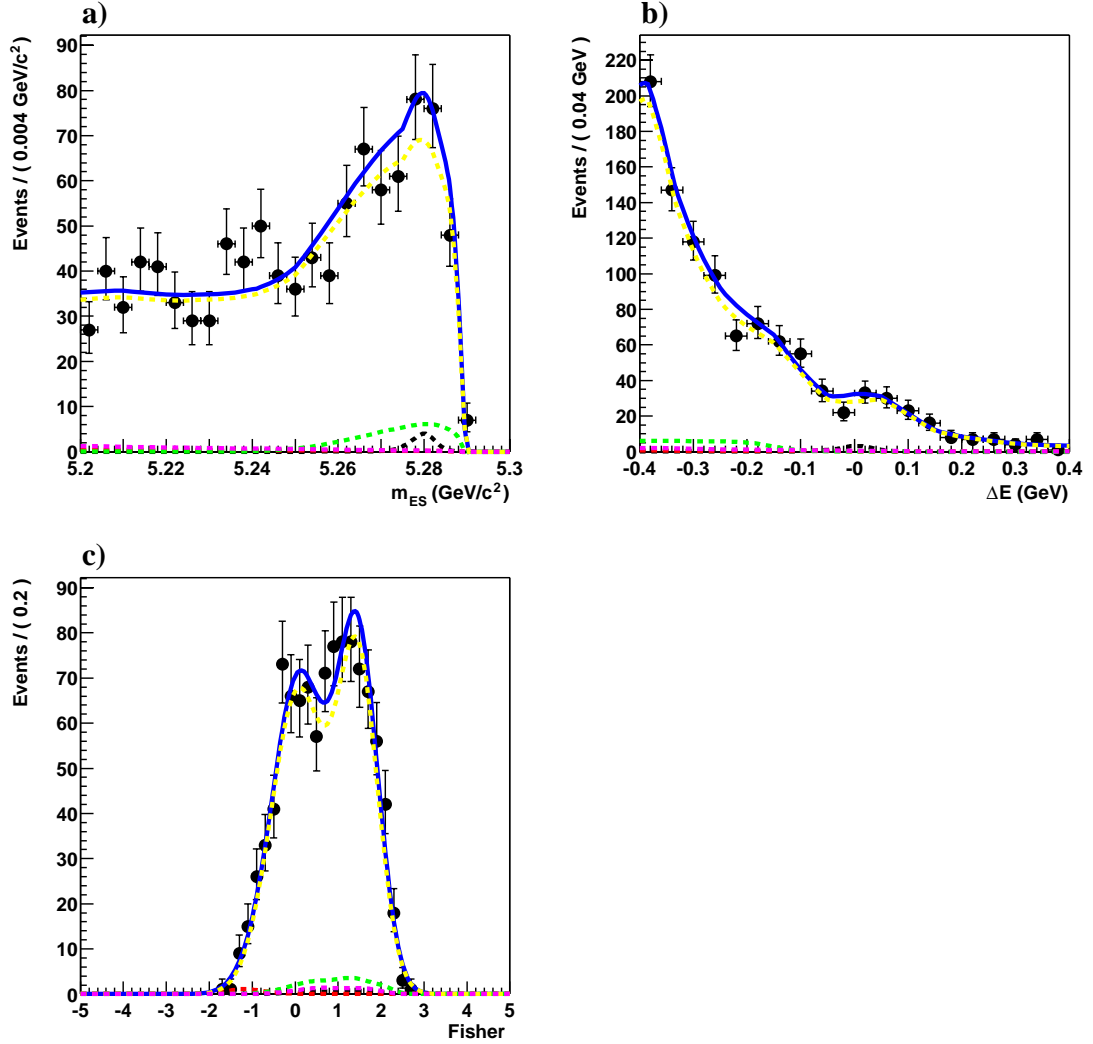


Figure 5.15: Projections in (a)  $m_{ES}$ , (b)  $\Delta E$ , and (c) the Fisher for the results of a yield fit to the entire inclusive  $J/\psi$  background Monte Carlo sample. Black dashed: signal  $B^0 \rightarrow J/\psi \pi^0$ . Green dashed:  $B^0 \rightarrow J/\psi K_S^0(\pi^0 \pi^0)$  background. Yellow dashed: inclusive  $J/\psi$  background. Magenta dashed:  $B\bar{B}$  generic background. Red dashed: continuum background. Blue solid: total. The expectations and results are given in Table 5.7.

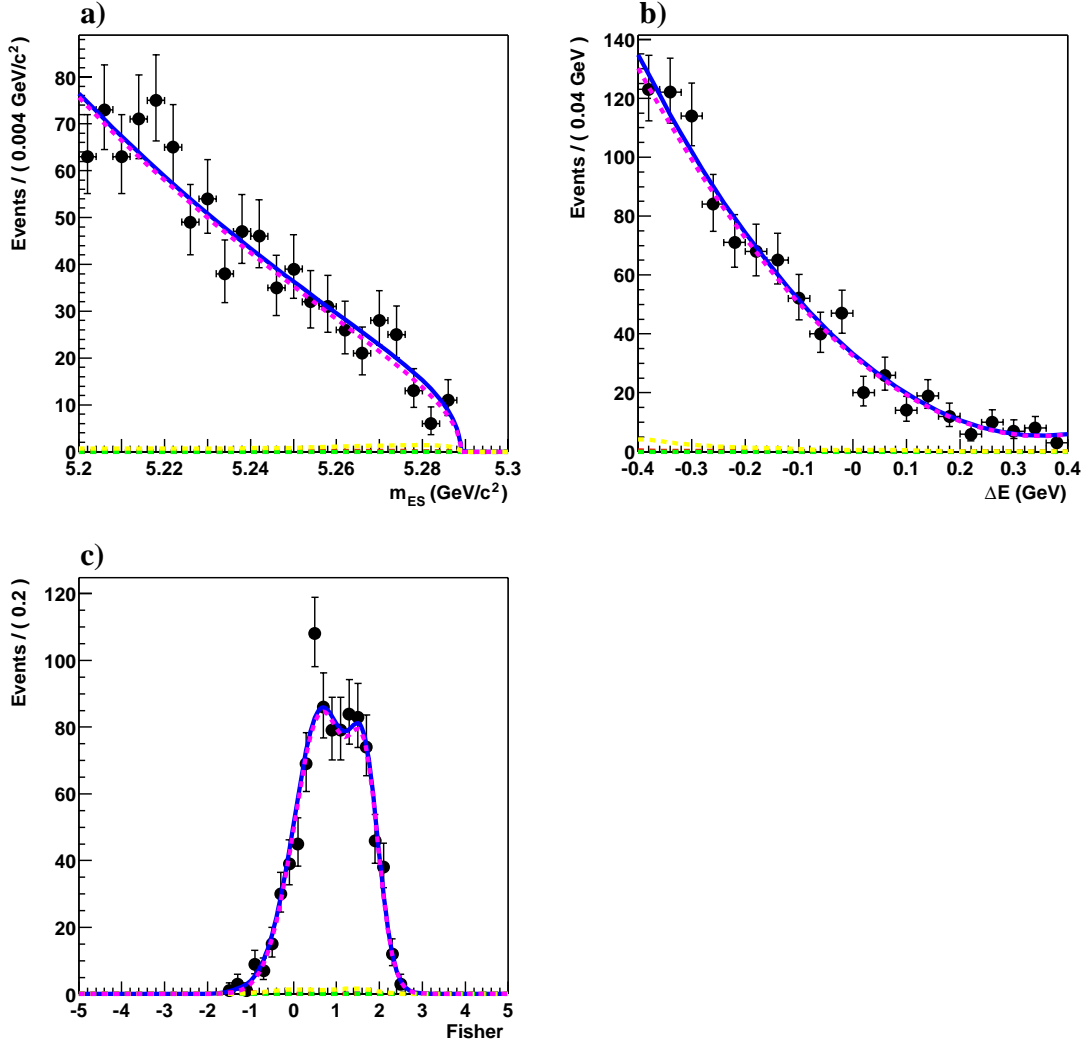


Figure 5.16: Projections in (a)  $m_{ES}$ , (b)  $\Delta E$ , and (c) the Fisher for the results of a yield fit to the entire  $B\bar{B}$  generic background Monte Carlo sample. Black dashed: signal  $B^0 \rightarrow J/\psi \pi^0$ . Green dashed:  $B^0 \rightarrow J/\psi K_S^0(\pi^0\pi^0)$  background. Yellow dashed: inclusive  $J/\psi$  background. Magenta dashed:  $B\bar{B}$  generic background. Red dashed: continuum background. Blue solid: total. The expectations and results are given in Table 5.7.

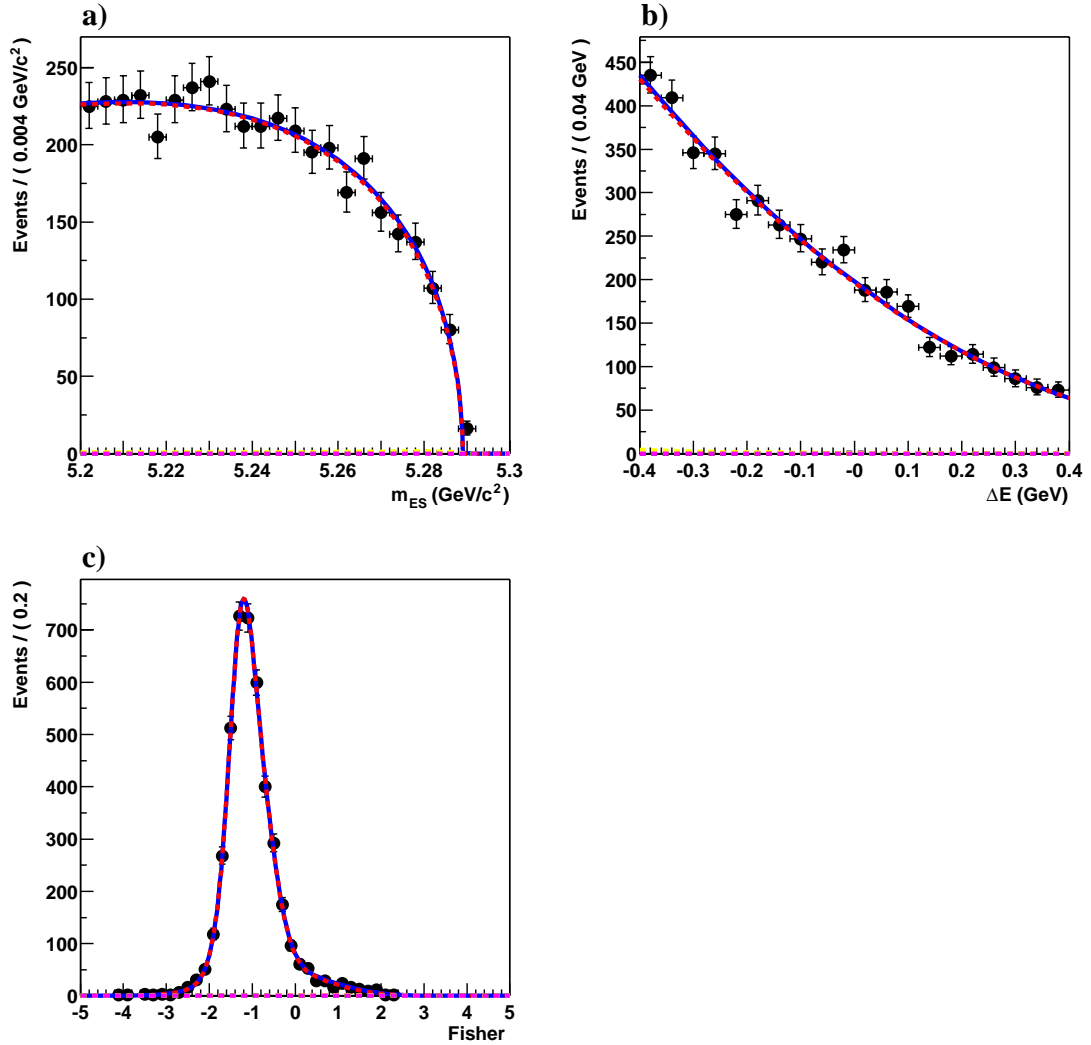


Figure 5.17: Projections in (a)  $m_{ES}$ , (b)  $\Delta E$ , and (c) the Fisher for the results of a yield fit to the entire  $J/\psi_{\text{fake}}$  offpeak data sample, used to model the continuum background. Black dashed: signal  $B^0 \rightarrow J/\psi \pi^0$ . Green dashed:  $B^0 \rightarrow J/\psi K_s^0(\pi^0\pi^0)$  background. Yellow dashed: inclusive  $J/\psi$  background. Magenta dashed:  $B\bar{B}$  generic background. Red dashed: continuum background. Blue solid: total. Note that the red and blue curves overlap. The expectations and results are given in Table 5.7.

Table 5.7: Results of yield fits to single sample types. For some of the cases, the fit does not attribute any events to one or more of the source types, and the associated fit parameters for the yields hit a lower limit at zero. For the first fit, about 2% of the signal is fit as  $B^0 \rightarrow J/\psi K_s^0(\pi^0\pi^0)$  as a result of the small correlated tails of the signal that are in the region populated by the  $B^0 \rightarrow J/\psi K_s^0(\pi^0\pi^0)$  background.

	Fit results	Expected
Fit to signal $B^0 \rightarrow J/\psi \pi^0$ MC sample		
$B^0 \rightarrow J/\psi \pi^0$	$10923.0 \pm 105.3$	11209
$B^0 \rightarrow J/\psi K_s^0(\pi^0\pi^0)$	$263.1 \pm 21.3$	0
Inclusive $J/\psi$	$0 \text{ (at limit)} \pm 7.54 \times 10^{-2}$	0
$B\bar{B}$ generic	$18.5 \pm 7.1$	0
Continuum	$3.7 \pm 2.7$	0
Fit to $B^0 \rightarrow J/\psi K_s^0(\pi^0\pi^0)$ background MC sample		
$B^0 \rightarrow J/\psi \pi^0$	$10.3 \pm 6.3$	0
$B^0 \rightarrow J/\psi K_s^0(\pi^0\pi^0)$	$6713.8 \pm 83.2$	6769
Inclusive $J/\psi$	$40.6 \pm 16.2$	0
$B\bar{B}$ generic	$0 \text{ (at limit)} \pm 1.34 \times 10^{-2}$	0
Continuum	$4.5 \pm 4.2$	0
Fit to inclusive $J/\psi$ background MC sample		
$B^0 \rightarrow J/\psi \pi^0$	$7.4 \pm 4.3$	0
$B^0 \rightarrow J/\psi K_s^0(\pi^0\pi^0)$	$37.3 \pm 19.3$	0
Inclusive $J/\psi$	$952.3 \pm 56.0$	1018
$B\bar{B}$ generic	$14.6 \pm 36.0$	0
Continuum	$6.3 \pm 8.5$	0
Fit to $B\bar{B}$ generic background MC sample		
$B^0 \rightarrow J/\psi \pi^0$	$0 \text{ (at limit)} \pm 3.88 \times 10^{-4}$	0
$B^0 \rightarrow J/\psi K_s^0(\pi^0\pi^0)$	$0 \text{ (at limit)} \pm 7.65 \times 10^{-2}$	0
Inclusive $J/\psi$	$19.9 \pm 24.8$	0
$B\bar{B}$ generic	$887.5 \pm 38.3$	911
Continuum	$3.8 \pm 3.7$	0
Fit to continuum background data sample		
$B^0 \rightarrow J/\psi \pi^0$	$1.9 \pm 1.8$	0
$B^0 \rightarrow J/\psi K_s^0(\pi^0\pi^0)$	$3.1 \pm 3.0$	0
Inclusive $J/\psi$	$19.3 \pm 12.6$	0
$B\bar{B}$ generic	$0 \text{ (at limit)} \pm 7.20 \times 10^{-1}$	0
Continuum	$4265.8 \pm 66.4$	4290

Table 5.8: Results of likelihood fits for yields in mixtures of signal and background Monte Carlo events and *offpeak* data ( $J/\psi_{\text{fake}}$  sample) equivalent to  $71 \text{ fb}^{-1}$  of *onpeak* data. The projections of the PDFs, normalized by the yield fit results for mixture 1 from this table, are shown in Figure 5.18.

	Fit results	Expected	Global correlation
Mixture 1			
$B^0 \rightarrow J/\psi \pi^0$ signal	$76.0 \pm 9.6$	70	0.094
$B^0 \rightarrow J/\psi K_s^0(\pi^0 \pi^0)$ background	$182.1 \pm 22.6$	171	0.726
Inclusive $J/\psi$ background	$45.4 \pm 45.1$	89	0.904
$B\bar{B}$ generic background	$96.9 \pm 26.0$	73	0.854
Continuum background	$360.7 \pm 21.1$	358	0.292
Mixture 2			
$B^0 \rightarrow J/\psi \pi^0$ signal	$76.5 \pm 9.9$	70	0.115
$B^0 \rightarrow J/\psi K_s^0(\pi^0 \pi^0)$ background	$168.0 \pm 22.3$	171	0.651
Inclusive $J/\psi$ background	$74.1 \pm 38.3$	89	0.871
$B\bar{B}$ generic background	$85.1 \pm 23.4$	73	0.816
Continuum background	$357.3 \pm 20.7$	358	0.237

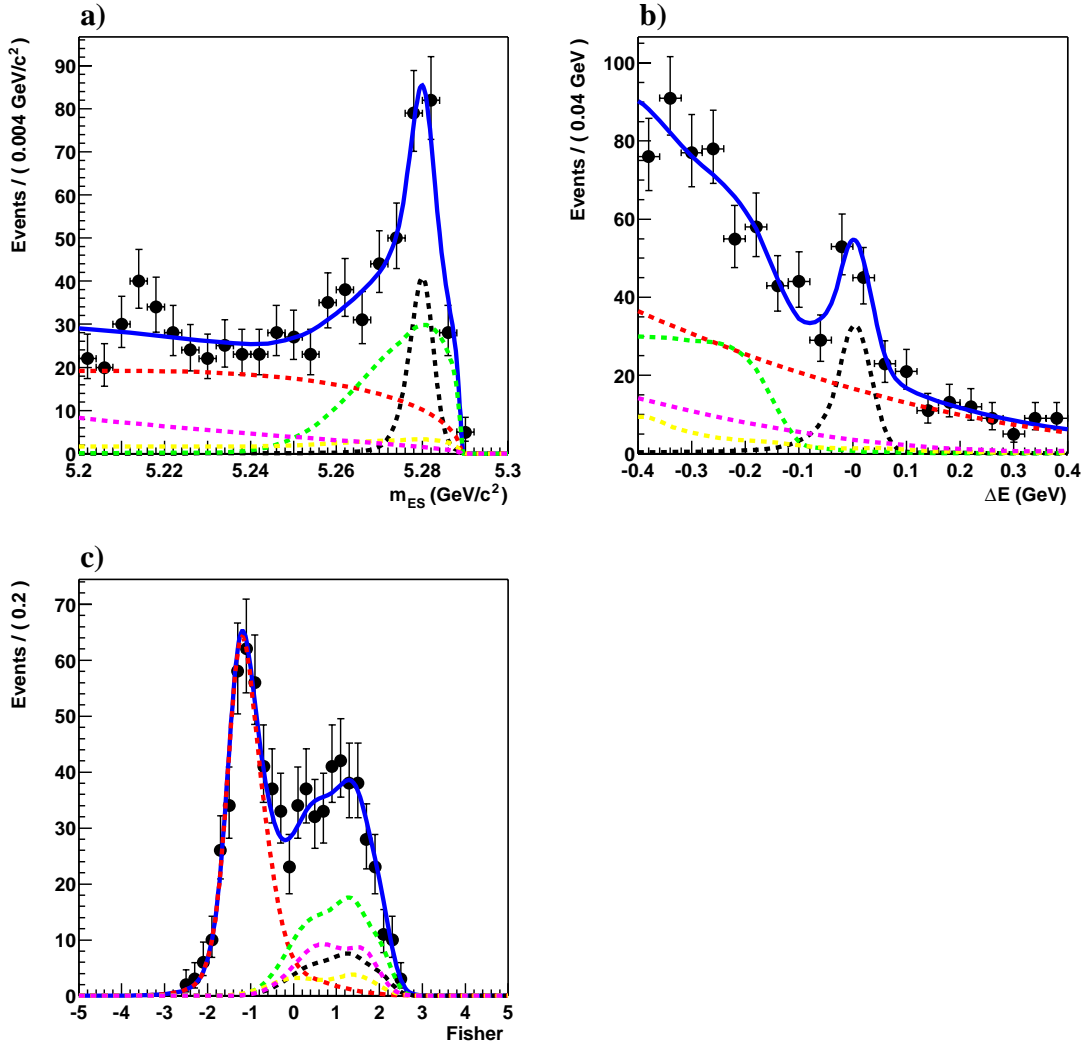


Figure 5.18: Projections in (a)  $m_{ES}$ , (b)  $\Delta E$ , and (c) the Fisher for the results of a yield fit to a mixture of signal and background Monte Carlo events and *offpeak* data ( $J/\psi_{\text{fake}}$  sample) equivalent to  $71 \text{ fb}^{-1}$  of *onpeak* data. Black dashed: signal  $B^0 \rightarrow J/\psi \pi^0$ . Green dashed:  $B^0 \rightarrow J/\psi K_S^0 (\pi^0 \pi^0)$  background. Yellow dashed: inclusive  $J/\psi$  background. Magenta dashed:  $B\bar{B}$  generic background. Red dashed: continuum background. Blue solid: total. The numerical results are given in Table 5.8.

## 5.8 Vertexing and $\Delta t$

As mentioned previously,  $\Delta t = t_{\text{rec}} - t_{\text{tag}}$  is the difference between the proper decay time of the reconstructed  $B$  meson and the proper decay time of the tagging  $B$  meson. This is calculated from the vertex position difference,  $\Delta z$ , between the two decays, along the beam axis [49].

In determining the location of the reconstructed  $B$  meson ( $B_{\text{rec}}$ ) vertex, all of the charged tracks that make up  $B_{\text{rec}}$  are used. The  $z$  resolution for the  $B_{\text{rec}}$  vertex position is approximately  $70 \mu\text{m}$  for data events. The tagging  $B$  meson ( $B_{\text{tag}}$ ) vertex is formed by all of the remaining charged tracks in the event (in other words, those not used in reconstructing  $B_{\text{rec}}$ ). The momentum, vertex location, and error matrix of  $B_{\text{rec}}$ , along with the position of the beam interaction point and the  $\Upsilon(4S)$  boost, are used to constrain the  $B_{\text{tag}}$  vertex position. Any  $K_S^0$  and  $\Lambda^0$  candidates are used in the  $B_{\text{tag}}$  vertex fit rather than their decay product candidates, so as to reduce bias in the fit due to these long-lived particles. Also, electron and positron candidates that appear to originate from  $\gamma \rightarrow e^+e^-$  conversions are not used in the  $B_{\text{tag}}$  vertex fit. Tracks with large  $\chi^2$  contributions ( $> 6$ ) are removed one at a time, and the fit is repeated, until all remaining tracks pass this requirement. The estimated uncertainty on the measurement of  $\Delta z$  is shown in Figure 3.16. The  $\Delta z$  resolution of approximately  $180 \mu\text{m}$  is limited by the  $B_{\text{tag}}$  vertex position resolution.

A good approximation to the expression used to calculate  $\Delta t$  from  $\Delta z$  is  $\Delta z = \beta\gamma c\Delta t$ , where  $\beta\gamma \approx 0.56$  is the boost. Small corrections are applied for the  $B$  momentum in the  $\Upsilon(4S)$  rest frame and a 20 mrad angular difference between the boost direction and the axis of symmetry of the *BABAR* detector. The following requirements are imposed prior to the  $CP$  asymmetry fit:

$$\begin{aligned} -20 < \Delta t < 20 \text{ ps} , \\ 0.0 < \sigma_{\Delta t} < 2.4 \text{ ps} , \end{aligned} \tag{5.17}$$

where  $\sigma_{\Delta t}$  is the estimated uncertainty on  $\Delta t$ . The distributions of  $\Delta t$  for signal and background are discussed in Section 5.10.

## 5.9 Flavor Tagging

### 5.9.1 The Moriond Tagger

The ultimate objective of the flavor tagging is to determine whether the neutral  $B$  meson that decays into  $J/\psi \pi^0$  is a  $B^0$  or a  $\bar{B}^0$  at the time of the decay of the tagging  $B$  meson. The tagging algorithm employed is called the Moriond tagger, details of which are given in Ref. [24]. The tagger takes advantage of correlations between the flavor and decay products of the tagging  $B$  meson. For example, the charge of the lepton in the decay  $B^0 \rightarrow D^{*-} \ell^+ \nu_\ell$  or  $\bar{B}^0 \rightarrow D^{*+} \ell^- \bar{\nu}_\ell$  indicates whether the decay is of a  $B^0$  or a  $\bar{B}^0$  meson. Similarly, the charge of the kaon in a decay of a  $D$  meson that is in turn the decay product of the original neutral  $B$  meson indicates the flavor of the  $B$  meson (a  $K^+$  implies a  $B^0$  and a  $K^-$  implies a  $\bar{B}^0$ ). Also, the negative charge of the low-momentum pion in the decay  $B^0 \rightarrow D^{*-} X^+ (D^{*-} \rightarrow \bar{D}^0 \pi^-)$  demonstrates that it is a  $B^0$  decay, and there is similar utility in  $\bar{B}^0 \rightarrow D^{*+} X^- (D^{*+} \rightarrow D^0 \pi^+)$  decays.

The tagger takes as input a list that is essentially the `ChargedTracks` list, but with particle identification applied. Discriminating variables are formed and a set of output tag values are calculated for physically motivated categories. These are further grouped into four final categories, which for the rest of this thesis will be referred to as Cat1, Cat2, Cat3, and Cat4. Tagged events are assigned to one of these four mutually exclusive categories. Cat1 includes events with a high-momentum lepton, such as in the  $B^0 \rightarrow D^{*-} \ell^+ \nu_\ell$  decays mentioned above, and it includes events with both a high-momentum lepton and a kaon from a  $D$  decay, as described above, if both pieces of information are available. Cat2 includes events with a kaon and a low-momentum pion with opposite charge. Both Cat2 and Cat3 include events with only the kaon information, and which category the event is assigned to depends on the estimated probability of determining the correct neutral  $B$  meson flavor. Cat3 includes the remaining low-momentum pion events from  $D^*$  decays. All remaining tagged events are assigned to Cat4. Untagged events are excluded from further consideration.

The tagging efficiency  $\epsilon_\alpha$ , the average probability of incorrectly tagging a  $B^0$  as a  $\bar{B}^0$  ( $w_\alpha^{B^0}$ ) or a  $\bar{B}^0$  as a  $B^0$  ( $w_\alpha^{\bar{B}^0}$ ), and  $\Delta w_\alpha = w_\alpha^{B^0} - w_\alpha^{\bar{B}^0}$  are shown in Table 5.9 for each

Table 5.9: The tagging efficiency  $\epsilon_\alpha$ , the average probability of incorrectly tagging a  $B^0$  as a  $\bar{B}^0$  ( $w_\alpha^{B^0}$ ) or a  $\bar{B}^0$  as a  $B^0$  ( $w_\alpha^{\bar{B}^0}$ ),  $\Delta w_\alpha = w_\alpha^{B^0} - w_\alpha^{\bar{B}^0}$ , and the effective tagging efficiency  $Q$  are shown for each category  $\alpha$ , as extracted from the  $B_{\text{flav}}$  data sample.

Category	$\epsilon$ (%)	$w$ (%)	$\Delta w$ (%)	$Q$ (%)
Cat1	$9.1 \pm 0.2$	$3.3 \pm 0.6$	$-1.5 \pm 1.1$	$7.9 \pm 0.3$
Cat2	$16.7 \pm 0.2$	$10.0 \pm 0.7$	$-1.3 \pm 1.1$	$10.7 \pm 0.4$
Cat3	$19.8 \pm 0.3$	$20.9 \pm 0.8$	$-4.4 \pm 1.2$	$6.7 \pm 0.4$
Cat4	$20.0 \pm 0.3$	$31.5 \pm 0.9$	$-2.4 \pm 1.3$	$2.7 \pm 0.3$
All	$65.6 \pm 0.5$			$28.1 \pm 0.7$

tagging category  $\alpha$ . These are the values extracted from a large data sample ( $B_{\text{flav}}$ ) of neutral  $B$  decays to flavor eigenstates consisting of the channels  $D^{(*)-}h^+(h^+ = \pi^+, \rho^+, \text{ and } a_1^+)$  and  $J/\psi K^{*0}(K^{*0} \rightarrow K^+\pi^-)$  [24]. In the  $B_{\text{flav}}$  sample, the decay products reveal the flavor of the neutral  $B$  meson, and so the tagging performance can be characterized by using this sample. The table also shows the effective tagging efficiency,  $Q$ , defined as

$$Q \equiv \sum_{\alpha} \epsilon_{\alpha} (1 - 2w_{\alpha})^2. \quad (5.18)$$

This is a useful measure of the quality of the tagging algorithm since the statistical error of the asymmetry measurement is related to  $Q$  by  $\sigma \propto 1/\sqrt{Q}$ .

### 5.9.2 Tagging Results for Signal and Background Samples

The results of the tagging, in terms of numbers of events, are shown for the signal Monte Carlo sample, background samples, and *onpeak* data in tables 5.10–5.12.

### 5.9.3 Tagging Dependence Study of Event Selection Variables and $\Delta t$

In forming the  $CP$  asymmetry likelihood fit, it is important to identify any dependence of  $m_{\text{ES}}$ ,  $\Delta E$ , the Fisher discriminant, or  $\Delta t$  on the tagging category. This is because the likelihood fit for the  $CP$  asymmetry is subdivided internally based on the tagging

Table 5.10: Tagging results for the signal Monte Carlo sample.

	$B^0 \rightarrow J/\psi \pi^0$ MC		
	$B^0$	$\bar{B}^0$	Total
Cat1	655	638	1293
Cat2	959	966	1925
Cat3	1113	1046	2159
Cat4	1173	1157	2330
None	-	-	3502

Table 5.11: Tagging results for the background samples.

	$B^0 \rightarrow J/\psi K_s^0(\pi^0 \pi^0)$ MC			Inclusive $J/\psi$ MC			$B\bar{B}$ generic MC			continuum data		
	$B^0$	$\bar{B}^0$	Total	$B^0$	$\bar{B}^0$	Total	$B^0$	$\bar{B}^0$	Total	$B^0$	$\bar{B}^0$	Total
Cat1	376	319	695	30	30	60	3	7	10	10	13	23
Cat2	619	562	1181	146	98	244	60	70	130	258	261	519
Cat3	720	621	1341	105	96	201	130	120	250	354	297	651
Cat4	719	696	1415	110	102	212	86	81	167	534	515	1049
None	-	-	2137	-	-	301	-	-	354	-	-	2048

Table 5.12: Tagging results for the full *onpeak* data sample.

	<i>Onpeak</i> data		
	$B^0$	$\bar{B}^0$	Total
Cat1	20	19	39
Cat2	90	68	158
Cat3	111	108	219
Cat4	126	111	237
None	-	-	495

category of each event, as will be clarified in Section 5.11.1. For each sample discussed in Section 5.5, the distributions of these variables are plotted, broken down by tagging category. A Kolmogorov-Smirnov (KS) test is performed between the distributions for each category and the category called Cat4, which has the highest statistics in most cases. The test is based on a normally distributed difference between cumulative density functions, and returns a probability. Two distributions are consistent with each other as long as the result of the KS test is between about 0.01 and 1.0. The plots and comparisons are shown in figures 5.19–5.22. One of two cases that has a result less than 0.01 is the comparison between the non-tagged and Cat4 categories of the continuum background Fisher discriminant distribution. This is not a problem, as only the tagged events are included in the  $CP$  fit. The other case with a KS test result less than 0.01 is the comparison between Cat3 and Cat4 for the signal Monte Carlo sample  $\Delta t$  distribution. This is also acceptable since, as will be explained in Section 5.10, the  $\Delta t$  modeling for the signal is split by tagging category to take just this sort of difference into account.

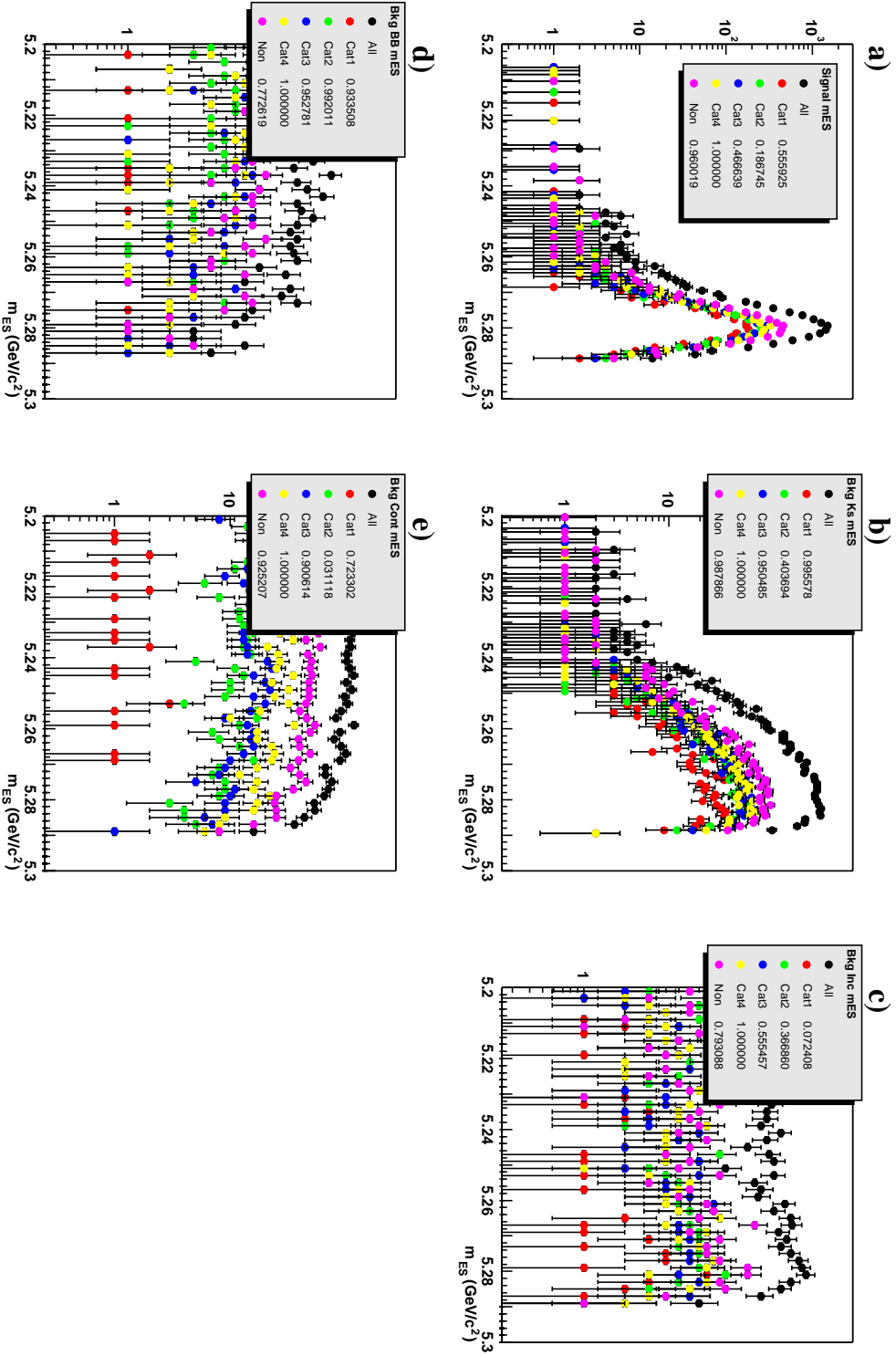


Figure 5.19: The distribution of  $m_{ES}$  is plotted by tagging category for each source type: (a) signal  $B^0 \rightarrow J/\psi \pi^0$ , (b)  $B^0 \rightarrow J/\psi K_S^0(\pi^0 \pi^0)$  background, (c) inclusive  $J/\psi$  background, (d)  $B\bar{B}$  generic, and (e) continuum background. The results of KS tests between Cat4 and each of the other tagging categories are shown in the legends.

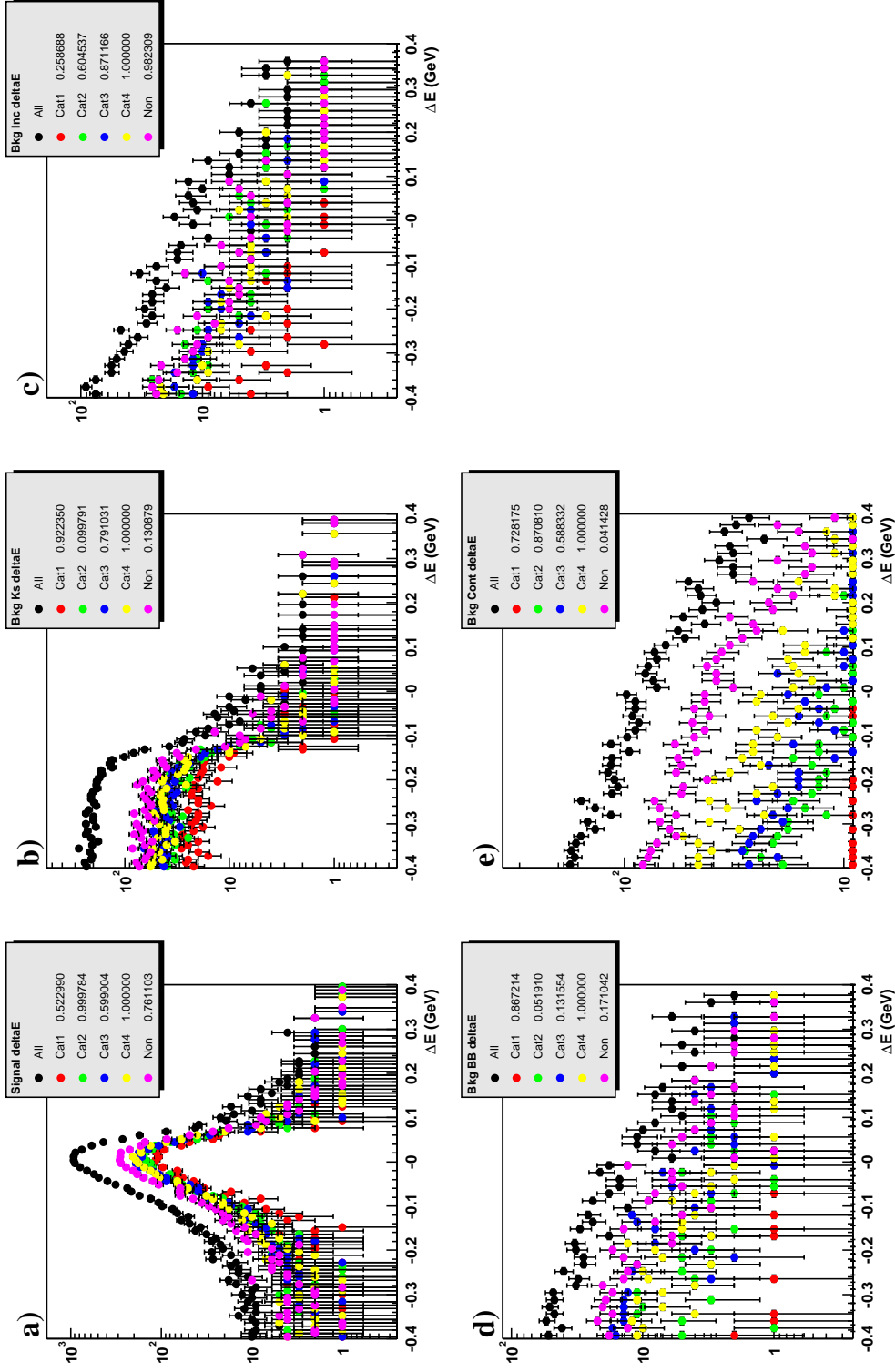


Figure 5.20: The distribution of  $\Delta E$  is plotted by tagging category for each source type: (a) signal  $B^0 \rightarrow J/\psi\pi^0$ , (b)  $B^0 \rightarrow J/\psi K_s^0(\pi^0\pi^0)$  background, (c) inclusive  $J/\psi$  background, (d)  $B\bar{B}$  generic, and (e) continuum background. The results of KS tests between Cat4 and each of the other tagging categories are shown in the legends.

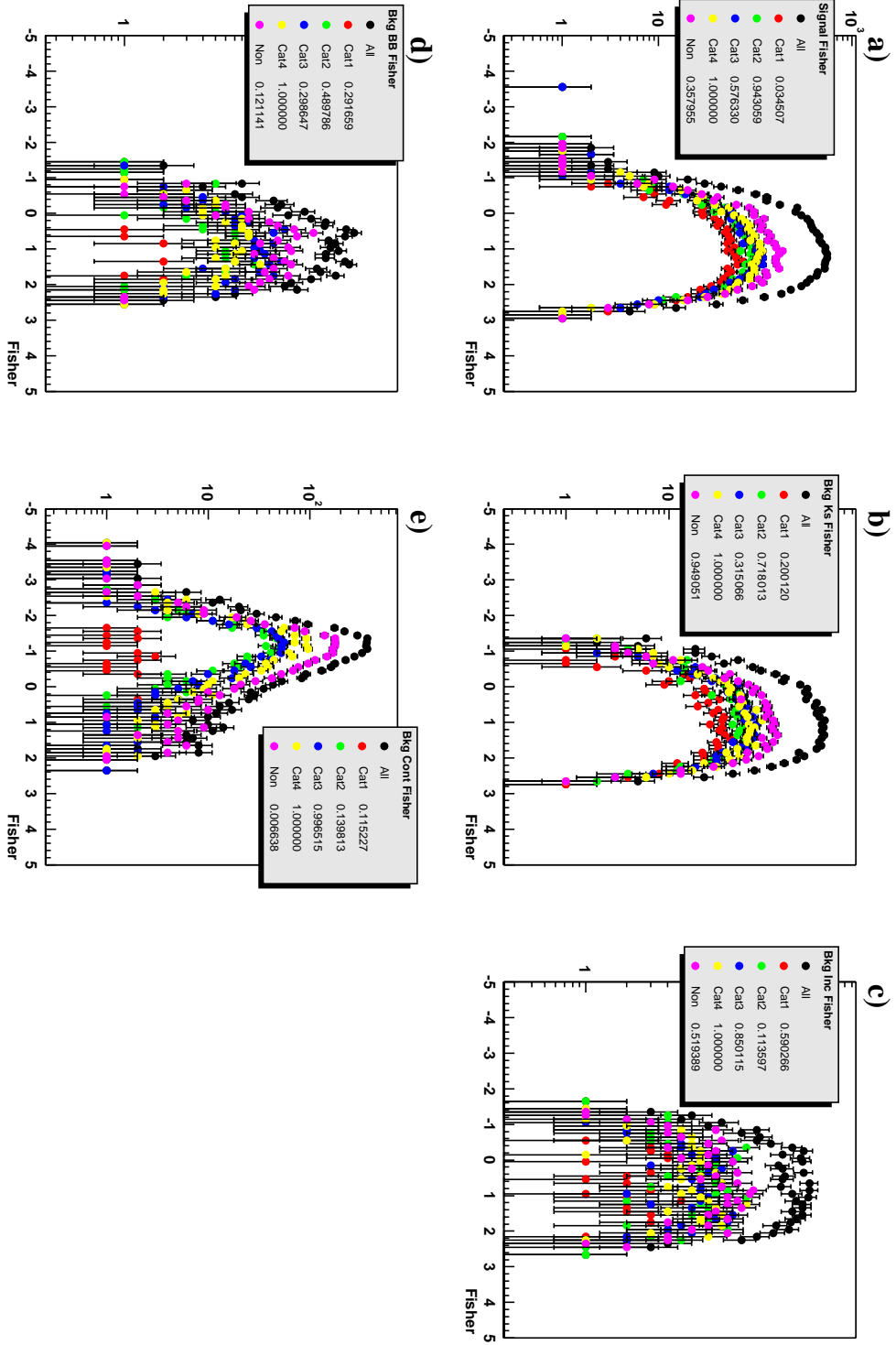


Figure 5.21: The distribution of the Fisher discriminant is plotted by tagging category for each source type: (a) signal  $B^0 \rightarrow J/\psi \pi^0$ , (b)  $B^0 \rightarrow J/\psi K_s^0(\pi^0 \pi^0)$  background, (c) inclusive  $J/\psi$  background, (d)  $B\bar{B}$  generic, and (e) continuum background. The results of KS tests between Cat4 and each of the other tagging categories are shown in the legends.

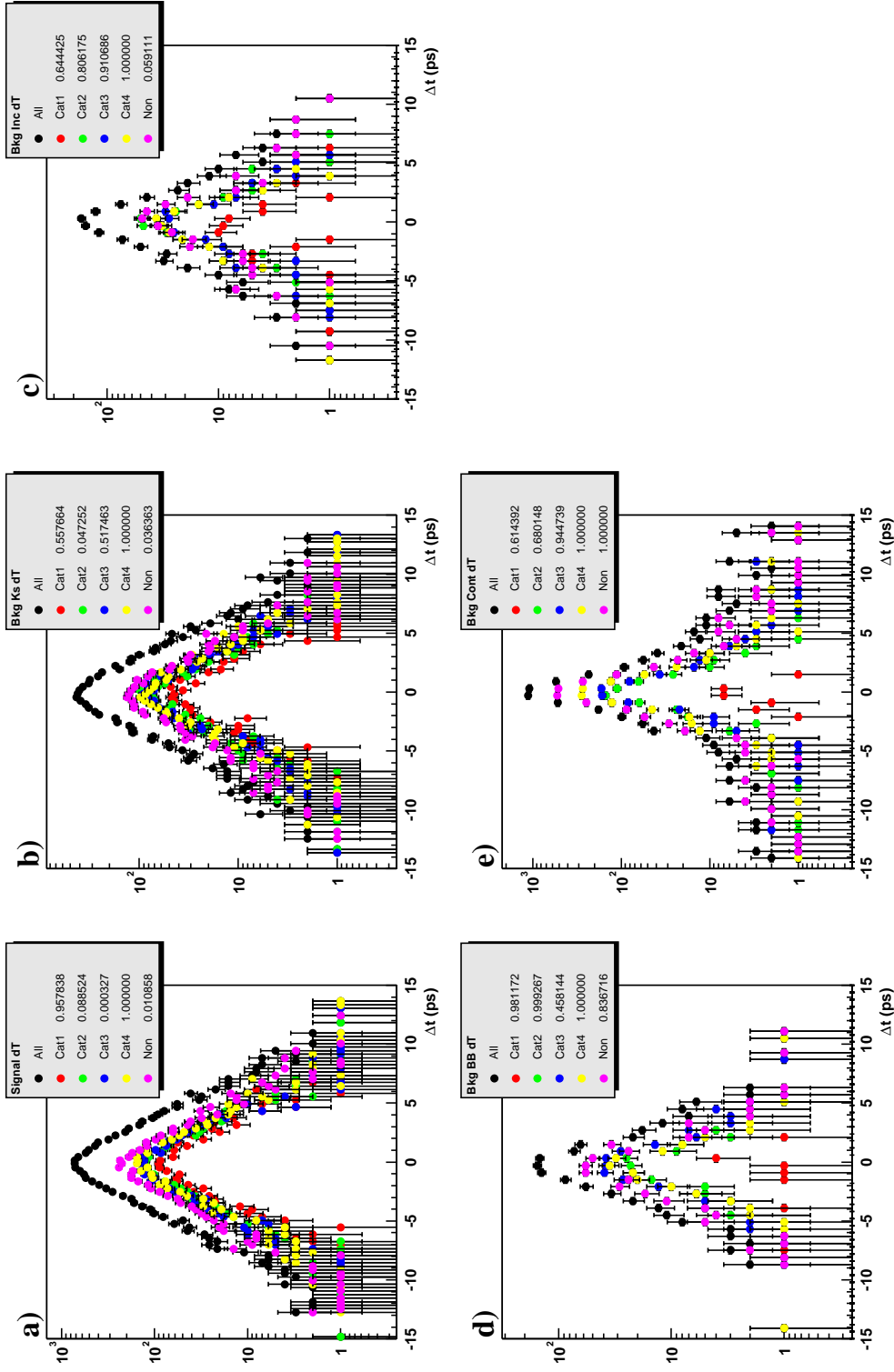


Figure 5.22: The distribution of  $\Delta t$  is plotted by tagging category for each source type: (a) signal  $B^0 \rightarrow J/\psi \pi^0$ , (b)  $B^0 \rightarrow J/\psi K_S^0(\pi^0 \pi^0)$  background, (c) inclusive  $J/\psi$  background, (d)  $B\bar{B}$  generic, and (e) continuum background. The results of KS tests between Cat4 and each of the other tagging categories are shown in the legends.

## 5.10 Probability Density Functions for $\Delta t$

The PDFs used to describe the  $\Delta t$  distributions of the signal and background sources are each a convolution of a resolution function  $\mathcal{R}$  and decay time distribution  $\mathcal{D}$ :

$$\mathcal{P}(\Delta t, \sigma_{\Delta t}) = \mathcal{R}(\delta t, \sigma_{\Delta t}) \otimes \mathcal{D}(\Delta t_{\text{true}}) , \quad (5.19)$$

where  $\Delta t$  and  $\Delta t_{\text{true}}$  are the measured and true decay time differences,  $\delta t = \Delta t - \Delta t_{\text{true}}$ , and  $\sigma_{\Delta t}$  is the estimated event-by-event error on  $\Delta t$ .

### 5.10.1 Signal $B^0 \rightarrow J/\psi \pi^0$

For the signal, the resolution function consists of the sum of three Gaussians, which will be referred to as the core, tail, and outlier:

$$\begin{aligned} \mathcal{R}_{\text{Sig}} = & f_{\text{core}} \frac{e^{-\frac{1}{2} \left( \frac{\Delta t - b_{\text{core}}}{s_{\text{core}} \sigma_{\Delta t}} \right)^2}}{s_{\text{core}} \sigma_{\Delta t} \sqrt{2\pi}} + (1 - f_{\text{core}} - f_{\text{outl}}) \frac{e^{-\frac{1}{2} \left( \frac{\Delta t - b_{\text{tail}}}{s_{\text{tail}} \sigma_{\Delta t}} \right)^2}}{s_{\text{tail}} \sigma_{\Delta t} \sqrt{2\pi}} \\ & + f_{\text{outl}} \frac{e^{-\frac{1}{2} \left( \frac{\Delta t - b_{\text{outl}}}{s_{\text{outl}}} \right)^2}}{s_{\text{outl}} \sqrt{2\pi}} . \end{aligned} \quad (5.20)$$

The means of the Gaussians are biased, by an amount  $b$ , away from zero due to the charm content of the side of the event used for tagging, for some of the events. This occurs because the charmed particles that produce candidate tracks that are part of the  $B_{\text{tag}}$  vertex travel prior to secondary decays and the  $B_{\text{tag}}$  vertex is shifted from the true location. For the core and tail Gaussians this bias is multiplied by the estimated event-by-event uncertainty on  $\Delta t$ . The widths of the core and tail Gaussians are the products of  $\sigma_{\Delta t}$  and a scale factor  $s$ , which appears in the denominators of the exponentials. The outlier Gaussian takes a conventional form.

Of the eight parameters in equation 5.20, three are fixed:  $s_{\text{tail}} = 3.0$  ps,  $s_{\text{outl}} = 8.0$  ps, and  $b_{\text{outl}} = 0.0$  ps. The remaining five are taken from the large  $B_{\text{flav}}$  data sample that was introduced in Section 5.9.1. Actually, both data and Monte Carlo

simulation versions of this sample are used, depending on whether the PDF is being used in a fit to a mixture of Monte Carlo events or *onpeak* data. In either case, the bias of the core Gaussian is split to have different values for each of the four tagging categories.

The decay model is the combination of an exponential and oscillatory  $CP$  decay, as in equation 2.39 for  $f_{\pm}(\Delta t)$ , but is diluted by the effects of  $B$ -flavor tagging:

$$\mathcal{D}_{\alpha,f}^{\pm}(\Delta t) = \frac{e^{-|\Delta t|/\tau_{B^0}}}{4\tau_{B^0}} \left\{ (1 \mp \Delta w_{\alpha}) \pm S_f (1 - 2w_{\alpha}) \sin(\Delta m_d \Delta t) \mp C_f (1 - 2w_{\alpha}) \cos(\Delta m_d \Delta t) \right\}, \quad (5.21)$$

where  $\mathcal{D}_{\alpha,f}^+$  ( $\mathcal{D}_{\alpha,f}^-$ ) is for a  $B^0$  ( $\bar{B}^0$ ) tagging meson. As mentioned previously, the variable  $w_{\alpha}$  is the average probability of incorrectly tagging a  $B^0$  as a  $\bar{B}^0$  ( $w_{\alpha}^{B^0}$ ) or a  $\bar{B}^0$  as a  $B^0$  ( $w_{\alpha}^{\bar{B}^0}$ ), and  $\Delta w_{\alpha} = w_{\alpha}^{B^0} - w_{\alpha}^{\bar{B}^0}$ . The combination  $(1 - 2w_{\alpha})$  is referred to as the dilution and would be one for perfect tagging and zero for random tagging. Both  $w_{\alpha}$  and  $\Delta w_{\alpha}$  are determined using the  $B_{\text{flav}}$  data or Monte Carlo sample, and take on different values for the four tagging categories  $\alpha$ . The values  $\Delta m_d = 0.489 \text{ ps}^{-1}$  and  $\tau_{B^0} = 1.542 \text{ ps}$  that are used are from the 2002 PDG [25]. The extraction of the coefficients  $S_{J/\psi\pi^0}$  and  $C_{J/\psi\pi^0}$  is the primary target of this measurement.

Figure 5.23 shows a fit of the  $B^0 \rightarrow J/\psi\pi^0$  Monte Carlo sample using the  $\Delta t$  PDF. The fixed values of the parameters used in the fit, obtained from the  $B_{\text{flav}}$  sample, can be seen in Table 5.13.

### 5.10.2 $B^0 \rightarrow J/\psi K_s^0(\pi^0\pi^0)$ Background

The PDF used to model the  $\Delta t$  distribution for the  $B^0 \rightarrow J/\psi K_s^0(\pi^0\pi^0)$  background takes on the same form as that of the signal. The resolution function is the triple Gaussian given in equation 5.20, and the physics model is the one given in equation 5.21. The value of  $S_{J/\psi K_s^0} = \sin 2\beta = 0.74$  is fixed from the *BABAR* measurement [24], and  $C_{J/\psi K_s^0}$  is fixed to 0. The splitting of parameters by tagging category is the same as for the signal, and the values are again taken from the Monte Carlo or data  $B_{\text{flav}}$  sample (Table 5.13). Figure 5.24 shows a fit to the  $B^0 \rightarrow J/\psi K_s^0(\pi^0\pi^0)$  Monte Carlo.

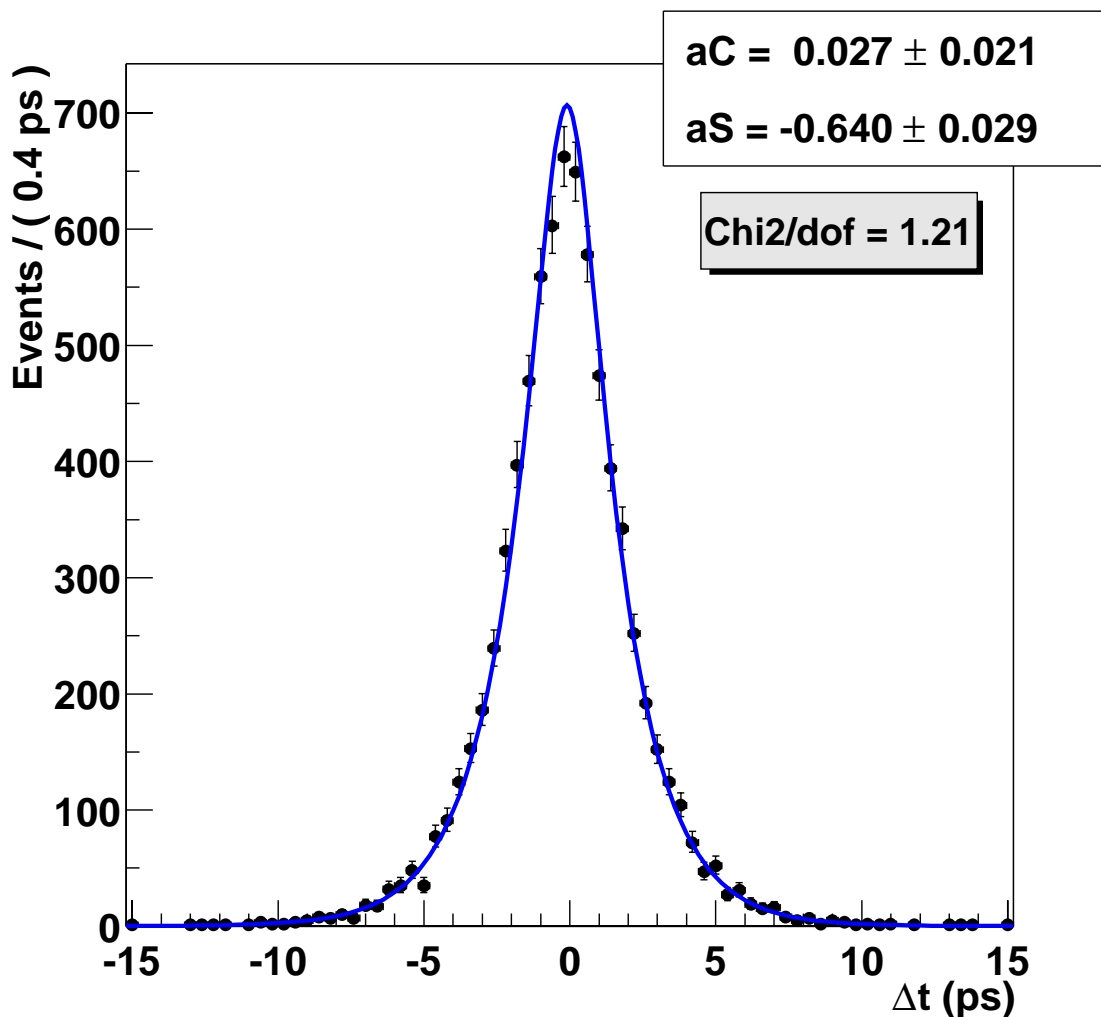


Figure 5.23: Signal  $\Delta t$  PDF fit to the signal Monte Carlo sample. This fit uses the parameters taken from the  $B_{\text{flav}}$  Monte Carlo sample and serves to verify that the parameterization is correct. The only free parameters are the coefficients of the cosine and sine terms of the asymmetry. The Monte Carlo sample was generated with values of  $C_{J/\psi \pi^0} = 0.0$  and  $S_{J/\psi \pi^0} = -0.70$ . The signal  $\Delta t$  PDF used in the full  $CP$  fit uses parameters taken from the  $B_{\text{flav}}$  data sample.

Table 5.13: Values of resolution and physics model parameters used in the  $\Delta t$  PDFs for  $B^0 \rightarrow J/\psi \pi^0$  signal and the  $B^0 \rightarrow J/\psi K_S^0(\pi^0\pi^0)$  background.

Parameter	Value from $B_{\text{flav}}$ Monte Carlo	Value from $B_{\text{flav}}$ data
$b_{\text{core}}$ Cat1	$-0.011 \pm 0.084$ ps	$0.015 \pm 0.063$ ps
$b_{\text{core}}$ Cat2	$-0.220 \pm 0.069$ ps	$-0.229 \pm 0.052$ ps
$b_{\text{core}}$ Cat3	$-0.232 \pm 0.060$ ps	$-0.245 \pm 0.046$ ps
$b_{\text{core}}$ Cat4	$-0.195 \pm 0.061$ ps	$-0.206 \pm 0.047$ ps
$s_{\text{core}}$	$1.147 \pm 0.057$ ps	$1.095 \pm 0.049$ ps
$b_{\text{tail}}$	$-2.734 \pm 1.421$ ps	$-0.992 \pm 0.287$ ps
$s_{\text{tail}}$	3.0 ps	3.0 ps
$b_{\text{outl}}$	0.0 ps	0.0 ps
$s_{\text{outl}}$	8.0 ps	8.0 ps
$f_{\text{core}}$	$0.966 \pm 0.022$	$0.886 \pm 0.021$
$f_{\text{outl}}$	$0.003 \pm 0.0020$	$0.002 \pm 0.001$
$w$ Cat1	$0.0145 \pm 0.010$	$0.033 \pm 0.006$
$w$ Cat2	$0.095 \pm 0.012$	$0.100 \pm 0.007$
$w$ Cat3	$0.188 \pm 0.013$	$0.209 \pm 0.008$
$w$ Cat4	$0.294 \pm 0.014$	$0.315 \pm 0.009$
$\Delta w$ Cat1	$0.013 \pm 0.016$	$-0.015 \pm 0.011$
$\Delta w$ Cat2	$-0.023 \pm 0.017$	$-0.013 \pm 0.011$
$\Delta w$ Cat3	$-0.024 \pm 0.018$	$-0.044 \pm 0.012$
$\Delta w$ Cat4	$-0.033 \pm 0.019$	$-0.024 \pm 0.013$

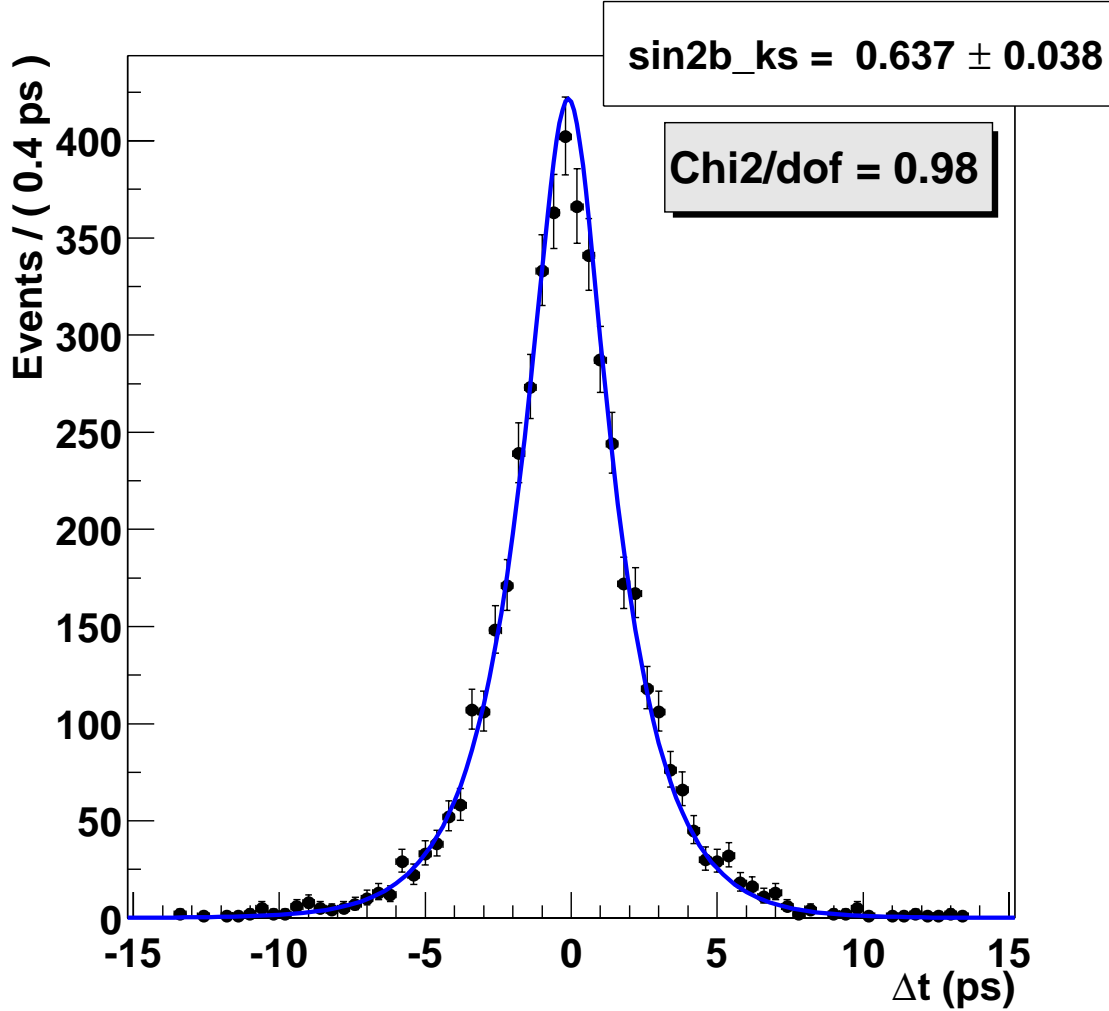


Figure 5.24:  $B^0 \rightarrow J/\psi K_S^0(\pi^0\pi^0)$   $\Delta t$  PDF fit to the  $B^0 \rightarrow J/\psi K_S^0(\pi^0\pi^0)$  Monte Carlo sample. This fit uses the parameters taken from the  $B_{\text{flav}}$  Monte Carlo sample and serves to verify that the parameterization is correct. The only free parameter is the coefficient of the sine term of the asymmetry. The Monte Carlo sample was generated with  $S_{J/\psi K_S^0} = 0.70$ . The  $B^0 \rightarrow J/\psi K_S^0(\pi^0\pi^0)$   $\Delta t$  PDF used in the full  $CP$  fit uses parameters taken from the  $B_{\text{flav}}$  data sample.

### 5.10.3 Inclusive $J/\psi$ Background

The parameterization of the  $\Delta t$  PDF for the inclusive  $J/\psi$  background consists of a lifetime component and a prompt component. Recalling that the  $J/\psi$  is properly reconstructed as coming from the  $B_{\text{rec}}$  meson for this source, the lifetime component accounts for the regime where remaining true  $B_{\text{rec}}$  tracks are **not** erroneously used in determining the  $B_{\text{tag}}$  vertex position. The prompt component accounts for the case when true  $B_{\text{rec}}$  tracks are erroneously used in calculating the location of the  $B_{\text{rec}}$  vertex, pulling the lifetime toward zero. The form of the PDF is

$$\begin{aligned} \mathcal{P}_{\text{Inc}} \Delta t = & f_{\text{lifetime}} \left\{ f_{\text{core}}^{\text{life}} \frac{e^{-\frac{1}{2} \left( \frac{\Delta t - b_{\text{core}}^{\text{life}}}{s_{\text{core}}^{\text{life}} \sigma_{\Delta t}} \right)^2}}{s_{\text{core}}^{\text{life}} \sigma_{\Delta t} \sqrt{2\pi}} + (1 - f_{\text{core}}^{\text{life}}) \frac{e^{-\frac{1}{2} \left( \frac{\Delta t - b_{\text{outl}}}{s_{\text{outl}}} \right)^2}}{s_{\text{outl}} \sqrt{2\pi}} \right\} \otimes e^{-\frac{|\Delta t|}{\tau_B}} \\ & + f_{\text{prompt}} \left\{ f_{\text{core}}^{\text{prompt}} \frac{e^{-\frac{1}{2} \left( \frac{\Delta t - b_{\text{core}}^{\text{prompt}}}{s_{\text{core}}^{\text{prompt}} \sigma_{\Delta t}} \right)^2}}{s_{\text{core}}^{\text{prompt}} \sigma_{\Delta t} \sqrt{2\pi}} + (1 - f_{\text{core}}^{\text{prompt}}) \frac{e^{-\frac{1}{2} \left( \frac{\Delta t - b_{\text{outl}}}{s_{\text{outl}}} \right)^2}}{s_{\text{outl}} \sqrt{2\pi}} \right\}. \quad (5.22) \end{aligned}$$

The fraction that is the lifetime component,  $f_{\text{lifetime}}$ , is one of the parameters taken from a likelihood fit to the inclusive  $J/\psi$  Monte Carlo sample. The prompt fraction,  $f_{\text{prompt}}$ , is just  $1 - f_{\text{lifetime}}$ . The resolution function for each component is a double Gaussian, where the width of each core Gaussian is the product of the estimated event-by-event uncertainty and a scale factor. Once again, the bias and scale factor of the outlier Gaussians are fixed to 0.0 ps and 8.0 ps respectively.

The decay lifetime parameter,  $\tau_B$ , is also determined in the fit to the inclusive  $J/\psi$  Monte Carlo sample. As expected, the resulting value falls in the range of the neutral and charged  $B$  meson lifetimes ( $1.542 \pm 0.016$  ps and  $1.674 \pm 0.018$  ps respectively in the 2002 PDG [25]).

The plot of the fit to the inclusive  $J/\psi$  Monte Carlo sample is shown in Figure 5.25, along with the resulting parameters.

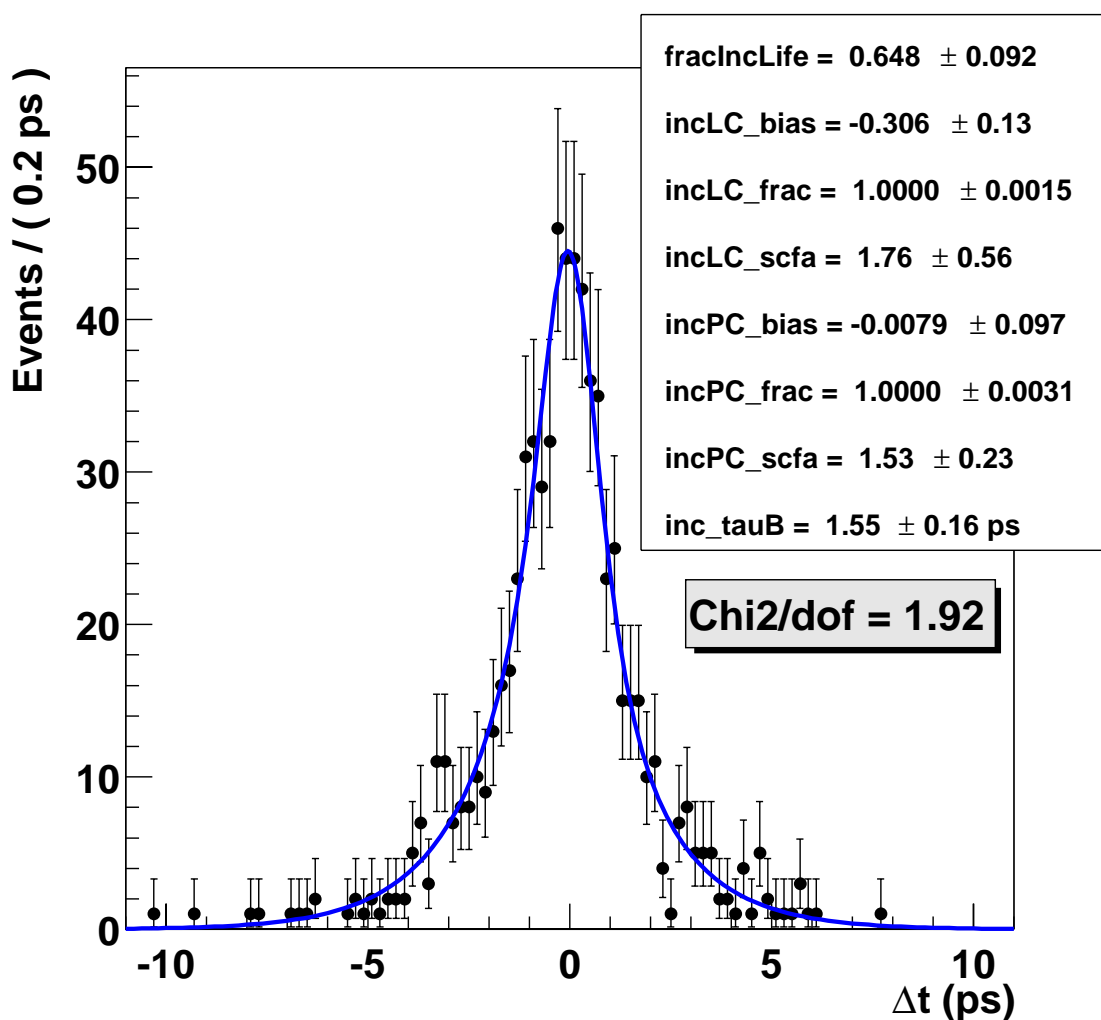


Figure 5.25: Inclusive  $J/\psi$   $\Delta t$  PDF fit to the inclusive  $J/\psi$  Monte Carlo sample. The fit parameters of the PDF, which includes a lifetime component (L) and a prompt component (P), each dominated by a core (C) Gaussian, are discussed in Section 5.10.3 of the text. The PDF used in the full  $CP$  fit uses the parameters that result from the above fit.

### 5.10.4 $B\bar{B}$ Generic Background

The form of the PDF used to model the  $B\bar{B}$  generic background  $\Delta t$  shape is the same as that used for inclusive  $J/\psi$ . However, in this case the parameters in equation 5.22 are determined from a likelihood fit to the filtered  $B\bar{B}$  generic sample. The prompt component fits for the scenario where the two lepton candidates used to reconstruct the  $J/\psi$  candidate come from different  $B$  mesons. The lifetime component covers the case when the lepton candidates come from the same  $B$  meson. The relative fraction of the two components that results from the fit agrees with the expectations for this sample, as described in Section 5.5. The fit and parameters are shown in Figure 5.26.

### 5.10.5 Continuum Background

The  $\Delta t$  PDF for the continuum background consists of a double Gaussian of the following form:

$$\mathcal{P}_{\text{Cont}} \Delta t = f_{\text{core}} \frac{e^{-\frac{1}{2}(\frac{\Delta t - b_{\text{core}}}{s_{\text{core}} \sigma_{\Delta t}})^2}}{s_{\text{core}} \sigma_{\Delta t} \sqrt{2\pi}} + (1 - f_{\text{core}}) \frac{e^{-\frac{1}{2}(\frac{\Delta t - b_{\text{outl}}}{s_{\text{outl}}})^2}}{s_{\text{outl}} \sqrt{2\pi}}, \quad (5.23)$$

where  $b_{\text{outl}} = 0.0$  ps and  $s_{\text{outl}} = 8.0$  ps are fixed and the estimated event-by-event uncertainty on  $\Delta t$  only multiplies the scale factor for the core Gaussian. The three parameters  $f_{\text{core}}$ ,  $b_{\text{core}}$ , and  $s_{\text{core}}$  are determined from a fit to the  $J/\psi_{\text{fake}}$  data sample, the results of which are shown in Figure 5.27.

## 5.11 CP Asymmetry Likelihood Fits

### 5.11.1 Fit Implementation

The  $CP$  asymmetry unbinned likelihood fit, as with the yield fits, is implemented using the RooFit package, where a compiled C++ class has been written to instantiate

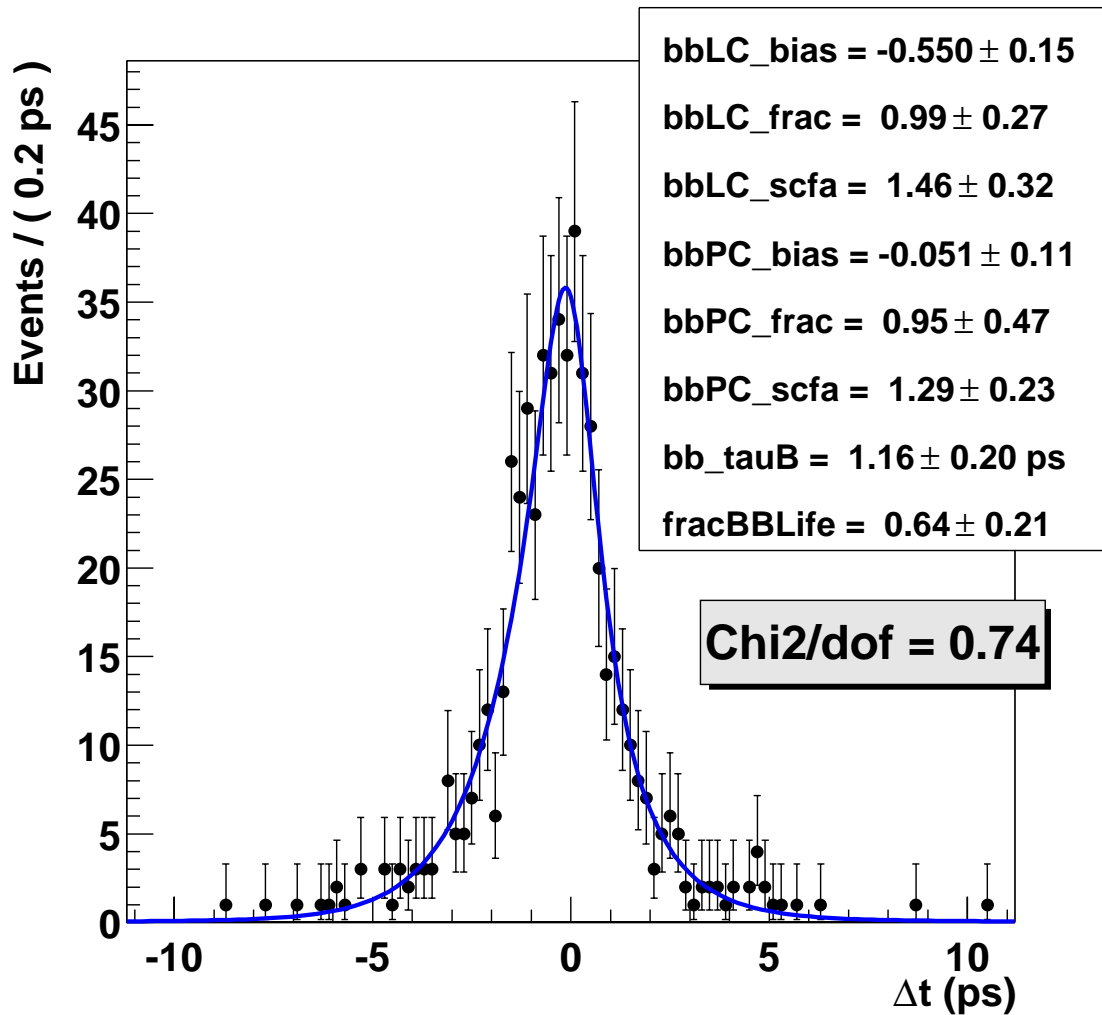


Figure 5.26:  $\Delta t$  PDF fit for  $B\bar{B}$  generic background, as determined from a fit to the generator-level filtered  $B\bar{B}$  generic Monte Carlo sample. The fit parameters are discussed in Section 5.10.4 of the text. The PDF used in the full  $CP$  fit uses the parameters that result from the above fit.

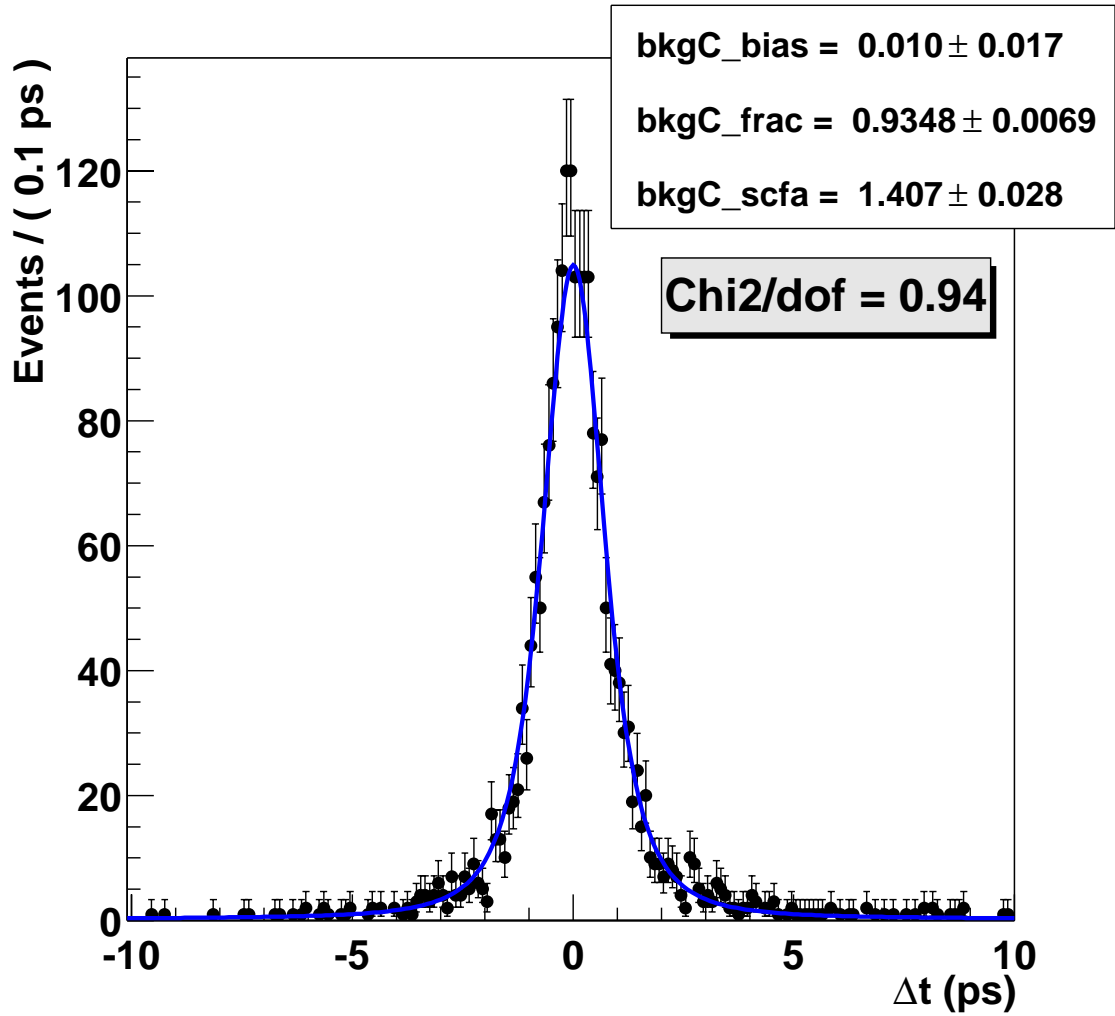


Figure 5.27: Continuum background  $\Delta t$  PDF, as determined from a fit to the  $J/\psi_{\text{fake}}$  data sample. The PDF used in the full  $CP$  fit uses the parameters that result from the above fit.

and combine the event selection and  $\Delta t$  PDFs. The form of the likelihood is

$$\begin{aligned} \mathcal{L} = & \frac{e^{-\sum_{j=1}^5 n_j}}{N!} \prod_{i=1}^N \\ & \{ f_{\alpha_i}^{\text{Sig}} n_{\text{Sig}} (\mathcal{P}_{\text{Sig}} m_{\text{ES}} \mathcal{P}_{\text{Sig } \Delta E} \mathcal{P}_{\text{Sig } \Delta t}) \\ & + f_{\alpha_i}^{\text{Ks}} n_{\text{Ks}} (\mathcal{P}_{\text{Ks}} m_{\text{ES}-\Delta E} \mathcal{P}_{\text{Ks } \Delta t}) \\ & + f_{\alpha_i}^{\text{Inc}} n_{\text{Inc}} (\mathcal{P}_{\text{Inc}} m_{\text{ES}-\Delta E} \mathcal{P}_{\text{Inc } \Delta t}) \\ & + f_{\alpha_i}^{\text{BB}} n_{\text{BB}} (\mathcal{P}_{\text{BB}} m_{\text{ES}} \mathcal{P}_{\text{BB } \Delta E} \mathcal{P}_{\text{BB } \Delta t}) \\ & + f_{\alpha_i}^{\text{Cont}} n_{\text{Cont}} (\mathcal{P}_{\text{Cont}} m_{\text{ES}} \mathcal{P}_{\text{Cont } \Delta E} \mathcal{P}_{\text{Cont } \Delta t}) \} , \end{aligned} \quad (5.24)$$

where  $N$  is the number of input events. A key difference between this likelihood and the one defined in equation 5.16 for the yield tests is that this likelihood includes the  $\Delta t$  PDFs for the signal and backgrounds. It also utilizes the tagging information. This fit is performed on tagged events only, and since each event  $i$  has an associated tagging category  $\alpha_i$ , the parameters  $f_{\alpha_i}^j$  are the tagging fractions for each of the categories (Cat1, Cat2, Cat3, or Cat4) for each of the signal or background types  $j$ . To keep the sum of the tagging fractions for each source equal to one, the fraction of Cat4 is fixed to:

$$f_{\text{Cat4}}^j = (1 - f_{\text{Cat1}}^j - f_{\text{Cat2}}^j - f_{\text{Cat3}}^j) . \quad (5.25)$$

The values for the tagging fractions are taken from the  $B_{\text{flav}}$  data sample for  $B^0 \rightarrow J/\psi \pi^0$  signal and  $B^0 \rightarrow J/\psi K_S^0(\pi^0 \pi^0)$  background. They are taken from the relevant Monte Carlo sample for inclusive  $J/\psi$  background and  $B\bar{B}$  generic background, and they are taken from the  $J/\psi_{\text{fake}}$  data sample for the continuum background. The values of these fractions are given in Table 5.14.

In addition to utilizing the tagging and  $\Delta t$  information, the  $CP$  asymmetry fits have two important differences with respect to the validation yield fits.

First, a blind  $CP$  fit to the data revealed that the Fisher discriminant output in one bin around  $-1.6$  differs between data and the likelihood fit result by an amount that either represents a discrepancy or a large statistical fluctuation. The decision was

Table 5.14: Tagging fractions for signal and background samples. The text of Section 5.11.1 gives the origins of these numbers. Note that  $f_{\text{Cat4}}^j$  is not given in the table, for it is constrained through equation 5.25.

	$B^0 \rightarrow J/\psi \pi^0$ and $B^0 \rightarrow J/\psi K_s^0(\pi^0 \pi^0)$	Inclusive $J/\psi$	$B\bar{B}$ generic	Continuum
$f_{\text{Cat1}}$	0.1389	0.0837	0.01795	0.01026
$f_{\text{Cat2}}$	0.2540	0.3403	0.2334	0.2315
$f_{\text{Cat3}}$	0.3025	0.2803	0.4488	0.2904

thus made to cut on the Fisher variable, requiring it to be greater than  $-0.8$ . This requirement is 99% efficient for signal and rejects 71% of the continuum background. The plot of the projection of the Fisher discriminant is included in Figure 5.34, which is only used as a cross-check (Section 5.13).

Second, the location of the peak of the  $\Delta E$  distribution for the signal differs for data and Monte Carlo simulation and it is best to let this parameter float in any fit to data. There is another cross-check in Section 5.13 that shows the effects of fixing the value to the one extracted from the signal Monte Carlo sample.

Unless otherwise noted, the nominal fit configuration is to place the cut on the Fisher discriminant and float the signal  $\Delta E$  peak position.

### 5.11.2 Blinding Strategy

The blinding strategy used is the same as that for the “golden mode” *BABAR* measurements. In this case, when fitting *onpeak* data, the values of  $C_{J/\psi \pi^0}$  and  $S_{J/\psi \pi^0}$  are shifted by a hidden offset and undergo a hidden sign flip, where the offset and sign flip are determined by an ASCII character string. Furthermore, the plot of  $\Delta t$  is not split by  $B$  meson flavor until the asymmetry result is unblinded.

### 5.11.3 Time-Dependent Fits to Mixtures of Samples

To check that the fitting technique can separate the signal and background contributions, and can extract the  $CP$  asymmetry coefficients, the full  $CP$  asymmetry fit is

Table 5.15: Expectations are shown for  $81 \text{ fb}^{-1}$ , along with the total tagging efficiencies and efficiencies of the requirement on the Fisher discriminant, given sequentially, with statistical uncertainties. The last column shows the number of events of each sample type used in  $CP$  fits to mixtures of samples.

Sample type	Expected before tagging and fisher cut	Tagging efficiency (%)	Efficiency (%) of cut on $-0.8 < \mathcal{F}$	$CP$ fit expectation
$B^0 \rightarrow J/\psi \pi^0$ signal	80	$65.6 \pm 0.6$	$99.2 \pm 0.1$	52
$B^0 \rightarrow J/\psi K_s^0(\pi^0 \pi^0)$ background	194	$65.6 \pm 0.6$	$98.7 \pm 0.2$	125
Inclusive $J/\psi$ background	101	$70.4 \pm 1.4$	$95.5 \pm 0.8$	68
$B\bar{B}$ generic background	83	$61.1 \pm 1.6$	$98.0 \pm 0.6$	50
Continuum background	406	$52.3 \pm 0.8$	$27.0 \pm 0.9$	57

performed to mixtures of Monte Carlo samples and the  $J/\psi_{\text{fake}}$  sample equivalent to  $81 \text{ fb}^{-1}$ . The amount of each sample to include in the fits is calculated starting from the expectations that were given in Table 5.8. These numbers are then multiplied by the total tagging efficiencies and the efficiency for the cut on the Fisher discriminant. These numbers and the calculated expectations are shown in Table 5.15.

The results of  $CP$  fits to mixtures of Monte Carlo samples and the  $J/\psi_{\text{fake}}$  data sample are given in Table 5.16 and shown in Figure 5.28. By performing the fit on collections of events of known signal and background composition, and finding good matches between the expectations and the fit results, this study verifies that the fit is able to separate the different contributions. In addition, this goes beyond what was done for the yield fit consistency check since this likelihood fit includes the  $\Delta t$  information and the fit finds values for  $C_{J/\psi \pi^0}$  and  $S_{J/\psi \pi^0}$  that agree with the expectations from the generated Monte Carlo simulation reasonably well.

#### 5.11.4 Time-Dependent Fit to Full Dataset

The unblinded results of the  $CP$  fit to  $81.1 \text{ fb}^{-1}$  of *onpeak* data, for all free parameters, are given in Table 5.17. There are  $40 \pm 7$  signal events in the total sample of 438 selected events. The table includes the values of the  $CP$  asymmetry coefficients, with statistical uncertainties:  $C_{J/\psi \pi^0} = 0.38 \pm 0.41$  and  $S_{J/\psi \pi^0} = 0.05 \pm 0.49$ .

Table 5.16: Results of  $CP$  likelihood fits to mixtures of signal and background Monte Carlo events and the  $J/\psi_{\text{fake}}$  data equivalent to  $81 \text{ fb}^{-1}$ . The projections of the PDFs are shown in Figure 5.28.

	Fit results	Expected	Global correlation
Mixture 1			
$C_{J/\psi\pi^0}$	$-0.47 \pm 0.27$	0	0.172
$S_{J/\psi\pi^0}$	$-0.19 \pm 0.37$	-0.7	0.172
Signal $\Delta E$ peak position (MeV)	$0.0121 \pm 0.0050$	0.0039	0.057
$B^0 \rightarrow J/\psi\pi^0$ signal	$57.8 \pm 8.2$	52	0.097
$B^0 \rightarrow J/\psi K_S^0(\pi^0\pi^0)$ background	$140.7 \pm 18.7$	125	0.655
Inclusive $J/\psi$ background	$76.5 \pm 32.1$	68	0.858
$B\bar{B}$ generic background	$70.6 \pm 23.7$	50	0.839
Continuum background	$38.5 \pm 18.1$	57	0.751
Mixture 2			
$C_{J/\psi\pi^0}$	$0.02 \pm 0.28$	0	0.040
$S_{J/\psi\pi^0}$	$-0.25 \pm 0.37$	-0.7	0.041
Signal $\Delta E$ peak position (MeV)	$-0.0010 \pm 0.0055$	0.0039	0.093
$B^0 \rightarrow J/\psi\pi^0$ signal	$61.8 \pm 8.7$	52	0.129
$B^0 \rightarrow J/\psi K_S^0(\pi^0\pi^0)$ background	$132.7 \pm 16.7$	125	0.594
Inclusive $J/\psi$ background	$43.7 \pm 26.5$	68	0.829
$B\bar{B}$ generic background	$58.7 \pm 21.5$	50	0.827
Continuum background	$56.0 \pm 17.9$	57	0.742

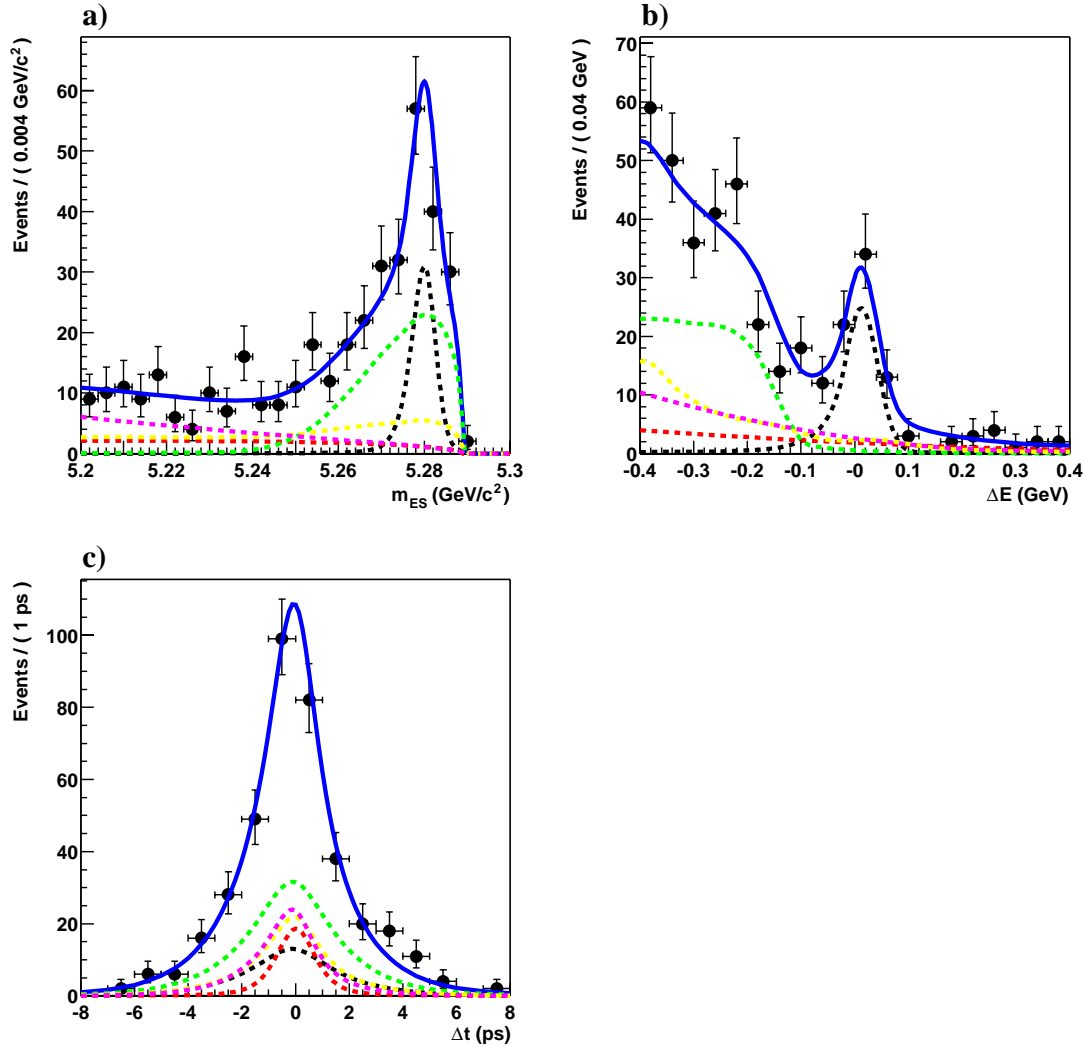


Figure 5.28: Projections in (a)  $m_{ES}$ , (b)  $\Delta E$ , and (c)  $\Delta t$  for the results of a  $CP$  fit to a mixture of signal and background Monte Carlo events and  $J/\psi_{\text{fake}}$  data equivalent to  $81 \text{ fb}^{-1}$ . Black dashed: signal  $B^0 \rightarrow J/\psi \pi^0$ . Green dashed:  $B^0 \rightarrow J/\psi K_s^0(\pi^0\pi^0)$  background. Yellow dashed: inclusive  $J/\psi$  background. Magenta dashed:  $B\bar{B}$  generic background. Red dashed: continuum background. Blue solid: total. The numerical results are given in Table 5.16.

Table 5.17: Results of a  $CP$  likelihood fit to  $81.1 \text{ fb}^{-1}$  of *onpeak* data, for the full region  $-0.4 < \Delta E < 0.4 \text{ GeV}$  and  $m_{\text{ES}} > 5.2 \text{ GeV}/c^2$ . Errors are statistical only. The projections of the PDFs are shown in Figure 5.29.

	Fit results	Expected	Global correlation
$C_{J/\psi\pi^0}$	$0.38 \pm 0.41$	–	0.134
$S_{J/\psi\pi^0}$	$0.05 \pm 0.49$	–	0.148
Signal $\Delta E$ peak position (MeV)	$-0.0132 \pm 0.0072$	–	0.145
$B^0 \rightarrow J/\psi\pi^0$ signal	$40.0 \pm 7.3$	$\sim 52$	0.107
$B^0 \rightarrow J/\psi K_S^0(\pi^0\pi^0)$ background	$140.2 \pm 19.4$	125	0.649
Inclusive $J/\psi$ background	$108.8 \pm 34.9$	68	0.852
$B\bar{B}$ generic background	$51.9 \pm 24.9$	50	0.821
Continuum background	$96.9 \pm 21.7$	57	0.731

The projections in  $m_{\text{ES}}$ ,  $\Delta E$ , and  $\Delta t$  are shown in Figure 5.29. The sub-figures 5.29(a), 5.29(c), and 5.29(e) each show the contributions of the signal and four background types, as well as the data points and total fit results, over the full region  $-0.4 < \Delta E < 0.4 \text{ GeV}$  and  $m_{\text{ES}} > 5.2 \text{ GeV}/c^2$ . Figure 5.29(b) shows the projection in  $m_{\text{ES}}$  with the requirement  $-0.11 < \Delta E < 0.11 \text{ GeV}$ , which reveals the signal peak more clearly. Within this plot, the further restricted region  $m_{\text{ES}} > 5.27 \text{ GeV}/c^2$  contains 49 data events, of which about 12 events are fit as background. The enhancement in the background distribution at large  $m_{\text{ES}}$ , visible in this plot, is due to contributions from  $B^0 \rightarrow J/\psi K_S^0(\pi^0\pi^0)$  and inclusive  $J/\psi$  decays. Figure 5.29(d) shows the projection in  $\Delta E$  with the requirement  $-0.11 < \Delta E < 0.11 \text{ GeV}$ . The signal peak is visible, as is its small shift toward negative  $\Delta E$ . Figure 5.29(f) shows the projection in  $\Delta t$  with the requirements  $-0.11 < \Delta E < 0.11 \text{ GeV}$  and  $m_{\text{ES}} > 5.27 \text{ GeV}/c^2$ .

The yields and asymmetry as functions of  $\Delta t$ , overlaid with projections of the likelihood fit results, are shown in Figure 5.30. The yields are shown separately for  $B^0$ - and  $\bar{B}^0$ -flavor tags, in figures 5.30(a) and 5.30(b), respectively. Figure 5.30(c) shows the observed asymmetry, proportional to the sum of sine and cosine terms, diluted by the effects of sometimes incorrectly tagging the  $B$ -meson flavor.

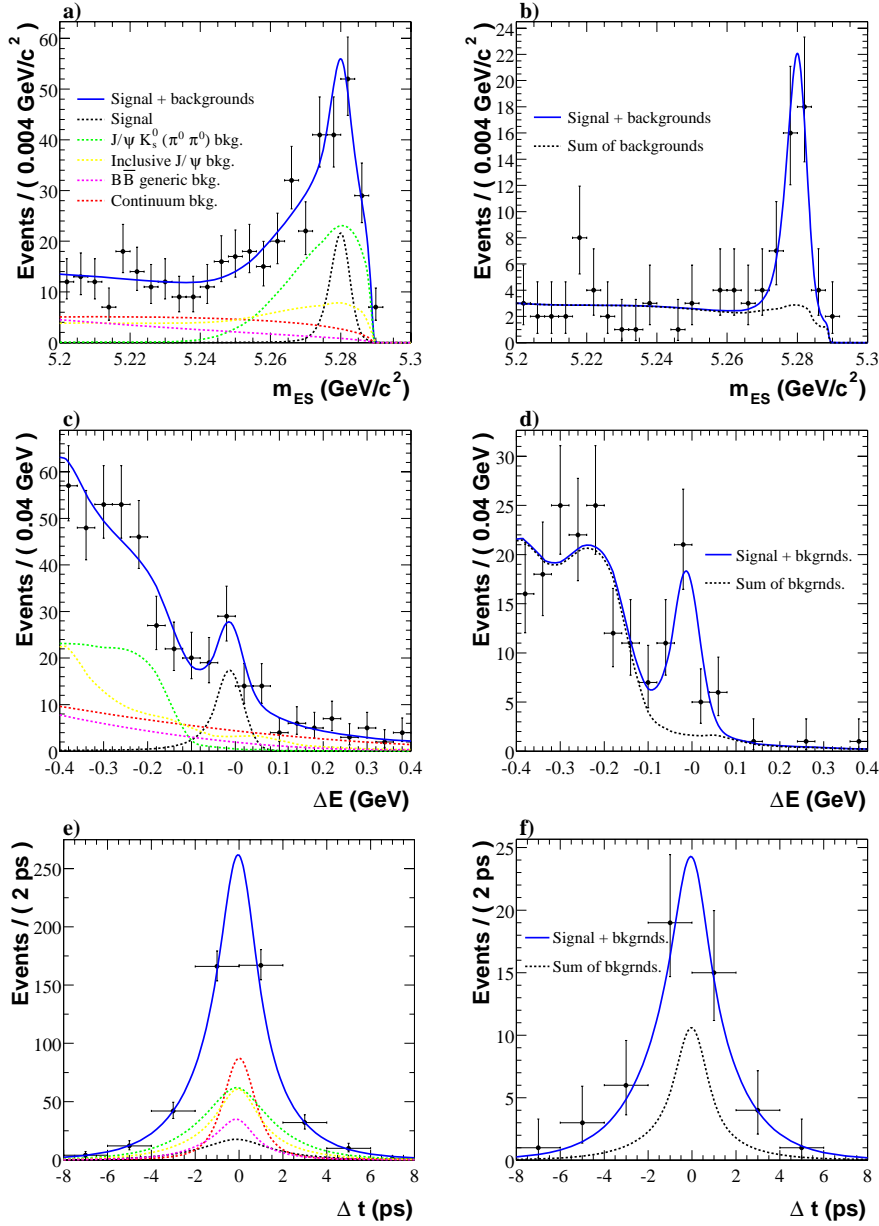


Figure 5.29: Projections in a)  $m_{ES}$ , c)  $\Delta E$ , and e)  $\Delta t$  for the results of a  $CP$  fit to  $81.1 \text{ fb}^{-1}$  of *onpeak* data, for the full region  $-0.4 < \Delta E < 0.4 \text{ GeV}$  and  $m_{ES} > 5.2 \text{ GeV}/c^2$ . The legend in a) applies to the plots on the left hand side. The projection in b)  $m_{ES}$  is shown with the requirement  $-0.11 < \Delta E < 0.11 \text{ GeV}$ . The projection in d)  $\Delta E$  is shown with the requirement  $m_{ES} > 5.27 \text{ GeV}/c^2$ . The projection in f)  $\Delta t$  is shown with the requirements  $-0.11 < \Delta E < 0.11 \text{ GeV}$  and  $m_{ES} > 5.27 \text{ GeV}/c^2$ . The numerical results are given in Table 5.17.

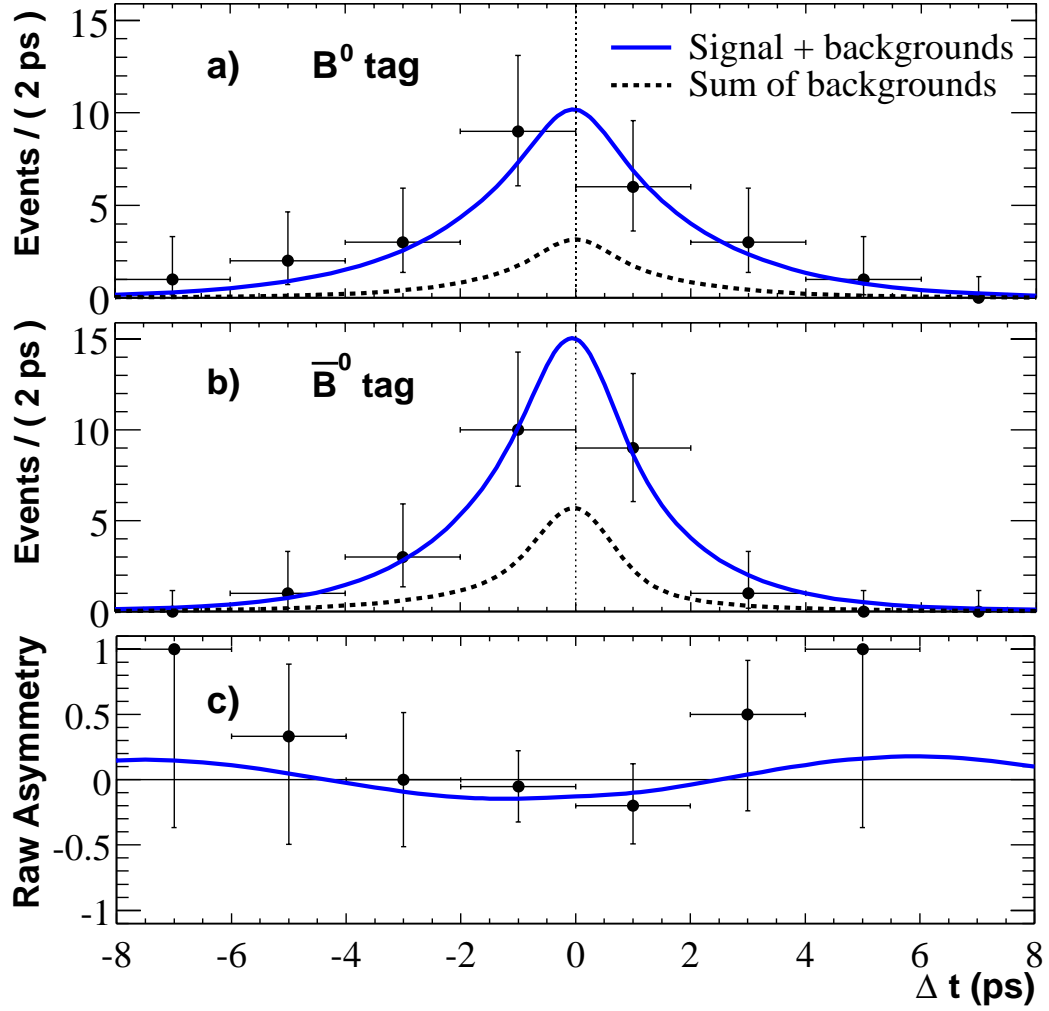


Figure 5.30: Distributions of events a) with a  $B^0$  tag ( $N_{B^0}$ ), b) with a  $\bar{B}^0$  tag ( $N_{\bar{B}^0}$ ), and c) the raw asymmetry  $(N_{B^0} - N_{\bar{B}^0}) / (N_{B^0} + N_{\bar{B}^0})$ , as functions of  $\Delta t$ . Candidates in these plots are required to satisfy  $-0.11 < \Delta E < 0.11$  GeV and  $m_{ES} > 5.27$  GeV/ $c^2$ . Of the 49 signal and background events in this region, 25 have a  $B^0$  tag and 24 have a  $\bar{B}^0$  tag, with fit background contributions of approximately 5 and 7 events, respectively. The curves are projections that use the values of the other variables in the likelihood to determine the contributions to the signal and backgrounds.

## 5.12 Systematic Studies

### 5.12.1 Variation of PDF Parameters and Tagging Fractions

The general procedure is to repeat the fit with each parameter varied by  $\pm 1\sigma$ . For each of the two asymmetry coefficients, the differences between the value with and without the variation is calculated and the larger of the two differences from shifting the parameter up and down is taken as the contribution to the uncertainty. These individual systematic errors are then combined in quadrature. They are presented here, grouped by the source of the error and then given in total. In some cases the size of the variation requires special consideration, and those situations are also discussed below.

- Parameters from  $m_{\text{ES}}$  and  $\Delta E$  PDFs. Unless otherwise noted here, the magnitude of the variations for these parameters are taken from the same sources as the parameters themselves. For the signal, the Monte Carlo events have been reanalyzed with an energy rescaling, particle killing, and an energy dependent smearing (ranging from 1.6% to 3.0%), all applied to the neutrals. The differences between the  $m_{\text{ES}}$  and  $\Delta E$  PDF parameter values with and without these corrections are examined. In any case where this difference is greater than the statistical error on the value of the parameter found in the fit to the original sample, this difference is used as the size of the parameter variation for determining the contribution to the systematic uncertainty. This was the case for all of the signal  $\Delta E$  parameters, but for none of the signal  $m_{\text{ES}}$  parameters. The sizes of the variations, and the resulting systematics, can be seen in Table 5.18.
- $m_{\text{ES}}$  endpoint. The  $m_{\text{ES}}$  endpoint, as used in the Argus function, is varied by  $\pm 0.002 \text{ GeV}/c^2$ .

The results of the variation of the above parameters can be seen in Table 5.18. The systematic due to these sources is 0.048 on  $C_{J/\psi \pi^0}$  and 0.130 on  $S_{J/\psi \pi^0}$ .

- Tagging fractions. The amounts by which the tagging fractions are varied are calculated from the counting statistics of the samples from which these fractions

are extracted.

The results of the tagging fraction variations are shown in Table 5.19 and contribute a systematic uncertainty of 0.002 on  $C_{J/\psi\pi^0}$  and 0.007 on  $S_{J/\psi\pi^0}$ .

- $\Delta t$  resolutions. For the most part, the sizes of the variations of the  $\Delta t$  parameters are taken from the same sources as the parameters themselves. The exceptions are for the tail scale factor, the outlier bias, and the outlier scale factor. In these cases, the parameters have been fixed rather than extracted from a particular sample, so the variations are estimated from the uncertainties on other resolution parameters. The sizes of the variations appear, along with the resulting systematic uncertainties, in tables 5.20 and 5.21.
- Dilutions. The average mis-tagging rates,  $w_\alpha$ , and the differences in the mis-tagging rates,  $\Delta w_\alpha$ , for each tagging category, are varied by  $\pm 1\sigma$ , where the  $\sigma$  for each parameter is taken from the  $B_{\text{flav}}$  data sample.
- Background lifetimes. The variations of the parameters for the lifetime components of the inclusive  $J/\psi$  and  $B\bar{B}$  generic backgrounds are taken from the fits to the corresponding Monte Carlo samples. The same is true for the fractions of the lifetime components for these two background sources. As a cross-check, these fractions are also varied by a larger amount, as described in Section 5.13.
- Physics parameters. The variations used for  $\Delta m_d$  and  $\tau_{B^0}$  are the uncertainties on the 2002 PDG values for these quantities [25]. The size of the variation of  $\sin 2\beta$  for the  $B^0 \rightarrow J/\psi K_S^0(\pi^0\pi^0)$  background is taken from the *BABAR* measurement [24].

The results of the variations of the above four bulleted items can be seen in Table 5.20 and 5.21. The total systematic due to these sources is 0.027 on  $C_{J/\psi\pi^0}$  and 0.022 on  $S_{J/\psi\pi^0}$ .

Table 5.18: Systematics from variation of event selection PDF parameters. The  $m_{ES}$  and  $\Delta E$  PDF parameters are varied up and down, and for each asymmetry coefficient, the larger deviation from the nominal fit is taken in quadrature as a contribution to the systematic uncertainty. The items in this table contribute 0.048 for  $C_{J/\psi \pi^0}$  and 0.130 for  $S_{J/\psi \pi^0}$ . The dominant contribution to  $S_{J/\psi \pi^0}$  comes from the power-law parameter of the the signal  $\Delta E$  PDF.

Parameter name	Value for fit	Change in $C_{J/\psi \pi^0}$			Change in $S_{J/\psi \pi^0}$		
		Up $1\sigma$	Down $1\sigma$	Larger difference	Up $1\sigma$	Down $1\sigma$	Larger difference
$m_{ES}$ Sig $m$	$5.28 \pm 0.0000436$	-0.00063	0.00062	-0.00063	0.0014	-0.0014	0.0014
$m_{ES}$ Sig $r$	$0.12882 \pm 0.00625$	0.0021	-0.0022	-0.0022	-0.00085	0.00096	0.00096
$m_{ES}$ Sig $\sigma$	$0.0025084 \pm 0.0000355$	0.00087	-0.00095	-0.00095	0.00012	0.00054	0.00054
$m_{ES}$ Sig $\sigma_{Grun}$ frac	$0.94188 \pm 0.00727$	-0.00059	0.00041	-0.00059	-0.0018	0.0022	0.0022
$m_{ES}$ Sig $\xi$	$-257.8 \pm 14.3$	0.0021	-0.0022	-0.0022	-0.0011	0.0017	0.0017
$m_{ES}$ Sig endpoint	$5.289 \pm 0.002$	-0.013	0.015	0.015	0.011	-0.016	-0.016
$m_{ES}$ BB bkg $\xi$	$19.33 \pm 3.92$	-0.00033	-0.00023	-0.00033	-0.00049	0.00092	0.00092
$m_{ES}$ Cont bkg $\xi$	$-16.41 \pm 1.73$	0.00046	-0.00093	-0.00093	-0.00096	0.0013	0.0013
$m_{ES}$ Cont/BB bkg endpoint	$5.289 \pm 0.002$	-0.00014	-0.00051	-0.00051	0.00056	-0.00016	0.00056
$\Delta E$ Sig $\alpha$	$0.962 \pm 0.157$	0.0023	-0.012	-0.012	0.0015	0.00080	0.0015
$\Delta E$ Sig $\sigma$	$0.03056 \pm 0.00122$	-0.0059	0.0072	0.0072	0.0092	-0.0083	0.0092
$\Delta E$ Sig $n$	$5.3 \pm 12.1$	0.013	0.036	0.036	0.0053	-0.13	-0.13
$\Delta E$ Sig CB frac	$0.94572 \pm 0.00574$	0.0013	-0.0012	-0.0013	0.0015	-0.0014	0.0015
$\Delta E$ Sig $A_1$	$-1.409 \pm 0.563$	0.019	-0.0095	-0.0095	0.019	0.0070	-0.014
$\Delta E$ Sig $A_2$	$-2.56 \pm 1.29$	0.016	-0.011	-0.016	-0.011	0.0073	-0.011
$\Delta E$ BB bkg $A_1$	$-4.777 \pm 0.287$	0.00093	-0.0015	-0.0015	0.0015	-0.00047	0.0015
$\Delta E$ BB bkg $A_2$	$6.807 \pm 0.999$	0.00033	-0.00084	-0.00084	0.0016	-0.0016	0.0016
$\Delta E$ Cont bkg $A_1$	$-2.3361 \pm 0.0901$	-0.00037	0.00045	0.00045	-0.00013	0.00036	0.00036
$\Delta E$ Cont bkg $A_2$	$1.621 \pm 0.342$	-0.00080	0.00074	-0.00080	0.000044	0.00011	0.00011

Table 5.19: Systematics from variation of the tagging fractions. The tagging fractions are varied up and down, and for each asymmetry coefficient, the larger deviation from the nominal fit is taken in quadrature as a contribution to the systematic uncertainty. The items in this table contribute 0.002 for  $C_{J/\psi\pi^0}$  and 0.007 for  $S_{J/\psi\pi^0}$ .

Parameter name	Value for fit	Change in $C_{J/\psi\pi^0}$			Change in $S_{J/\psi\pi^0}$		
		Up $1\sigma$	Down $1\sigma$	Larger difference	Up $1\sigma$	Down $1\sigma$	Larger difference
$f_{\text{Cat1}}^{\text{Sig}}$	$0.1389 \pm 0.0029$	-0.00054	0.00053	-0.00054	-0.00047	0.00049	0.00049
$f_{\text{Cat2}}^{\text{Sig}}$	$0.2540 \pm 0.0043$	-0.00019	0.00018	-0.00019	-0.00027	0.00028	0.00028
$f_{\text{Cat3}}^{\text{Sig}}$	$0.3025 \pm 0.0049$	0.00035	-0.00038	-0.00038	0.00076	-0.00074	0.00076
$f_{\text{Cat1}}^{\text{Ks}}$	$0.1389 \pm 0.0029$	0.00011	-0.00021	-0.00021	0.0012	-0.00073	0.0012
$f_{\text{Cat2}}^{\text{Ks}}$	$0.2540 \pm 0.0043$	-0.00053	-0.00027	-0.00027	0.0013	-0.00099	0.0013
$f_{\text{Cat3}}^{\text{Ks}}$	$0.3025 \pm 0.0049$	-0.00048	0.00030	-0.00048	0.00051	-0.00011	0.00051
$f_{\text{Cat1}}^{\text{Inc}}$	$0.0837 \pm 0.0112$	0.00040	-0.00063	-0.00063	0.0016	0.00028	0.0016
$f_{\text{Cat2}}^{\text{Inc}}$	$0.3403 \pm 0.0252$	-0.00075	0.000030	-0.00075	0.0020	-0.00031	0.0020
$f_{\text{Cat3}}^{\text{Inc}}$	$0.2803 \pm 0.0224$	0.00059	-0.00012	0.00059	-0.00012	0.0053	0.0053
$f_{\text{Cat1}}^{\text{BB}}$	$0.0180 \pm 0.0057$	-0.000063	-0.00045	-0.00045	0.0013	-0.00098	0.0013
$f_{\text{Cat2}}^{\text{BB}}$	$0.2334 \pm 0.0227$	-0.000083	0.00065	0.00065	0.0020	-0.0012	0.0020
$f_{\text{Cat3}}^{\text{BB}}$	$0.4488 \pm 0.0342$	0.00075	0.000058	0.00075	0.00092	-0.00092	-0.00092
$f_{\text{Cat1}}^{\text{Cont}}$	$0.0103 \pm 0.0022$	0.00015	-0.00076	-0.00076	0.0011	-0.00085	0.0011
$f_{\text{Cat2}}^{\text{Cont}}$	$0.2315 \pm 0.0113$	-0.00033	-0.00025	-0.00033	0.0019	-0.0017	0.0019
$f_{\text{Cat3}}^{\text{Cont}}$	$0.2904 \pm 0.0129$	0.00014	0.00072	0.00072	0.00028	-0.00021	0.00028

Table 5.20: Systematics from variation of  $\Delta t$  PDF parameters. The  $\Delta t$  decay time and resolution PDF parameters are varied up and down, and for each asymmetry coefficient, the larger deviation from the nominal fit is taken in quadrature as a contribution to the systematic uncertainty. The list of  $\Delta t$  PDF parameters is continued in Table 5.21. The items in this table and the items in Table 5.21, when combined, contribute 0.027 for  $C_{J/\psi \pi^0}$  and 0.022 for  $S_{J/\psi \pi^0}$ .

Parameter name	Value for fit	Change in $C_{J/\psi \pi^0}$			Change in $S_{J/\psi \pi^0}$		
		Up $1\sigma$	Down $1\sigma$	Larger difference	Up $1\sigma$	Down $1\sigma$	Larger difference
Sig $f_{core}$	$0.886 \pm 0.021$	-0.0080	0.0076	-0.0080	-0.0012	0.0013	0.0013
Sig $f_{out1}$	$0.002 \pm 0.001$	0.00018	-0.00018	-0.00018	0.000061	-0.000061	-0.000061
Sig/Ks $b_{Cat1}$	$0.015 \pm 0.063$	-0.00066	0.00029	-0.00066	-0.0039	0.0042	0.0042
Sig/Ks $b_{Cat2}$	$-0.229 \pm 0.052$	0.0030	-0.0028	0.0030	-0.0076	0.0076	0.0076
Sig/Ks $b_{Cat3}$	$-0.245 \pm 0.046$	0.0016	-0.0019	-0.0019	0.00029	0.00013	0.00029
Sig/Ks $b_{Cat4}$	$-0.206 \pm 0.047$	0.00045	-0.00061	-0.00061	0.0025	-0.0020	0.0025
Sig/Ks $score$	$1.095 \pm 0.049$	0.0094	-0.0096	-0.0096	0.0044	-0.0036	0.0044
Sig/Ks $b_{tail}$	$-0.99 \pm 0.29$	-0.00081	0.00071	-0.00081	0.0019	-0.0021	-0.0021
Sig/Ks $stail$	$3.0 \pm 0.1$	0.00094	-0.0011	-0.0011	-0.00065	0.00067	0.00067
Sig/Ks $inc/BB/Cont_{bout1}$	$0.0 \pm 0.7$	-0.00024	0.0000069	-0.00024	-0.00039	0.00067	0.00067
Sig/Ks $inc/BB/Cont_{sout1}$	$8.0 \pm 0.1$	-0.000093	-0.000026	-0.000093	-0.00021	0.00071	0.00071
Sig/Ks $w_{Cat1}$	$0.033 \pm 0.006$	0.00022	-0.00019	0.00022	-0.0020	0.0019	-0.0020
Sig/Ks $w_{Cat2}$	$0.100 \pm 0.007$	0.00041	-0.00041	-0.00041	-0.0023	0.0027	0.0027
Sig/Ks $w_{Cat3}$	$0.209 \pm 0.008$	-0.00060	0.00056	-0.0060	0.0058	-0.0051	0.0058
Sig/Ks $w_{Cat4}$	$0.315 \pm 0.009$	-0.00097	0.00094	-0.0097	0.0029	-0.0024	0.0029
Sig/Ks $\Delta w_{Cat1}$	$-0.015 \pm 0.011$	0.0042	-0.0043	-0.0043	-0.00083	0.0013	0.0013
Sig/Ks $\Delta w_{Cat2}$	$-0.013 \pm 0.011$	0.0056	-0.0060	-0.0060	0.0030	-0.0028	0.0030
Sig/Ks $\Delta w_{Cat3}$	$-0.044 \pm 0.012$	0.0086	-0.0087	-0.0087	0.0013	-0.00078	0.0013
Sig/Ks $\Delta w_{Cat4}$	$-0.024 \pm 0.013$	0.0059	-0.0060	-0.0060	0.0010	-0.00046	0.0010
$T_{B^0}$	$1.542 \pm 0.016$	-0.0029	0.0025	-0.0029	-0.00043	0.00079	0.00079
$\Delta m_d$	$0.489 \pm 0.008$	-0.015	0.015	-0.015	-0.00020	0.00076	0.00076
Ks $bkg_{fcore}$	$0.886 \pm 0.021$	0.00035	-0.00040	-0.00040	0.00056	-0.00064	-0.00064
Ks $bkg_{fout1}$	$0.002 \pm 0.001$	-0.000038	-0.000044	-0.000044	-0.00015	0.00069	0.00069
Ks $bkg_{sin2\theta}$	$0.74 \pm 0.07$	0.00025	-0.000038	0.00025	0.0059	-0.0052	0.0059

Table 5.21: Continuation from Table 5.20. Systematics from variation of  $\Delta t$  PDF parameters. The systematic uncertainty contributions from the remaining  $\Delta t$  decay time and resolution PDF parameters are listed.

Parameter name	Value for fit	Change in $C_{J/\psi\pi^0}$			Change in $S_{J/\psi\pi^0}$		
		Up $1\sigma$	Down $1\sigma$	Larger difference	Up $1\sigma$	Down $1\sigma$	Larger difference
Inc bkg $f_{\text{lifetime}}$	$0.648 \pm 0.092$	-0.0037	0.0026	-0.0037	0.0025	-0.000093	0.0025
Inc bkg $f_{\text{core}}^{\text{all}}$	$1.0000 \pm 0.0015$	0.00	-0.000015	-0.000015	0.00	0.00075	0.00075
Inc bkg $b_{\text{core}}^{\text{all}}$	$-0.31 \pm 0.13$	0.00095	-0.0011	-0.0011	0.0019	-0.00062	0.0019
Inc bkg $s_{\text{core}}^{\text{all}}$	$1.76 \pm 0.56$	-0.0023	-0.00079	-0.0023	0.0023	0.0024	0.0024
Inc bkg $f_{\text{core}}^{\text{prompt}}$	$1.0000 \pm 0.0031$	0.00	-0.000052	-0.000052	0.00	0.00077	0.00077
Inc bkg $b_{\text{core}}^{\text{prompt}}$	$-0.008 \pm 0.097$	-0.00065	-0.00036	-0.00065	-0.0011	0.0022	0.0022
Inc bkg $s_{\text{core}}^{\text{prompt}}$	$1.53 \pm 0.23$	-0.0017	-0.00033	-0.0017	0.0024	-0.0016	0.0024
Inc bkg $\tau_B$	$1.55 \pm 0.16$	-0.00059	-0.00041	-0.00059	0.0027	-0.0014	0.0027
BB bkg $f_{\text{lifetime}}$	$0.64 \pm 0.21$	-0.0019	0.0022	0.0022	0.0030	-0.0044	-0.0044
BB bkg $f_{\text{core}}^{\text{all}}$	$0.99 \pm 0.27$	-0.000051	0.0022	0.0022	0.00088	-0.011	-0.011
BB bkg $b_{\text{core}}^{\text{all}}$	$-0.55 \pm 0.15$	0.00044	-0.0010	-0.0010	0.0014	-0.00080	0.0014
BB bkg $s_{\text{core}}^{\text{all}}$	$1.46 \pm 0.32$	-0.00016	0.00043	0.0043	0.0015	-0.00081	0.0015
BB bkg $f_{\text{core}}^{\text{prompt}}$	$0.95 \pm 0.47$	-0.0000055	0.00073	0.00073	0.00096	-0.00068	-0.00068
BB bkg $b_{\text{core}}^{\text{prompt}}$	$-0.05 \pm 0.11$	-0.0000037	-0.00061	-0.00061	0.0015	-0.00083	0.0015
BB bkg $s_{\text{core}}^{\text{prompt}}$	$1.29 \pm 0.23$	-0.00063	-0.00064	-0.00064	-0.00012	-0.00068	-0.00068
BB bkg $\tau_B$	$1.16 \pm 0.20$	-0.0011	0.0013	0.0013	0.0027	-0.0038	-0.0038
Cont bkg $f_{\text{core}}$	$0.9348 \pm 0.0069$	-0.00049	0.00032	-0.00049	-0.000016	0.00046	0.00046
Cont bkg $b_{\text{core}}$	$0.010 \pm 0.017$	-0.00053	0.000080	-0.00053	0.00091	-0.00065	0.00091
Cont bkg $s_{\text{core}}$	$1.407 \pm 0.028$	0.00082	-0.0012	-0.0012	0.00070	-0.00044	0.00070

### 5.12.2 Additional Systematics

- Impact of EMC energy scale on  $B^0 \rightarrow J/\psi K_S^0(\pi^0\pi^0)$  background. The fit is repeated after applying the energy rescaling, particle killing, and energy dependent smearing to the  $B^0 \rightarrow J/\psi K_S^0(\pi^0\pi^0)$  Monte Carlo sample. Any changes in the  $m_{\text{ES}}$  and  $\Delta E$  distributions are accounted for in the two-dimensional histogram PDF, and the differences between these fit results and the nominal fit results represent a contribution to the systematic error of 0.009 on  $C_{J/\psi \pi^0}$  and 0.002 on  $S_{J/\psi \pi^0}$ .
- Choice of the two-dimensional histogram PDFs. The binning for the two-dimensional histogram PDFs for  $m_{\text{ES}}$  versus  $\Delta E$  of the  $B^0 \rightarrow J/\psi K_S^0(\pi^0\pi^0)$  and inclusive  $J/\psi$  backgrounds is altered for an additional fit. For the  $B^0 \rightarrow J/\psi K_S^0(\pi^0\pi^0)$  histogram, the  $m_{\text{ES}}$  axis is changed from 16 variably sized bins to 20 fixed bins and the  $\Delta E$  axis is changed from 20 fixed bins to 15 fixed bins. For the inclusive  $J/\psi$  histogram, the  $m_{\text{ES}}$  and  $\Delta E$  axes are changed from 12 and 9 variably sized bins to 17 and 14 fixed bins, respectively. The resulting differences with the nominal fit give a systematic contribution of 0.009 on  $C_{J/\psi \pi^0}$  and 0.029 on  $S_{J/\psi \pi^0}$ .
- $\Delta E$ - $m_{\text{ES}}$  correlation in signal. The strategy for evaluating this systematic uncertainty is to model  $m_{\text{ES}}$  versus  $\Delta E$  for signal using a two-dimensional histogram based PDF rather than two one-dimensional PDFs. The fit is repeated after constructing a two-dimensional PDF for the signal  $m_{\text{ES}}$  and  $\Delta E$  distributions, with 50 bins for  $m_{\text{ES}}$  and 40 bins for  $\Delta E$ . The contribution to the systematics from this source is 0.073 on  $C_{J/\psi \pi^0}$  and 0.079 on  $S_{J/\psi \pi^0}$ . Changes to the statistical errors on the fit values of  $C_{J/\psi \pi^0}$  and  $S_{J/\psi \pi^0}$  with this configuration are negligible.

Table 5.22: Summary of systematic errors, as discussed in sections 5.12.1–5.12.3.

Source	Error on $C_{J/\psi \pi^0}$	Error on $S_{J/\psi \pi^0}$
Parameter variations		
$m_{\text{ES}}$ and $\Delta E$ parameters	0.048	0.130
Tagging fractions	0.002	0.007
$\Delta t$ parameters	0.027	0.022
Additional systematics		
$\Delta E$ – $m_{\text{ES}}$ correlation in signal	0.073	0.079
EMC energy scale $B^0 \rightarrow J/\psi K_s^0(\pi^0\pi^0)$	0.009	0.002
Choice of two-D histogram PDFs	0.009	0.029
Beam spot, boost/vtx., misalignment	0.012	0.012
Total systematic uncertainty	0.093	0.157

### 5.12.3 Systematics in Common with the “golden modes”

The systematic uncertainties due to the following sources are taken from studies performed for the “golden modes”. They are updated studies similar to those documented in Ref. [49]. The contributions to the error are given in parenthesis.

- Beam spot position (0.005).
- Uncertainty on boost and  $z$  scale (0.003).
- SVT misalignment (0.01).

### 5.12.4 Summary of Systematic Uncertainties

A summary of the systematic errors, along with the total combined systematic uncertainty, is given in Table 5.22. The dominant source is uncertainty within signal  $\Delta E$  PDF.

## 5.13 Cross-checks

### 5.13.1 Larger Variation of Parameters

As one of the cross-checks, the fractions of the lifetime components within the inclusive  $J/\psi$  and  $B\bar{B}$  generic background  $\Delta t$  PDFs are varied up and down by 30%, rather than the 9.2% and 21% respectively that come from the fit to the original Monte Carlo samples. This larger variation would contribute systematics of 0.014 on  $C_{J/\psi \pi^0}$  and 0.015 on  $S_{J/\psi \pi^0}$  for these two parameters. These contributions are not large enough to impact the overall error, and this calculation serves as a test that the fit is stable in these parameters.

### 5.13.2 Validation of the Fisher on an Alternate Data Sample

The shape of the Fisher discriminant is compared between the signal  $B^0 \rightarrow J/\psi \pi^0$  Monte Carlo sample and  $56 \text{ fb}^{-1}$  of  $B^0 \rightarrow J/\psi K_s^0(\pi^+\pi^-)$  data. This verifies that the Fisher shape constructed in Monte Carlo simulation closely models that found in a sample of real charmonium  $B$  decays. The two distributions are shown in Figure 5.31.

### 5.13.3 Monte Carlo Samples with Different Asymmetries

Another test of the  $CP$  fit is performed by running it on signal Monte Carlo samples produced with a variety of values of  $C_{J/\psi \pi^0}$  and  $S_{J/\psi \pi^0}$ . The Monte Carlo sample typically contain from 10,000 to 12,000 events. Some samples were generated with  $C_{J/\psi \pi^0} = 0$  and  $S_{J/\psi \pi^0}$  taking on several different values. Other samples were generated with a range of values for  $C_{J/\psi \pi^0}$ , but with  $S_{J/\psi \pi^0}$  near  $-0.7$ . The results of these fits are given in Figure 5.32. The agreement between the generated combinations and the fit results shows that the fit contains a good model for the decay time behavior and is sensitive to the asymmetry coefficients

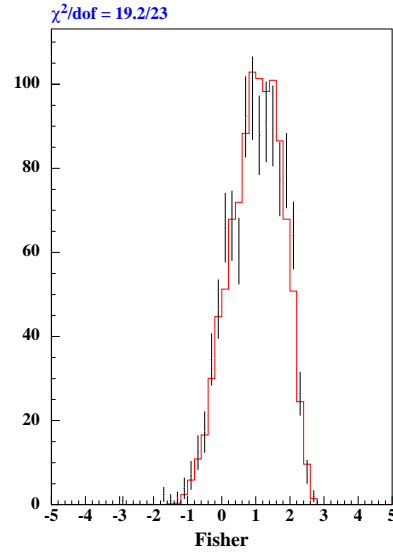


Figure 5.31: The output of the Fisher discriminant is shown for the signal  $B^0 \rightarrow J/\psi \pi^0$  Monte Carlo sample (red histogram) and  $56 \text{ fb}^{-1}$  of  $B^0 \rightarrow J/\psi K_S^0(\pi^+\pi^-)$  data (black points).

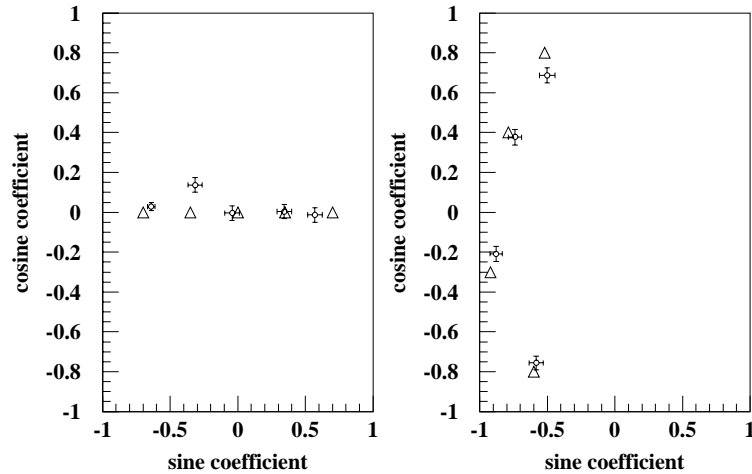


Figure 5.32: The coefficients of the asymmetry are plotted (points) for  $CP$  fits to samples of Monte Carlo simulation generated with various asymmetries (triangles). Each triangle represents a sample, typically containing 10,000 to 12,000 events, generated with the values of  $S_{J/\psi \pi^0}$  and  $C_{J/\psi \pi^0}$  given on the  $x$  and  $y$  axes.

### 5.13.4 Toy Monte Carlo Study

Fast parameterized Monte Carlo (toy Monte Carlo) experiments are used to check for biases in the fit results for  $C_{J/\psi \pi^0}$  and  $S_{J/\psi \pi^0}$ , and to predict the size of the statistical errors on these asymmetry coefficients. For example, 100 experiments with the same number and composition of events as the data have been generated with  $C_{J/\psi \pi^0} = 0.35$  and  $S_{J/\psi \pi^0} = -0.7$ . These experiments are run through the asymmetry fit and the resulting distributions of  $C_{J/\psi \pi^0}$ ,  $-S_{J/\psi \pi^0}$ , and their statistical errors are shown in Figure 5.33. Note that the extra minus sign in the  $S_{J/\psi \pi^0}$  plot is simply due to a change in convention after this study was performed. The figure also shows the pull for each coefficient, defined for example as  $(C_{\text{measured}} - C_{\text{expected}})/\sigma_C$ . That the mean of the pulls are well centered at zero and the sigma of the pulls are approximately one demonstrates that the results of the 100 experiments are not biased and are well distributed around the expectations. The plots of the statistical errors show that the values of the statistical errors from data,  $\sigma_C = 0.41$  and  $\sigma_S = 0.49$ , are well within the expected ranges. A variety of such toy Monte Carlo experiments with different values of  $C_{J/\psi \pi^0}$  and  $S_{J/\psi \pi^0}$  have been generated, and no significant biases are seen. This indicates that the fit should perform well on data, and that no bias corrections are needed.

### 5.13.5 CP Fit, Including the Fisher as a PDF

The CP fit on data is performed with the PDFs for the Fisher discriminant included in the likelihood. The projections of  $m_{\text{ES}}$ ,  $\Delta E$ , the Fisher, and  $\Delta t$  are shown in Figure 5.34 and the fit results are summarized in Table 5.23. This configuration may be less optimal than the nominal fit, where a cut is placed on the Fisher, due to some uncertainty about whether a difference seen between the Fisher output in data and the shape returned by the likelihood fit in one bin of the continuum dominated portion of the fisher plot (around  $-1.6$ ) is a discrepancy in the modeling or a large statistical fluctuation. This prompted the decision to cut on the Fisher output, requiring  $\mathcal{F} > -0.8$ . The similarity of the asymmetry coefficients extracted from this cross-check and those extracted from the nominal fit gives confidence that the fit is well constructed.

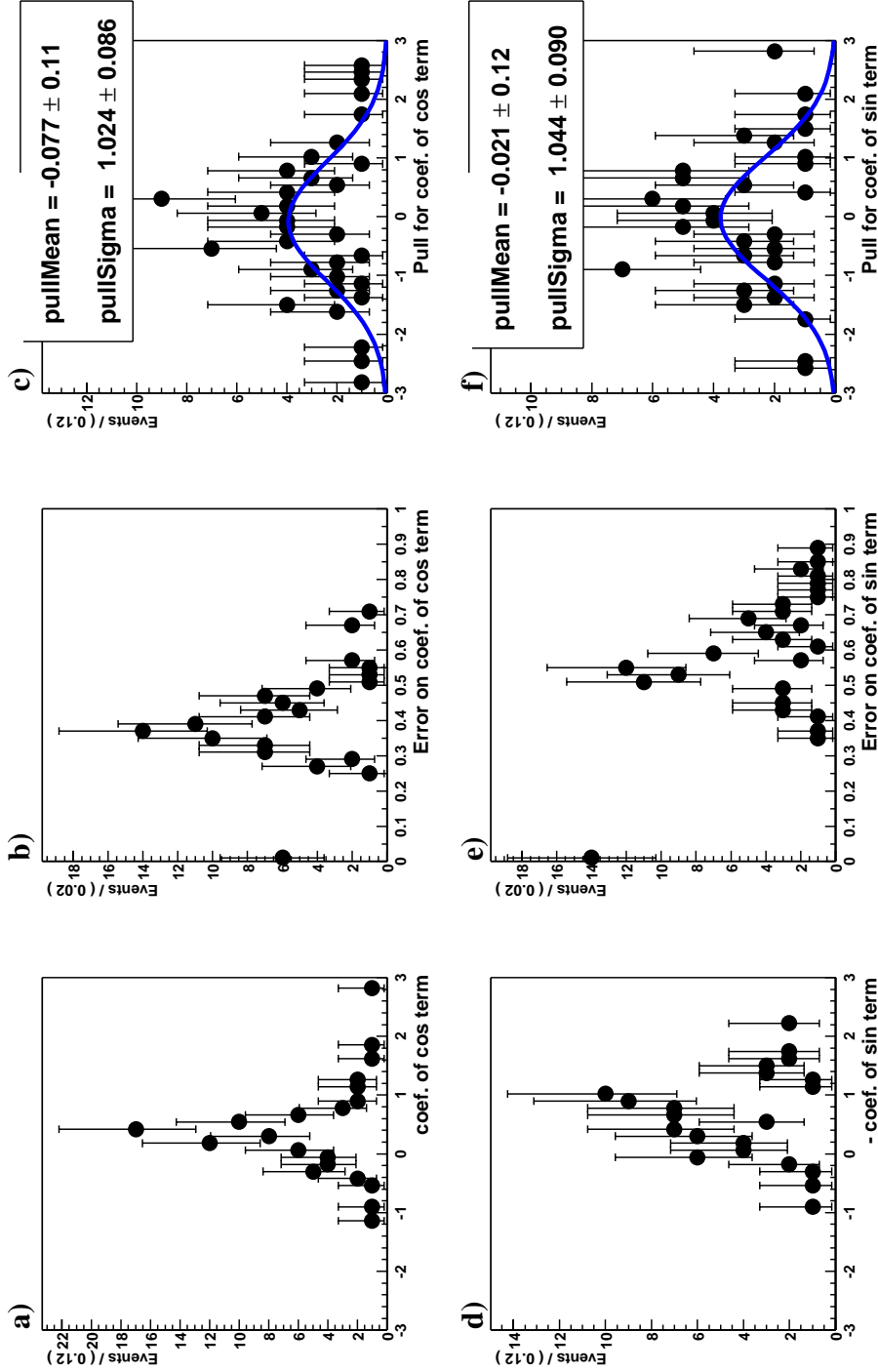


Figure 5.33: The distributions of (a)  $C_{J/\psi\pi^0}$ , (b) the statistical error on  $C_{J/\psi\pi^0}$ , (c) the pull for  $C_{J/\psi\pi^0}$ , (d)  $-S_{J/\psi\pi^0}$ , (e) the statistical error on  $S_{J/\psi\pi^0}$ , and (f) the pull for  $S_{J/\psi\pi^0}$  are shown for a set of 100 toy Monte Carlo experiments generated with the values  $C_{J/\psi\pi^0} = 0.35$  and  $S_{J/\psi\pi^0} = -0.7$ . The extra minus sign in (d) is just due to a sign convention change after this study was performed.

### 5.13.6 CP Fit, Fixing the Signal $\Delta E$ Peak Position to the Monte Carlo Value

The peak position of the  $\Delta E$  distribution of the signal Monte Carlo simulation differs by as much as 18 MeV from that of the data, and therefore the nominal fit allows the value to float. As an alternate configuration, the  $CP$  fit to data is performed with the signal  $\Delta E$  peak position fixed to that obtained from the Monte Carlo simulation. The discrepancy in the  $\Delta E$  peak position is visible on the plot in Figure 5.35. The results are given in Table 5.23, but they serve only to learn something about the impact of using the wrong signal  $\Delta E$  peak position, as is done in this cross-check.

### 5.13.7 CP Fit, Cutting on Both the Fisher and $\Delta E$

The  $CP$  likelihood fit is performed after placing cuts on both the Fisher and  $\Delta E$ . The cut on the Fisher is the same as in the nominal fit ( $-0.8 < \mathcal{F}$ ) and the cut on  $\Delta E$  is  $-0.112 < \Delta E < 0.112$ . This results in a clean signal peak in  $m_{ES}$ , as seen in Figure 5.36. However, the remaining background levels of some of the sources are too low to fit and must be fixed to the estimated yields. This is a disadvantage as compared with the nominal fit, but the results given in Table 5.23 demonstrate the stability of  $C_{J/\psi \pi^0}$  and  $S_{J/\psi \pi^0}$ .

## 5.14 Summary of CP Asymmetry Results

An unbinned extended maximum likelihood fit, performed on  $81.1 \text{ fb}^{-1}$  of data collected at *BABAR*, yields  $40 \pm 7$  signal events and the parameters of time-dependent  $CP$  asymmetry for the decay  $B^0 \rightarrow J/\psi \pi^0$ :

$$\begin{aligned} C_{J/\psi \pi^0} &= 0.38 \pm 0.41 \text{ (stat)} \pm 0.09 \text{ (syst)} , \\ S_{J/\psi \pi^0} &= 0.05 \pm 0.49 \text{ (stat)} \pm 0.16 \text{ (syst)} . \end{aligned}$$

Table 5.23: Results of  $CP$  likelihood fits to  $71\text{ fb}^{-1}$  of data using alternate, non-optimal, configurations. The different configurations are explained in the text, and the projections are shown in figures 5.34–5.36.

	Fit results	Expected	Global correlation
Nominal fit, for reference			
$C_{J/\psi\pi^0}$	$0.47 \pm 0.44$	–	0.128
$S_{J/\psi\pi^0}$	$0.02 \pm 0.50$	–	0.147
Signal $\Delta E$ peak position (MeV)	$-0.0147 \pm 0.0081$	–	0.158
$B^0 \rightarrow J/\psi\pi^0$ signal	$34.8 \pm 6.8$	$\sim 48$	0.099
$B^0 \rightarrow J/\psi K_S^0(\pi^0\pi^0)$ background	$117.6 \pm 17.8$	115	0.648
Inclusive $J/\psi$ background	$88.5 \pm 32.0$	60	0.848
$B\bar{B}$ generic background	$47.0 \pm 23.3$	44	0.818
Continuum background	$92.2 \pm 20.8$	51	0.734
Including the Fisher PDF			
$C_{J/\psi\pi^0}$	$0.53 \pm 0.44$	–	0.111
$S_{J/\psi\pi^0}$	$-0.03 \pm 0.51$	–	0.118
Signal $\Delta E$ peak position (MeV)	$-0.0146 \pm 0.0081$	–	0.151
$B^0 \rightarrow J/\psi\pi^0$ signal	$34.6 \pm 6.7$	$\sim 48$	0.095
$B^0 \rightarrow J/\psi K_S^0(\pi^0\pi^0)$ background	$119.8 \pm 16.7$	117	0.596
Inclusive $J/\psi$ background	$93.1 \pm 28.9$	63	0.813
$B\bar{B}$ generic background	$49.0 \pm 16.7$	45	0.727
Continuum background	$270.5 \pm 18.2$	187	0.244
Fixing the signal $\Delta E$ mean			
$C_{J/\psi\pi^0}$	$0.40 \pm 0.45$	–	0.117
$S_{J/\psi\pi^0}$	$-0.10 \pm 0.50$	–	0.125
Signal $\Delta E$ peak position (MeV)	fixed at MC value	–	–
$B^0 \rightarrow J/\psi\pi^0$ signal	$34.1 \pm 6.7$	$\sim 48$	0.107
$B^0 \rightarrow J/\psi K_S^0(\pi^0\pi^0)$ background	$121.5 \pm 17.9$	115	0.647
Inclusive $J/\psi$ background	$81.2 \pm 31.8$	60	0.848
$B\bar{B}$ generic background	$49.8 \pm 23.4$	44	0.820
Continuum background	$93.5 \pm 20.8$	51	0.733
Cutting on the Fisher and $\Delta E$			
$C_{J/\psi\pi^0}$	$0.50 \pm 0.44$	–	0.080
$S_{J/\psi\pi^0}$	$-0.16 \pm 0.51$	–	0.085
$B^0 \rightarrow J/\psi\pi^0$ signal	$33.1 \pm 6.9$	$\sim 44$	0.357
$B^0 \rightarrow J/\psi K_S^0(\pi^0\pi^0)$ background	fixed at 3.3	3.3	–
Inclusive $J/\psi$ background	$10.8 \pm 13.0$	10	0.813
$B\bar{B}$ generic background	fixed at 8.4	8.4	–
Continuum background	$26.3 \pm 11.5$	14	0.795

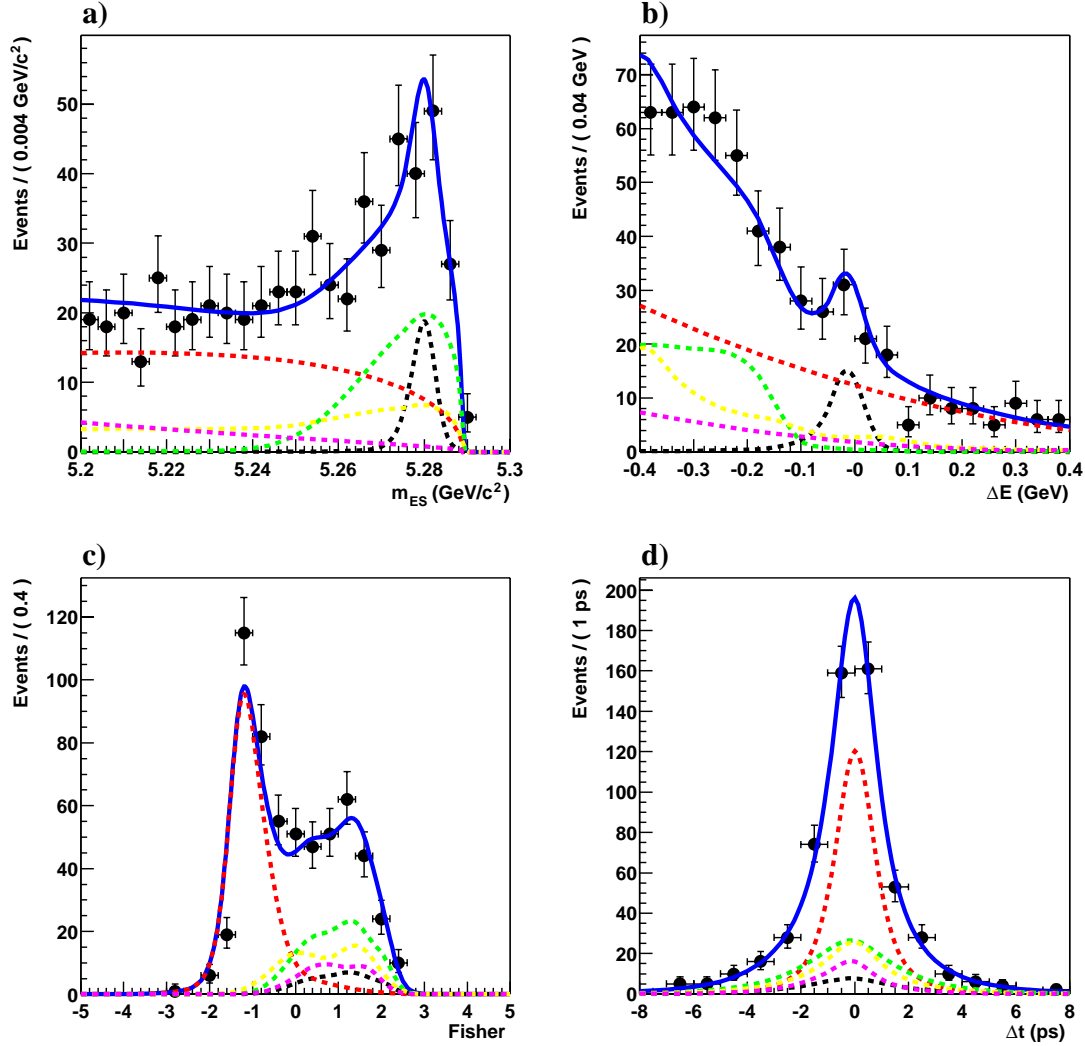


Figure 5.34: Projections of (a)  $m_{ES}$ , (b)  $\Delta E$ , (c) the Fisher, and (d)  $\Delta t$  for the results of a  $CP$  fit to  $71 \text{ fb}^{-1}$  of *onpeak* data using an alternate configuration where the PDF for the Fisher is included in the fit. The fit results are stable with respect to the nominal fit, which cuts on the Fisher, but this configuration is not used due to the potential disagreement in the Fisher output between the data and the fit results in the lower portion of the distribution (continuum region). Black dashed: signal  $B^0 \rightarrow J/\psi \pi^0$ . Green dashed:  $B^0 \rightarrow J/\psi K_s^0 (\pi^0 \pi^0)$  background. Yellow dashed: inclusive  $J/\psi$  background. Magenta dashed:  $B\bar{B}$  generic background. Red dashed: continuum background. Blue solid: total. The numerical results are given in Table 5.23.

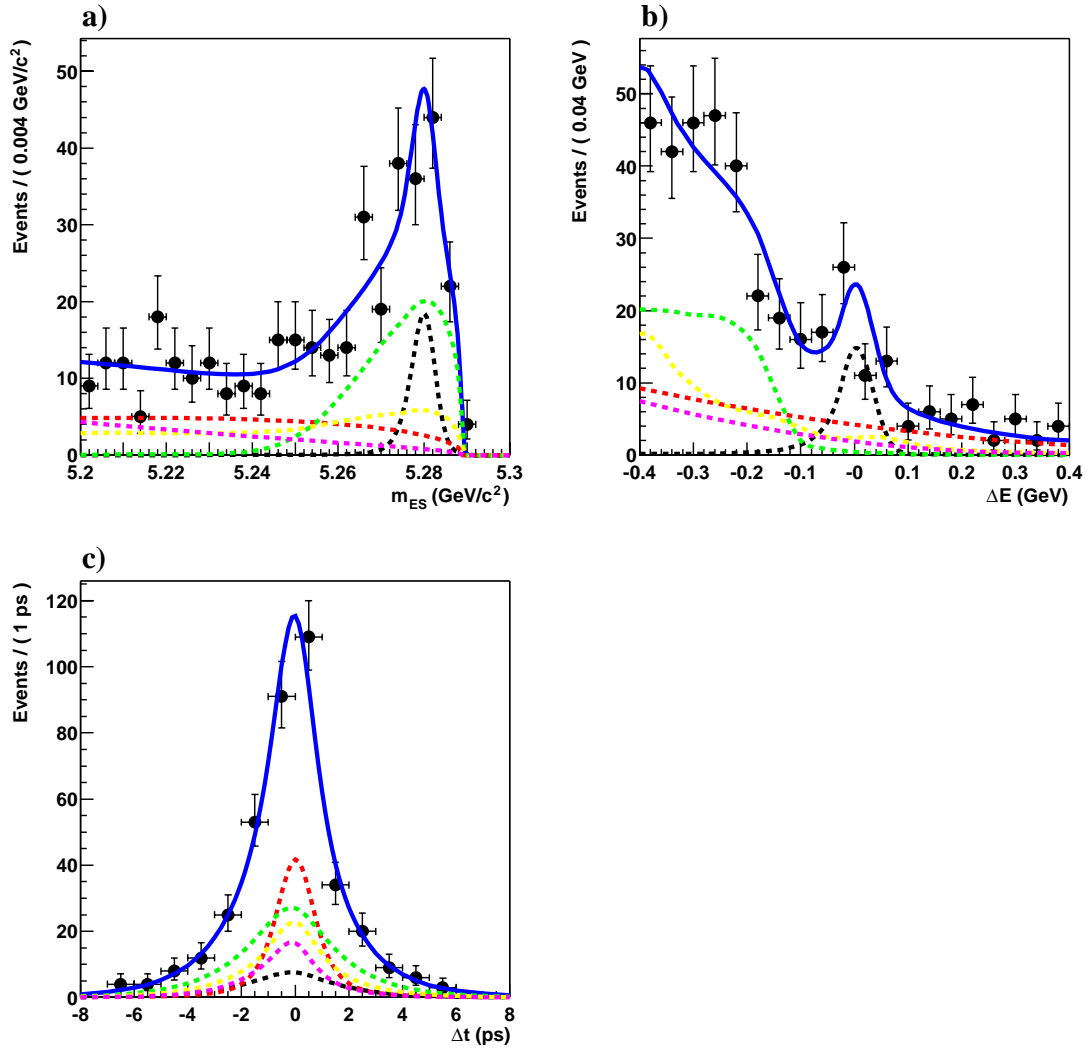


Figure 5.35: Projections of (a)  $m_{ES}$ , (b)  $\Delta E$ , and (c)  $\Delta t$  for the results of a  $CP$  fit to  $71 \text{ fb}^{-1}$  of *onpeak* data using an alternate configuration where the signal  $\Delta E$  peak position is fixed to the value extracted from Monte Carlo simulation. The shift in  $\Delta E$  is visible in the plot and explains the choice of floating the signal  $\Delta E$  peak position in the nominal fit. Black dashed: signal  $B^0 \rightarrow J/\psi \pi^0$ . Green dashed:  $B^0 \rightarrow J/\psi K_S^0(\pi^0\pi^0)$  background. Yellow dashed: inclusive  $J/\psi$  background. Magenta dashed:  $B\bar{B}$  generic background. Red dashed: continuum background. Blue solid: total. The numerical results are given in Table 5.23.

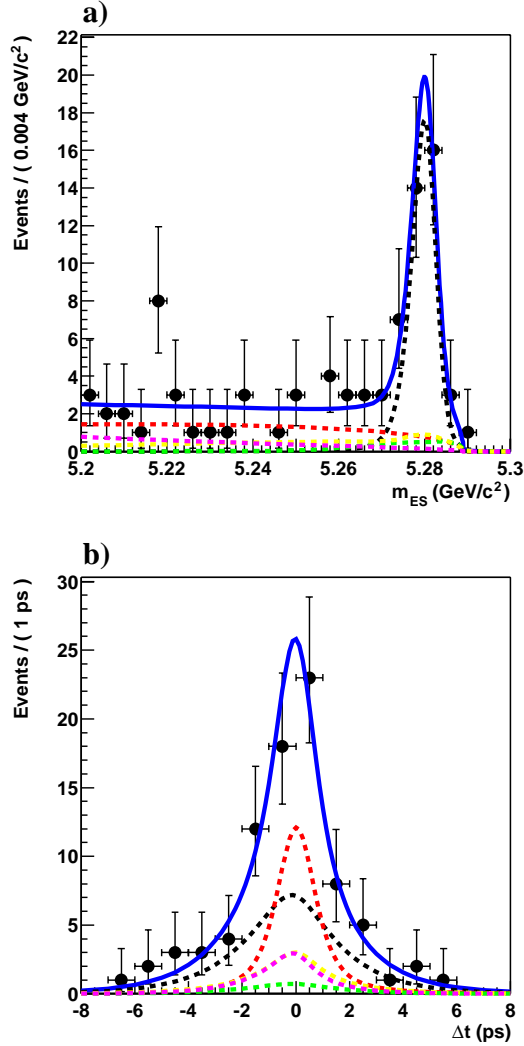


Figure 5.36: Projections of (a)  $m_{ES}$  and (b)  $\Delta E$  for the results of a  $CP$  fit to  $71 \text{ fb}^{-1}$  of *onpeak* data using an alternate configuration where a cut is placed on both the Fisher discriminant and  $\Delta E$ . This leaves a clean signal peak, but reduces the background to a level where two of the background contributions must be fixed in the fit. Black dashed: signal  $B^0 \rightarrow J/\psi \pi^0$ . Green dashed:  $B^0 \rightarrow J/\psi K_S^0(\pi^0\pi^0)$  background. Yellow dashed: inclusive  $J/\psi$  background. Magenta dashed:  $B\bar{B}$  generic background. Red dashed: continuum background. Blue solid: total. The numerical results are given in Table 5.23.

These results, along with the possibility of observing penguin contributions in  $B^0 \rightarrow J/\psi \pi^0$ , and experimentally constraining such amplitudes in  $B^0 \rightarrow J/\psi K_S^0$ , are discussed in the next chapter.

# Chapter 6

## Conclusions

This chapter summarizes the results of the branching fraction and time-dependent  $CP$  asymmetry measurements in neutral  $B$  decays to  $J/\psi\pi^0$ . It compares the measurements from *BABAR* to those from Belle, as well as to the world averages. Relying on the formalism introduced in Chapter 2, these concluding sections present the constraints provided by the current measurements. There are also extrapolations to anticipated larger data samples.

### 6.1 Branching Fraction Measurement

The final result from Chapter 4 is the branching fraction for  $B^0 \rightarrow J/\psi\pi^0$  decays, measured at *BABAR* using  $20.7 \text{ fb}^{-1}$  of data:

$$\mathcal{B}(B^0 \rightarrow J/\psi\pi^0) = (2.0 \pm 0.6 \text{ (stat)} \pm 0.2 \text{ (syst)}) \times 10^{-5} . \quad (6.1)$$

This measurement dominates the 2002 PDG world average of  $\mathcal{B}(B^0 \rightarrow J/\psi\pi^0) = (2.1 \pm 0.5) \times 10^{-5}$  [25], which also includes a result from the CLEO2 experiment of  $\mathcal{B}(B^0 \rightarrow J/\psi\pi^0) = (2.0_{-0.9}^{+1.1} \text{(stat)} \pm 0.2 \text{ (syst)}) \times 10^{-5}$  [50]. The average does not yet include a preliminary result from the Belle collaboration using  $78.1 \text{ fb}^{-1}$  of data:  $\mathcal{B}(B^0 \rightarrow J/\psi\pi^0) = (1.8 \pm 0.3 \text{ (stat)} \pm 0.2 \text{ (syst)}) \times 10^{-5}$  [51].

As mentioned in Section 4.1, an expectation for the branching fraction, neglecting

contributions from penguin diagrams, can be estimated using

$$\mathcal{B}(B^0 \rightarrow J/\psi \pi^0)_{\text{expected}} = \lambda_{\text{CKM}}^2 \mathcal{B}(B^0 \rightarrow J/\psi K^0) . \quad (6.2)$$

Using the measured world average  $\mathcal{B}(B^0 \rightarrow J/\psi K^0) = (8.7 \pm 0.5) \times 10^{-4}$  and  $\lambda_{\text{CKM}} = 0.2229 \pm 0.0022$  [25], we calculate  $\mathcal{B}(B^0 \rightarrow J/\psi \pi^0)_{\text{expected}} = (4.3 \pm 0.3) \times 10^{-5}$ . This expectation and the measured result for  $B^0 \rightarrow J/\psi \pi^0$  agree in order of magnitude, but they differ by about  $3.5\sigma$ . This discrepancy is an indication of the importance of the penguin diagram contributions in  $B^0 \rightarrow J/\psi \pi^0$ .

For the sake of comparison, the *BABAR* measurement of the ratio of branching fractions for the charged modes,  $\mathcal{B}(B^\pm \rightarrow J/\psi \pi^\pm)/\mathcal{B}(B^\pm \rightarrow J/\psi K^\pm)$ , also using  $20.7 \text{ fb}^{-1}$  of data, is  $0.0391 \pm 0.0078$  (stat)  $\pm 0.0019$  (syst) [52]. This is consistent with  $\lambda_{\text{CKM}}^2 = 0.04968 \pm 0.00098$ , in contrast to the charged modes, where the ratio is  $0.024 \pm 0.006$ . The fact that the neutral mode includes an indication of penguin diagram contributions, but the charged mode does not, will motivate future studies.

A more general expression for the ratio of branching fractions, including the effects of penguin diagrams, is the following:

$$\frac{\mathcal{B}(B^0 \rightarrow J/\psi \pi^0)}{\mathcal{B}(B^0 \rightarrow J/\psi K^0)} = \lambda_{\text{CKM}}^2 [1 + r^2 - 2r \cos(\gamma - \delta)] , \quad (6.3)$$

where  $r$  is given in Equation 2.36,  $\gamma$  is one of the unitarity triangle angles (Equation 2.25), and  $\delta$  is given in Equation 2.32. The ratio of the world average measured neutral-mode branching fractions is used to place constraints on  $r$  and  $\delta$ . Figure 6.1 shows the  $1\sigma$ ,  $2\sigma$ , and  $3\sigma$  contours, using Equation 6.3, and fixing the value  $\gamma = 60^\circ$ , which lies in the favored range [25]. Note that the quantity  $r$  includes the factor  $\sqrt{\rho^2 + \eta^2}$ , which is approximately  $0.42 \pm 0.07$ . The contours provide evidence for penguin diagram contributions. It is interesting that the case with  $r = 1$ ,  $\gamma = 60^\circ$ , and  $\delta = 0^\circ$  reduces to the expression in Equation 6.2, so it is as equally improbable as the no penguin diagrams case.

Measuring the branching fraction of  $B^0 \rightarrow J/\psi \pi^0$  decays is important for two primary reasons. First, it enhances our understanding of a physical process, adding to

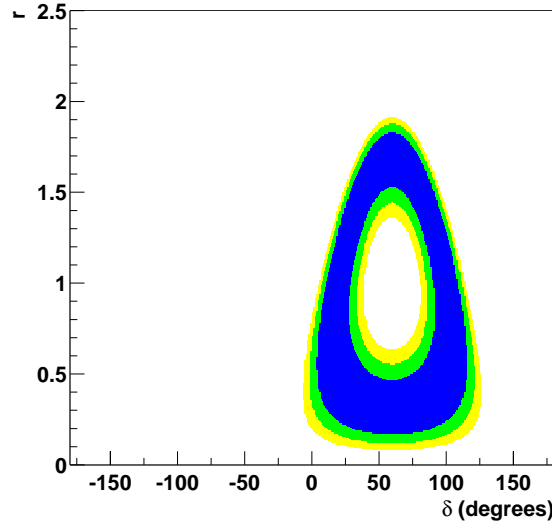


Figure 6.1: Constraints on  $r$  and  $\delta$  are shown, derived from the ratio of world average branching fractions of  $B^0 \rightarrow J/\psi \pi^0$  and  $B^0 \rightarrow J/\psi K^0$  decays. The contours correspond to  $1\sigma$  (blue),  $2\sigma$  (green), and  $3\sigma$  (yellow) constraints.

our overall picture of the interactions of particles. Second, it contributes to constraining the size of penguin contributions. As shown in the next section, the constraints on  $r$  and  $\delta$  from the ratio of branching fractions can be combined with similar constraints based on the  $CP$  asymmetry measurement in  $B^0 \rightarrow J/\psi \pi^0$  decays.

## 6.2 Time-Dependent $CP$ Asymmetry Measurement

The results of the  $CP$  asymmetry measurement, for  $B^0 \rightarrow J/\psi \pi^0$  decays, using  $81.1 \text{ fb}^{-1}$  of data collected at *BABAR*, as described in Chapter 5, are

$$\begin{aligned}
 C_{J/\psi \pi^0} &= 0.38 \pm 0.41 \text{ (stat)} \pm 0.09 \text{ (syst)} , & (\text{BABAR}) & & (6.4) \\
 S_{J/\psi \pi^0} &= 0.05 \pm 0.49 \text{ (stat)} \pm 0.16 \text{ (syst)} .
 \end{aligned}$$

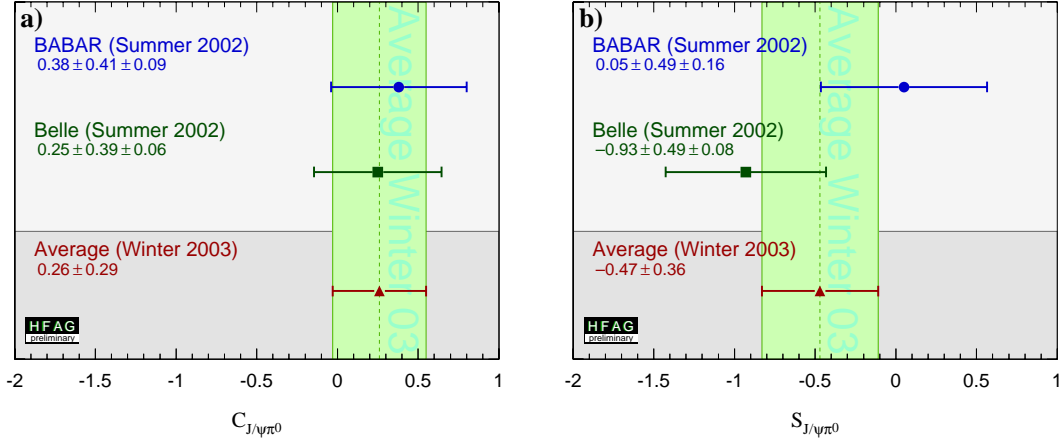


Figure 6.2: The results for the parameters (a)  $C_{J/\psi\pi^0}$  and (b)  $S_{J/\psi\pi^0}$  of the time-dependent  $CP$  asymmetry from *BABAR*, Belle, and the world average.

The Belle collaboration has produced preliminary results [53], on a similar data sample of  $78 \text{ fb}^{-1}$ , yielding the asymmetry parameters:

$$\begin{aligned} C_{J/\psi\pi^0} &= 0.25 \pm 0.39 \text{ (stat)} \pm 0.06 \text{ (syst)} , & (\text{Belle}) & \quad (6.5) \\ S_{J/\psi\pi^0} &= -0.93 \pm 0.49 \text{ (stat)} \pm 0.08 \text{ (syst)} . \end{aligned}$$

An average has been formed, taking into account the correlations between  $S_{J/\psi\pi^0}$  and  $C_{J/\psi\pi^0}$  of  $-0.12$  and  $-0.23$ , for *BABAR* and Belle, respectively. The world average coefficients of the cosine and sine terms of the asymmetry are:

$$\begin{aligned} C_{J/\psi\pi^0} &= 0.26 \pm 0.29 , & (\text{world average}) & \quad (6.6) \\ S_{J/\psi\pi^0} &= -0.47 \pm 0.36 . \end{aligned}$$

These results are summarized graphically in Figure 6.2, which shows that the results of the two experiments are in agreement.

When interpreting these results, it is important to recall that in the absence of

penguin contributions, the expectations for the coefficients are the following:

$$\begin{aligned} C_{J/\psi \pi^0} &= 0 , & (\text{without penguins}) & & (6.7) \\ S_{J/\psi \pi^0} &= -\sin 2\beta \approx -0.74 . \end{aligned}$$

With the current statistics, the *BABAR* results, the Belle results, and the world average are all consistent with Equation 6.7. However, as introduced in Section 2.4.3, we expect the tree and penguin amplitudes in  $B^0 \rightarrow J/\psi \pi^0$  to interfere with each other, and give asymmetry results different from those listed in Equation 6.7.

We have at our disposal the expressions for  $C_{J/\psi \pi^0}$  and  $S_{J/\psi \pi^0}$  that include the effects of the penguin diagrams:

$$\begin{aligned} S_{J/\psi \pi^0} &= \frac{-\sin 2\beta + 2r \sin(2\beta - \gamma) \cos(\delta) - r^2 \sin(2\beta - 2\gamma)}{1 + r^2 - 2r \cos(\gamma) \cos(\delta)} , & (6.8) \\ C_{J/\psi \pi^0} &= \frac{-2r \sin(\gamma) \sin(\delta)}{1 + r^2 - 2r \cos(\gamma) \cos(\delta)} , \end{aligned}$$

with

$$r = \sqrt{\rho^2 + \eta^2} \frac{P_u - P_t}{T + P_c - P_t} . \quad (6.9)$$

These allow us to investigate the constraints on the ratio of the penguin diagram amplitude to the tree diagram amplitude, both for the current data sample size and extrapolated for future large data samples. This can be done for  $B^0 \rightarrow J/\psi \pi^0$ , and with certain assumptions can be used to study the impact of penguin diagram contributions on the *CP* asymmetry in  $B^0 \rightarrow J/\psi K_s^0$ .

The expressions in Equation 6.8 are written in terms of  $r$  (Equation 6.9), the strong phase  $\delta$ , and the unitarity triangle angles  $\beta$  and  $\gamma$ . To investigate  $r$  as a function  $\delta$ , we select the measured value  $\beta = 23.9^\circ$ , corresponding to  $\sin 2\beta = 0.74$ , and use the value  $\gamma = 60^\circ$ . A plot of the  $1\sigma$ ,  $2\sigma$ , and  $3\sigma$  contours in the  $r$  versus  $\delta$  plane is shown in Figure 6.3 for the world average  $B^0 \rightarrow J/\psi \pi^0$  asymmetry results, using the current uncertainties. This figure shows that the current results already provide a weak upper-bound on the penguin contributions.

To predict the constraint on  $r$  available from a considerably larger data sample,

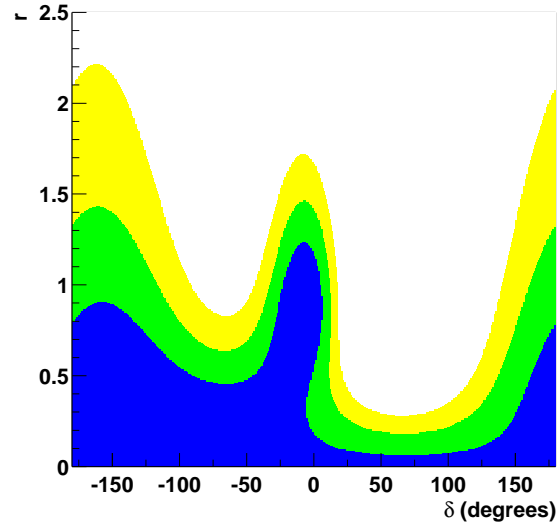


Figure 6.3: Constraints on  $r$  and  $\delta$  are shown for the world average  $CP$  asymmetry results for  $B^0 \rightarrow J/\psi \pi^0$  decays. The contours correspond to  $1\sigma$  (blue),  $2\sigma$  (green), and  $3\sigma$  (yellow) constraints.

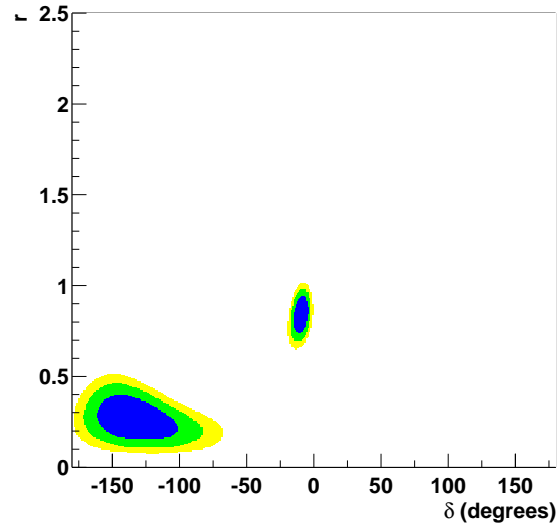


Figure 6.4: Constraints on  $r$  and  $\delta$  are shown for the world average  $CP$  asymmetry central values for  $B^0 \rightarrow J/\psi \pi^0$  decays, but with uncertainties extrapolated to  $2\text{ab}^{-1}$ . The contours correspond to  $1\sigma$  (blue),  $2\sigma$  (green), and  $3\sigma$  (yellow) constraints.

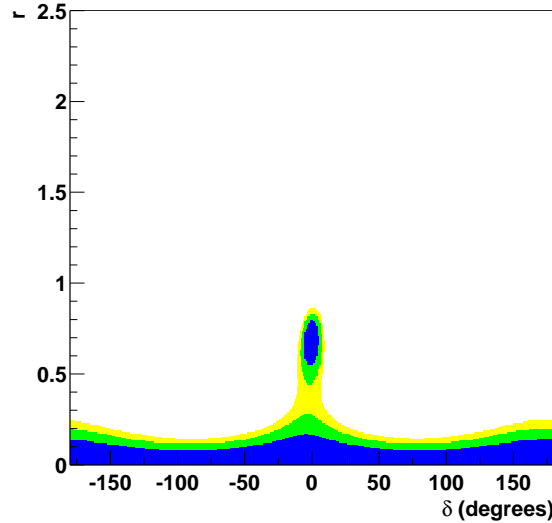


Figure 6.5: Constraints on  $r$  and  $\delta$  are shown assuming  $C_{J/\psi\pi^0} = 0$  and  $S_{J/\psi\pi^0} = -0.74$ , with uncertainties extrapolated to  $2ab^{-1}$ . The contours correspond to  $1\sigma$  (blue),  $2\sigma$  (green), and  $3\sigma$  (yellow) constraints.

the world average central values for the  $B^0 \rightarrow J/\psi\pi^0$  asymmetry results are again used, but with uncertainties projected for  $2ab^{-1}$ . The uncertainties are 0.085 and 0.10, for the  $C_{J/\psi\pi^0}$  and  $S_{J/\psi\pi^0}$  terms, respectively. The plot of  $r$  versus  $\delta$  under these conditions is shown in Figure 6.4. There are two distinct regions. Although the solution around  $\delta = -130^\circ$  has a larger area, there is an ambiguity between two such regions. Such a large data sample, which provides the visible constraints on  $r$  and  $\delta$ , is obtainable at the  $B$  Factories, after potential accelerator and detector upgrades.

Another study examines a case where we set the central values for the  $CP$  asymmetry in  $B^0 \rightarrow J/\psi\pi^0$  decays to match the prediction corresponding to no penguin contributions (Equation 6.7). This is done for an extrapolation to  $2ab^{-1}$  of data, again assuming  $\beta = 23.9^\circ$  and  $\gamma = 60^\circ$ . The contours are shown in Figure 6.5. The constraints show to what degree such a measurement would begin to rule out penguin contributions. This would be a surprising scenario, given the present indications for penguin contributions.

As mentioned at the end of Section 6.1, the constraints on  $r$  and  $\delta$ , from the

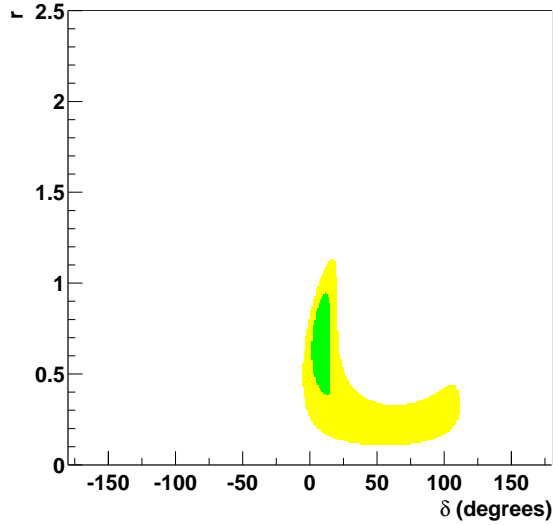


Figure 6.6: Constraints on  $r$  and  $\delta$  are shown for the combination of the world average  $B^0 \rightarrow J/\psi \pi^0$  asymmetry and the ratio between the world average branching fractions of  $B^0 \rightarrow J/\psi \pi^0$  and  $B^0 \rightarrow J/\psi K^0$ . The contours correspond to  $2\sigma$  (green) and  $3\sigma$  (yellow) constraints.

asymmetry measurement in  $B^0 \rightarrow J/\psi \pi^0$  and from the ratio of branching fractions of  $B^0 \rightarrow J/\psi \pi^0$  and  $B^0 \rightarrow J/\psi K^0$  decays, can be combined. The resulting contours, using the world averages for the branching fractions and asymmetry measurements, are shown in Figure 6.6. These contours use the values  $\beta = 23.9^\circ$ ,  $\gamma = 60^\circ$ , and  $\lambda_{\text{CKM}} = 0.2229$ . The figure shows that the two sets of constraints, when combined, do not have a  $1\sigma$  overlap. They give a single region with  $2\sigma$  and  $3\sigma$  constraints.

It is worth noting the dependence on the value of  $\gamma$  for the contours derived from the ratio of branching fractions and  $CP$  asymmetry measurements, as well as for the combined contours. The expression for the ratio of branching fractions (Equation 6.3) contains the term  $\cos(\gamma - \delta)$ , so higher values of  $\gamma$  shift the contours in Figure 6.1 to the right (higher  $\delta$ ), while lower values of  $\gamma$  shift the contours to the left (lower  $\delta$ ). The dependence is more complicated for the contours constructed using the  $CP$  asymmetry results. For higher values of  $\gamma$ , the region near  $\delta = \pm 180^\circ$  reaches to higher values of  $r$ , while the extent of the bump in  $r$  near  $\delta = 0^\circ$  is diminished. The reverse

is true for lower values of  $\gamma$ . This is true, at least, for values of  $\gamma$  within  $\pm 15^\circ$  of the favored value of  $60^\circ$ . The impact on the contours derived from the combination of the two measurements is that for higher values of  $\gamma$ , the allowed region shifts downward and to the right in the  $r$  versus  $\delta$  plane, while for lower values of  $\gamma$  the allowed region shifts mostly to the left, with more overlap.

As a final study, values of  $r$  from the  $B^0 \rightarrow J/\psi \pi^0$  asymmetry measurement are used to constrain the possible difference, due to penguin diagram contributions, between the coefficient of  $\sin(\Delta m_d \Delta t)$  that is extracted by the measurement of the  $CP$  asymmetry in  $B^0 \rightarrow J/\psi K_s^0$  decays,  $S_{J/\psi K_s^0}$ , and the value of  $\sin 2\beta$ . The difference between these two quantities, up to order  $\lambda_{\text{CKM}}^2$ , is

$$S_{J/\psi K_s^0} - \sin 2\beta = -2\lambda_{\text{CKM}}^2 r \cos(2\beta) \sin \gamma \cos \delta . \quad (6.10)$$

Figure 6.7(a) shows the  $1\sigma$  constraints on this difference, as a function of integrated luminosity, for a possible value of  $r$  derived from the current world average  $B^0 \rightarrow J/\psi \pi^0$  asymmetry central values. The other parameters are taken to be  $\beta = 23.9^\circ$  and  $\gamma = 60^\circ$ . The chosen values of  $r$  corresponds to the solution near  $\delta = 0^\circ$  in Figure 6.4. In this study,  $\cos \delta$  is set at  $\pm 1$ , corresponding to  $\delta = 0^\circ$  or  $\delta = 180^\circ$ . This places an upper bound on the impact of  $\delta$  on  $|S_{J/\psi K_s^0} - \sin 2\beta|$ . Figure 6.7(b) shows a similar constraint, but using a value of  $r$  that assumes  $C_{J/\psi \pi^0} = 0$  and  $S_{J/\psi \pi^0} = -0.74$ , neglecting the small non-zero solution at  $\delta = 0^\circ$  shown in Figure 6.5. For both Figures 6.7(a) and (b), the  $1\sigma$  constraints are shown before and after the inclusion of theoretical uncertainties. A 20% uncertainty is given for the possibility of  $SU(3)$  symmetry breaking, applicable here because of uncertainties as to whether or not the quantity  $r$  is identical for decays of the type  $\bar{b} \rightarrow c\bar{c}\bar{d}$  and decays of the type  $\bar{b} \rightarrow c\bar{c}\bar{s}$ . An uncertainty due to possible final state rescattering is not included.

Constraining the size of the possible discrepancy, due to penguin diagram contributions, between what is measured for the asymmetry coefficient in  $B^0 \rightarrow J/\psi K_s^0$  decays and the true value of  $\sin 2\beta$  is particularly important if the size of the difference is comparable to, or larger than, some of the theoretical uncertainties in the prediction of the value of  $\sin 2\beta$ . At the higher end of the range shown in Figure 6.7(a),

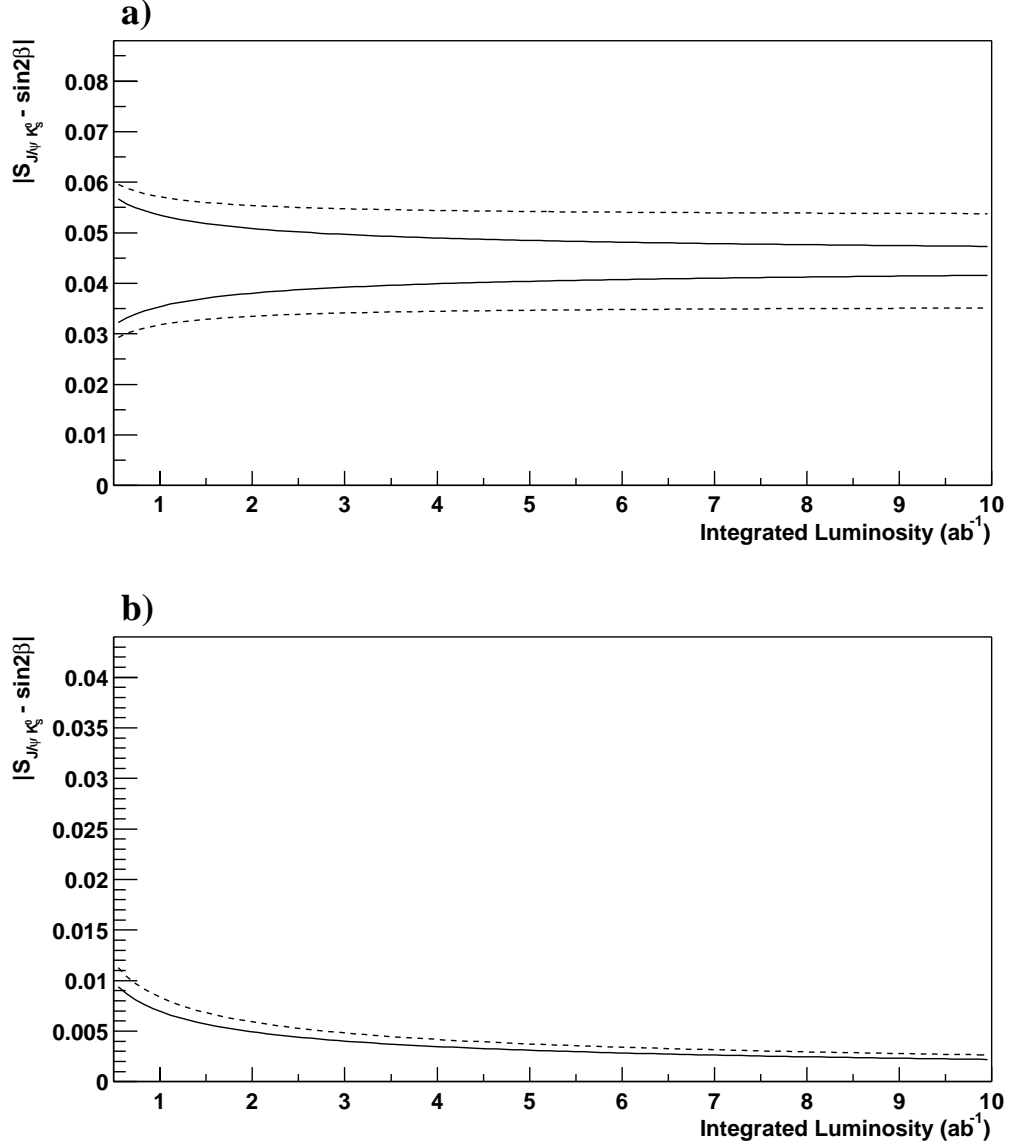


Figure 6.7: Constraints on  $|S_{J/\psi K_S^0} - \sin 2\beta|$  as a function of integrated luminosity. The  $1\sigma$  constraints are shown for (a) the world average central value for  $r$  obtained from the  $B^0 \rightarrow J/\psi \pi^0$  asymmetry measurement and (b) for values corresponding to  $C_{J/\psi \pi^0} = 0$  and  $S_{J/\psi \pi^0} = -0.74$ . Note that the vertical scales are different in (a) and (b). The solid lines neglect theoretical uncertainties from SU(3) symmetry breaking, while the dashed lines include these uncertainties.

this appears to be the case. It also becomes more relevant as the measurement gains precision, and as we start to include other information in the extraction of  $\sin 2\beta$  from the asymmetry measurement, such as the contribution of higher-order terms in the expansion of the Wolfenstein parameterized CKM matrix elements.

### 6.3 Final Thoughts

The understanding of  $CP$  violation has come a long way since its discovery in 1964 in the kaon system. Theoretical work predicted large  $CP$  violating effects in the  $B$ -meson system and proposed a rich formalism with relationships between measurable quantities and model parameters. The  $B$ -Factories have observed  $CP$  asymmetries in  $B$  decays, measuring  $\sin 2\beta$  to high precision. This has served as a confirmation of the CKM picture, and has prompted us to look more deeply for clues about the matter–antimatter asymmetry of the universe.

The decay  $B^0 \rightarrow J/\psi \pi^0$  provides an arena for studying the influence of penguin diagram contributions. It has tree and penguin amplitudes that enter at similar levels and the interference between the two may yield a  $CP$  asymmetry result that differs from that of  $B^0 \rightarrow J/\psi K_S^0$ . The measurements presented in this thesis have been used to constrain the size of the penguin contributions in  $B^0 \rightarrow J/\psi \pi^0$ , and have been applied to place constraints on the impact of penguin contributions on the  $CP$  asymmetry measurement in  $B^0 \rightarrow J/\psi K_S^0$ .